Cape Peninsula
University of Technology

Optimisation of Solid Rocket Motor Blast Tube and Nozzle Assemblies using Computational Fluid Dynamics.

by

Kelly Burchell Scholtz

Thesis submitted in fulfilment of the requirements for the degree

Master of Technology: **Mechanical Engineering**

in the Faculty of **Engineering**

at the Cape Peninsula University of Technology

Supervisor: **Prof. Graeme J. Oliver**

Bellville
February 2017

Declaration

I declare that the contents of this thesis represent my own unaided work, and that the thesis has not previously been submitted for academic examination towards any qualification. Furthermore, it represents my own opinions and not necessarily those of the Cape Peninsula University of Technology.

Signed this ___ day of _____ 20___

_____

Kelly Burchell Scholtz.

Abstract

A framework for optimising a tactical solid rocket motor nozzle is established and investigated within the ANSYS Workbench environment. Simulated results are validated against thrust measurements from the static bench firing of a full-scale rocket. Grid independence is checked and achieved using inflation based meshing. A rocket nozzle contour is parametrized using multiple control points along a spline contour. The design of experiments table is populated by a central composite design method and the resulting response surfaces are used to find a thrust optimised rocket nozzle geometry. CFD results are based on Favre-mass averaged Navier-Stokes equations with turbulence closure implemented with the Menter SST model. Two optimisation algorithms (Shifted Hammersley Sampling and Nonlinear Programming by Quadratic Lagrangian) are used to establish viable candidates for maximum thrust. Comparisons are made with a circular arc, Rao parabolic approximation and conical nozzle geometries including the CFD simulation there-off. The effect of nozzle length on thrust is simulated and optimised within the framework. Results generally show increased thrust as well as demonstrating the framework's potential for further investigations into nozzle geometry optimisation and off-design point characterisation.

Published Work

The following paper has been submitted for review to the journal *Aerospace Science and Technology*:

- K.B. Scholtz and G.J. Oliver. Design optimisation of tactical solid rocket motor nozzles. *Submitted for review to Aerospace Science and Technology*, May 2016.

Contents

List of Figures

List of Tables

List of Abbreviations

AoA	Angle of Attack
CCD	Central Composite Design
CFD	Computational Fluid Dynamics
DOE	Design of Experiments
DOF	Degrees of Freedom
DNS	Direct Numerical Simulation
LES	Large Eddy Simulation
NLPQL	Nonlinear Programming by Quadratic Lagrangian
NPR	Nozzle Pressure Ratio
RANS	Reynolds-Averaged Navier-Stokes
SST	Shear Stress Transport

List of Symbols

a	Speed of sound
a_0	Total speed of sound
a^*	Characteristic speed of sound
A, A_n	Area and Area at n
A^*	Characteristic Area
c_p	Specific heat of gas at constant pressure
c_v	Specific heat of gas at constant volume
D_ω	Cross diffusion term
ρ	Density
ρ_0	Total density
ρ^*	Characteristic density
$\bar{G}_k$	Generation of k due to mean velocity gradients
G_ω	Generation of ω
e	Internal energy
E	Total energy
F_m	Momentum thrust
F_t	Total thrust
F_p	Pressure thrust

$\vec{F}$	Body forces
γ	Specific heat ratio
$\vec{g}$	Gravitational acceleration
h	Enthalpy
I	Unit tensor
$\vec{J}_j$	Diffusion flux of species j
k	Thermal conductivity or turbulent kinetic energy as specified in the text
k_{eff}	Effective thermal conductivity
k_t	Turbulent thermal conductivity
$\dot{m}$	Mass flow rate
M	Mach number
M_∞	Free stream Mach number
M^*	Characteristic Mach number
$\ddot{M}$	Molecular weight
γ	Turbulence kinetic energy dissipation rate
$\Gamma_{\omega,k}$	Effective diffusivity of ω or k
ω	Specific dissipation rate
p	Pressure
p_0	Total pressure
p^*	Characteristic pressure
$\dot{Q}$	Total rate of heat addition
q	Heat

r_i	Radius of curvature of initial expansion
R_n	Radius of control point n at x_n
R_e	Radius at nozzle exit
R	Specific gas constant
$\grave{R}$	Universal gas constant
$d\mathbf{S}$	Elemental area on the surface S
S	Area of closed surface S
s	Entropy
S_m	Mass source term
S_E	Potential energy source term
S_h	Heat source term
S_{Mn}	Source term for body forces along axis n
S_ω,S_k	User defined source terms
T	Temperature
T^*	Characteristic temperature
T_0	Total Temperature
τ	Compressibility of fluid
τ_{nn}	Viscous stresses on plane nn
$\overline{\overline{\tau}}$	Stress tensor
τ_T	Isothermal compressibility
τ_s	Isentropic compressibility
θ_i	Initial expansion angle

θ_e	Final expansion angle
u, v, w	x,y,z components of Velocity
u_i	Is the sum the mean and fluctuating velocity components with $i = 1, 2, 3$
μ	Molecular viscosity
V	Velocity
$\mathbf{V}$	Local Velocity
$\vec{v}$	Velocity vectors u,v,w
v	Specific volume or y component of velocity as specified in the text
x_n	Distance to control point n from nozzle exit
x_t	Nozzle length
$Y_{\omega,k}$	Dissipation of ω or k due to turbulence

1 Overview and Rationale

1.1 Introduction

There are high demands being placed on the improvement in performance of tactical missile solid rocket motors (SRM's). This is partly due to the rate at which threats are evolving (faster, more agile and the improved ability to detect incoming missiles) and with the increased performance of competing missile systems there are strong demands on larger stand-off distances to improve survivability of the launching platforms (i.e. faster and longer range missiles are required). The implication being that there are increasing demands on shorter design cycles to keep up with the evolving threats. Computational fluid dynamics (CFD) is used alongside traditional design and experimental approaches. CFD enables improved evaluation of concepts and a better understanding of the flow field within a particular SRM blast tube and nozzle system. The type of SRM being studied typically produces gas flow within the blast tube–nozzle assembly with velocities in the region of Mach 4 and the effect of turbulence being significant. CFD simulations at these flow rates tend to be unstable and maintaining low cell Courant numbers is difficult.

Although analytical solutions can be useful in early design stages they inherently fall short in representing the complexity of the system being studied. Zikanov (2010) in his book "Essential Computational Fluid Dynamics" demonstrates the limitations of an analytical approach by looking at the Poiseuille's solution for flow in an infinitely long pipe; although the solution is insightful, it is only correct for an infinitely long pipe with constant temperature and a perfectly incompressible fluid. Experimental work can be invaluable in the design process and it is often the only way to evaluate and verify the final design, however, in the early design stages, it can be costly and time-consuming. CFD allows for a rapid evaluation of concepts and a better understanding of the complexity of fluid systems. The flow in a solid rocket motor is indeed a complex system; it is a time-dependent, compressible, chemically reacting supersonic flow with heat transfer and complex shock structures. The uses and benefits of CFD are already clearly demonstrated extensively in the industry (Yumuşak and Eyi, 2012; Yumuşak, 2013; Hunter, 1998; Chen

et al., 2011; Ewing *et al.*, 2012). The purpose of this study is to apply this method to an industry specific problem (namely a tactical SRM nozzle) and develop a working procedure for evaluating, testing and optimising current and future designs. There has already been considerable work done on the topic as is demonstrated in Section 1.5, however, there is still little information available to suit more defence specific requirements and designs. Tactical missile nozzles differ from conventional space application rockets in that they often require an extension between the rear of the motor and the nozzle (commonly known as the blast tube) to balance the center of gravity (Sutton and Biblarz, 2001) and also provide an area to mount a thrust vector control guidance system that could operate within the exhaust plume while still maintaining the overall rocket diameter (Ellis and Berdoyes, 2012). Tactical nozzles are generally of considerably smaller scale than space application nozzles with air-to-air tactical nozzle exit diameters typically < 200 mm calibre. Tactical SRM nozzles are often operating at under-expanded conditions (see Chapter 2) due to space limitations when compared with a typical space launch nozzle running close to the optimum area and expansion ratios. Available nozzle optimisation works tend to focus on space application liquid propellant (Cai *et al.*, 2007; Yumuşak and Eyi, 2012) and SRM nozzles (Balabel *et al.*, 2011, 2009; Yumuşak, 2013) which do not include blast tubes in the simulation and optimisation process. Limited works that include blast tube design have been done by Tahsini and Ebrahimi (2006) and Javed *et al.* (2013) and focus on blast tube diameters, lengths and roughness effects on pressure and thrust and do not include nozzle contour design.

This work develops a framework within the ANSYS Workbench environment to parametrize, mesh, solve and optimise tactical SRM nozzle contours. The focus is on thrust as the objective function and goes on to include reducing nozzle length while attempting to maintain maximum thrust. The response surface optimisation method (ANSYS, 2015a) is used. The response surfaces allow for fewer design cycles to be run by providing various interpolation methods between simulated design points. A face-centered central composite design (CCD) was used as a design of experiments (DOE) sampling scheme. Two response surface types are used; namely a full 2^{nd}-order polynomial for initial surfaces and a Kriging algorithm for further refinement and improved fit for higher order variations. The characterised simulation responses are then put through a Shifted Hammersley Sampling (Screening) and Nonlinear Programming by Quadratic Lagrangian (NLPQL) optimisation algorithm. The CFD solutions are handled through ANSYS Fluent and are based on RANS equations for compressible flow with turbulence closure implemented with the Menter SST model.

1.2 Problem Statement

Develop a simulation and optimisation process applicable to tactical missiles to determine the optimal nozzle geometry for maximum thrust for given operating conditions.

1.3 Aims of the Research

- Optimise rocket nozzle contours for maximum thrust using CFD.

- Develop a parametric framework that allows for nozzle optimisation to be implemented across multiple nozzle applications and conditions with a minimum user input.

- Validate computational fluid dynamic findings with experimental and theoretical results.

1.4 Limitations of the Study

The emphasis of this research is on finding optimum geometry by way of an ANSYS Workbench framework for a tactical SRM blast tube and nozzle assembly using CFD for use in the defence industry. The work is limited to nozzle contour and length variations at steady state operating conditions for chemically frozen flow. The work is further limited to only the blast tube and nozzle assemblies and assumes incoming boundary conditions from the rocket motor grain or combustion chamber based on internal ballistic simulations (not included in this work).

1.5 Literature Review

CFD is used extensively in the aerospace industry, with the early development of CFD in the 60's and 70's being driven by the aerospace industry itself (Anderson, 1995). It has since been commonly used as a tool for evaluating rocket nozzles and their associated phenomena. Relevant early works by Sabnis *et al.* (1989) and Lupoglazoff and Vuillot (1992) demonstrated the use of CFD for turbulent compressible flow in rocket motors. The former using a modified $k - \epsilon$ turbulence model to successfully simulate internal flow in a planar nozzle-less solid rocket cold-flow model. The latter having simulated internal vortex shedding phenomenon for an SRM with both viscous and inviscid flow regimes (Navier-Stokes and Euler respectively). Deshpande *et al.* (2014), Biju Kuttan and Sajesh

(2013) and Natta *et al.* (2012) all used the CFD software ANSYS Fluent with some success to analyse a convergent-divergent rocket nozzle. Their works were similar in looking at varied divergent angle axisymmetric conical nozzles. They generally were able to compare the effects of divergent angle on static pressure, velocity, temperature and turbulence intensities. Their works had limited experimental validation of the CFD results but did show agreement with theoretical calculations. Natta *et al.* (2012)'s work was not validated but could be confirmed using one-dimensional theory that can be generally applied directly to conical nozzles. The work was limited to near ambient temperature air as the working fluid. These works all clearly show CFD's ability to capture the basic physics of convergent-divergent nozzle flow. Namely, choked Mach 1 throat conditions with further expansion leading to increased fluid velocities. There is also evidence of its ability to capture wall bounded flow effects on the working fluid, seen in the near wall velocity and temperature profiles.

Turbulence causes eddies in the flow with varied scales of time and length. Capturing the effects of this turbulence is an important aspect of CFD modelling and simulation as it can have a large effect on the results. A method for capturing the effect of turbulence is, therefore, vital to the success of the simulation. The industry common current methods can be grouped into three main categories, namely: Turbulence models for RANS equations, LES and DNS (Orszag, 1970). A full description of the methods can be found in Versteeg and Malalasekera (2007) from which the brief descriptions to follow are summarised. For the purpose of this work it is sufficient to mention that DNS is completely beyond the scope of this work in terms of computational resources and industrial feasibility. DNS involves capturing all the turbulent time and length scales, necessitating grids fine enough to capture the Kolmogorov length scales as well as time steps that are smaller than the period of the fastest fluctuations. LES involve resolving the larger eddies above a set cutoff length found suitable to the problem. While the smaller eddies are described by a sub-grid-scale stresses model. LES shows good progress in industry and the ability to model flow instabilities being well suited to many problems, with only a modest increase in computational requirements. LES is three-dimensional by nature, not well validated for rocket nozzle flow and beyond the scope of application of this work which will concentrate on axisymmetric simulations using RANS. With RANS, the additional terms appearing due to the interactions between the various turbulent fluctuations need closure; this is achieved by the implementation of various turbulence models which predict the Reynolds stresses and scalar transport terms. Well known turbulent models for RANS are the Spalart-Allmaras (Spalart and Allmaras, 1992), $k-\epsilon$ (Launder and Spalding, 1974), $k-\omega$ (Wilcox, 2008), Menter SST model (Menter, 1993), Algebraic stress model and Reynolds stress model . Literature shows common use of the $k-\epsilon$ model with Deshpande *et al.* (2014), Biju Kuttan and Sajesh (2013), Yumuşak (2013) and Wang *et al.* (2014)

all using it to successfully model rocket nozzle flows. However, Balabel *et al.* (2011)'s comparison on the various turbulence models and their ability to predict flows in rocket nozzles with varied NPR's (nozzle pressure ratios) showed with validation that the Menter SST turbulence model gave the best overall performance in terms of computational time and accuracy. It was concluded that this may be attributed to the gradual transition from the standard $k-\omega$ model at the near-wall region to the $k-\epsilon$ model in the fully turbulent region further from the wall. Their work tested the turbulence models against experimental measurements taken by Hunter (1998). Further use of the SST model in rocket applications was demonstrated by Ostlund and Jaran (1999) with both works concluding that the Menter SST $k-\omega$ model showed good agreement when predicting turbulent flow characteristics in sonic rocket nozzles. It is however noted that the standard $k-\epsilon$ and $k-\omega$ models also show reasonable agreement with experimental results, particularly with full flowing nozzles. The work by Versteeg and Malalasekera (2007) concluded that tests showed the SST model to have superior performance for zero pressure gradients and adverse pressure gradient boundary layers, free shear layers and a NACA4412 aerofoil. It was also noted that it made for a good general purpose turbulence model. With the growing use of the SST model in industry evident and the general success demonstrated in the literature, this work will use the Menter SST $k-\omega$ model (with validation) to simulate and optimise SRM nozzle flow.

Due to the accessibility and constraints on experimental test firings of full-scale rocket motors, there is limited data available to correlate CFD results with. The literature generally reflects this; often sub-scale tests using non-reacting gases are used in the validation of their results. Sub-scale experimental results for the J-2S nozzle (Nave and Coffey, 1973) have been used by Moríñigo and Salvá (2008) in validating their CFD work on the start-up process in an optimised rocket nozzle. Their work showed good agreement with experimental results and highlights the ability of CFD to capture the complex flow phenomena such as flow separation from the nozzle wall and the detection of compression and expansion waves within the nozzle. The ability to simulate these flow features are important when working with nozzle optimisation; flow separation during the start-up and shutdown of a rocket motor can cause large side loading on the nozzle while shock-waves within the nozzle are associated with velocity drops and can affect the performance negatively. The experimental work done by Hunter (1998) and Mason *et al.* (1980) have well-documented wall and center-line pressure results for experimental two-dimensional non-axisymmetric nozzles. The former having simulation results in good agreement with experimental results (for NPR's ≥ 2) when using the RANS code PAB3D and the $k-\epsilon$ turbulent model. Both works used air as the working fluid for experimental purposes.

Numerical optimisation methods for rocket nozzles were notably demonstrated by Rao

(1958) in which he used the calculus of variation and method of characteristics to describe isentropic flow within a nozzle and from which, construct a thrust optimised nozzle contour. Although not the first use of the method of characteristics for nozzle design (Anderson, 1995), Rao's method improved on previous works by reducing the complexity of the solution by using; prescribed sonic and subsonic radii in the throats, fixed length nozzle, working from a design exit Mach number characteristic line and having a control surface defined by the latter. This work formed the basis for later parabolic approximations for a typical Rao nozzle (Sutton and Biblarz, 2001; Rao, 1961, 1960). Rao's work demonstrated the ability of a contoured nozzle (of shorter length) to outperform a more conventional conical nozzle. The above work was based on the assumption of inviscid isentropic flow, and further allowances would be needed to account for boundary layer effects.

A paper by Allman and Hoffman (1981) demonstrated a direct optimisation approach to nozzle design as well as early parametrization of nozzle contours, a polynomial ($y(x) = a + bx + cx^2$ with a,b and c defined by θ_a and y_e, initial angle of expansion and nozzle exit radius respectively) is used to parametrize the exit contour. The direct optimisation approach allowed for off-design variables to be considered and results were comparable to Rao nozzles of various lengths. With modern computing it is now possible to solve the full RANS equations for viscous flow, allowing for a more detailed nozzle contour optimisation. An SRM nozzle is primarily designed to efficiently expand the hot exhaust gases to deliver maximum thrust to the missile, the objective function of optimisation being to maximise thrust. Cai *et al.* (2007); Yildizlar and Eyi (2014); Yumuşak and Eyi (2012) did work on nozzle optimisation aimed at maximising rocket nozzle thrust. With objective functions all defined as the integral form of the rocket nozzle thrust equation (see Equation 2.5), namely $F_t = \int_{A_2} \left(\rho u^2 + p\right) dA$. Cai *et al.* (2007) ran optimisation algorithms (Successive quadratic programming, Genetic algorithm and Interdigitation strategy) on nozzle contour design with the Genetic algorithm and Interdigitation strategy both producing similar results showing theoretical increases in thrust coefficients of 1.448 % and 1.501 % respectively. Attributing these results to the reduction in friction and divergent losses obtained via optimised geometry. The Successive quadratic programming algorithm reportedly failed to produce a global optimum, assuming that the successful results from the prior two methods are the benchmark for a global optimum. Parametrization was achieved with a 7 control point cubic function describing the contour, using fixed distances from the exit for the control points x positions. Work on design optimisation by Yumuşak and Eyi (2012) showed the effect of shape function in their case on optimisation results, showing a 4.09 % thrust increase with Hicks-Henne shape function over baseline and 1.63 % over a Taurus-II nozzle. This could be contributed to the inherent ability of the geometric shapes produced by the various functions being more suited to efficient supersonic expansion however the possibility exists that a specific shape function is

merely more suited to the specific optimisation algorithm used. Their work used a gradient based optimisation algorithm. Similarly, work by Yumuşak (2013) on viscous flow rocket motor design optimisation used a gradient-based numerical optimisation model within the commercially available constrained optimisation package DOT, results showed a 3.09 % increase in thrust using a Hicks-Henne shape function compared to 0.71 % increase using Wagner shape functions.

The reasons behind the choices made in using certain optimisation algorithms are unclear from the limited rocket specific literature available. The choice of Cai *et al.* (2007) to use a genetic algorithm is in line with optimisation trends in building optimisation literature (Nguyen *et al.*, 2014; Corbera *et al.*, 2016; Uebel *et al.*, 2016) which are based on the genetic algorithms abilities for searching large search spaces as well as being a global optimisation routine. It does not, however, guarantee a local minimum (Nguyen *et al.*, 2014). Its main differentiating factor as used in the MOGA method is that it is suited for multiple objective function optimisations with discontinuous functions where local optimum traps are likely (ANSYS, 2015a). A strategy suggested is to use a global approach (genetic algorithm) to explore the initial local optimum areas and further optimise these areas using more accurate local algorithms (gradient based) in search of the global optimum.

A recent paper by Schomberg *et al.* (2014) presented at the 50th Joint Propulsion Conference highlighted a method of parametrization for nozzle contours using a series of circular arcs, the results of which showed possible reductions in nozzle length of equivalent conventional nozzle contours without a reduction in thrust. With the advent of high-speed computing, the trend for nozzle design is towards using a parametric design solution which allows greater flexibility than the traditional design charts, table 1.1 below presents an overview of the limited optimisation specific literature available. This work will contribute to the parametrisation and optimisation methods for tactical SRM nozzles detailed above.

Table 1.1: Nozzle Optimisation Literature Overview

Article/Paper	**Solution Method**	**Viscous Treatment**	**Geometry/ Parametrization**	**Optimisation**	**Result**	**Comments**
(Yildizlar and Eyi, 2014)	3D Euler equations using Newton's method.	Inviscid.	3D Planar nozzle using Hicks-Henne Shape function for expansion contour only.	Gradient Method.	0.36% thrust increase.	Unknown baseline geometry background and lack of validation.
(Schomberg *et al.*, 2014)	Axisymmetric and 3D RANS.	Spalart–Allmaras and Menter SST.	Finite series of circular arcs.	User varied parameters.	7.5% length reduction compared with scaled Vulcain 2 Rao nozzle.	Only single arc was demonstrated. Possibility of this method being developed further.
(Biju Kuttan and Sajesh, 2013)	Axisymmetric RANS.	$k-\epsilon$.	Divergent angle controlled conical nozzle.	User varied parameters.	15°shock-free nozzle.	Optimisation of conical nozzles is not current.
(Cai *et al.*, 2007)	Lower-Upper decomposition for solving Navier-Stokes, Euler and species transport equations.	Inviscid and Navier-Stokes.	7 control points cubic spline interpolation.	Successive quadratic programming, genetic algorithm and interdigitation strategy.	1.5 % thrust increase.	Unknown baseline geometry background. Inclusion of chemically reacting flow.

Table 1.1 Continued: Nozzle Optimisation Literature Overview

(Rao, 1958)	Calculus of variation.	Inviscid.	Method of Characteristics construction.	Finite Solution.	Reduced length thrust optimised nozzles compared to conical nozzles.	Excellent results even by modern standards. Good benchmark case. Used extensively.
(Wang, 2013)	Axisymmetric RANS.	Spalart–Allmaras.	Rao, Conical and User Defined.	User varied parameters	Increased thrust	Results not clear and lack of validation.
(Yumuşak, 2013)	Explicit finite difference method used to solve axisymmetric RANS	$k - \epsilon$.	Hicks-Henne, Wagner and patched polynomial shape function for expansion contour only.	DOT (gradient-based optimisation package).	3.09 % thrust increase with Hicks-Henne shape function over baseline.	Conical nozzle used as a baseline. Includes combustion chamber geometry optimisation.
(Yumuşak and Eyi, 2012)	Axisymmetric Euler equations and finite rate chemistry model using Newton's method.	Inviscid	Hicks-Henne, Wagner and patched polynomial shape function for expansion contour only.	DOT (gradient-based optimisation package).	4.09 % thrust increase with Hicks-Henne shape function over baseline and 1.63 % over Taurus-II nozzle.	Baseline is a conical nozzle. No comparison with non-reacting flow made.

2 Fluid Flow in Rocket Nozzles

2.1 Fundamentals

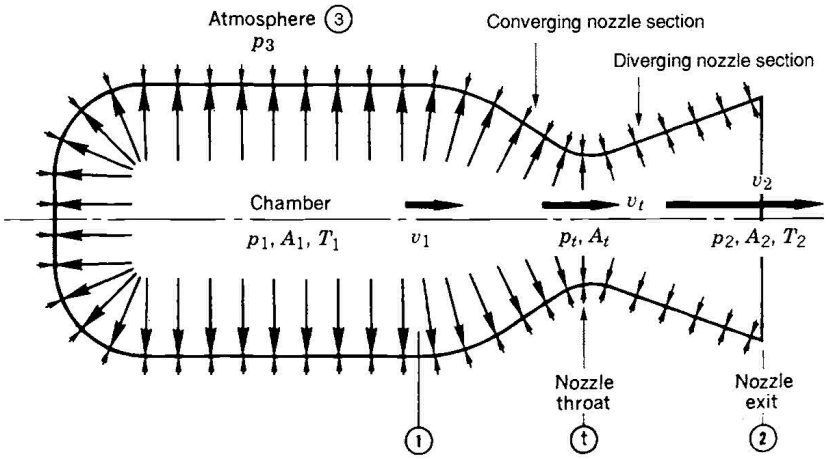

Figure 2.1: Representative rocket motor pressure balance (Sutton and Biblarz, 2001)

A rocket is a device that generates thrust by the high-speed ejection of particles through a nozzle. Pressure is generated in the combustion chamber which produces a longitudinal pressure imbalance (see Figure 2.1). The imbalance acting on the front of the chamber is a consequence of the polar opening at the rear (nozzle). The effect of this imbalance is to accelerate the gases through the nozzle. With a super-sonic nozzle, the further expansion after the throat produces an increase in particle speed which further adds to the imparted momentum. The bulk of the thrust is produced though this principle and is suitably named the *momentum thrust*, it is shown to be (Sutton and Biblarz, 2001)

$$F_m = \int_{A_2} \left(\rho u_2^2\right) dA \tag{2.1}$$

which for quasi-one-dimensional flow (i.e. constant cross-sectional flow properties) is shown

to be

$$F_m = \dot{m} u_2 \tag{2.2}$$

A second contribution to the thrust is the longitudinal pressure forces acting on the divergent section of the nozzle, the imbalance here is due to the atmospheric pressure acting on the cross section of the motor. This thrust contribution is suitable named the *pressure thrust*, it is shown to be (Sutton and Biblarz, 2001)

$$F_p = \int_{A_2} (p_2 - p_3)\, dA \tag{2.3}$$

which for quasi-one-dimensional flow (i.e. constant cross-sectional flow properties) is shown to be

$$F_p = (p_2 - p_3) A_2 \tag{2.4}$$

Thus, for a steady operating nozzle traveling through a homogenous atmosphere the *total thrust* is defined as (Sutton and Biblarz, 2001)

$$F_t = \int_{A_2} \left(\rho u_2^2 + [p_2 - p_3]\right) dA \tag{2.5}$$

which for uniform cross-sectional flow properties reduces to

$$F_t = \dot{m} u_2 + (p_2 - p_3) A_2 \tag{2.6}$$

Due to the interdependence of the pressure and momentum terms it can be seen (Sutton and Biblarz, 2001) that maximum thrust is produced with $p_2 = p_3$, requiring that the combustion gasses be expanded to the prevalent atmospheric pressure and is referred to as the *optimum expansion ratio*. For this condition the total thrust equation reduces to that of the momentum thrust equation. Further expansion produces a low pressure condition at the rear of the motor essential slowing it down. Conversely, under-expanding the gas does not produce the maximum momentum thrust contribution. For a rocket operating in a vacuum the thrust equation reduces to

$$F_t = \dot{m} u_2 + p_2 A_2 \tag{2.7}$$

and is termed the *vacuum thrust* (Sutton and Biblarz, 2001).

One-dimensional flow is flow in which it is considered that the state variables associated with flow (p, T, ρ, u and e) vary only as a function of one spatial coordinate e.g. x. Essentially the flow is restricted to one of constant area Anderson (1995). Nozzles are simplified analytically to a one-dimensional problem but with varying cross-sectional area. This is known as quasi-one-dimensional flow. Similarly to one-dimensional flow, the properties of flow for quasi-one-dimensional flow are assumed to vary as a function of x only. However, with quasi-one-dimensional flow varied-area flow boundary is included (see figure 2.2). The variations in flow area are considered to change gradually with $A = A(x)$. The assumption allows one to neglect the three-dimensional effects of a varied flow area and essentially means that quasi-one-dimensional flow is one of uniform cross-sectional flow properties varying with x. While quasi-one-dimensional flow is only an approximation of full three-dimensional flow it is often sufficient for basic axis-symmetric nozzle designs (Sutton and Biblarz, 2001; Anderson, 1995).

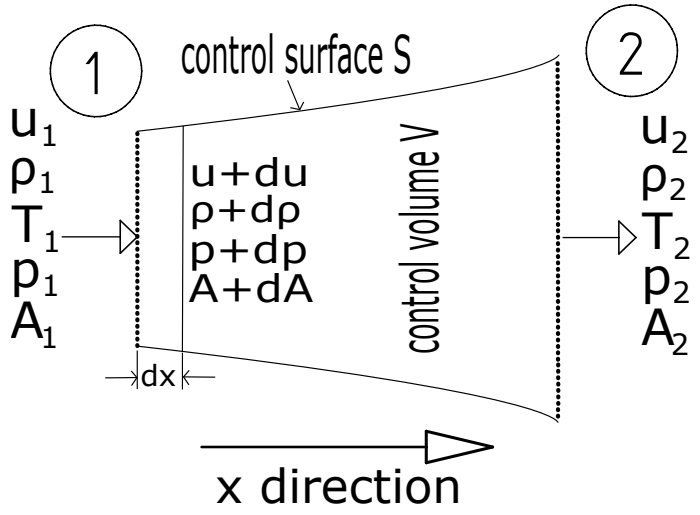

Figure 2.2: Control volume and differential volume element for quasi one-dimensinal flow (Adapted from Anderson (1995))

The application of fluid flow laws (continuity, momentum and energy equations) to quasi-one-dimensional flow problem gives rise to the area-velocity relation (Anderson, 1995):

$$\frac{dA}{A} = (M^2 - 1)\frac{du}{u} \tag{2.8}$$

This relationship is pivotal in understanding sub-sonic and sonic nozzle flow and makes up the basis for the nozzle theory presented here. The relevant points for this work are:

- for flows where $0 > M \leq 1$ (sub-sonic) it can be seen from Eq. 2.8 that increase in flow area is associated with a decrease in velocity and vice versa (Anderson, 1995)

- for flows where $M > 1$ (sonic) it can be seen from Eq. 2.8 that an increase in flow area is associated with an increase in velocity and vice versa (Anderson, 1995)

The application of this is further explored in Section 2.3 as Isentropic Convergent-Divergent Nozzle Flow.

The means of producing the high-pressure gas is determined by the type of rocket. The three classical rocket motor types are Liquid Propellant, Hybrid Propellant and Solid Propellant motors (see Figures 2.3 and 2.4). Liquid propellant motors typically inject pressurised fuel and oxidizer into the combustion chamber where the combustion takes place. A hybrid motor typically has a solid fuel filled combustion chamber into which oxidizer is injected for combustion. SRM's have their fuel and oxidizer stored within the combustion chamber greatly reducing the complexity of the system. This work focuses on tactical SRM's as seen in Figure 2.4. Noticeably different to other rocket motor types, tactical rockets have a *blast tube* to accommodate the rear mounted guidance systems. At the fore-end of the motor an *igniter* is fitted which produces the initial ignition of the exposed propellant surface. The propellant is referred to as the *grain*. Once ignited the propellant surface burns back producing the combustion gases which are ejected through the blast tube and out of the *nozzle*. The *convergent section* of the blast tube accelerates the gas until choked sonic flow is reached at the nozzle *throat* area, the gas is then further expanded and accelerated to super-sonic speeds in the *divergent section* where it is finally expelled to the atmosphere at the rear. The receding burning nature and hence changing exposed surface area of a solid rocket grain allows one to tailor the thrust profile by varying the initial grain shape. For further reading regarding rocket motor types see Sutton and Biblarz (2001); Simmons (2000).

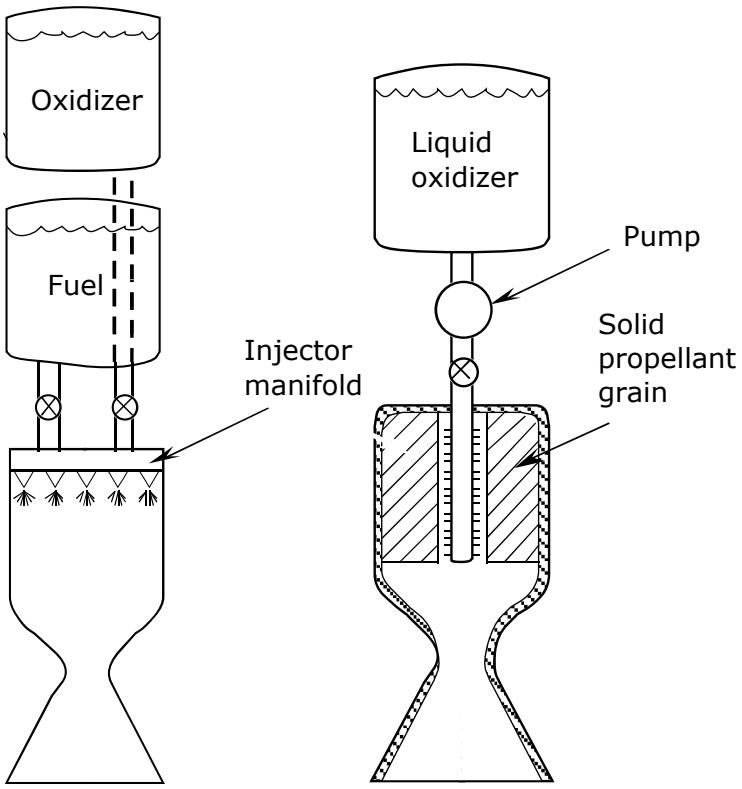

Figure 2.3: Liquid rocket motor (left) and hybrid rocket motor (right) - adapted from Simmons (2000)

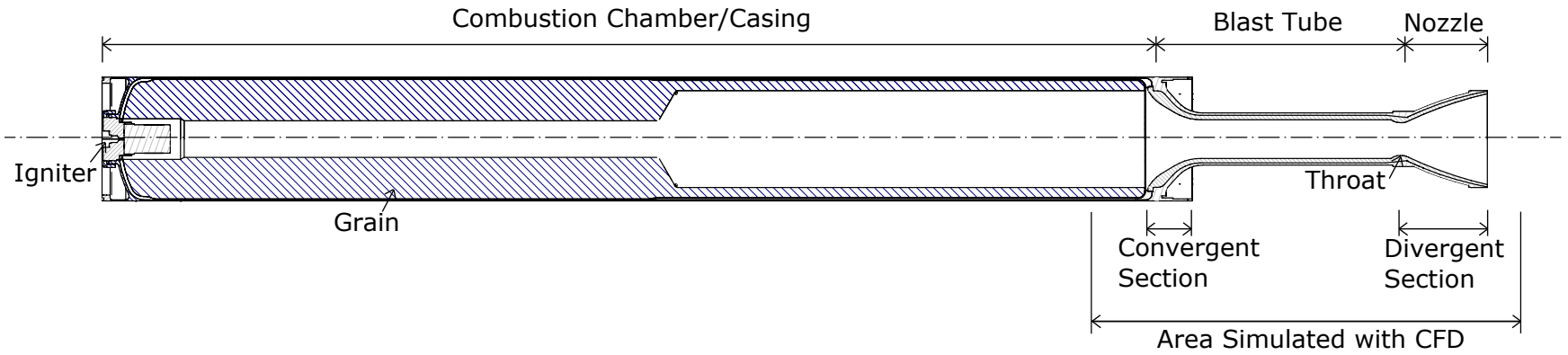

Figure 2.4: Tactical solid rocket motor cross-section

2.2 Nozzle and Nozzle Flow Types

The common rocket nozzle types and associated flow conditions are shown in Figure 2.5. This work is focused on the traditional convergent-divergent nozzle (de Laval nozzles), specifically the conical and contoured bell-shaped nozzle profiles.

The conical nozzle is one of the simplest nozzle types often used for smaller nozzle applications and is inherently easy to manufacture (Sutton and Biblarz, 2001). The half angle of a conical nozzle is its primary design parameter given a fixed expansion ratio. For maximum thrust in a nozzle, one would ideally want the exhaust gas to exit axially producing thrust in the direction of intended motion. For a conical nozzle to produce near axial flow the half angle would need to be minimised, this, however, makes for impractical nozzle lengths (with associated mass increases and boundary layer effects) to achieve the desired expansion ratio. The losses due to non-axial flow in a nozzle are known as *divergent losses*, losses due to the nozzle wall interactions with the flow (no-slip conditions prevalent near the wall and boundary layer effects) are termed *friction losses*. These losses make up the bulk of the losses in a nozzle due to divergent contour profiles.

It is this trade-off between divergent losses, friction losses and size constraints that a contoured nozzle addresses. With high relative pressure and large pressure gradients immediately downstream of the throat, a rapid expansion rate of the gas can be achieved without wall separation. As the gas is further expanded with associated pressure drop the rate of expansion is reduced by turning the expansion angle back towards axial which in turn decreases divergent losses and minimises nozzle length. The efficacy of how this expansion and then straightening is applied was notably improved by Rao (1958) who mathematically tailored the contour in an attempt to balance the compression and expansion waves that occur when turning super-sonic flow. Common practice is to relate truncated nozzle lengths back to a 15° half angle conical nozzle as a comparative measure of length (Sutton and Biblarz, 2001).

There are three main flow types associated with conical and contoured nozzles:

Under-expanded nozzle flow (see Figures 2.5 and 2.6) occurs when the expansion ratio does not allow for the gas to full expand within the nozzle to the prevalent atmospheric pressure (i.e. $p_2 > p_3$). There is still the potential for the gas to be further expanded and accelerated. When the gas leaves the nozzle it immediately expands until the static gas pressure adjusts to the atmospheric (i.e $p_2 \rightarrow p_3$). For this to happen in super-sonic flow, the exhaust stream expands through a Prandtl-Meyer expansion fan process.

Over-expanded nozzle flow (see Figures 2.5 and 2.6) occurs when the expansion ratio

attempts to expand the gas within the nozzle to below the prevalent atmospheric pressure (i.e. $p_2 < p_3$). With slight over-expansion, the gases flow full within the nozzle and then contract outside of the nozzle. There are losses associated with this due to the negative pressure thrust generated. With a further increase in the expansion, the gas is unable to follow the wall contour and separates. There is flow recirculation into the nozzle combined with a system of oblique shocks (Simmons, 2000).

Matched pressure nozzle flow (see Figures 2.5 and 2.6) occurs when the gas is expanded within the nozzle to match the prevalent atmospheric pressure at the exit (i.e. $p_2 = p_3$). This is found to be the optimal expansion ratio for maximum thrust. It is worth noting that for a given chamber pressure and expansion ratio that this condition applies only at a certain design altitude, and for a rocket operating at various altitudes a compromise is therefore needed.

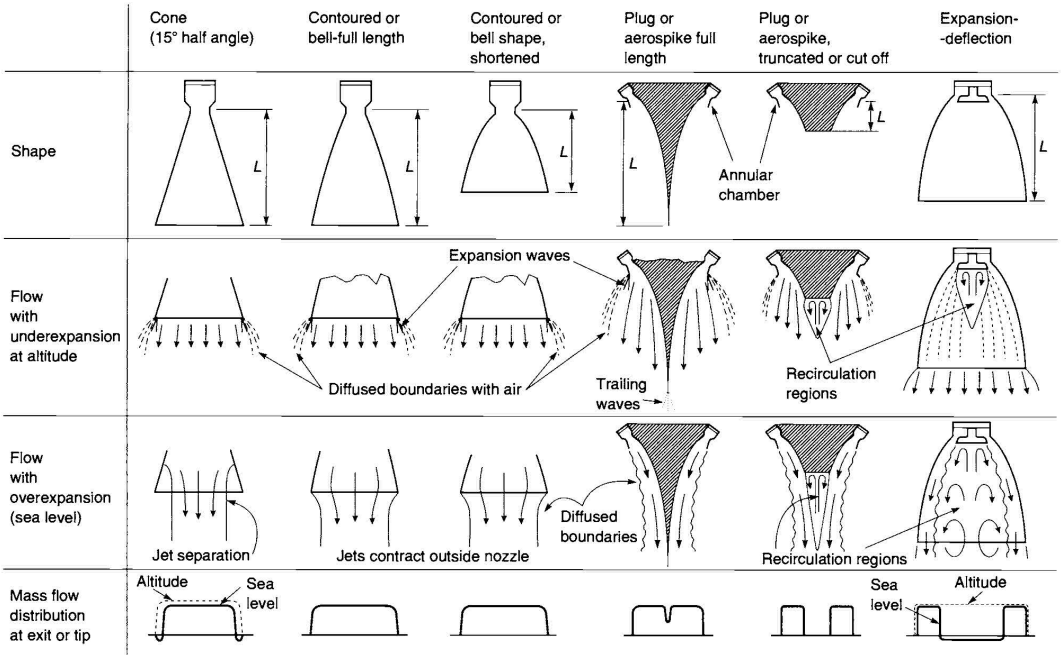

Figure 2.5: Nozzle and nozzle flow types (Sutton and Biblarz, 2001)

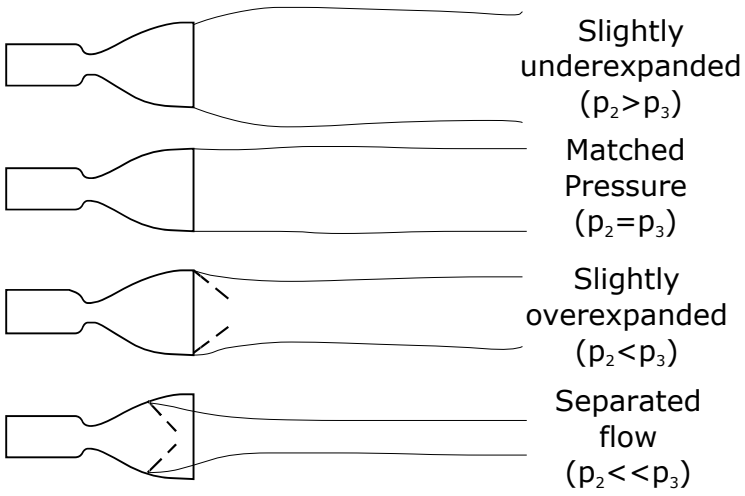

Figure 2.6: Nozzle flows (Simmons, 2000)

2.3 Isentropic Convergent-Divergent Nozzle Flow

Isentropic flow is the movement of fluid that is both adiabatic and reversible. I.e. there is no heat added and the effects of friction and dissipation are ignored. While isentropic nozzle flow is an extension of the compressible flow theory, it is has been included under Rocket and Nozzle Theory as an application of compressible flow to a particular problem, namely convergent-divergent nozzles.

There are a few assumptions made in applying this theory, from Sutton and Biblarz (2001) we describe the *Ideal Rocket*:

- The working substance is homogeneous.
- All the species of the working fluid are gaseous.
- The working fluid obeys the perfect gas law.
- There is no heat transfer across the rocket wall.
- There is no appreciable friction and all boundary layer effects are neglected
- There are no shock waves or discontinuities in the nozzle flow.
- The propellant flow is steady and constant. The expansion of the working fluid is uniform and steady. Transient effects are of very short duration and can be neglected.
- All exhaust gases leaving the nozzle are axial.
- The gas properties are considered uniform across any section normal to the nozzle axis and flow.
- Chemical equilibrium is established within the rocket chamber and the gas composition does not change in the nozzle.

In keeping relevant, only choked sonic throat flow with super-sonic divergent section flow is considered. That is to say that the pressure ratio across the nozzle is kept suitably high enough that sonic throat conditions are maintained. It should be clear that only one isentropic solution exists for a divergent super-sonic expansion and it is determined solely by the area ratio $\frac{A}{A^*}$ presented below.

Considering the two nozzles in Figure 2.7, with throat condition A^*, M^* and $u^* = a^*$ and local conditions at any distance x from the throat A, M and u. The application of quasi-one-dimensional flow theory for sonic conditions on the area-velocity relationship (2.8) produces (Anderson, 1995)

$$\left(\frac{A}{A^*}\right)^2 = \frac{1}{M^2}\left[\frac{2}{\gamma+1}\left(1+\frac{\gamma-1}{2}M^2\right)\right]^{\frac{\gamma+1}{\gamma-1}} \tag{2.9}$$

this is the *area-Mach number relation*. It shows that the Mach number is a function of the A/A^* ratio, has two values (both a sonic and sub-sonic solution) and that A must be equal to or greater than A^* for isentropic flow. Applied to the local throat area ratios (varying as a function of x) of the nozzles in Figure 2.7, the local Mach numbers can be plotted. Substituting into stagnation pressure and temperature equations (see Sutton and Biblarz (2001)) the values for pressure and temperature ratio can be plotted. It is seen that for the tactical nozzle the sub-sonic acceleration in the convergent section up to throat conditions is essentially frozen for the parallel section of the blast tube with the final area reduction before the throat producing the choked condition. This is due to the flow conditions being a function of the A/A^* ratio only which is constant for the parallel section. In practice, there would need to be a small pressure drop as well as friction losses across the parallel section for flow to exist (Anderson, 1995).

For a pressure ratio suitably high enough to produce super-sonic expansion initially in the divergent section but low enough that the expansion is over-expanded in the nozzle (i.e. the nozzle expands the gas to below the nozzle exit pressure) a normal shock wave will exist in the nozzle (see Figure 2.8a). The location of which is due to the requirement that the properties behind the wave be such that the nozzle exit pressure p_{e4} is achieved. With the Mach plot (see Figure 2.8b and 2.8c) showing the drop back to subsonic flow found behind the shock wave. With further increases in the pressure ratio across the nozzle, the normal shock moves towards the nozzle exit with the optimal expansion solution being with the normal shock at the exit. The isentropic design Mach solution being just before the shock wave at the exit (Anderson, 1995).

The quasi-one-dimensional and isentropic theories allow for the calculation and analysis of convergent-divergent nozzle flow. The results are cross-sectional constant values and do not provide insight regarding the actual physical contour of a supersonic nozzle (Anderson, 1995).

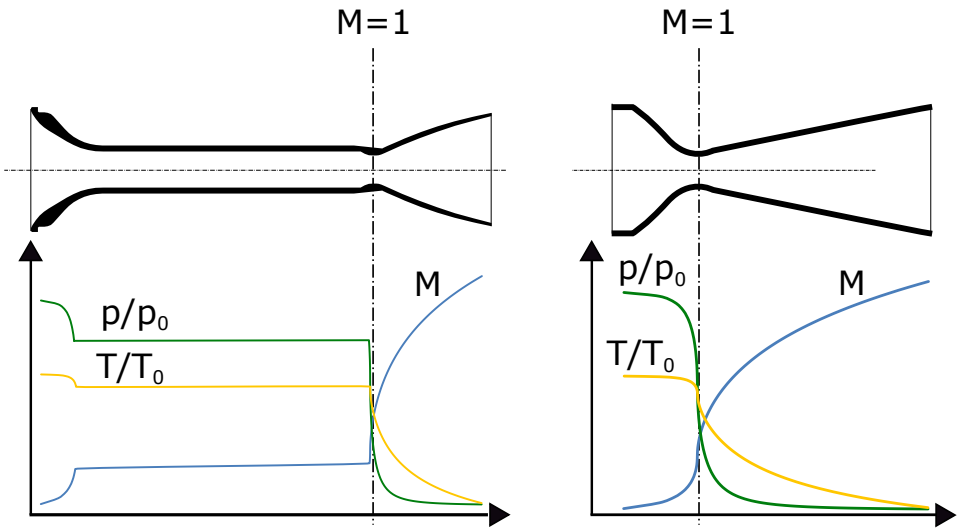

Figure 2.7: Isentropic nozzle flow through a tactical rocket nozzle (left) and a conventional de Laval nozzle (right) - Not to Scale - Adapted from Anderson (1995) to include a tactical rocket nozzle and blast tube type design

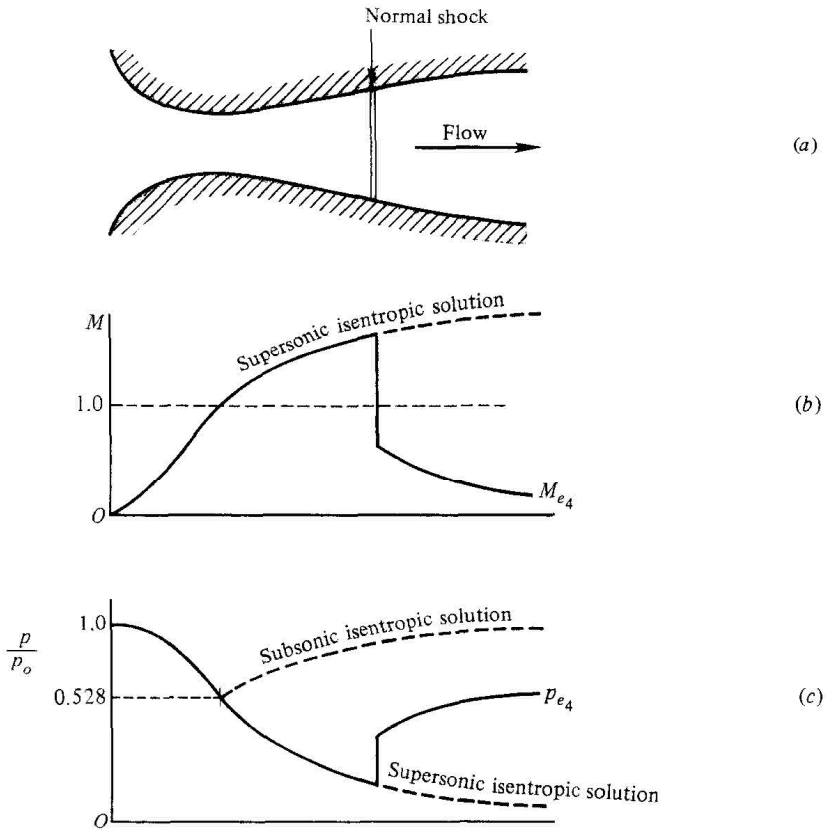

Figure 2.8: Flow with a normal shock wave inside a convergent-divergent nozzle (Anderson, 1995)

3 Computational Fluid Dynamics

CFD is the analysis of systems involving fluid flow, heat transfer and associated phenomena by means of computer-based simulation (Versteeg and Malalasekera, 2007). This work uses the ANSYS Fluent Code from within Ansys Workbench (ANSYS, 2015b). ANSYS Fluent is a finite volume method numerical solution technique. The computational domain is meshed into cells representing finite control volumes for which the integration of the governing equations for fluid flow are applied. The resulting integral equations are then discretized into a system of algebraic equations that are then solved iteratively (Versteeg and Malalasekera, 2007).

The finite volume method considers a fluid element (see Figure 3.1) through which the fluid flows. By applying the conservation laws to the finite volume the governing equations of fluid flow can be determined and are presented in the subsections that follow.

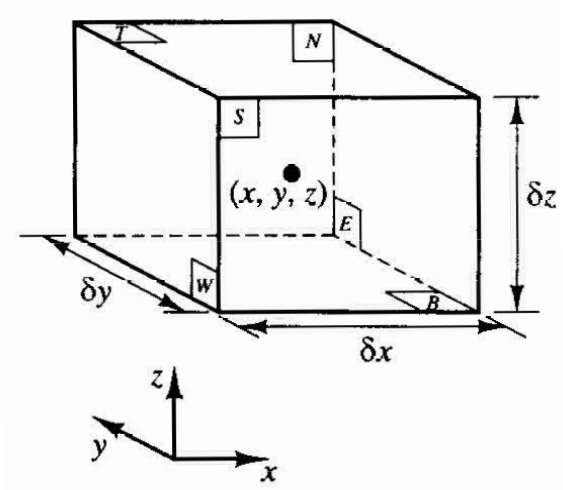

Figure 3.1: Fluid element for conservation laws (Versteeg and Malalasekera, 2007)

The CFD method used solves for a rocket nozzle fluid flow that is compressible i.e the fluid flow has variable density. In reality all fluids are compressible to some extent, however, the assumption of in-compressibility is made for most liquid flows. In the case of sonic combustion gas flow convergent-divergent rocket nozzles, compressibility cannot be ignored.

The compressible flow theory used in this work (see Section 5.5) is based on that presented by Anderson (1995). It can be shown that for gas flow with speeds below Mach 0.3, the fluid can be considered incompressible (Anderson, 1995), however, for rocket nozzle flow with sonic choked flow in the throat and speeds in the region of Mach 4.0 at the exit the need to account for compressibility becomes important. For the purpose of this work the assumption is made that the exhaust gases behave as an *ideal gas* and therefore obey the perfect gas laws . By definition, *a perfect gas is one in which intermolecular forces are neglected* (Anderson, 1995).

With the Mach number a thermodynamic property of the fluid (i.e. varying with the fluid properties) and defined as $M = V/a$. The categorized various flow types by Mach number (Anderson, 1995) are:

Subsonic Flow (see Figure 3.2) - Defined as the free stream Mach number $M_\infty < 0.8$, characterised by smooth streamlines and continuous varying fluid properties.

Transonic Flow (see Figure 3.3) - Defined as the free stream Mach number $0.8 > M_\infty > 1.0$, characterised by a free stream that remains subsonic, however, there are local regions around disturbances that are supersonic .

Supersonic Flow (see Figures 3.4 and 3.5) - Defined as the free stream Mach number $M_\infty > 1.0$, characterized by a free stream that is completely supersonic, bow shock present and downstream disturbances have no effect on upstream flow as the pressure disturbances cannot travel upstream at greater than Mach 1.

Hypersonic Flow (see Figure 3.6) - Defined as the free stream Mach number $M_\infty > 5.0$, characterised by very large pressure, density and temperature changes across the shock. Oblique shock waves move closer to the surface. Mach 5 only being an indicative value with the change from supersonic to hypersonic being a gradual one.

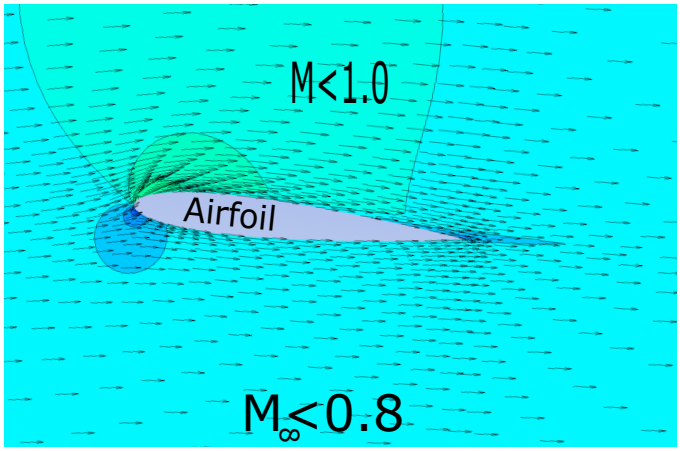

Figure 3.2: Subsonic flow around NACA 0012 airfoil, 6° AoA - Adapted from Anderson (1995)

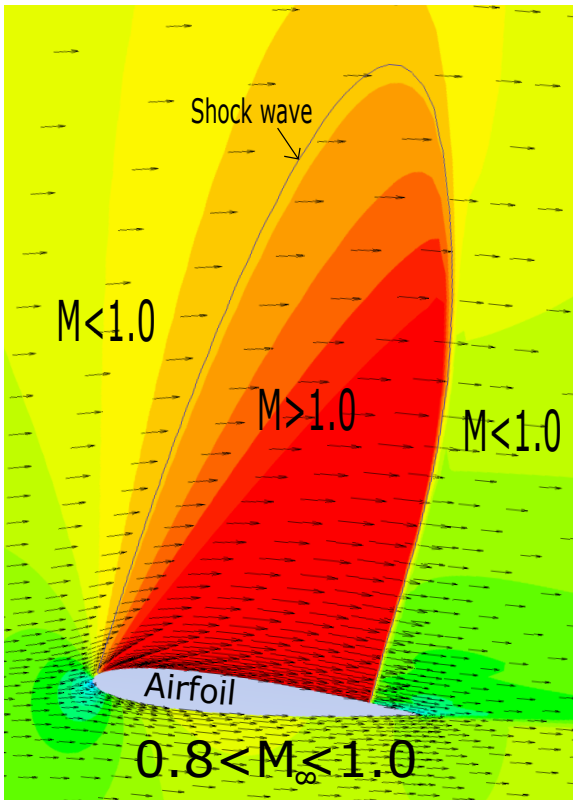

Figure 3.3: Transonic flow around NACA 0012 airfoil, 6° AoA - Adapted from Anderson (1995)

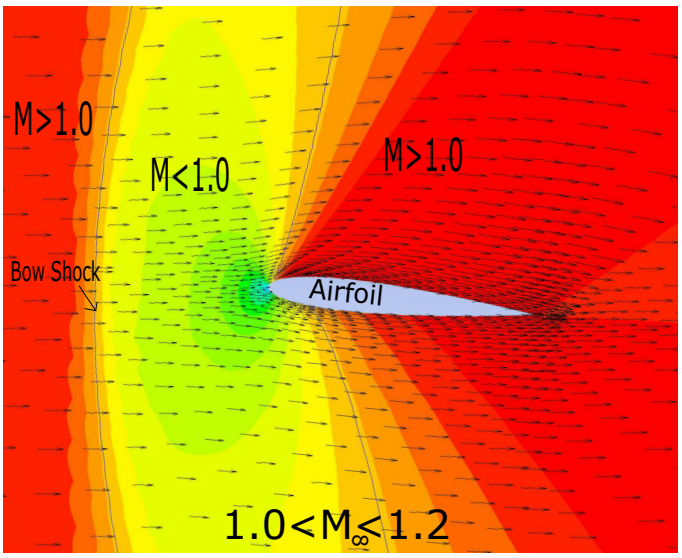

Figure 3.4: Sonic flow around NACA 0012 airfoil, 6° AoA - Adapted from Anderson (1995)

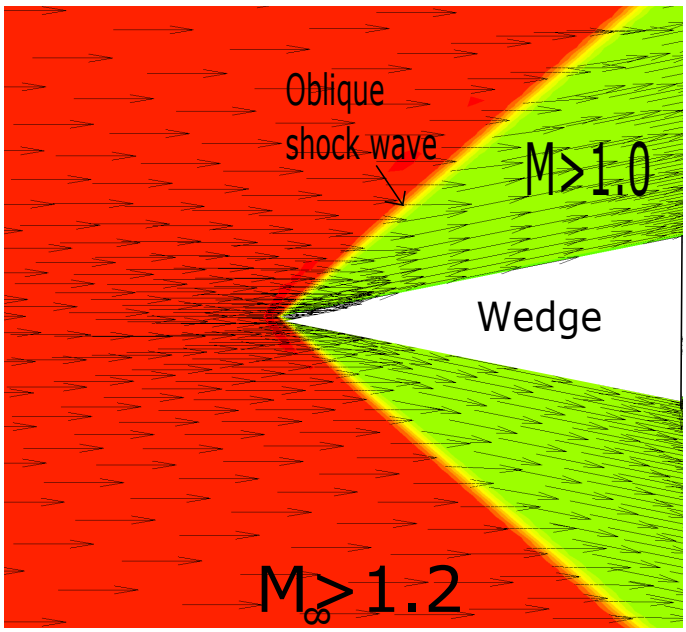

Figure 3.5: Sonic flow past a wedge - Adapted from Anderson (1995)

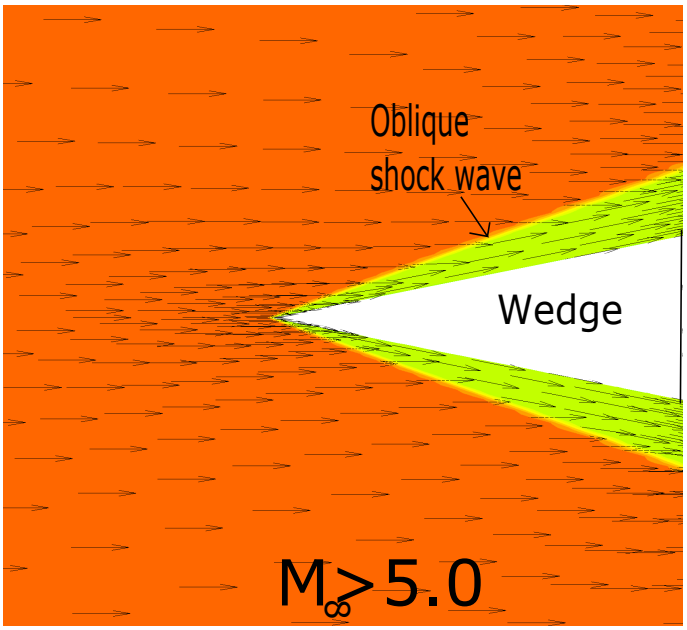

Figure 3.6: Hypersonic flow past a wedge - Adapted from Anderson (1995)

3.1 Continuity Equation

By applying the conservation of mass law (the net flow of mass into the fluid element is equal to the rate of increase of mass in the fluid element) to a fluid element such as in Figure 3.7. It can be seen that the *continuity equation* for unsteady three-dimensional mass conservation in a fluid element is, in compact vector notation (Versteeg and Malalasekera, 2007)

$$\frac{\partial \rho}{\partial t} + \nabla \cdot (\rho \vec{v}) = 0 \tag{3.1}$$

Modified to include the source term S_m (representing the mass added to the continuous phase from the dispersed second phase as well as any user-define sources) and with divergence represented by ∇ as used in the Fluent solver (ANSYS, 2015b)

$$\frac{\partial \rho}{\partial t} + \nabla \cdot (\rho \vec{v}) = S_m \tag{3.2}$$

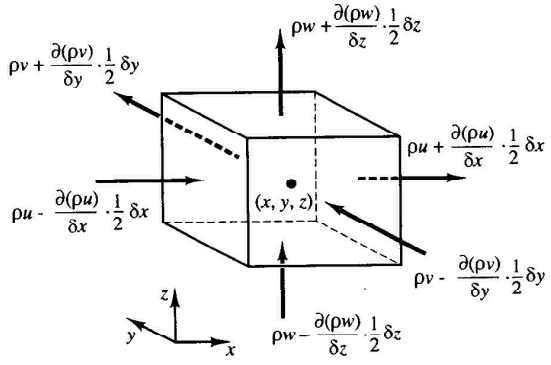

Figure 3.7: Mass flow in and out of an element (Versteeg and Malalasekera, 2007)

3.2 Momentum Equations

Applying Newton's second law (the rate of increase of momentum of a fluid particle is equal to the sum of the forces on the fluid particle) to the fluid element and represented

by Figure 3.8. The *x-component of the momentum equation* for three-dimensional flow is (Versteeg and Malalasekera, 2007)

$$\rho\frac{Du}{Dt} = \frac{\partial(-p+\tau_{xx})}{\partial x} + \frac{\partial\tau_{yx}}{\partial y} + \frac{\partial\tau_{zx}}{\partial z} + S_{Mx} \tag{3.3}$$

the *y-component of the momentum equation* (Versteeg and Malalasekera, 2007)

$$\rho\frac{Dv}{Dt} = \frac{\partial\tau_{xy}}{\partial x} + \frac{\partial(-p+\tau_{yy})}{\partial y} + \frac{\partial\tau_{zy}}{\partial z} + S_{My} \tag{3.4}$$

the *z-component of the momentum equation* (Versteeg and Malalasekera, 2007)

$$\rho\frac{Dw}{Dt} = \frac{\partial\tau_{xz}}{\partial x} + \frac{\partial\tau_{yz}}{\partial y} + \frac{\partial(-p+\tau_{zz})}{\partial z} + S_{Mz} \tag{3.5}$$

with the source terms S_{Mx}, S_{My} and S_{Mz} including contribution due to body forces only. Fluent uses the modified momentum equation presented in the conservative form as (ANSYS, 2015b)

$$\frac{\partial}{\partial t}(\rho\vec{v}) + \nabla\cdot(\rho\vec{v}\ \vec{v}) = -\nabla p + \nabla\cdot(\overline{\overline{\tau}}) + \rho\vec{g} + \vec{F} \tag{3.6}$$

with p the static pressure and $\overline{\overline{\tau}}$ the stress tensor (Equation 3.7). $\rho\vec{g}$ and $\vec{F}$ the gravitational and external body forces respectively. Additional model-dependent and user-defined source terms are include for in $\vec{F}$ (ANSYS, 2015b).

The *stress tensor* defined as (ANSYS, 2015b)

$$\overline{\overline{\tau}} = \mu\left[\left(\nabla\vec{v} + \nabla\vec{v}^T\right) - \frac{2}{3}\nabla\cdot\vec{v}I\right] \tag{3.7}$$

with μ the molecular viscosity, I the unit tensor and the second term on the right-hand side is the effect of volume dilation (ANSYS, 2015b).

3.3 Energy Equation

Applying the first law of thermodynamics (the rate of increase of energy of a fluid particle is equal to the sum of the net rate of heat added and the net rate of work done on the

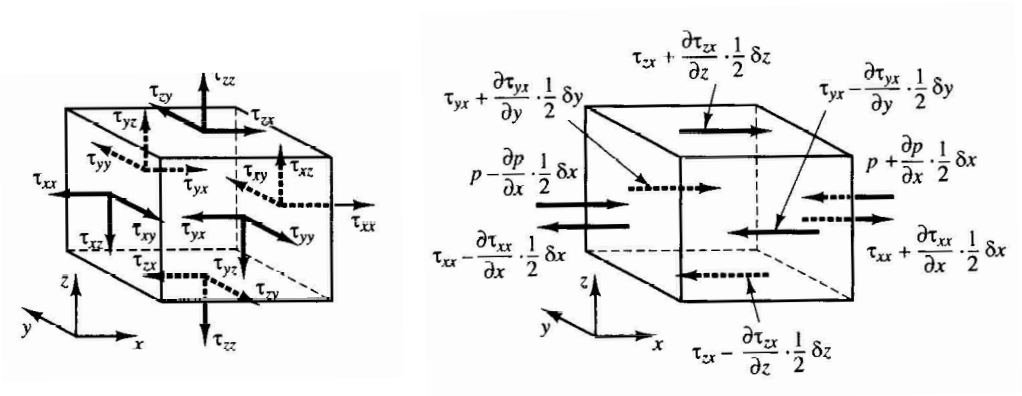

Figure 3.8: Stress components on three faces of fluid element (left) and stress components in the x-direction (right) (Versteeg and Malalasekera, 2007)

fluid particle) to the fluid element and represented by Figure 3.9. The *energy equation* for three-dimensional flow is (Versteeg and Malalasekera, 2007)

$$\begin{aligned}\rho\frac{DE}{Dt} = &-\nabla\cdot(p\vec{v}) + \left[\frac{\partial(u\tau_{xx})}{\partial x} + \frac{\partial(u\tau_{yx})}{\partial y} + \frac{\partial(u\tau_{zx})}{\partial z}\right.\\ &+ \frac{\partial(v\tau_{xy})}{\partial x} + \frac{\partial(v\tau_{yy})}{\partial y} + \frac{\partial(v\tau_{zy})}{\partial z} + \frac{\partial(w\tau_{xz})}{\partial x}\\ &\left.+ \frac{\partial(w\tau_{yz})}{\partial y} + \frac{\partial(w\tau_{zz})}{\partial z}\right] + \nabla\cdot(k\ \text{grad}\ T) + S_E\end{aligned} \tag{3.8}$$

with S_E the source term for the effect of potential energy changes and k the thermal conductivity. Fluent solves the energy equation presented in the following conservative form as (ANSYS, 2015b)

$$\frac{\partial}{\partial t}(\rho E) + \nabla\cdot(\vec{v}\ (\rho E + p)) = \nabla\cdot\left(k_{eff}\nabla T - \sum_j h_j\vec{J}_j + (\overline{\overline{\tau}}_{eff}\cdot\vec{v})\right) + S_h \tag{3.9}$$

With $\vec{J}_j$ the diffusion flux of species j, k_{eff} the effective conductivity $k + k_t$ (with k_t dependent on the turbulence model used) and the first three terms on the right hand side being energy transfer due to conduction, species diffusion and viscous dissipation respectively. The source term S_h is made up of the heat of chemical reactions as well as other volumetric heat sources where applicable (ANSYS, 2015b).

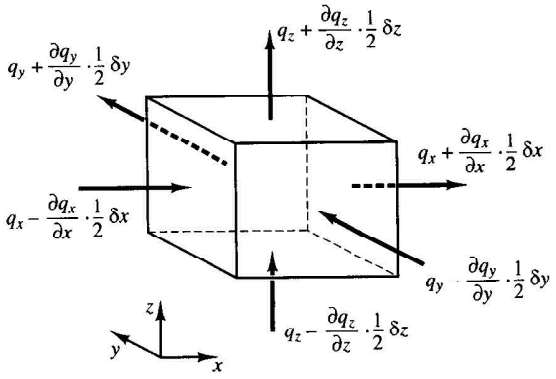

Figure 3.9: Components of the heat flux vector (Versteeg and Malalasekera, 2007)

3.4 Turbulence

Reynolds-Averaged Navier-Stokes Equations:

For turbulent flow the instantaneous continuity and momentum equations are decomposed into the mean and fluctuating components and represented in the Cartesian tensor form as (ANSYS, 2015b)

$$\frac{\partial \rho}{\partial t} + \frac{\partial}{\partial x_i}(\rho u_i) = 0 \tag{3.10}$$

$$\begin{aligned}\frac{\partial}{\partial t}(\rho u_i) + \frac{\partial}{\partial x_j}(\rho u_i u_j) = &-\frac{\partial p}{\partial x_i} + \frac{\partial}{\partial x_j}\left[\mu\left(\frac{\partial u_i}{\partial x_j} + \frac{\partial u_j}{\partial x_i} - \frac{2}{3}\delta_{ij}\frac{\partial u_l}{\partial x_l}\right)\right] \\ &+ \frac{\partial}{\partial x_j}(-\rho \bar{u_i}' \bar{u_j}')\end{aligned} \tag{3.11}$$

these are the *Reynolds-averaged Navier-Stokes* equations or with velocities representing mass-averaged values they can be interpreted as the *Favre-averaged Navier-Stokes* equations for variable density compressible flow. In order to close the RANS equations the additional Reynolds stresses ($-\rho \bar{u_i}' \bar{u_j}'$) that appear need to be modeled. For the purpose of this work the Menter SST model is used to solve for the Reynolds stresses. This involves solving the two additional transport equations given below (ANSYS, 2015b). The wall boundary conditions as used in the k-ω models is the Enhanced Wall Treatment method (ANSYS, 2015b). This method is a combination of wall-function and near-wall (low-Reynolds number approach) methods. It is a mesh based blending that switches

method depending on the grid. With a fine enough grid the viscous sub-layer is completely resolved and as the grid size is increased more of the near-wall layers become wall-function based (ANSYS, 2015b).

The Menter SST k-ω models turbulent kinetic energy transport equation:

$$\frac{\partial}{\partial t}(\rho k) + \frac{\partial}{\partial x_i}(\rho k u_i) = \frac{\partial}{\partial x_j}\left(\Gamma_k \frac{\partial k}{\partial x_j}\right) + \bar{G}_k - Y_k + S_k \tag{3.12}$$

With k the turbulence kinetic energy.

The specific dissipation rate transport equation:

$$\frac{\partial}{\partial t}(\rho \omega) + \frac{\partial}{\partial x_j}(\rho \omega u_j) = \frac{\partial}{\partial x_j}\left(\Gamma_\omega \frac{\partial \omega}{\partial x_j}\right) + G_\omega - Y_\omega + D_\omega + S_\omega \tag{3.13}$$

With w the specific dissipation rate.

4 Numerical Procedures for Optimisation

Optimisation by definition is an act, process, or methodology of making something (as a design, system, or decision) as fully perfect, functional, or effective as possible; specifically : the mathematical procedures (as finding the maximum of a function) involved in this (Dictionary, 2006). This work as per the definition uses a numerical algorithm to make a rocket nozzle geometry as effective as possible for the maximisation of its thrust (within the limitations of the method itself).

In optimisation, there is some uncertainty in knowing if an optimum is a local or global one within the search domain. A local optimum may still, however, produce improved results in comparison to current designs, there is, however still some uncertainty as to if it is the ultimate (or global optimum) design within the constraints set. For SRM nozzles the basic physics give some limitations for what is achievable based on the mass flow available from the propellant, operating pressure and the achievable expansion ratio allowed by the nozzles physical constraints. These "perfect" or ideal solutions for the objective function can be approximated from the quasi-one-dimensional flow theory (as used in section 5.5). With typical nozzle coefficients of approx 0.95 it can be seen there is approximately 5 % "available" or lost within the nozzle. Not all this additional thrust can be obtained from geometric changes to the nozzle alone as one cannot completely eliminate thermal losses to the nozzle structure as well as viscous and boundary layer effects. This work approaches the optimisation by using multiple optimisation methods detailed in section 4.1 as well as starting from different baseline geometries (see individual cases in chapter 5).

4.1 Optimisation Algorithms

ANSYS Fluent (ANSYS, 2015a) incorporates design optimisation through ANSYS Workbench and ANSYS DesignXplorer. Available optimisation methods for the goal-driven control surface method are Shifted-Hammersley Sampling (Screening), Nonlinear Programming by Quadratic Lagrangian (NLPQL), Mixed-Integer Sequential Quadratic Programming (MISQP) and Multi-Objective Genetic Algorithm (MOGA). The methods are

Method	Single Objective	Multiple Objectives	Local Search	Global Search	Discrete	Manufacturable Values	Parametric Relationships
Screening		X		X	X	X	X
NLPQL	X		X				X
MISQP	X		X		X	X	X
MOGA		X		X	X	X	X
Adaptive Single Objective	X			X		X	
Adaptive Multiple Objective		X		X		X	X
External Optimiser	Capabilities are determined by the optimiser, as defined in the optimisation extension						

Figure 4.1: ANSYS optimisation methods (ANSYS, 2015a)

individually discussed in sections 4.1.1, 4.1.2, 4.1.3 and 4.1.4. Figure 4.1 tabulates the available methods in ANSYS and their capability's. The last three methods (Adaptive Single Objective, Adaptive Multiple Objective and External Optimiser) are not discussed further as Adaptive Single and Multiple Objective methods are only applicable to direct optimisation methods (not used in this work) while the last is not a method itself, only the functionality to use an alternative external optimizer.

4.1.1 Shifted-Hammersley Sampling (Screening)

The Screening option is a Shifted Hammersley Sampling method that simply sorts these generated samples based on applied constraints and objectives, in this way it is a purely global method in that it is representative of an even distribution of points in the domain with no focused search near actual optima. The Hammersley Sampling method is a quasi-random number generator and a type of Quasi-Monte Carlo sequence that randomly generates numbers to represent a uniform distribution. It is a low discrepancy sequence that populates points within a multi-dimensional cube in an even and optimum way (ANSYS, 2015a; Ulas and Diwekar, 2006).

For Hammersley sampling, an integer n can be shown in Radix-R notation (ANSYS, 2015a; Diwekar and Kalagnanam, 1997)

$$n = n_m + n_{m-1} * R + ... + n_0 \tag{4.1}$$

with the points reversed about the decimal point, the inverse radix number is (ANSYS, 2015a; Diwekar and Kalagnanam, 1997)

$$\phi_R(n) = n_m * R^{-1} + n_{m-1} * R^{-2} + ... + n_0 * R^{-(m-1)} \tag{4.2}$$

and the Hammersley sampled points in a k-dimensional space are given by (ANSYS, 2015a)

$$H_k(i) = [I/N_1, \phi_{R1}(i), \phi_{R2}(i), ..., , \phi_{Rk-1}(i)] \tag{4.3}$$

because the points above are centred closer to the origin (with the values ranging from 0 to < 1), ANSYS uses a shifting process that moves the points closer to the centre by an amount Δ

$$\Delta = \frac{N}{2} \tag{4.4}$$

The Screening optimisation approach itself is a pure sorting of the points generated by the Shifted-Hammersley Sampling. All other optimisation methods in ANSYS other than the NLPQL method use this same sampling method for the initial sample set.

The parameters used for the Screening optimisations are shown in table 4.1, with their descriptions shown below:

Table 4.1: Screening Optimisation Settings

Parameter	Setting
Number of Initial Samples	10000
Maximum Number of Candidates	10-40

Number of Initial Samples: This specifies how many initial samples are used in the

optimisation with a higher value improving results but with increased computational time. High values were used for this as it was not the limiting factor for processing, with individual CFD simulation times an order of magnitude longer than the optimisation solver.

Maximum Number of Candidates: The number of optimal candidates the optimisation will attempt to get. This is largely user-specific but you will always get the highest candidates from the optimisation no matter this value. For example, if the optimisation results produced values 100, 99, 98, 97, 96, 95, 94, 93, 92 and 91 and you selected 5 as Maximum Number of Candidates, the result that will be returned will be 100, 99, 98, 97 and 96. Values are chosen based on the level of refinement required for next level, with the consideration that for each candidate generated a full CFD simulation is required to validate it.

For more detailed explanations of the parameters see ANSYS (2015a).

4.1.2 Nonlinear Programming by Quadratic Lagrangian (NLPQL)

NLPQL is a gradient based single objective method. The NLPQL is a type of sequential quadratic programming method similar to the MISQP method (see section 4.1.3) with the assumption of continuously differentiable objective function and constraints. The NLPQL is recommended for use with continuous problems with one objective function. While better suited for local optimisation it does provide better accuracy than the global methods (Screening and MOGA) (ANSYS, 2015a).

The NLPQL method works by solving a formulated quadratic programming sub-problem at each iteration. The sub-problem is a linearization of the constraints and a quadratic approximation of the Lagrange function (Schittkowski and Zillober, 2003b) for the non-linear problem (NLP) of the form (ANSYS, 2015a)

$$\begin{aligned} &\text{Minimize } f = f(\{x\}) \\ &\text{subject to:} \\ &\qquad g_k(\{x\}) \leq 0, \forall k = 1, 2, ..., K \\ &\qquad h_I(\{x\}) = 0, \forall I = 1, 2, ..., L \end{aligned} \tag{4.5}$$

The first derivative; the gradient of a real function f(x) (Schittkowski and Zillober, 2003a)

$$\nabla f(x) := \left(\frac{\partial}{\partial x_1} f(x), ..., \frac{\partial}{\partial x_n} f(x)\right)^T \tag{4.6}$$

the second derivative; the Hessian matrix of f(x) (Schittkowski and Zillober, 2003a)

$$\nabla^2 f(x) := \left(\frac{\partial^2}{\partial x_i \partial x_j} f(x)\right)_{i,j=1,...,n} \tag{4.7}$$

the Jacobian matrix of a vector-valued function $F(x) = (f_1(x), ..., f_l(x))^T$ (Schittkowski and Zillober, 2003a)

$$\nabla F(x) := \left(\frac{\partial}{\partial x_i} f_j(x)\right)_{i=1,...,n;j=1,...,l} \tag{4.8}$$

with the Lagrangian Function (Schittkowski and Zillober, 2003a)

$$L(x, u) := f(x) - \sum_{j=1}^{m} u_j g_j(x) \tag{4.9}$$

with P the feasible region or set of all feasible solutions (Schittkowski and Zillober, 2003a)

$$P := \{x \epsilon R^n : g_j(x) = 0, j = 1, ..., m_e, g_j(x) \geq 0, j = m_e + 1, ..., m\} \tag{4.10}$$

and the active inequality constraints with respect to $x \epsilon P$ characterised by the index set (Schittkowski and Zillober, 2003a)

$$I(x) := \{j : g_j(x) = 0, m_e < j \leq m\} \tag{4.11}$$

an important aspect of nonlinear optimisation is the Karush-Kuhn-Tucker (KKT) conditions that state that at a local solution the gradient of the objective function can be expressed by a linear combination of gradients of active constraints and are the necessary conditions for the existence of an optimal point (ANSYS, 2015a; Schittkowski and Zillober, 2003a)

$$\begin{aligned}
&u_j^* \geq 0 \ , \ j = m_e + 1, ..., m, \\
&g_j(x^*) = 0 \ , \ j = 1, ..., m_e, \\
&g_j(x^*) \geq 0 \ , \ j = m_e + 1, ..., m, \\
&\nabla_x L(x^* u^*) = 0, \\
&u_j^* g_j(x*) = 0 \ , \ j = m_e + 1, ..., m
\end{aligned} \tag{4.12}$$

The NLPQL method defines a quadratic approximation and an approximation of the Lagrangian function (Equation 4.9) and Hessian Matrix (Equation 4.7) respectively using a quasi-Newton matrix B_k. Giving the sub-problem (Schittkowski and Zillober, 2003a)

$$\begin{aligned}
&\min \ \frac{1}{2} d^T B_k d + \nabla f(x_k)^T d \ , \ d \epsilon R^n : \\
&\nabla g_j(x_k)^T d + g_j(x_k) = 0 \ , \ j = 1, ..., m_e, \\
&\nabla g_j(x_k)^T d + g_j(x_k) \geq 0 \ , \ j = m_e + 1, ..., m,
\end{aligned} \tag{4.13}$$

A line search stepping from iteration k to $k + 1$ generally ensures convergence (Schittkowski and Zillober, 2003a). The set of non-linear equations is solved using Newtons iterative method (ANSYS, 2015a). The Hessian matrix is estimated and updated in a Broyden–Fletcher–Goldfarb–Shanno (BFGS) (Blomgren, 2015) type line search (ANSYS, 2015a).

The parameters used for the NLPQL optimisations are shown in table 4.2, with their functions defined below:

Finite Difference Approximation: The default strategy (either Central or Forward Difference) for estimating the objective function gradient when analytical methods do not apply.

Table 4.2: NLPQL Optimisation Settings

Parameter	Setting
Finite Difference Approximation	Central
Allowable Convergence (%)	1E-06
Maximum Number of Iterations	2000
Maximum Number of Candidates	10-40

Allowable Convergence (%): The tolerance for Karush-Kuhn-Tucker criteria, with lower values producing more accurate slower results and higher values producing less accurate faster results.

Maximum Number of Iterations: Maximum number of iterations the algorithm will execute without finding convergence.

Maximum Number of Candidates: Same as Screening method (see Section 4.1.1).

For more detailed explanations of the parameters see ANSYS (2015a).

4.1.3 Mixed-Integer Sequential Quadratic Programming (MISQP)

MISPQ is a gradient based single objective method. The MISPQ method is a type of modified sequential quadratic programming method similar to the NLPQL method (see section 4.1.2) but with the assumption that the problem functions are twice continuously differentiable and with the inclusion of integer variables (including binary) (Exler *et al.*, 2012). If the number of integers is set to zero the MISPQ code behaves like a standard trust region stabilised Sequential Quadratic Programming (SQP) code for continuous optimisation. The MISPQ method is typically designed for use with highly non-linear and non-convex problems but still suitable for relaxable mixed-integer problems (Exler *et al.*, 2012). MISPQ is a local optimisation method with better accuracy than the global methods (Screening and MOGA) (ANSYS, 2015a).

The MISPQ method works by linearizing the constraints and generating a quadratic approximation of the Lagrangian function, with the mixed-integer quadratic problems successively generated and solved by the branch-and-cut method (ANSYS, 2015a). The method solves mixed-integer non-linear problem (MINLP) of the form (ANSYS, 2015a)

$$
\begin{aligned}
&\text{Minimize } f(x,y) \\
&\text{subject to:} \\
&\qquad g_j(\{x,y\}) = 0, j = 1,...,m_e, \\
&\qquad g_j(\{x,y\}) \geq 0, j = m_e+1,...,m \\
&\text{where} \\
&\qquad x \,\epsilon\, \mathbb{R}^{n_c},\ y \,\epsilon\, \mathbb{N}^{n_i} \\
&\qquad x_l \ \leq\ x\ \leq\ x_u\ ,\ y_l\ \leq\ y\ \leq\ y_u
\end{aligned}
\tag{4.14}
$$

where x and y denotes the continuous variables and integer variables respectively and with n_c and n_i the number of continuous variables and a number of integer variables respectively. With subscripts u and l the upper and lower bounds of the variables respectively.

The Lagrangian function for MINLP is (Exler *et al.*, 2012)

$$
\begin{aligned}
L(x,y,u,v_l,v_u,w_l,w_u) \ :=\ & f(x,y) - \sum_{j=1}^{m} u_j g_j(x,y) - v_l^T(x - x_l) \\
& - v_u^T(x_u - x) - w_l^T(y - y_l) - w_u^T(y_u - y),
\end{aligned}
\tag{4.15}
$$

with u_j the Lagrangian multiplier for the j-th constraint, where v_l and v_u are the upper and lower bound multipliers respectively for the continuous variables and where w_l and w_u are the upper and lower bound multipliers respectively for the integer variables.

The Hessian of the Lagrangian function is approximated by the quasi-Newton update formula BFGS. A branch-and-cut method is used with algorithm stabilisation using the trust region method both detailed in Exler *et al.* (2012) and with the trust region method based on Yuan (1995). The MISPQ algorithm itself is included in Exler *et al.* (2012).

The parameters used for the MISQP optimisations are shown in table 4.3, with their functions defined below:

Finite Difference Approximation: Same as NLPQL method (see Section 4.1.2).

Allowable Convergence (%): Same as NLPQL method (see Section 4.1.2).

Maximum Number of Iterations: Same as NLPQL method (see Section 4.1.2).

Table 4.3: MISQP Optimisation Settings

Parameter	Setting
Finite Difference Approximation	Central
Allowable Convergence (%)	1E-06
Maximum Number of Iterations	2000
Maximum Number of Candidates	10-40

Maximum Number of Candidates: Same as Screening method (see Section 4.1.1).

For more detailed explanations of the parameters see ANSYS (2015a).

4.1.4 Multi-Objective Genetic Algorithm (MOGA)

Genetic Algorithms (GAs) were originally invented by John Holland as a method for studying genetic adaption or evolution in nature. It used genetic-inspired mathematical operators for selection, cross-over, mutation and inversion to move from one population group to another, something akin to numerical "natural selection" (Mitchell, 1998). GAs as in this work are commonly used for function optimisation where parameters are adjusted to maximise a certain parametric function. A basic GA consists of solution vectors ($x \epsilon X$) called chromosomes with discrete units called genes. The genes are the parametric control variables for one or more features of the chromosomes. The chromosomes in this work can be considered the individual design candidates, a set of which is called a population (Konak *et al.*, 2006). The initial population is quasi-randomly generated by use of the Shifted-Hammersley Sampling method as used in the Screening optimisation algorithm (see Section 4.1.1). A cross-over operator pairs chromosomes to produce new chromosomes (aka Parents and Children). An iterative process of the cross-over operator on parents selected based on a fitness function (f{x}, a rank based system that increases the probability of being chosen based on the parent's performance in satisfying the maximisation or minimization of the objective function) produces a new more "fit" population of chromosomes. Mutation is the process of continually adding small changes (on a gene level) to the population. This adds numerical diversity to the population in an attempt to evade local optima stagnation by allowing non-dominant design alternatives (genes in this case) the chance to "evolve" (Konak *et al.*, 2006).

The MOGA as used in Ansys is a hybrid variant of the Non-dominated Sorted Genetic Algorithm-II algorithm designed to work with multiple objective functions (ANSYS, 2015a). An important part of MOGA is the concept of Pareto Dominance, where the objectives and constraints represent a compromise in each other there is no single optimum

that is best for all objectives and constraints. The Pareto set is a group of Pareto optima or non-dominant solutions, solutions that when deciding between one over another you will always sacrifice an objective or constraint for the gain in another (Konak *et al.*, 2006; ANSYS, 2015a).

The optimisation problem is to minimize a set of objective functions (ANSYS, 2015a):

$$min\ \vec{\mathrm{f}}(\mathrm{x}) \tag{4.16}$$

with the set of all feasible solutions x in the space X (ANSYS, 2015a):

$$\mathrm{x}\epsilon X \tag{4.17}$$

the solution of the scalar optimisation problem:

$$min\ \mathrm{f}_i(\mathrm{x}) = \mathrm{f}_i^* \tag{4.18}$$

the vector $\mathrm{f}^* = (\mathrm{f}_i^*, ..., \mathrm{f}_k^*)^i$ is named ideal for a multi-objective problem; and the points in X which determined this vector are the ideal solution (ANSYS, 2015a).

A point $\mathrm{x}^{'}\epsilon X$ is said to be Pareto Optimal for the problem if there is no other vector $\mathrm{x}\epsilon X$ that $\mathrm{f}_i(\mathrm{x}) \leq \mathrm{f}_i(\mathrm{x}^*)$ for all $i, ..., k$ and for at least one objective function $\mathrm{f}_i(\mathrm{x}) < \mathrm{f}_i(\mathrm{X}^*)$ (ANSYS, 2015a; Konak *et al.*, 2006). The values for the objective function for a Pareto Set is called the Pareto Front, with the goals of the optimisation to explore these fronts locally (intensified search in certain regions) and globally (search equally across the front) as well as extending the fronts in both directions exploring new extremes (Konak *et al.*, 2006). These conflicting goals are achieved with the MOGA through cross-over and mutation.

The cross-over operator works by combining two parent chromosomes to produce two new children by using the equations (ANSYS, 2015a):

$$\text{Child 1} = \mathbf{a} * \text{Parent1} + (1 - \mathbf{a}) * \text{Parent2} \tag{4.19}$$

$$\text{Child 2} = (1 - \mathbf{a}) * \text{Parent1} + \mathbf{a} * \text{Parent2} \tag{4.20}$$

with **a** the cross-over ratio, randomly producing different combinations of parent weighting to the children.

The mutation operator works by adding a small value δ (within the boundaries and calculated from a polynomial distribution) to the parent gene to produce a mutated child gene (ANSYS, 2015a):

$$\text{Child} = \text{Parent} + (Upperbound - LowerBound)\delta \tag{4.21}$$

The MOGA method is diagrammatically represented in figure 4.2. The parameters used for the MOGA optimisations are shown in table 4.4, with their functions defined below:

Table 4.4: MOGA Optimisation Settings

Parameter	Setting
Number of Initial Samples	10000
Maximum Number of Candidates	10-40
Number of Samples Per Iteration	2500
Maximum Allowable Pareto %	70
Convergence Stability %	0-2
Maximum Number of Iterations	2000

Number of Initial Samples: Same as Screening method (see Section 4.1.1).

Maximum Number of Candidates: Same as Screening method (see Section 4.1.1).

Number of Samples Per Iteration: Total number of samples solved in one iteration.

Maximum Allowable Pareto %: The percentage representative of the number of the MOGA front points required for convergence.

Convergence Stability Percentage: A percentage representative of the amount the population is allowed to deviates from the mean for convergence.

Maximum Number of Iterations: Same as NLPQL method (see Section 4.1.2).

For more detailed explanations of the parameters see ANSYS (2015a).

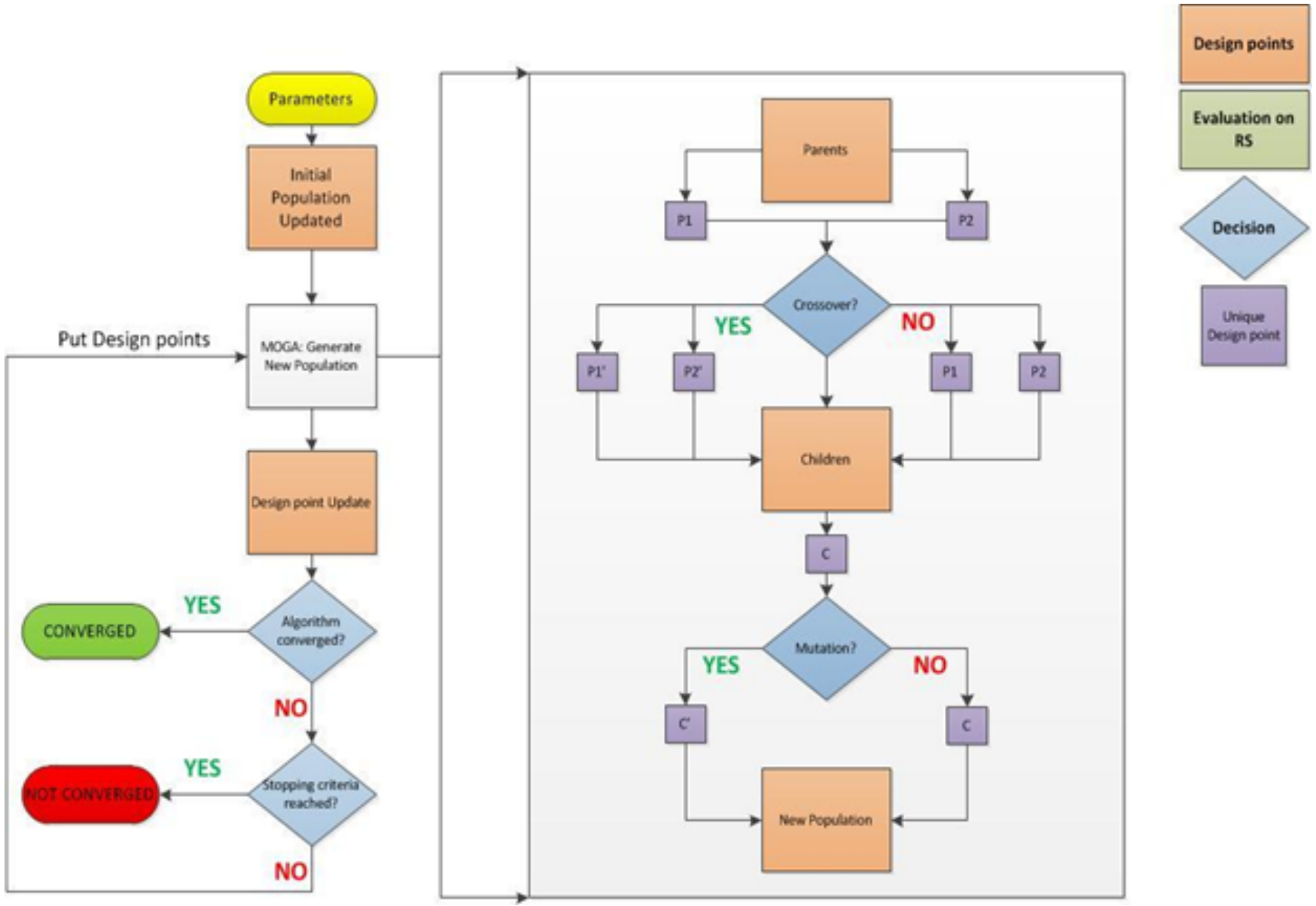

Figure 4.2: MOGA workflow (ANSYS, 2015a)

4.2 Parametrization

A baseline geometric model of a tactical SRM nozzle is parametrized with multiple spline control points (see Figure 4.3 below or Appendix A.1), namely x_n and R_n with $n = 1, 2, 3, 4...$ Further control points are R_t, r_i, θ_i, R_e, θ_e and x_t. Parameters r_i and θ_i allow for simple parametric control over the throat initial expansion angle and radius of curvature, with parameters R_t and R_e giving control over the nozzle expansion ratio and with θ_e and x_t giving control over nozzle exit angle and nozzle length respectively. A similar parametrization approach was used by (Cai *et al.*, 2007) coupled with three different optimisation routines. The parameters are constrained such that there can only be expansion and no contraction in the nozzle geometry which helps avoid spurious design points (for this application) and reduces computational time. Implementation is by constraining parameters such that $x_t > x_4 > x_3 > x_2 > x_1$ and $R_e > R_1 > R_2 > R_3 > R_4$.

Differently to this work, circular arc (with singular expansion arc) and parabolic Rao nozzle parameterization approaches would have only a single useful geometric solution that is defined or constrained solely by θ_i, θ_e, x_t and R_e. For the spline based method used , there are multiple surfaces that can be further defined by the position of the control point/s (x_n,R_n) as is demonstrated in Figure 4.4 (also Appendix A.2) below. The addition of the control point/s gives control over the expansion "weighting" within the nozzle i.e it shifts the surface expansion rate back and forth within the nozzle. For this work, the throat diameter is fixed based on the internal ballistics of the rocket motor and the area ratio fixed due to physical size constraints on the nozzle exit for case 1 and 2. The various cases (see section 5.6) were run through the framework with the effective variable combinations shown in Table 4.5.

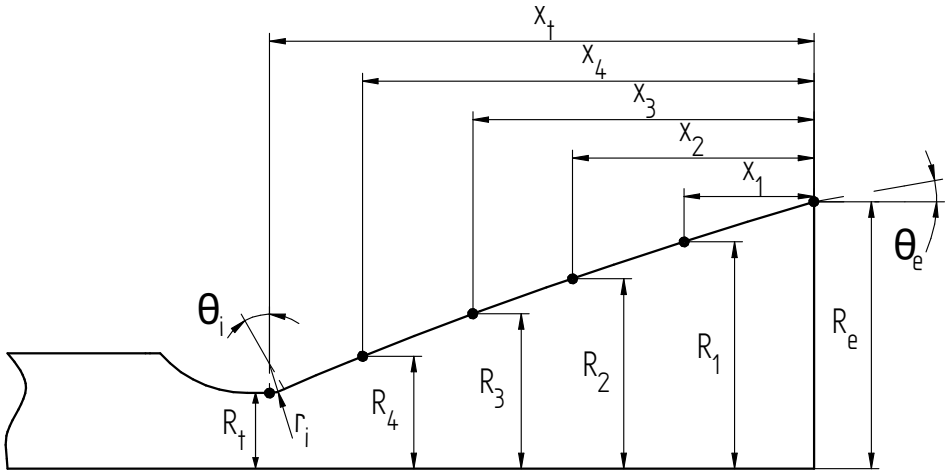

Figure 4.3: Parametrized rocket nozzle

Table 4.5: Case Variables

Case	# of Variables	Variables
1	5	$x_2, R_2, r_i, \theta_i, \theta_e$
2	7	$R_1, R_2, R_3, R_4, r_i, \theta_i, \theta_e$
3	6	$x_2, x_t, R_2, r_i, \theta_i, \theta_e$
4	5	$x_2, R_2, r_i, \theta_i, \theta_e$
5	5	$x_2, R_2, r_i, \theta_i, \theta_e$
6	5	$x_2, R_2, r_i, \theta_i, \theta_e$

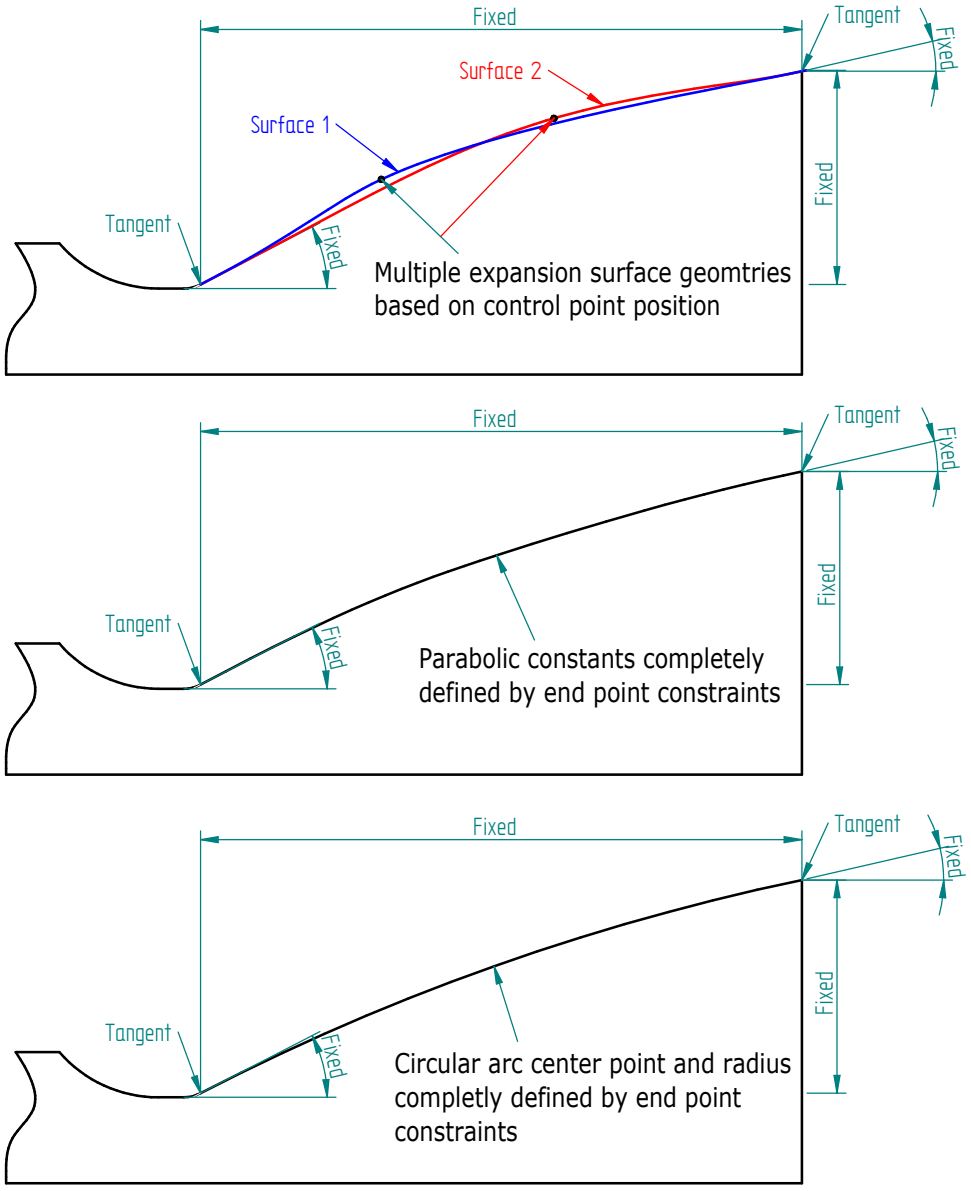

Figure 4.4: Spline (top) , parabolic Rao (middle) and circular arc (bottom) geometry comparison

4.3 Response Surfaces

Response surfaces are a method used to characterise the input and output variable relationships. The response surface is built from the DOE samples and provides quick approximations of the output parameters at unknown design points. The standard response surface used in ANSYS is a Full 2nd-Order Polynomial (see section 4.3.1 with four additional methods available (Kriging, Non-Parametric Regression, Neural Network and Sparse Grid). ANSYS guidelines recommend always starting with the standard response surface and if needed changing over to a Kriging response surface (ANSYS, 2015a). This work uses both these methods in all cases, the methods are described in sections 4.3.1 and 4.3.2. For details on the other methods see ANSYS (2015b,a). Table 4.6 summarises the methods available.

Table 4.6: Response Surface Meta-Model Characteristics - adapted from ANSYS (2015a)

Meta-Model Type	Characteristics
Standard	-Default meta-model; creates a Standard Response Surface -Effective when the variation of the output is smooth with regard to the input parameters
Kriging	-Efficient in a large number of cases -Suited to highly nonlinear responses -Do NOT use when results are noisy; Kriging is an interpolation that matches the points exactly -Always use verification points to check Goodness of Fit
Sparse Grid	-Suited for studies containing discontinuities -Use when solve is fast
Non-Parametric Regression	-Suited to nonlinear responses -Use when results are noisy -Typically slow to compute
Neural Network	-Suited to highly nonlinear responses -Use when results are noisy -Control over the algorithm is very limited

4.3.1 Standard response surface - Full 2nd-order polynomial

The standard response surface is a second-order polynomial regression model with n sampling points. The corresponding output values at each sampling point are known. The regression analysis determines an approximation of the input-output variables relationship. The quality of this approximation is improved by using a Yeo-Johnson transformation.

The output as a function of the input variables defines the surface (ANSYS, 2015a). The general definition for the regression models is (ANSYS, 2015a)

The error sum of squares:

$$SSE = \sum_{i=1}^{n} (y_i - \hat{y}_i)^2 = (\{y\} - \{\hat{y}\})^T (\{y\} - \{\hat{y}\}) \tag{4.22}$$

where

y_i = value of the output parameter at the ith

y_i = value of the regression model at the ith

superscript T denotes a matrix transpose.

The regression sum of squares:

$$SSR = \sum_{i=1}^{n} (\hat{y}_i - \overline{y})^2 \tag{4.23}$$

where

$$\overline{y}_i = \frac{1}{n} \sum_{i=1}^{n} y_i$$

The total sum of squares:

$$SST = \sum_{i=1}^{n} (y_i - \overline{y})^2 \tag{4.24}$$

The 2nd order polynomial response is simply a multi-linear regression analysis of the form (ANSYS, 2015a)

$$y_i = [t]_i \{c\} + \epsilon$$

where

$$\{c\} = [c_1 c_2 ... c_p]^T \ = \ \text{vector of the regression parameters of the regression model} \tag{4.25}$$

with $[t]$ the row vector of regression terms of the response surface model at the ith sampled location,p the total number of regression parameters and ϵ an unobserved random error.

4.3.2 Kriging response surface

The Kriging response surface provides an exact interpolation and covers the whole experimental area, it is a global meta-model of the simulation (Van Beers and Kleijnen, 2004). It works by combining a polynomial model (similar to the standard response in section 4.3.1) with local deviations that fit the points exactly. The unknown function of interest $y(x)$ is made of $f(x)$, polynomial function of x and $Z(x)$ a realization of a normally distributed Gaussian random process with mean zero, variance σ^2 , and non-zero covariance (ANSYS, 2015a)

$$y(x) = f(x) + Z(x) \tag{4.26}$$

with Z(x) the covariance matrix (the basic form is shown in Van Beers and Kleijnen (2004)) given by (ANSYS, 2015a)

$$Cov[Z(x^i), Z(x^j)] = \sigma^2 R([r(x^i, x^j)]) \tag{4.27}$$

R is a N*N symmetric, positive definite correlation matrix. $r(x^i, x^j)$ is the Gaussian spatial correlation of the function between any two of the N sample points x_i and x_j.

4.4 Overview of the Optimisation Process

The optimisation framework was setup in ANSYS Workbench. It involves a two loop process diagrammatically shown in Figure 4.5. The first part of the simulation (solver loop) involves populating a DOE design table with sufficient design points to characterise the optimisation search domain (represented as response surfaces). This involves defining the input variables as well as their limits to drive the design points. The variables are based on a parametric nozzle geometry (see Section 4.2). The DOE design table iteratively updates the parametric model. For each iteration, the updated geometry is re-meshed and fixed boundary name selections defined. The mesh is passed to the solver where boundary conditions are applied according to the naming convention defined in the mesh. The solver runs the simulation until the convergence criteria (see section 5.1) is met and then

populates the design point outputs (thrust and mass flow rate) with the solution variables. This loop continues until all the design points are solved. The second loop of the simulation (optimisation and refinement loop) involves using the solved design points to construct variable response surfaces (see section 4.3), essentially characterising the response of both input and output variables to changes made. A goal seek optimisation (see section 4.1) is then performed using the response surfaces, a user defined amount of candidate design points are generated per optimisation method. The design point table is amended with the additional candidate points and then the solver loop starts again until completion. Further, the optimisation and refinement loop is restarted using the newly updated design table, producing a more refined response surface. This overall loop can be continued until the optimisation candidate points converge on their validation results in the solver loop or the objective result improvement from each iteration stalls.

For this work, the goal-driven optimisation was used which incorporates a response surface type characterization and optimisation. This is different to a direct optimisation system which is single-component and utilises direct solves (ANSYS, 2015a). The objective function of the optimisation is to maximize thrust ($F_t = \int_{A_2} \left(\rho u^2 + p\right) dA$). The CCD was used to generate the points needed to characterise the initial response surface. The characterised simulation responses were then put through a case dependent choice of optimisation algorithms. A user-defined number of candidate design points are generated and further used to validate and refine the response surface. Further refinement points were manually added to the response surface in areas of low resolution and in proximity to possible optima candidates. The refined response surfaces were put through a second optimisation routine again with a case dependent choice of optimisation algorithms and final candidate points validated and compared. While all optimisation methods were used, optimisation results for case 6 (see 5.6.6) in which each method was used for the single case showed minor differences between method choice. The results of which are plotted in figure 4.6, showing a maximum difference between methods of 3.6 N with the top candidates varying from 14415.6 to 14412.0 N. The choice of method per case was ultimately based on best practices and guidelines (ANSYS, 2015a) for goal-driven optimisation where a global algorithm (Screening or MOGA) is initially used to locate possible optima regions and then a more accurate but local method (NLPQL or MISPQ, which are both gradient based) is then used to zoom in on these local optima. For example, the Screening method is typically used for the preliminary design due to its global non-iterative fast solutions while the NLPQL algorithm is used for further more accurate optimisation results (ANSYS, 2015a). This work did not have a multiple objective case which would have necessitated the use of the Screening or MOGA method only for response surface optimisation, being the only multiple-objective compatible methods available in Ansys Workbench.

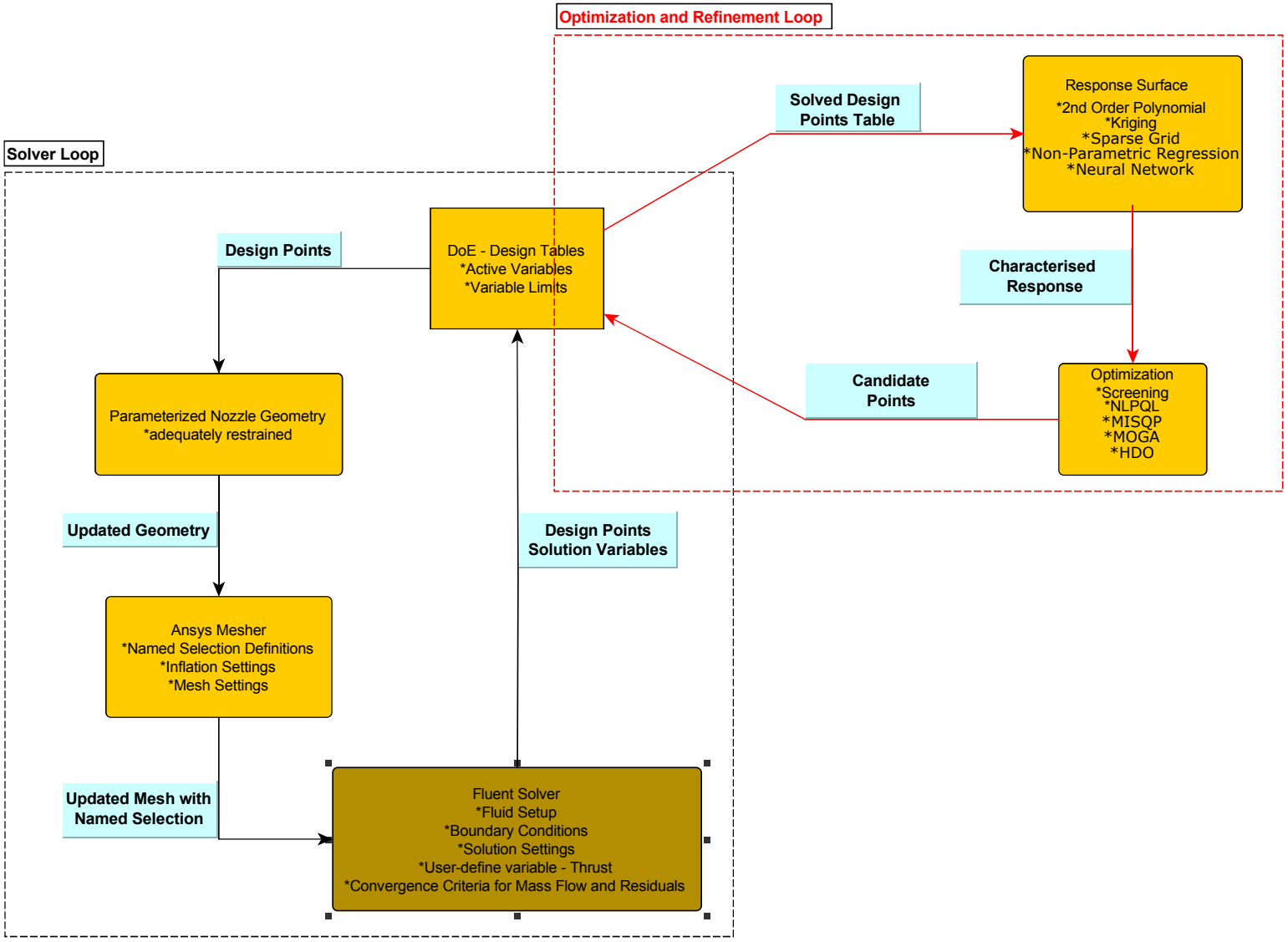

Figure 4.5: Optimisation method - Process flow diagram

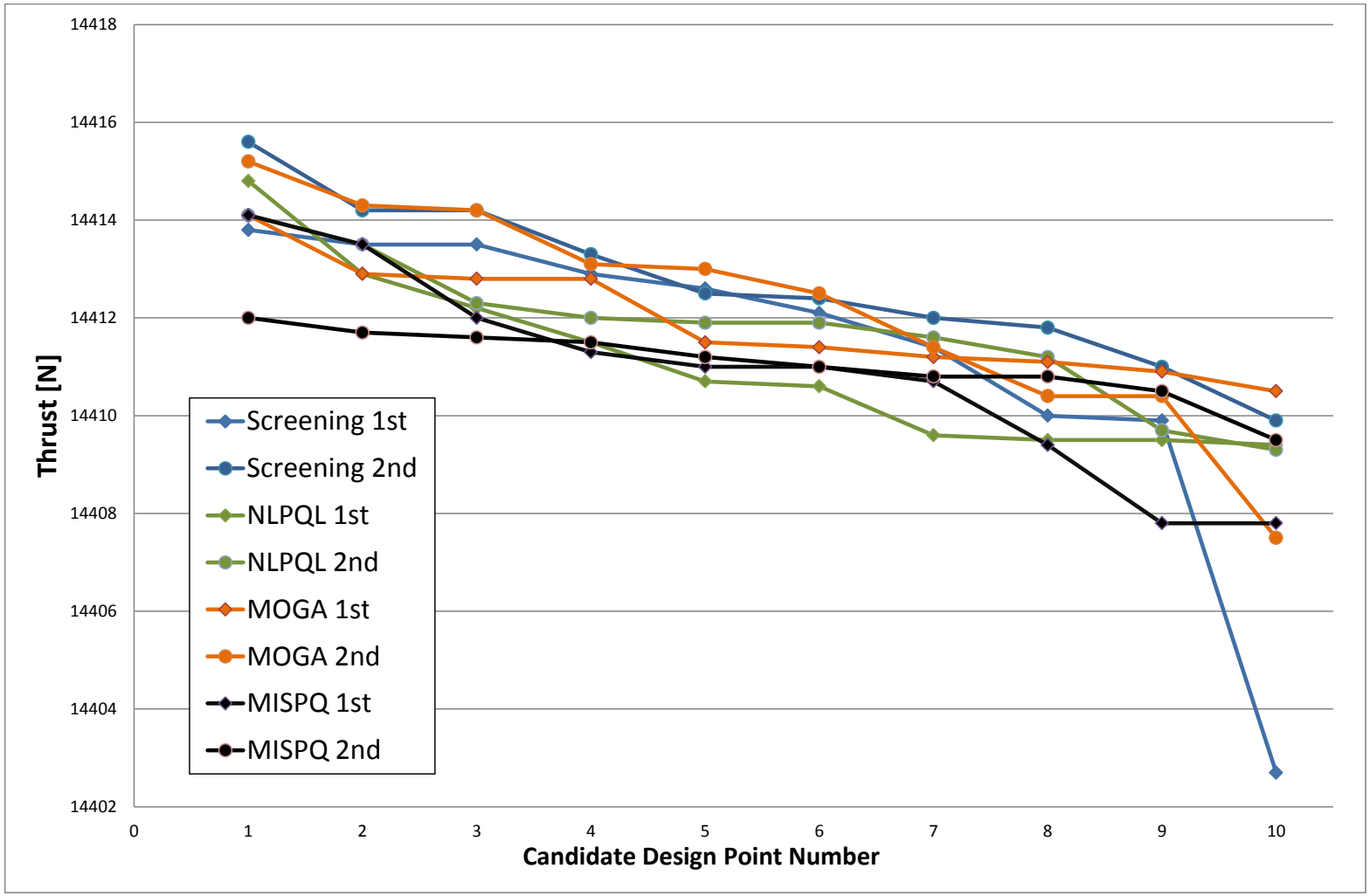

Figure 4.6: Optimisation method comparison - CASE 6

5 Numerical Results

5.1 Simulation Method

This work uses the density-based solution method with the implicit linearization of the governing equations. The method is chosen for its efficiency in dealing with high-speed compressible flow (ANSYS, 2015b) as well as the experimental and theoretical work done in chapter 6 and 5.5 respectively. The convergence criteria are that all scaled residuals are to be less than $1x10^{-3}$ and mass flow rate at the nozzle exit to converge to the fourth decimal place. The fluid properties used are presented in Table 5.1 and are based on in-house general combustion modelling parameters. The Fluent solver settings for this work are presented in Table 5.2.

A tabular transient boundary profile approach was used for both gauge and total pressures for the transient case. Linear interpolation is used between time steps. The table values are read into Fluent as a user defined profile using the terminal prompt command "file $\rightarrow$ read-transient-table". The format is as per Table 5.3 below (see Appendix D Figure D.2 for sample of actual tables used).

Table 5.1: HTPB Based Propellant Combustion Gas Properties

Property	Value
Density (kg/m^3)	Ideal Gas Law
Specfic heat ($j/kg.K$)	1823.8
Thermal Conductivity ($w/m.K$)	0.22395
Viscosity ($kg/m.s$)	$7.9786e-05$
Molecular Weight ($kg/k.mol$)	25.609
Combustion chamber temperature (K)	2500

Table 5.2: Solver Settings

Setting	Steady-State	Transient
Solver Type	Density	Density
Time	Steady	Transient
2D Space	Axisymmetric	Axisymmetric
Initialization	Hybrid	Hybrid
Time Step	NA	1e-5 s
Models	———	———
Energy Equation	On	On
Viscous	$k-\omega$ SST	$k-\omega$ SST
Solution Method	———	———
Formulation	Implicit	Implicit
Flux Type	Roe-FDS	Roe-FDS
Spatial Discretization	———	———
Gradient	Least Squares	Least Squares
Flow	2nd Order Upwind	2nd Order Upwind
Turbulent Kinetic Energy	2nd Order Upwind	2nd Order Upwind
Specific Dissipation Rate	2nd Order Upwind	2nd Order Upwind
Transient Formulation	NA	First Order Implicit
Solution Control	———	———
Courant Number	5	2
Turbulent Kinetic Energy	0.8	0.8
Specific Dissipation Rate	0.8	0.8
Turbulent Viscosity	1	0.9
Solid	1	1
Boundary Conditions	———	———
Operating Pressure	0 Pa	0 Pa
Pressure Inlet	———	———
Total Pressure	1e+07	Transient*
Initial Pressure	0.9e+07	Transient*
Turbulent Intensity	3%	3%
Turbulent Viscosity Ratio	10	10
Temperature	2500K	2500K
Pressure Outlet	———	———
Gauge Pressure	101325 Pa	101325 Pa
Temperature	300 K	300 K
Atmospheric Inlet	———	———
Total Pressure	NA	101325 Pa
Initial Pressure	NA	101325 Pa
Turbulent Intensity	NA	1%
Turbulent Viscosity Ratio	NA	10
Temperature	NA	300K

Table 5.3: Tabular Transient Profile

profile-name	n-field	n-data	periodic	
field-name-1	field-name-2	...	...	field-name-n-field
v-1-1	v-2-1	...	...	v-n-field-1
...	...	...	...	...
v-1-n-data	v-2-n-data	...	...	v-n-field-n-data

5.2 Domain and Mesh Method

Two domain types are used for this work.

The primary type used for the optimisation work was a truncated exhaust domain and mesh with a 50 mm section of the combustion chamber included for the inlet (chosen based on the work done in Section 5.4). The domain and mesh can be seen in Appendix B Figures B.1 and B.2 with the named selections shown. Element size was set at 0.75 mm with a wall inflation method based on a first layer thickness of 0.02 mm, 30 layers and 1.1 growth rate. Meshing method was set to automatic. The element mesh quality metric was on average 0.62, the inflation elements tend to negatively distort the results which are typically based on element squareness and aspect ratios. The validation work did not, however, show a large effect on simulated results which is in part due to the flow being aligned with the high aspect ratio elements and therefore producing a lower level of grid induced discretization errors while improving near wall resolution (Versteeg and Malalasekera, 2007).

The secondary type of domain used is the extended exhaust domain. Similar to the truncated domain a 50 mm section of the combustion chamber is used. The nozzle exit is however extended to include an approximately 2000 mm X 600 mm domain of exhaust area as seen in Appendix B Figures B.3 and B.4 with the named selections shown. Element size for the nozzle was set at 1.50 mm with no wall inflation. The exhaust area required a recorded meshing method allowing for the nozzle to be meshed first with the exhaust following. The mapped face meshing method was used for the exhaust with element size set to 2.0 mm. With the considerably larger domain size, smaller element sizes were not feasible with the computing power available. The element mesh quality metric was high with an average of 0.99. This would be due to near square elements and no wall inflation being used.

5.3 Grid Independence

A Grid independence study was done on element sizes varying from 0.15 to 3.0 mm. Two meshing approaches were considered. Firstly, wall inflation based quad mesh with first cell height approx. 0.02 mm giving y^+ values of less than 5 for the nozzle wall exit profile. Secondly, a structured quad mesh with no wall inflation giving varied y^+ values with cell size. For the cell sizes mentioned above the second mesh approach yields y^+ values ranging from < 100 to < 1500 for the nozzle wall exit profile. Further wall refinements yielding $y^+ < 1$ gave marginally improved velocity profiles with no improvement on thrust

prediction and greatly increased computational expense; these results have been omitted from Figure 5.1 which shows a low y^+ sensitivity which corresponds with the results for Couette flow simulations performed by Menter *et al.* (2003) as well as Fluent guidelines for Enhanced Wall Treatment (EWT) ANSYS (2015b). Once the number of elements exceeds $1.25x10^5$, corresponding to an element size of approx. 0.5 mm, it is shown further increases in element count do not contribute significantly to the improvement of thrust prediction and the negligible increase in fidelity comes at an ever increasing computational expense. It can be seen in Figure 5.1 that both mesh methods gave similar thrust results for comparable element counts. It is also noted that although there is a clear refinement plateau, none of the results are grossly inconsistent with experimental results and can be seen to range from 1.0% to 1.5% for the meshes compared. The CFD results over-predicted the actual results. Further investigation into the results, namely on closer look at the exit velocity profiles Figure 5.2 and 5.3 it can be seen that the finer meshes gave better definition in high gradient areas (which is to be expected), while the inflation based mesh gives improved near wall velocity profiles and are in better agreement with no-slip wall requirements both consistent with near wall cell refinement. Element sizes of 0.75 mm and an inflation based meshing ($y^+ < 5$) was used for the design optimisation in this study. Ideally, a 0.5 mm element size could have been used but computational limitations prohibited this during the DOE and optimisation routines. Though 0.5 mm element size meshes gave more accurate results the 0.75 mm mesh allows for designs to be evaluated considerably faster (with a near 45 % reduction in element count) and with results only typically in the order of 0.01 % less accurate than those from the 0.5 mm element size meshes. The inflation based meshing affected cell count minimally with the added benefit of a higher near wall resolution as discussed above and thus was included in the analysis.

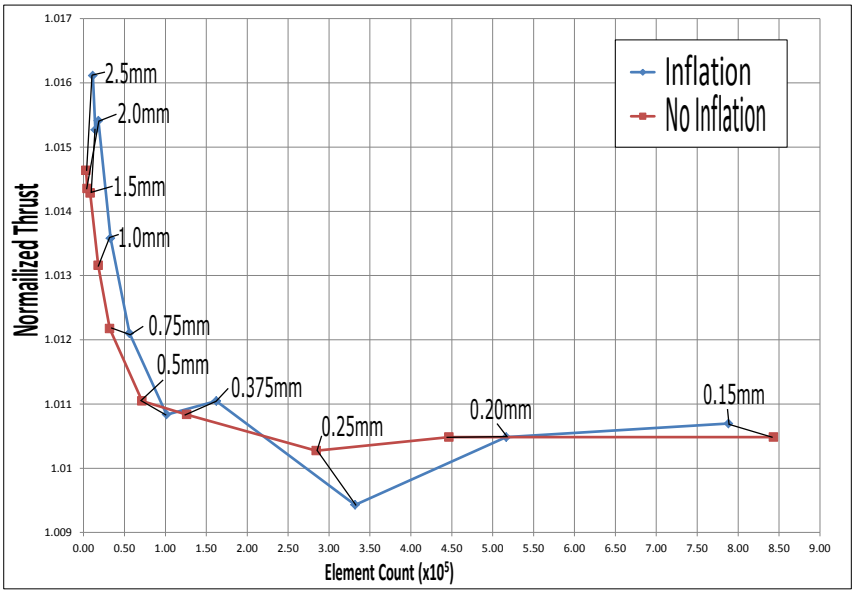

Figure 5.1: Grid independence

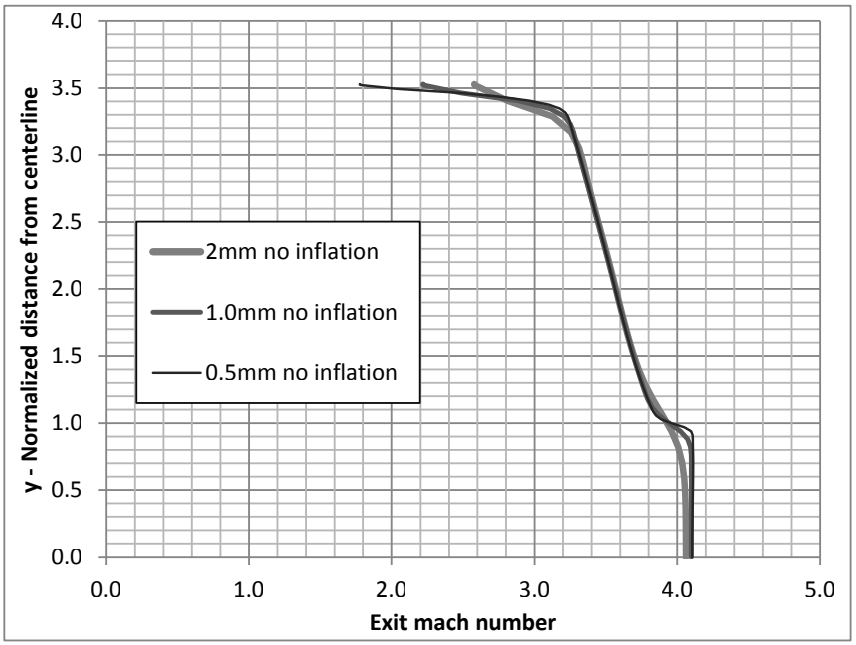

Figure 5.2: Nozzle exit velocity's for unrefined wall meshes

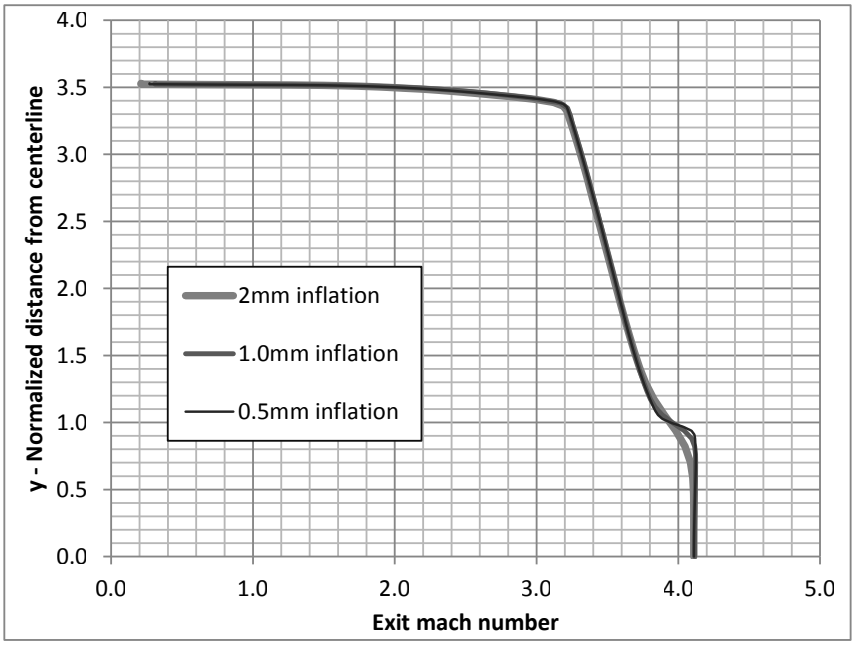

Figure 5.3: Nozzle exit velocity's for refined wall meshes

5.4 Domain Sensitivity

A domain sensitivity study was conducted to quantify the effects on the results of the varied placement of the inlet and outlet boundaries with respect to the nozzle and blast tube. Figure 2.4 previously showed a typical solid rocket motor with the computational domain shown as used in this study. Figure 5.4 shows the two domains (with meshes) considered, the final computational domain being truncated at the nozzle exit (middle) and includes a 50 mm long chamber section at the entry to the blast tube. The top shows the second domain considered where 2000 mm x 600 mm of the plume and atmosphere are included in the domain. The results are shown in Figure 5.5, the extended exit was simulated with varied cell sizes and it can be seen that it consistently over-predicted the truncated exit results by > 1 %. Although there is clear over prediction, it remains consistent and likely evident that there is no dramatic change in the physics of the simulation. It was noted that this was simulated under full nozzle flow conditions and most likely would change where back-flow into the nozzle occurs and where the truncated boundaries inability to model the complexity of the exit gas and atmosphere recirculation into the nozzle may give different results. With a full flowing nozzle, there should be no effect from downstream errors given that the flow is supersonic with pressure disturbances unable to move upstream of the boundary. The fluent solver produced stable solutions in line with expected thrust results and with well-defined nozzle near wall flow gradients. The inlet chamber length was extended in 50 mm increments. The results are graphed in Figure 5.5 (top axis). Results show that there is little influence on where the inlet boundary is placed with less than 0.1 % variation over a 200 mm increase in length. The truncated domain was seen to best suit the requirements of this study (namely to adapt the nozzle profile for optimum thrust) and at greatly reduced computational cost. There was no clear need to extend the chamber any further upstream, with the final $1.5D$ position based on where the input conditions supplied for validation in chapter 6 are given, namely 50 mm upstream of the blast tube.

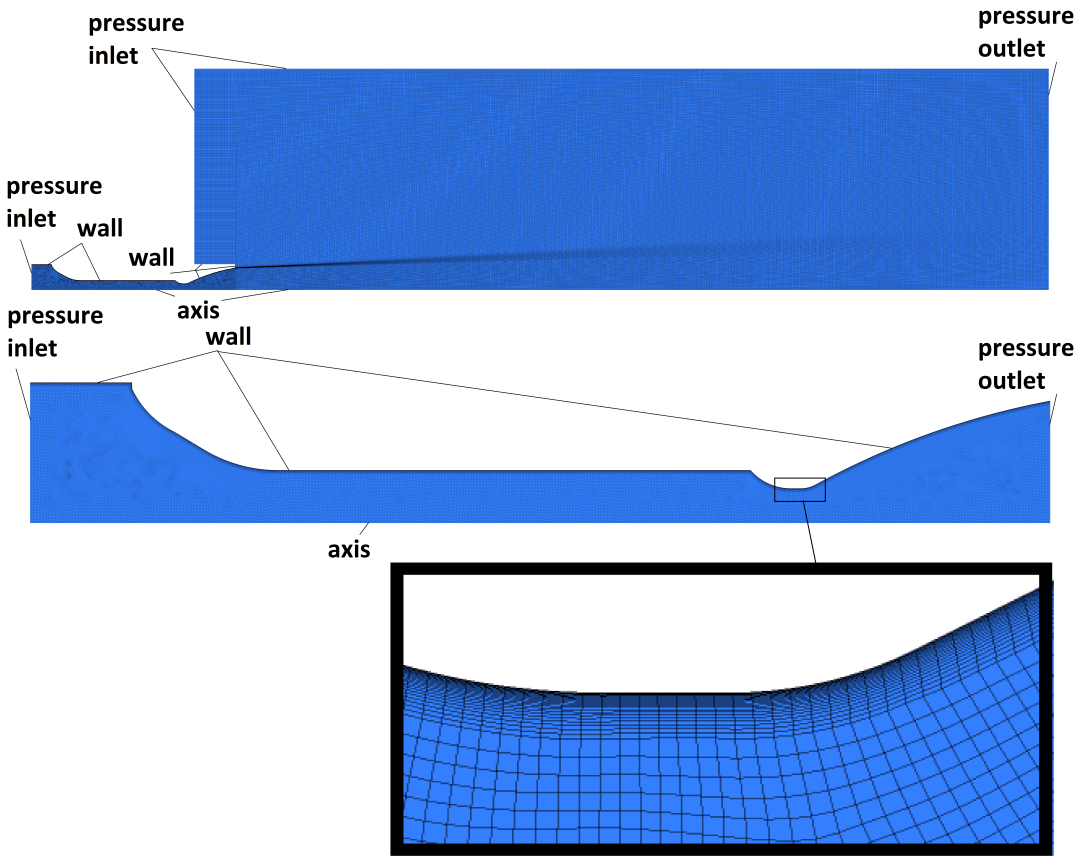

Figure 5.4: Computational domains - 2000 mm x 400 mm plume (top) , truncated (middle) and mesh detail (bottom)

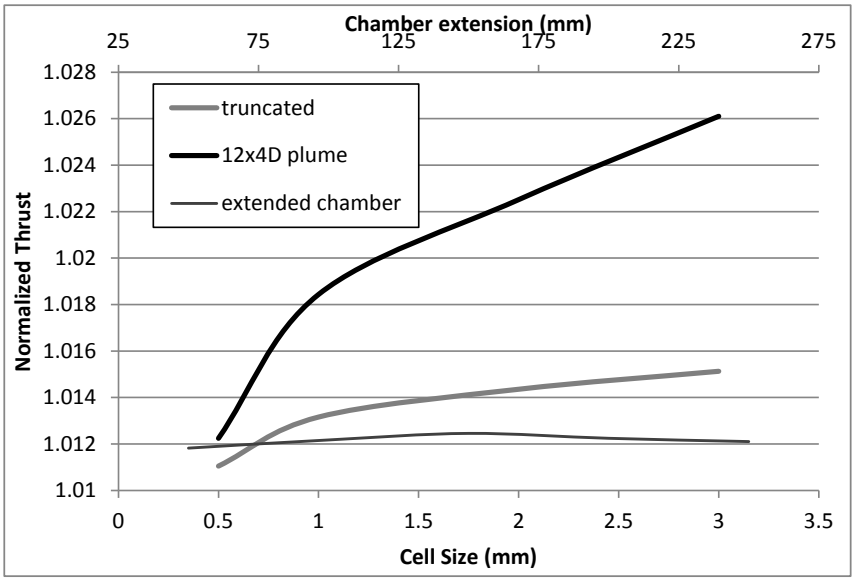

Figure 5.5: Domain sensitivity study

5.5 Theoretical

The theoretical work is based on the one-dimensional, quasi-one-dimensional and isentropic nozzle flow theory (Anderson, 1995; Sutton and Biblarz, 2001). The calculations are repetitive and have been implemented through Microsoft Excel (see Appendix D Figure D.1 for an extract of the spreadsheet). A full set of sample calculations is included below to demonstrate the theory and equations as used.

Looking at a single time point $t = 1$ where, from the transient inlet conditions $p_0 = 11282507.37\ Pa$. $T_0 = 2500\ K$, $\frac{A_e}{A_t} = 12.45595$, and Molecular Weight $= 25.609\ kg/k.mol$ which are given according to combustion temperature, fixed geometry and gas properties respectively.

From the equation of state ($\frac{p_0}{\rho_0} = RT_0$) and with $R = \frac{8314}{25.609}$ (see Anderson (1995); Sutton and Biblarz (2001)),

$$\begin{aligned} \rho_0 &= \frac{11282507.37}{324.65 \times 2500} \\ &= 13.9\ kg/m^3 \end{aligned} \tag{5.1}$$

Therefore, from the characteristic isentropic fluid flow relationships for density, temperature, and velocity (Anderson, 1995; Sutton and Biblarz, 2001) we get the characteristic density at the throat p^*

$$\begin{aligned} \frac{\rho^*}{\rho_0} &= \left(\frac{2}{\gamma+1}\right)^{\frac{1}{\gamma-1}} \\ \rho^* &= 13.9\left(\frac{2}{1.169+1}\right)^{\frac{1}{1.169-1}} \\ &= 8.601\ kg/m^3 \end{aligned} \tag{5.2}$$

the characteristic temperature at the throat T^*

$$\begin{aligned} \left(\frac{a^*}{a_0}\right)^2 = \frac{T^*}{T_0} &= \left(\frac{2}{\gamma+1}\right) \\ T^* &= 2500\left(\frac{2}{1.169+1}\right) \\ &= 2305.2\ K \end{aligned} \tag{5.3}$$

and the characteristic throat velocity a*

$$
\begin{aligned}
a^* &= \sqrt{\gamma R T^*} \\
a^* &= \sqrt{1.169 \times 324.65 \times 2305.2} \\
&= 935.339\, m/s
\end{aligned} \tag{5.4}
$$

The mass flow rate $\dot{m}$, calculated from throat conditions

$$
\begin{aligned}
\dot{m} &= \rho^* A^* a^* \\
&= 8.601 \times 0.000908 \times 935.339 \\
&= 7.3047\, kg/s
\end{aligned} \tag{5.5}
$$

From the Area-Mach Equation 2.9 , considering only the super sonic solution we get the exit Mach number M_e

$$
\begin{aligned}
\left(\frac{A}{A^*}\right)^2 &= \frac{1}{M_e^2}\left[\frac{2}{\gamma+1}\left(1+\frac{\gamma-1}{2}M_e^2\right)\right]^{\frac{\gamma+1}{\gamma-1}} \\
12.45595^2 &= \frac{1}{M_e^2}\left[\frac{2}{1.169+1}\left(1+\frac{1.169-1}{2}M_e^2\right)\right]^{\frac{1.169+1}{1.169-1}} \\
\therefore M_e &= 3.332
\end{aligned} \tag{5.6}
$$

From the stagnation isentropic fluid flow relationship for pressure and temperature (Anderson, 1995; Sutton and Biblarz, 2001), solving for exit pressure p_e

$$
\begin{aligned}
\frac{p_0}{p_e} &= \left(1+\frac{\gamma-1}{2}M_e^2\right)^{\frac{\gamma}{\gamma-1}} \\
p_e &= \frac{11282507.37}{\left(1+\frac{1.169-1}{2}(3.332)^2\right)^{\frac{1.169}{1.169-1}}} \\
&= 116016.6\, Pa
\end{aligned} \tag{5.7}
$$

and the temperature at the exit T_e

$$
\begin{aligned}
\frac{T_0}{T_e} &= 1+\frac{\gamma-1}{2}M_e^2 \\
T_e &= \frac{2500}{1+\frac{1.169-1}{2}(3.332)^2} \\
&= 1289.89\, K
\end{aligned} \tag{5.8}
$$

From speed of sound and Mach equations (Anderson, 1995), solving for speed of sound at the exit a_e

$$\begin{aligned} a_e &= \sqrt{(\gamma R T_e} \\ &= \sqrt{(1.169 \times 324.65 \times 1289.89} \\ &= 699.66\, m/s \end{aligned} \tag{5.9}$$

and solving for exit velocity V_e

$$\begin{aligned} M_e &= \frac{V_e}{a_e} \\ \therefore V_e &= 3.332 \times 699.66 \\ &= 2331.26\, m/s \end{aligned} \tag{5.10}$$

From Equation 2.6 solving for total thrust F_t

$$\begin{aligned} F_t &= \dot{m} V_e + (p_e - p_a) A_e \\ &= 7.3047 \times 2331.26 + [(116016.6 - 101325) \times 0.01131] \\ &= 17.195\, kN \end{aligned} \tag{5.11}$$

With the boundary set at 50 mm upstream from the blast tube, a pressure drop across the grain is experienced. Mach Numbers and gauge pressures for the front and rear of the motor were simulated using proprietary in-house internal ballistic software as discussed in chapter 6. Using Equation 5.7, a time based total pressure drop (see Appendix D Figure D.3 for extract of calculation spreadsheet and results) was calculated for the grain regression and applied to the experimental inlet conditions (as presented in chapter 6, the results of which are shown in Figure 5.6. It can be seen that the theory predicts that there is a greater pressure drop during the initial part of the firing, in-line with the fact the port size and grain geometry is smaller and more complex. As the grain burns out the pressure drop gets less with the grain essentially burning into a simple pipe cross section and accounting for the theoretical reduction in pressure drop. Figure 5.7 shows the various thrusts from calculations, simulations and experimental results. It can be seen clearly how the pressure drop correction brings all results closer in agreement with the experimental, specifically correcting the larger variations seen during initial burn time. A 95 % thrust coefficient was applied to the one-dimensional results (in-line with empirical nozzle correction factors commonly used within the company) bringing the one-dimensional (corrected) and CFD (corrected) in close agreement with each other as well

as the experimental results.

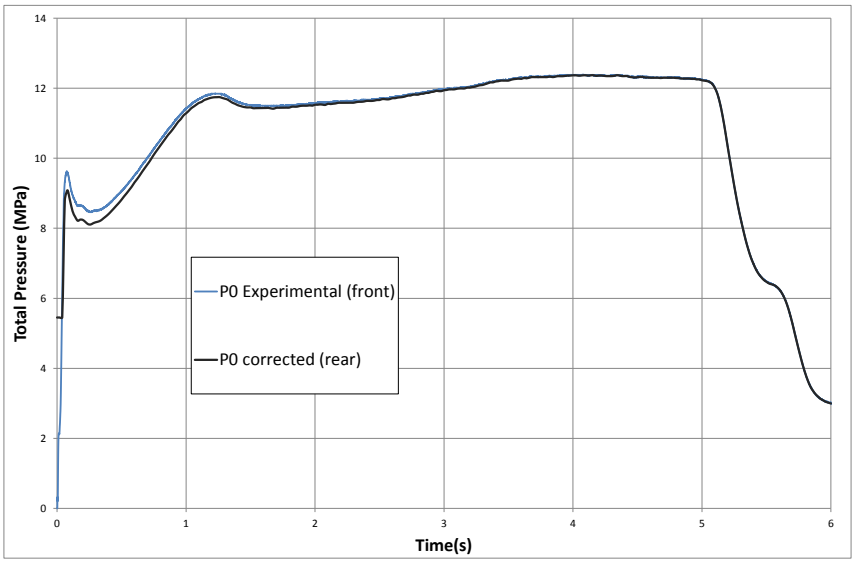

Figure 5.6: Grain pressure drop correction for inlet pressure boundary

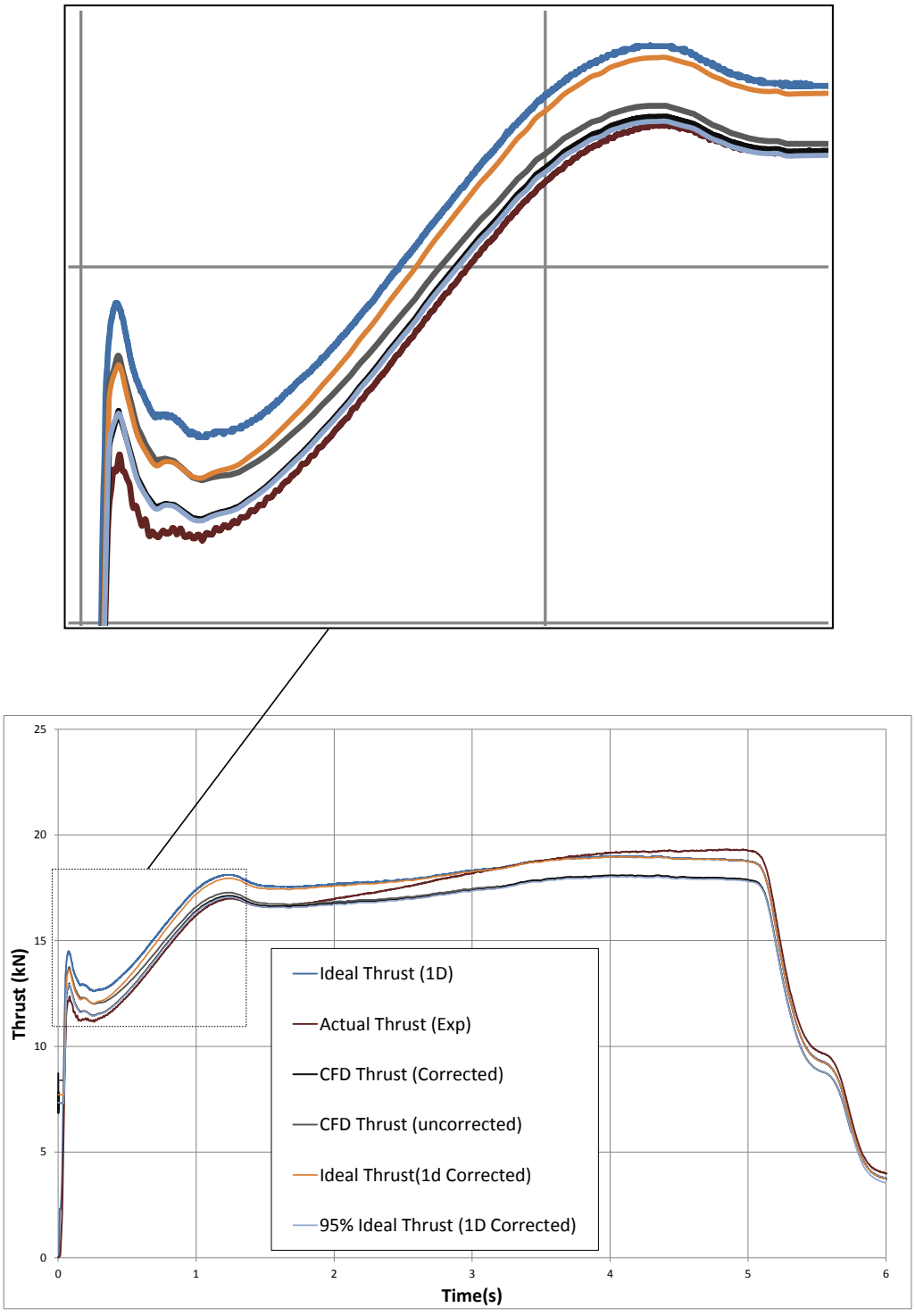

Figure 5.7: Theoretical, experimental and simulated thrust results

5.6 Case-by-Case Results

This section is separated by case.

Case 1 and 2 provide comparisons between two parametrisation methods, namely a single 2 DOF control point and 4 single DOF control points respectively. This case uses a near linear baseline geometry as the starting point for optimisation.

Case 3 uses the same framework and variables as case 1 but further looks at optimization of incrementally shorter nozzles. Four shorter nozzle lengths (-5 mm, -10 mm, -15 mm and -20 mm shorter than case 1) are compared.

Case 4 present a simulation of a parabolic approximation of a Rao nozzle contour as representative of an industry type design. The results are compared with that of the parametrically optimised contours.

Case 5 presents simulations and comparisons of full-length Rao approximation, 15° conical and parametrically optimised nozzles.

Case 6 presents the results of using the case 4 parabolic Rao approximation as a baseline for further optimisation.

5.6.1 CASE 1: Fixed area ratio [12.45:1] - Truncated (75 %) single spline control point

The case 1 study involves taking a fixed area ratio (12.45:1), fixed throat radius R_t (17 mm) and fixed length x_t (122.3 mm) nozzle design and optimising the expansion contour only. Case 1 uses only a single 2 DOF (x_2 and R_2) control point on the spline to minimise computational requirements while not completely limiting shape variations. Included in the study are two fixed contour alternatives for the purpose of comparison. Namely, a circular arc contour and a simple near linear baseline geometry based on the mean variable limits for the optimisation case. The full CFD results for the circular arc case can be seen in Appendix H, for the baseline for case 1 in Appendix G and for case study 1 (including case 1 design tables) in Appendix E.

Figure 5.8 and Figure 5.9 shows two final response surfaces (three-dimensional) for case 1 using both Standard and Kriging algorithms. The relationship is only shown for three variables per response surface for ease of display purposes. It is clear that the surfaces manage to capture design tradeoffs with variable changes. This is evident from the surface

peaks and troughs. 84 design points were used to define the surfaces sufficiently to get comparable results between the optimisation candidates and simulation results, the full design table (see Appendix E) shows further refinement points (total of 131 points) that were subsequently added for refinement but did not improve thrust results. The Kriging algorithm provided minor increases in detailed gradient variations as would be seen on close inspection of the surface and the quality of fit achieved. The standard method provided smoothing of the surface at the cost of the quality of fit achieved; this smoothing does have the effect of averaging the variations/error in thrust calculations due to minor variations in individual mesh generation and simulation convergence. There was no evidence either surface provided a better result than the other with results quickly converging on each other with increased refinement. The response surfaces also show a low sensitivity on final optimised design sizes with optimised thrust levels sitting on a plateau, indicating that the results are not typically local optimums within the prescribed constraints and design space. Full results showing a $+/-0.5$ mm on optimal design sizes giving typically $10N$ variations on thrust. The response surfaces show minor sensitivity to throat radius and radius of curvature as well as indicating the possibility that the optimum throat exit radius was outside of the search domain (the peak of the surface outside of the plot). For this comparison, the domain was not extended to accommodate smaller values for r_i.

Table 5.4 shows the top output candidates (from each method combination) from the optimisation of the case 1 and 2 response surfaces, with Figure 5.10 showing the corresponding geometry with the baseline as a reference. It can be seen that the results are comparable, with maximum thrust values achieved with all method combinations giving results within $+/-3.75$ N. This variation was similar to the variation between optimised and then validated values and hence no clear better method in this case. The results do show a clear increase in thrust from the baseline with a definite shift in geometry focus around a new optimised geometry. The geometry shows that there is an available tolerance on the spline (with minor thrust variations) which makes the optimisation results in an achievable real world design possibility. Results show there is a thrust increase over a circular arc based profile although minor.

Figure 5.11, 5.12 and 5.13 show Mach contour plot comparisons for case 1-1 vs. baseline, case 1-1 vs. circular arc and case 1-1 vs. 1-2 respectively. Mach contour plots for 1-3 and 1-4 are visually similar with 1-1 and 1-2 and have been omitted from the main text but can be found in Appendix E. Comparing the top thrust case 1-1 Mach plots with both baseline and circular arc cases shows that the gas can be expanded faster in the initial expansion part directly after the throat and higher Mach numbers can be achieved earlier in the nozzle. The result is higher exit Mach numbers at the boundary. The baseline is near-conical and shows almost constant cross-sectional exit Mach number where the

higher thrust nozzles (case 1-1 and circular arc) produce a faster "core" flow that reaches higher Mach numbers at the boundary. The circular arc and case 1-1 are similar, both producing fast core flows with a weak shock running through the nozzle from the initial throat expansion surface to the exit plane. The circular arc does not, however, manage to expand the gas to as high Mach numbers as case 1-1 as can be seen in Figure 5.13. Figure 5.14 shows exit velocity profiles for all case 1 results compared. The velocity profiles clearly show the minor variations between optimised cases. The results show there is an increase of exit area averaged Mach numbers of 1.5 % typically between optimised cases and the baseline. This accounts for part of the increased thrust simulated due to optimisation. The weak shock seen in the Mach plots is evident in the exit velocity plots where the optimised cases show a sudden drop in exit velocity between 10 and 20 mm from the centerline. The effect of the nozzle wall bounding the flow is clear from the velocity profiles, it shows the slowing of the near wall gas flow and its effect on the internal flow. The optimisation is limited by the wall and will not be able to produce maximum velocities across the complete exit plane, there will be reduced flow velocities the nearer the gas is to the wall.

Table 5.4: Case 1 and 2 - Thrust Results Summary

Case	Method		Thrust	
#	Response	Optimisation	Actual(N)	Var(N)
Base 1	n/a	n/a	14267.2	0
Circ Arc	n/a	n/a	14383.9	+116.7
$1-1$	Kriging	Screening	14409.8	+142.6
$1-2$	Standard	Screening	14409.4	+142.2
$1-3$	Standard	NLPQL	14405.1	+137.9
$1-4$	Kriging	NLPQL	14402.3	+135.1
Base 2	n/a	n/a	14267.2	0
$2-1$	Standard	NLPQL	14412.1	+144.9
$2-2$	Kriging	Screen	14396.1	+128.9
$2-3$	Standard	Screen	14393.8	+126.6
$2-4$	Kriging	NLPQL	14373.7	+106.5

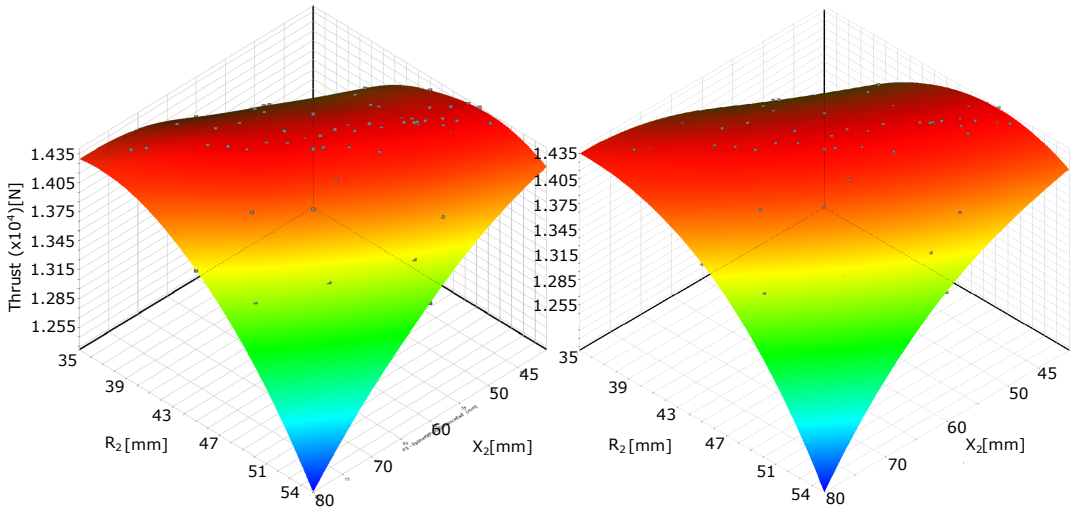

Figure 5.8: Case 1 - Response surfaces for spline control variables - Standard (left) and Kriging (right)

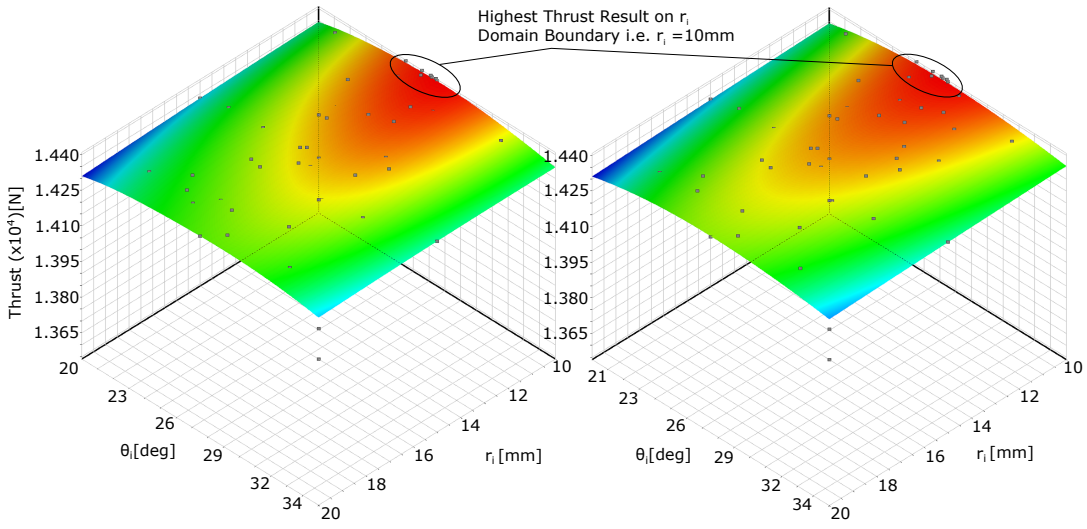

Figure 5.9: Case 1 - Response surfaces for throat control variables - Standard (left) and Kriging (right)

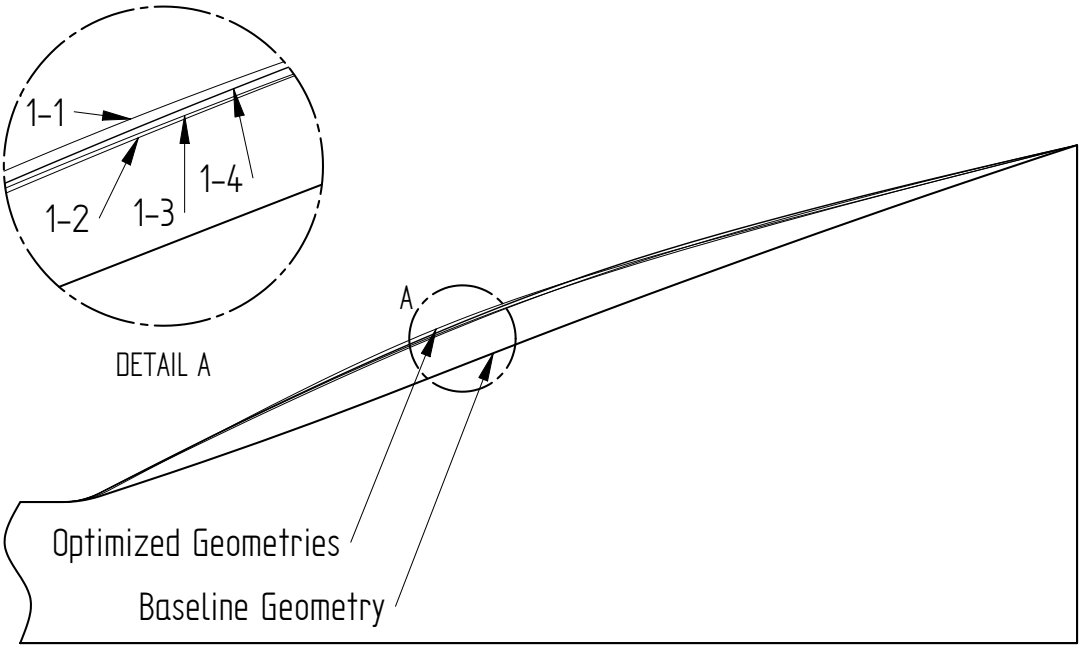

Figure 5.10: Case 1 - Geometry comparison ($1-1$, $1-2$, $1-3$, $1-4$ and baseline)

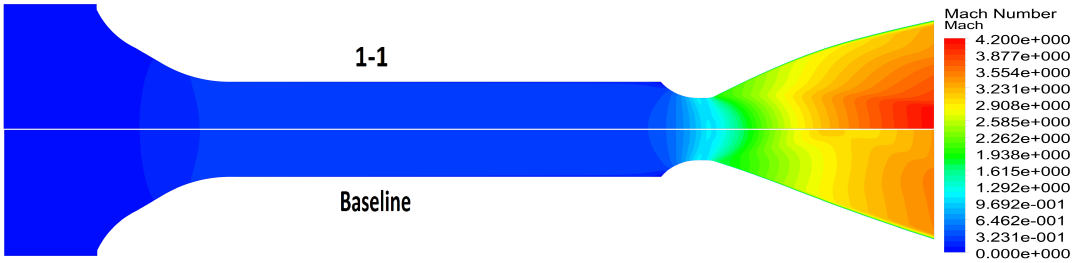

Figure 5.11: Mach number comparison of $1-1$ and baseline

Figure 5.12: Mach number comparison of $1-1$ and circular arc

Figure 5.13: Mach number comparison of $1-1$ and $1-2$

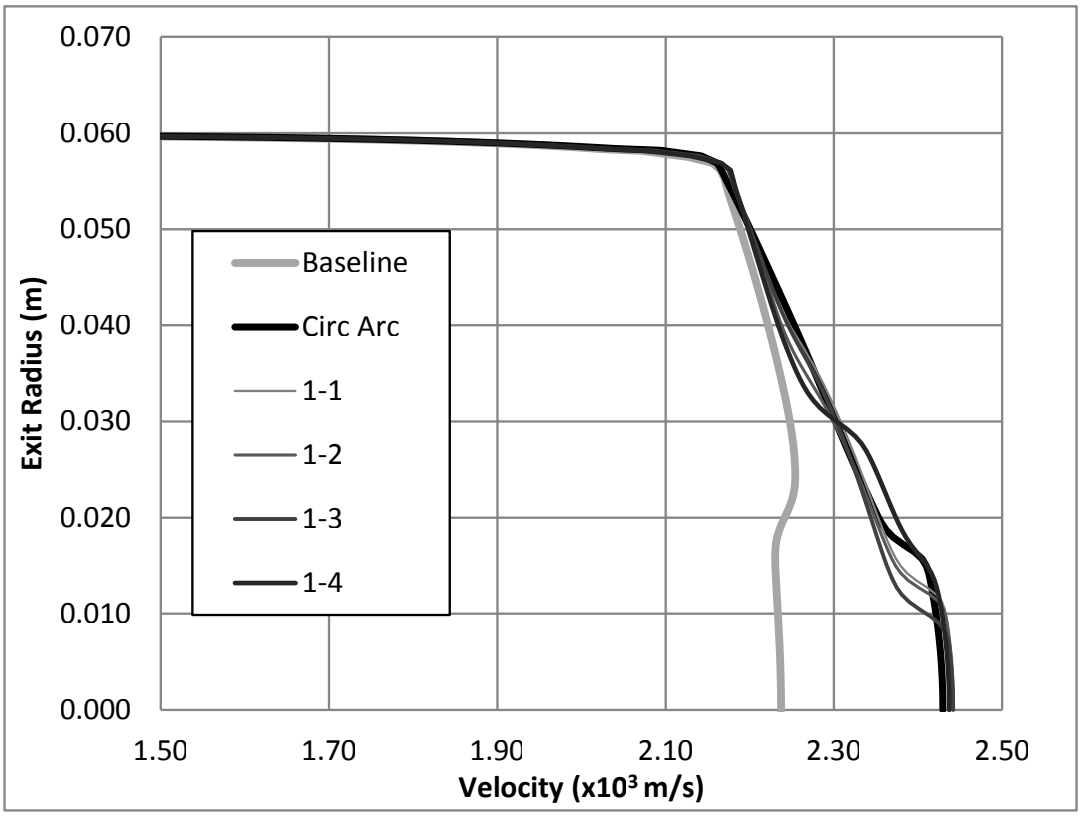

Figure 5.14: Case 1 - Exit velocities

5.6.2 CASE 2: Fixed area ratio [12.45:1] - Truncated (75 %) multiple spline control points

The case study 2 involves taking the same fixed area ratio (12.45:1), fixed throat radius R_t (17 mm) and fixed length x_t (122.3 mm) nozzle design as case 1 and similarly optimising the expansion contour only. Differently, case 2 uses 4 single DOF (R_1, R_2, R_3 and R_4) control points to increase the control over the contour. The x_1, x_2, x_3 and x_4 positions are kept fixed at 25, 55, 85 and 105 mm respectively. The fixed axial positions keep the variable domain to a manageable limit. The full CFD results as well as design tables for case study 2 can be seen in Appendix F.

Similarly to case 1, Figure 5.15 and Figure 5.16 show the Standard and Kriging response surfaces for 2 control point's effect (showing X_3 and X_4's effect on thrust) and the throat variables respectively for case 2. 99 refinement points were used to define the response surfaces. Similarly to case 1, there are only minor differences in response surfaces with the Kriging surface slightly more able to fit the refinement points. Table 5.4 shows the top candidates from each method combinations for case 1 and 2.

Figure 5.17 shows the geometries with the baseline as a reference. The baseline is the same geometrically as used in case 1 but with the parametrization changed to accommodate the case 2 variables. More variation can be seen in the case 2 geometry when compared with case 1. Details B and C show the larger variation in geometry with the latter clearly showing the variations in optimising the initial expansion contour. The geometries are more varied with the irregularities in the generated surfaces causing stronger shocks than case 1 within the nozzle emanating from the initial expansion surface as seen in Figure 5.18 for cases 2-2 and 2-4. The geometries show a wider variation around the case 1 results which would suggest further refinement is needed than within case 1 to achieve similar results. Figure 5.18 and figure 5.19 show sample Mach contour plots for case 2. It can be observed that the variation of results between methods has increased and that the optimisation result 2-1 is a close match to 1-1 with a comparable Mach contour plot. At lower levels of refinement, the variation was even greater. The exit velocities for case 2 are shown in Figure 5.20, again showing a general increase in exit velocity over the baseline. The stronger shocks in cases 2-2 and 2-4 has constrained the faster core flow and thereby reduced the area of higher speed exit flow when compared with case 1-1. The shock is seen in the same area as in case 1 (namely, 10-20 mm from the centerline) but produces a large drop than in case 1. Case 2-1 produced the highest exit velocities and thrust, comparing it to case 1 shows that the optimisation increased the extent to which the faster core flow reached. The initial expansion also produced the weakest shocks through the domain and is clear in both the Mach plots and velocity profiles which have straighter isolines and no

sudden velocity drops respectively.

The case 2 optimisation did produce the highest simulated thrust, albeit a marginal gain (+2.3 N). However, the results for case 2, in general, show an inability to consistently find the current optimum at these refinement levels and with fewer results near the currently simulated optimum.

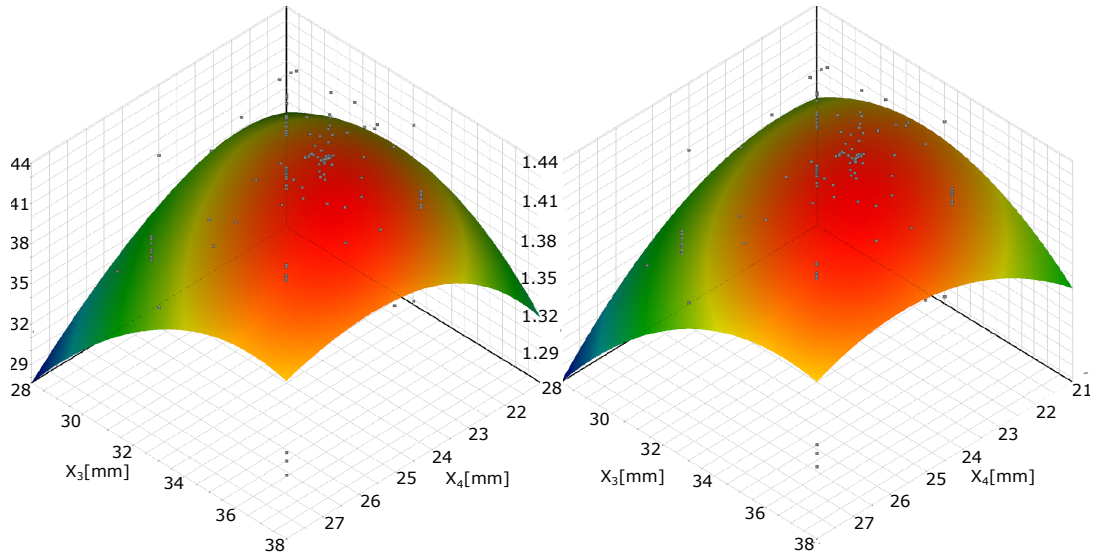

Figure 5.15: Case 2 - Response surfaces spline control variables - Standard (left) and Kriging (right)

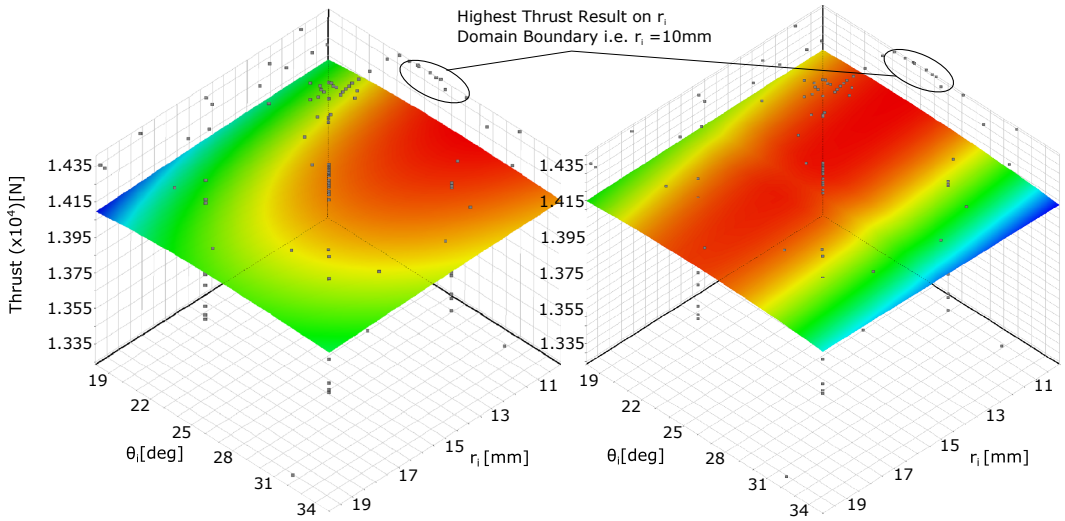

Figure 5.16: Case 2 - Response surfaces for throat control variables - Standard (left) and Kriging (right)

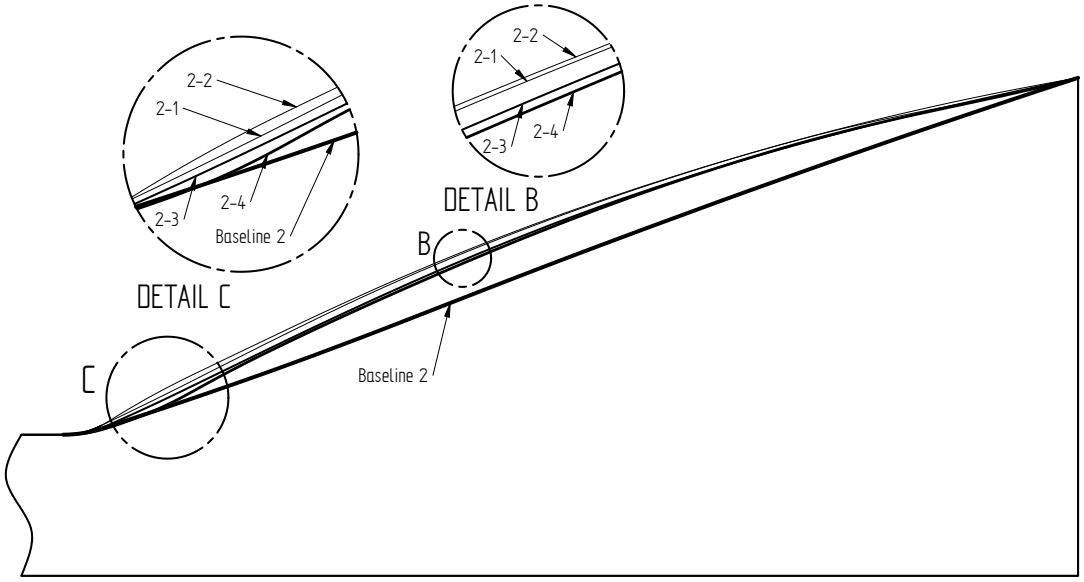

Figure 5.17: Case 2 - Geometry comparison ($2-1$, $2-2$, $2-3$, $2-4$ and baseline)

Figure 5.18: Mach number comparison of $2-2$ and $2-4$

Figure 5.19: Mach number comparison of $1-1$ and $2-1$

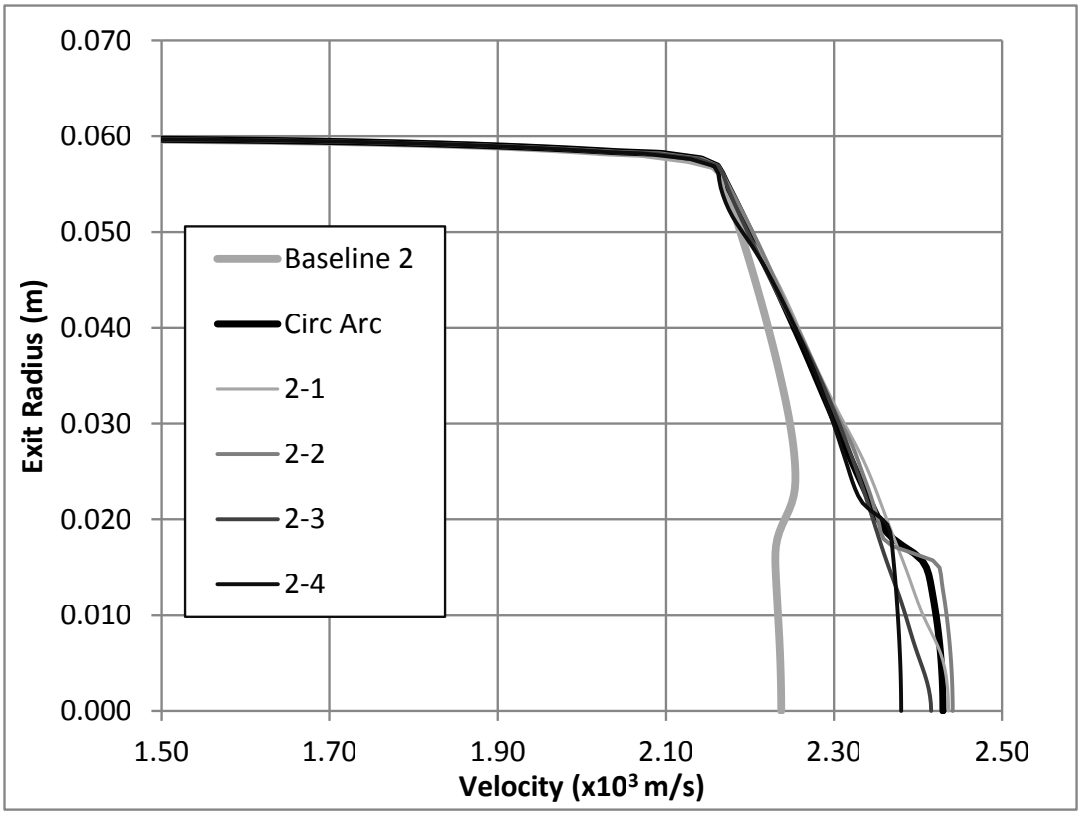

Figure 5.20: Case 2 - Exit velocities

5.6.3 CASE 3: Fixed area ratio [12.45:1] - Including length reduction

Case 3 uses the identical framework and variables as case 1 but further includes incremental length reductions to optimise extra-truncated nozzles. Case 1's maximum thrust result candidate (case 1-1) is truncated in 5 mm increments up until a total of -20 mm is achieved. The purpose of the case is to characterise reduced length nozzle thrust losses vs nozzle length. The domain was extended to include values of down to $5mm$ (compared to 10 mm) for r_i to address the issue of the optimums all sitting on the boundary in cases 1 and 2. The full CFD results for case study 3 can be seen in appendix I.

Looking at the design table in Appendix I.1 it can be seen that for the optimised cases the value r_i once again sits on the new boundary (namely a 5 mm radius). This begins to suggest the optimum geometry for this parametrization method might exclude an initial circular expansion (i.e. $r_i = 0$). The values for thrust and length are plotted in Figure 5.21 with the case 5-1 (see section 5.6.5) 161.02 mm length nozzle results included. There is a steady decrease in thrust with the reduction in nozzle length from case to case. This is evidence of there being an optimum length for accelerating the exhaust gases to a maximum with a constant area ratio. Too short a nozzle while reducing boundary losses does not expand the gas as efficiently and therefore a reduction in thrust is seen. While not conclusive the graph trendline suggests a reduction in thrust gains as the nozzle continues to be extended, a possible indication of where the increased boundary losses outweigh the more efficient expansion of a longer nozzle. Further data points are required to better refine the trendline for further extension of the nozzle.

Figures 5.22 and 5.23 show the combined exit velocity and comparative Mach plots respectively. The un-cropped exit velocity profiles, centerline pressure and centerline Mach number plots are included in appendix I. The velocity profiles confirm the reduced exit velocities indicated by the lower thrust results seen with near linear steps of reduced velocities at the exit. The near wall and core velocities both show similarly reduced velocities. The centerline plots show similar evidence with the pressure at exit increasing incrementally for the short nozzles, suggesting that although the exit area is the same the nozzle design has reached its maximum expansion rate. Through conventional quasi-one-dimensional theory, this observation would not be possible. Both centerline plots (pressure and Mach) follow the same expansion path up until the exit with only the end values truncated as per the case, this would suggest that the optimisation method finds a similar type of contour progression as an optimum for all cases. The Mach plot comparison shows the same trend with each successive plot being a shortened version of the previous, once again confirming an optimum length requirement. Included in the iso Mach comparison (Figure 5.23) are percentage reductions in both length and thrust when compared with the original case 1-1

results. It is evident that although shorting the nozzle reduces thrust there are greater percentage size reductions than there are thrust losses. A 16.35 % reduction in total nozzle length produces only a 1.29 % reduction in thrust suggesting that length vs thrust considerations should be included in optimal nozzle designs. The low effect on thrust as a percentage is due to the fact that a considerable part of the thrust is based on the choked flow and pressure at the throat with the further expansion in the nozzle contribution to a lesser degree.

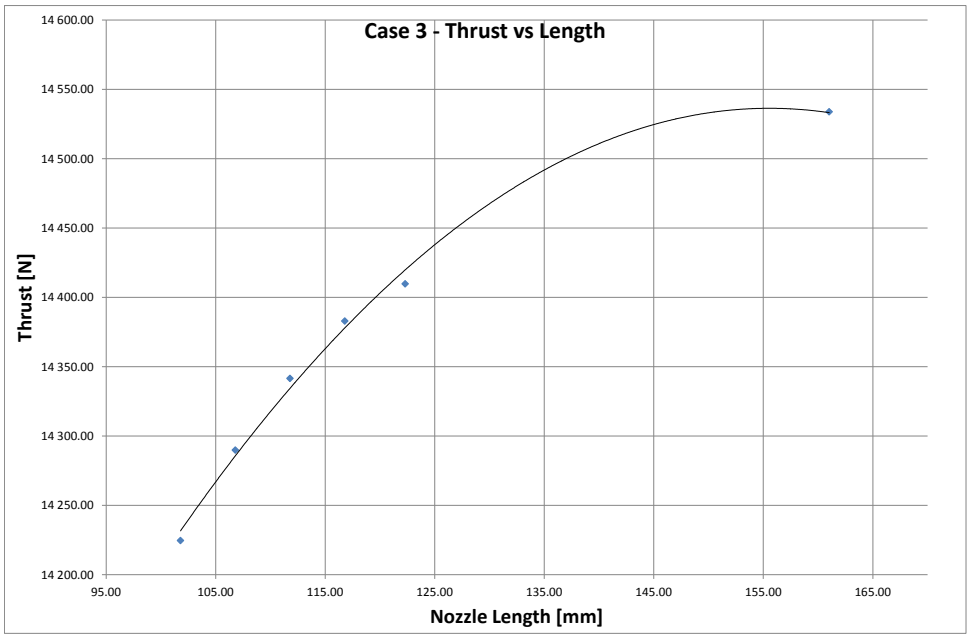

Figure 5.21: Thrust vs length for optimised truncated nozzles - Including Case 5-1

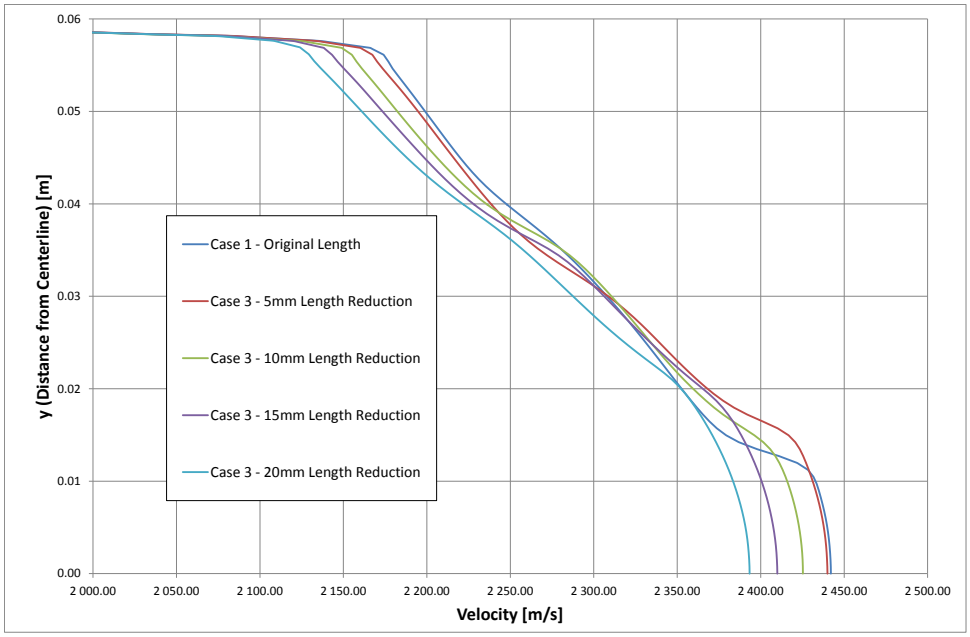

Figure 5.22: Case 3 - Exit velocities - Cropped

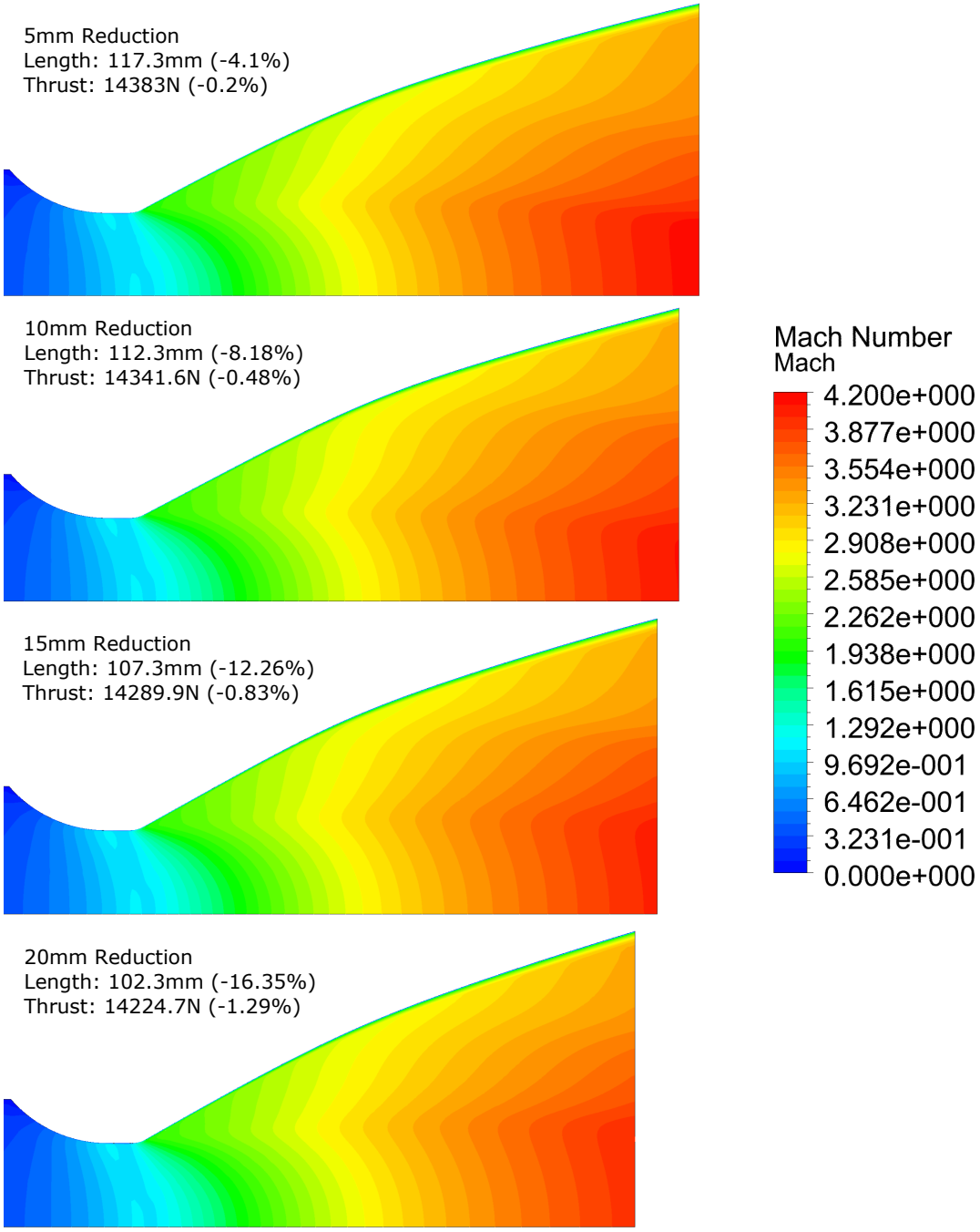

Figure 5.23: Case 3 - Iso Mach comparison

5.6.4 CASE 4: Fixed area ratio [12.45:1] - Truncated (75 %) Rao approximation comparison

A parabolic approximation of a Rao optimum thrust contoured nozzle is simulated as a comparative case representative of typical industry standard nozzles. No optimisation is implemented with this case and is used purely as a benchmark for the optimisation cases. Based on a 75 % truncated (calculated from a 15°conical nozzle of same expansion ratio) Parabolic Rao approximation (see Sutton and Biblarz (2001); Rao (1960)). An initial parabolic expansion angle of 28° and final expansion angle of 11.7° was used to define the contour and is based on the design table in figure 5.24. The full CFD results and design tables for case study 4 can be seen in Appendix J.

The parabolic approximation of a Rao nozzle is compared to the high thrust circular arc contour and maximum thrust optimised design (case 1-1) from case 1. Figures 5.25 and 5.26 are the exit velocity plot and Mach comparisons respectively for the above-mentioned nozzles. The parabolic approximation produces the highest thrust at 14411.8 N, the case 1-1 result is only 0.01 % lesser at 14410.2 N and the circular arc result lesser by 0.19 % at 14383.9 N. The exit velocities and Mach results are equally similar with each contour making up its velocity profile only marginally differently. The highest thrust results producing the highest peak core exit velocities but with reduced near-wall velocities. While the difference between the parabolic and case 1-1 results could be considered negligible the difference of either when compared with the circular arc is clearer. The parabolic Rao approximation is a simple designed-from-tables method (as with the circular arc) which for this case produces good results with no computational expense. The strength of the optimisation method (as used in case 1 and 2) would be apparent when exploring off design point conditions or in trade-off studies for which the design tables would not cater. The top optimised result from case 2-1 outperforms the parabolic result marginally with 14412.1 N of thrust.

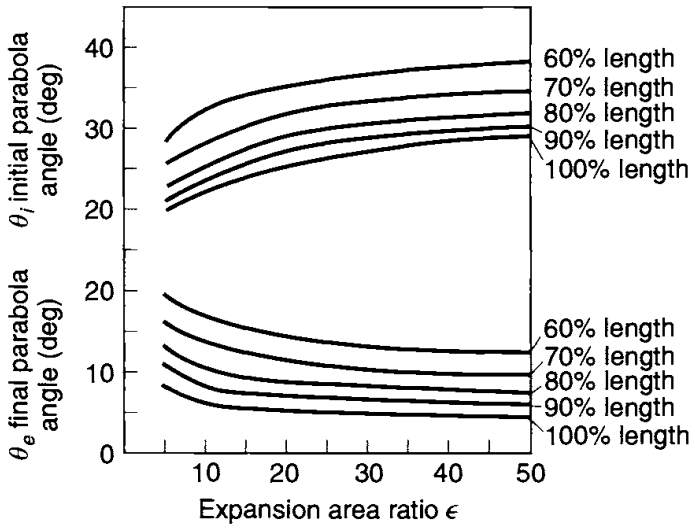

Figure 5.24: Parabolic design table guide for optimum thrust nozzle contours - used from Sutton and Biblarz (2001) and based on Rao (1960)

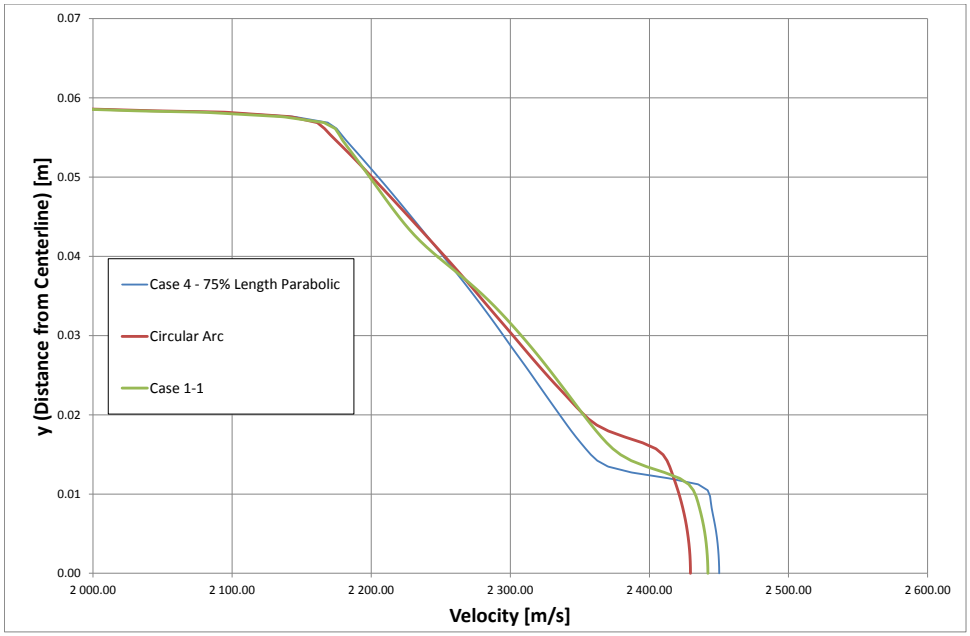

Figure 5.25: Case 4 - Exit velocities comparison - Cropped

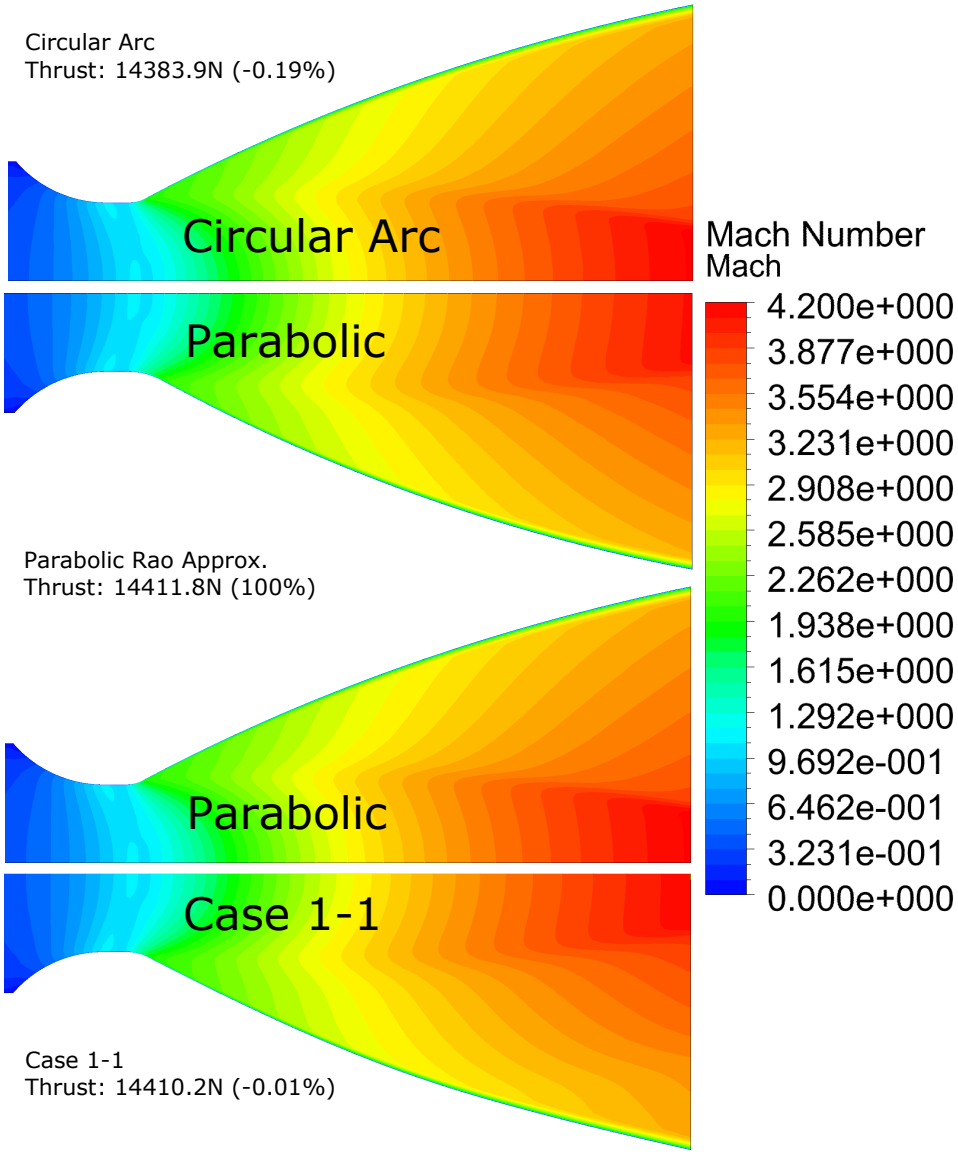

Figure 5.26: Case 4 - Iso Mach comparison

5.6.5 CASE 5: Fixed area ratio [12.45:1] - Full length (100 %) Rao approximation comparison

The case study 5 involves taking the case 1 fixed area ratio (12.45:1) and fixed throat radius R_t (17 mm) nozzle design and extending the length x_t from 122.3 to 161.02 mm. The length extension is based on a full-length 15° nozzle with the same area ratio. The single 2 DOF control point optimisation is then used to optimise the nozzle contour. A 15° conical nozzle is simulated as the benchmark of a typical unoptimised nozzle geometry. A parabolic contour of the same length is simulated as a comparison representative of thrust optimised designs. An initial parabolic expansion angle of 23° and final expansion angle of 6° was used to define the contour and is based on the design table in figure 5.24. The full CFD results and design tables for case study 5 can be seen in Appendix K.

Figure 5.27 is a sample response surface from case 5. Comparing with previous cases there is increased variation in the surface. Each response surface is based on a response point within the domain, the three-dimensional response surface is unable to capture all the variables on one surface and therefore generates surfaces based on fixed individual points looking at a combination of only 3 variables per surface and therefore individual responses are not directly comparable unless the same response point is used. Looking at the included response surface below as well as those in Appendix K there is increased undulation in the surfaces which is indicative of a more complex response (in this case) of the thrust to geometric variable changes. The variable domain (specifically the distance from the exit of the control point x_2 which has increased from 40-80 mm to 30-90 mm for case 1 and 5 respectively) has increased to account for the increased length and is a contributing factor to the change in response surfaces.

The thrust results for case 5 are shown in Table 5.5. The simple construction 15° conical nozzle produces 203 N (1.4%) less than the parabolic nozzle. With simple design tables, geometric construction methods and modern machine tools a parabolic nozzle is a clear alternative to a conventional conical nozzle with the 25% shorter case 1-1 optimised and case 4 parabolic nozzles producing approx 98 N (0.69%) greater thrust. In this case, the optimised nozzle produced the highest thrust with 221.9 N (1.55%) greater than the 15° conical nozzle and 123.7 N (0.86%) greater than the case 1-1 nozzle. Similarly to case 4, the parabolic Rao approximation nozzles produce good results comparable with the optimised cases.

The Mach plot comparison, temperature plot comparison, exit velocity results, centerline Mach plots and centerline pressure plots for case 5 are shown in Figures 5.28, 5.29, 5.30, 5.31 and 5.32 respectively. The Mach plots for the parabolic and case 5-1 nozzles show clear

evidence of compression/expansion shock concentrations on the centerline with the associated and expected drop in Mach number when passing through the shock. As with the optimised case 1-1 the waves start from the initial expansion surface but due to the longer nozzle geometry the waves reflect and meet on the centerline within the nozzle. The higher thrust case 5-1 has the concentration situated approximately 27 mm from the nozzle exit, while the parabolic concentration is further at approximately 56 mm. There is evidence from the plots of a similar occurrence in the 15° nozzle closer to the throat but to a lesser degree. The temperature plots show a rise across these shock areas which is due to the compression that occurs when passing through a shock wave. The centerline pressure plots confirm this pressure rise and the presence of a shock within the nozzle. The locations of the shocks are readily seen on the centerline Mach plots with a rapid drop in Mach number found across them. The centerline Mach number plots suggest that higher thrust values are obtained with the shock closer to the nozzle exit. The shock seen in all related plots at approx 380 mm from the inlet is the choked throat condition normal shock and is part of all supersonic nozzles where the subsonic inlet changes over to sonic conditions (i.e. at Mach 1). The case 5 exit velocity profiles show that the truncated case 1-1 nozzle produced higher core velocities yet still produced less thrust and is due to the fact that the core velocity makes up the lesser area weighted flow with the annular area nearer to the wall contributing more based on its area. The area averaged velocities for case 5-1 being $2236.82 m/s$ whereas the case 1-1 is $2231.59 m/s$. The effect of the shock is evident in the exit velocities with considerable drops for both case 5-1 and the parabolic approximation near to the centerline. The 15° nozzle produced a consistent yet low-speed exit profile. If the shocks in the optimised nozzles could be moved to lie on the exit plane without reducing the near-wall velocities a higher thrust nozzle could be achieved. The theoretical ideal would be a constant exit velocity across the boundary of maximum value based on the expansion ratio. This is however limited by the conditions for wall bounded flow with viscous shear near the wall unavoidable.

Table 5.5: Case 5 - Thrust results comparison

Case	Length (%)	Actual (N)	Var (N)
15° Conical	100	14312.0	0
Parabolic Rao Approx.	100	14515.0	+203.0
$5-1$ Optimised	100	14533.9	+221.9
$1-1$ Optimised	75	14410.2	+98.2

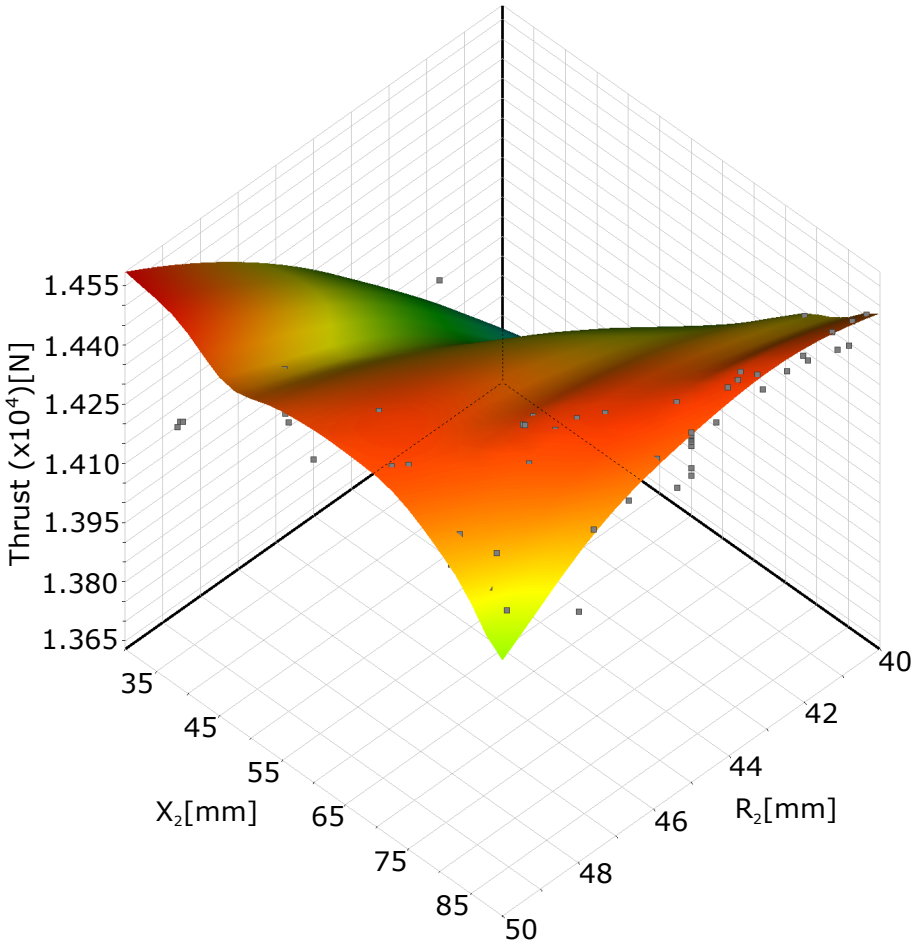

Figure 5.27: Case 5 - x_2 vs R_2 Kriging response surface

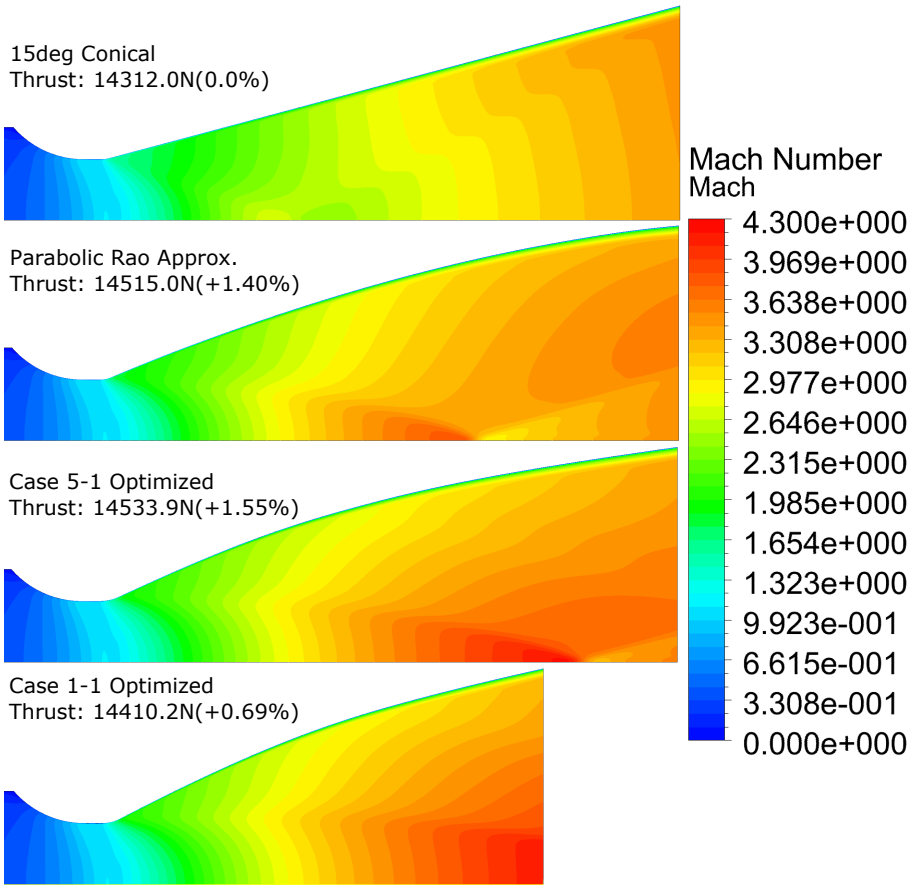

Figure 5.28: Case 5 - Iso Mach comparison

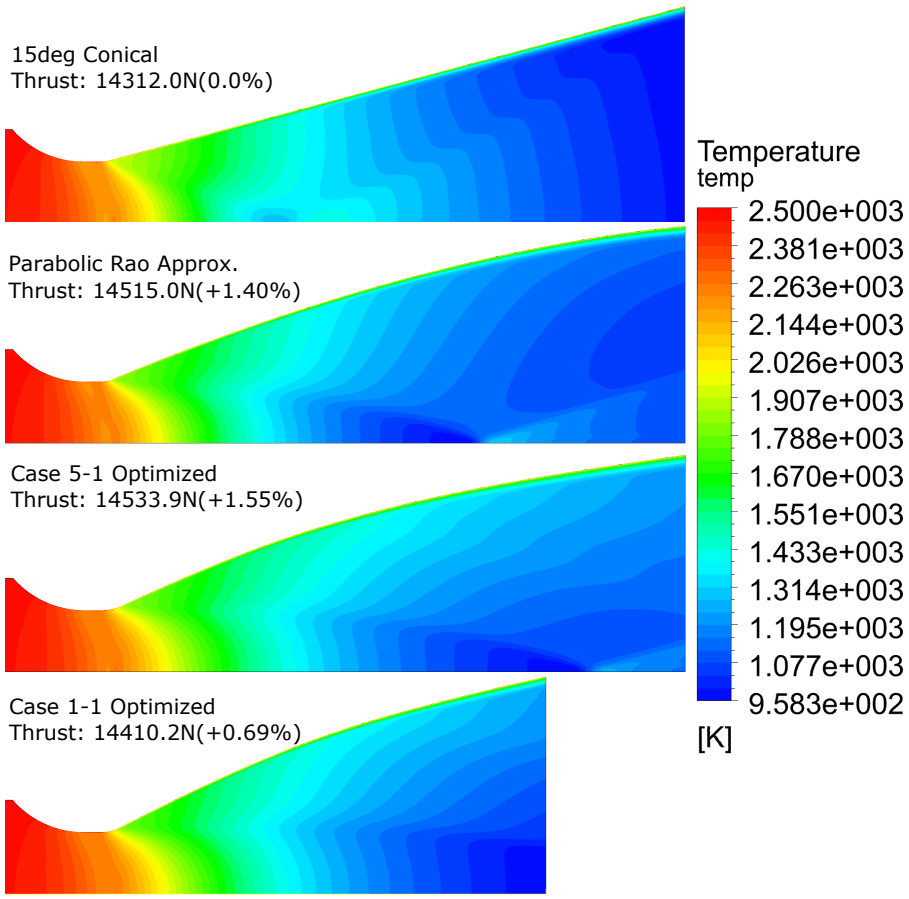

Figure 5.29: Case 5 - Iso Temp comparison

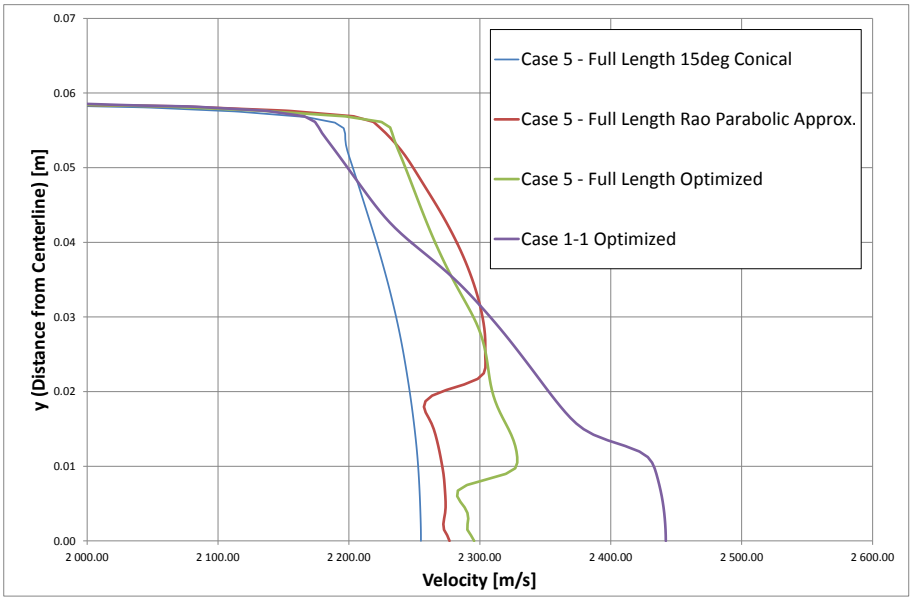

Figure 5.30: Case 5 - Exit velocities comparison - Cropped

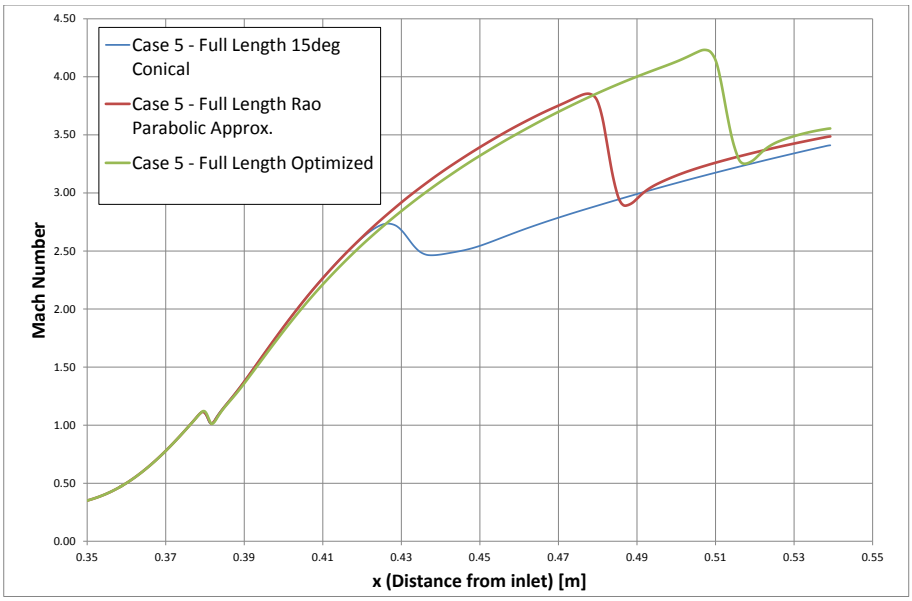

Figure 5.31: Case 5 - Centerline Mach numbers - Cropped to 0.35 m+ Data Only

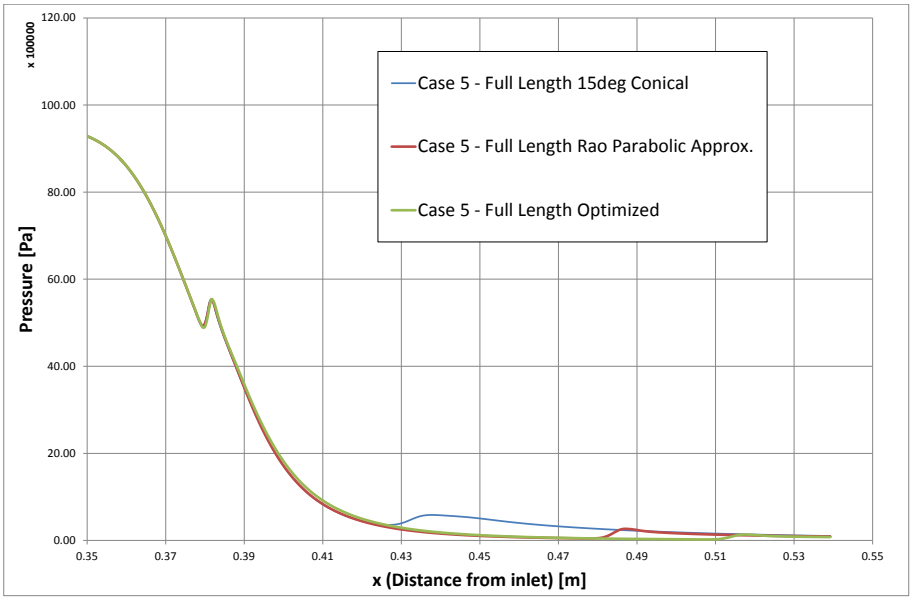

Figure 5.32: Case 5 - Centerline pressures - Cropped to 0.35 m+ Data Only

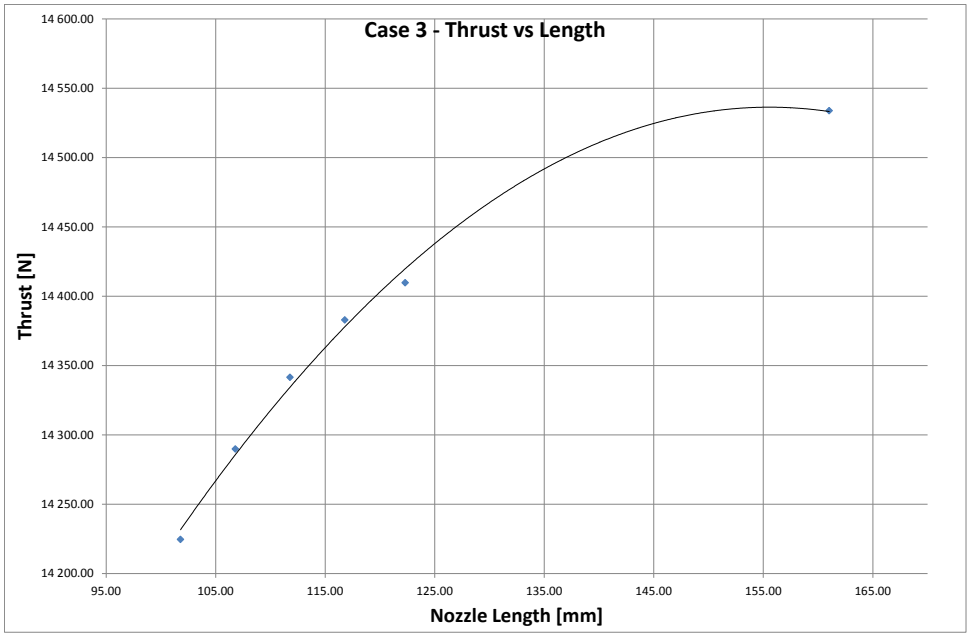

Figure 5.33: Thrust vs length for optimised truncated nozzles - Including Case 5-1

5.6.6 CASE 6: Fixed area ratio [12.45:1] - Truncated (75 %) Rao geometry baseline optimisation

Case study 6 involves taking the case 1 fixed area ratio (12.45:1) and fixed throat radius R_t (17 mm) nozzle design and imposing the case 4 Rao geometry constraints as the baseline geometry before optimisation. The single 2 DOF control point optimisation from case 1 is then used to optimise the nozzle contour. As with case 4, an initial expansion angle of 28° and final expansion angle of 11.7° was used to define the baseline contour and is based on the design table in figure 5.24. The full CFD results and design tables for case study 6 can be seen in Appendix L.

As seen in case 4 the Rao parabolic nozzle contour marginally outperforms the case 1 result. Looking at the results and velocity plots for case 6 in table 5.6 and figure 5.34 respectively it is seen that using the Rao parabolic geometry as a new baseline for optimisation produces the highest truncated (75 %) nozzle thrust result in this study. Higher near-wall velocities are achieved with the optimised geometry as seen in the exit velocity plot, only between approximately 18-32 mm from the wall (at exit) do the velocities drop below the other nozzles compared. On closer examination of the 3 geometries shown in figure 5.36 it is seen in detail A that the initial expansion rate is greatest for the optimised nozzle (without any notable increase in the mild shock starting on this surface as well as no separation - see figure 5.35) indicating the possibility that the other nozzle designs have not expanded the gas to its full potential over the initial profile. With the improved initial expansion, the nozzle is able to turn the flow more gradually over the length allowing for a slightly improved exit angle of 11.087° (with the implication of reduced divergence losses). Detail B and C both showing the effect of the reduced exit angle, namely that the optimised nozzle geometry is further expanded and has the flow "turned" back more towards the horizontal. The control point position for both case 1 and 6's geometry result has been indicated on the geometry (figure 5.36). In order to adapt the parametric spline to a Rao parabolic curve, the control point moved considerably closer to the nozzle (from 40 to 89.38 mm away from the exit), this suggests that there is possibly more potential for optimisation in the initial expansion area than the area used in case 1 (middle nozzle section). This adds some uncertainty to the reasons behind the improved thrust when using the parabolic baseline, it can be concluded that the baseline used has an effect on the optimisation result but not simply because the start point is a near optimal design but that the chosen baseline shifts the nozzle area around which the optimisation is centred.

The results and data at this point above were considered for further optimisation using alternative algorithms.It was noted that the optimisation method choice did not affect the results significantly. Using Case 6 as the example and taking the final response surfaces

obtained for further optimisation with the Screening, NLPQL, MISQP and MOGA algorithms to generate 10 candidates per method. Each candidate generated was then solved, the 40 new solved candidates were then used to further refine the response surface in an effort to find new areas of local optimums. The new response surface was then used for the second round of optimisation using the 4 algorithms, generating a total of 80 new optimum candidates. The results of which are shown in Table 5.7 and Figure 5.37. It can be seen that with the additional 80 optimised design points (201 total design points) using 4 optimisation algorithms there are two candidates from the second iteration using the Screening and MOGA method with increased thrusts of 14415.6 and 14415.2 N (increases of 0.7 and 0.3 N) respectively when compared with the thrust generated by the case 6 initial Screening/NLPQL approach with 121 total design points. The results show no clear preferred optimisation method for the case 6 nozzle, with the top results from each method likely within the meshing and numerical error for the simulations. The results for top candidates from each method are within 3.6N of each other from highest to lowest. With the Screening and MISPQ producing the highest and lowest result respectively. It is noted that with increased resolution of the response surfaces (and the solved design points) the effectiveness of the optimisation is reduced simply due to more of the domain and its near optimums having already being found.

Table 5.6: Case 6 - Thrust results comparison

Case	Length (%)	Actual (N)	Var (N)
Case 4 Parabolic Rao Approx.	75	14411.8	0
$6-1$ Rao Geometry Baseline Optimised	75	14414.9	$+3.1N$
$1-1$ Optimised	75	14410.2	$-1.6N$

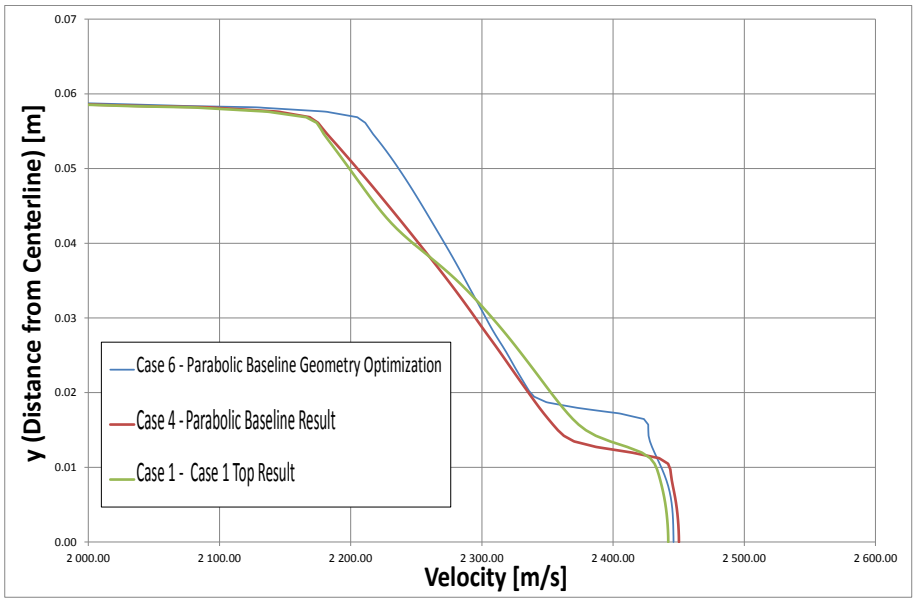

Figure 5.34: Case 6 - Exit velocities comparison

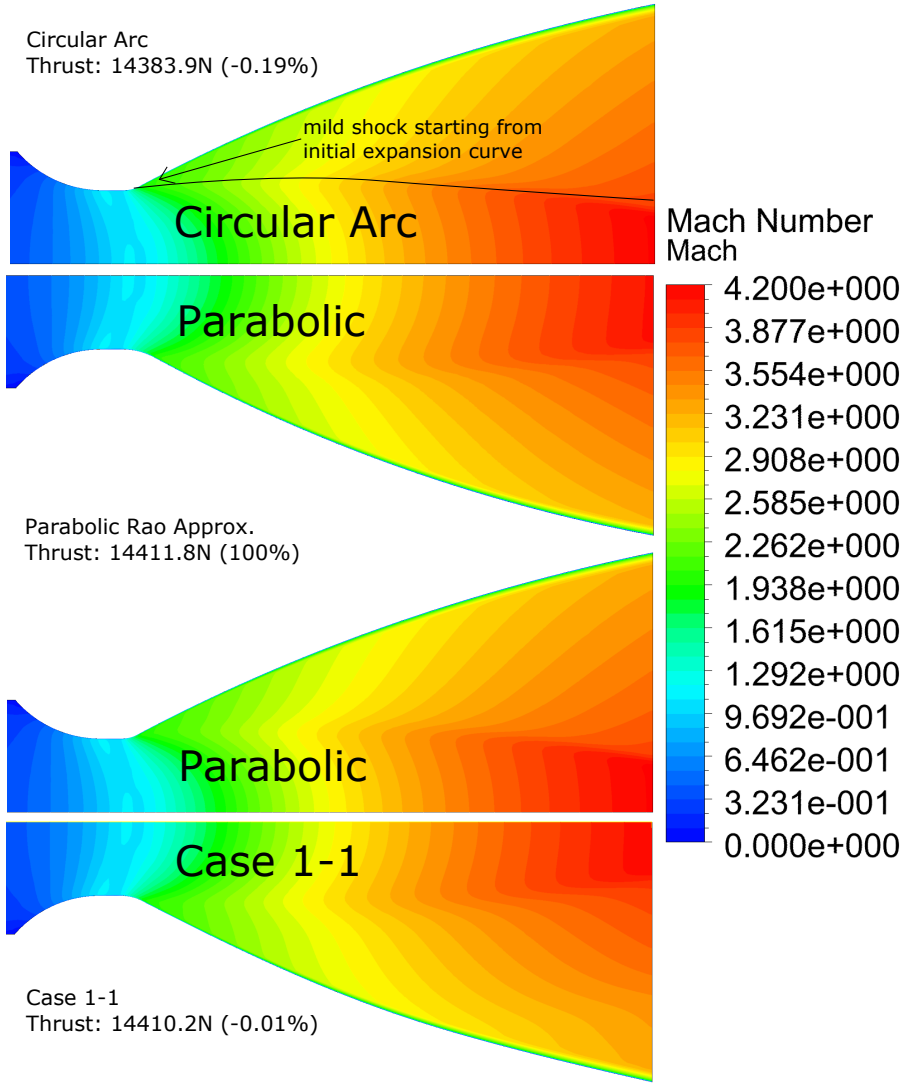

Figure 5.35: Case 6 - Iso Mach comparison

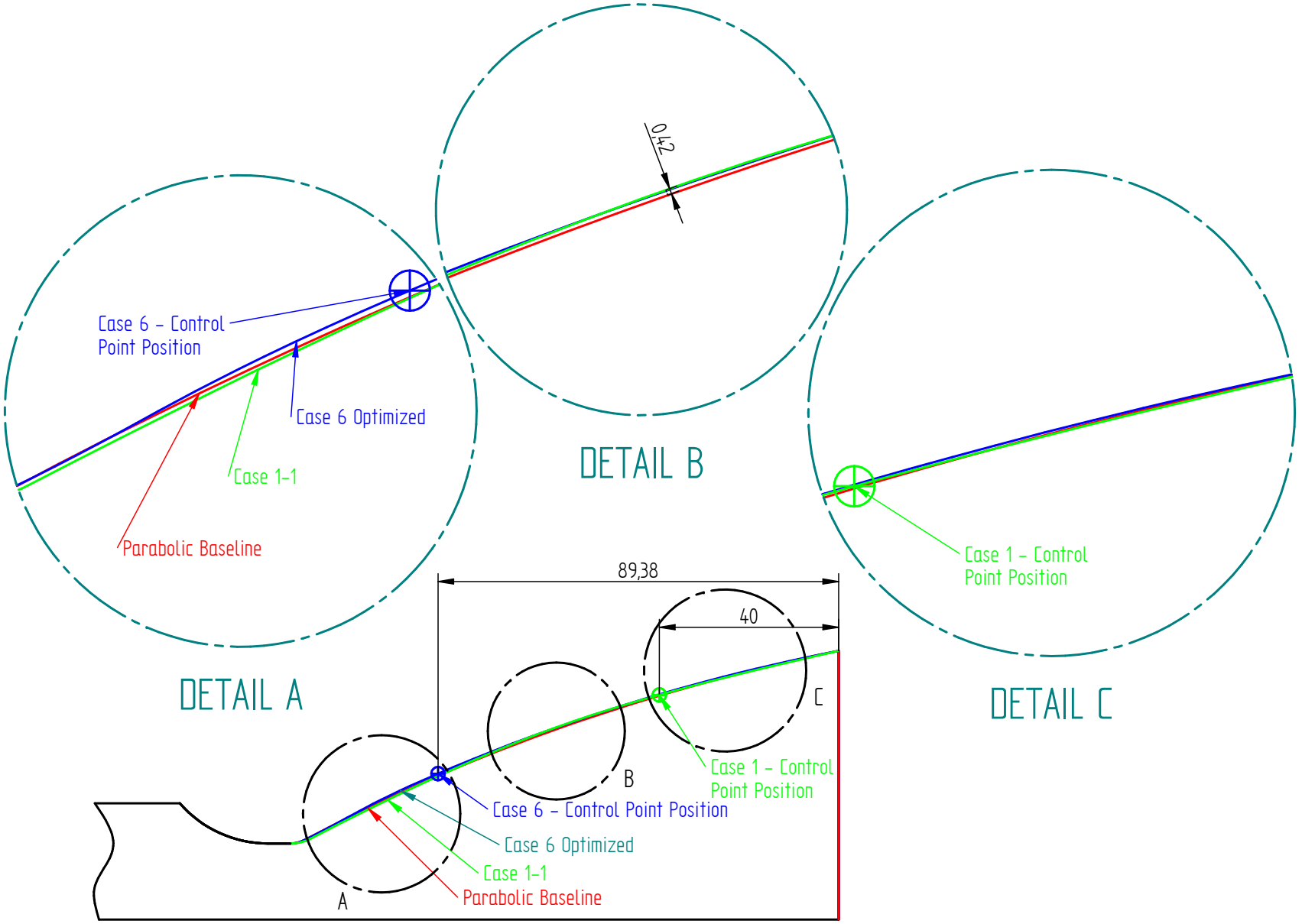

Figure 5.36: Case 6 - Geometry comparison

Table 5.7: Optimisation method comparison - CASE 6

Optimisation	Candidate									
Algorithm	1	2	3	4	5	6	7	8	9	10
Screening 1st	14413.8	14413.5	14413.5	14412.9	14412.6	14412.1	14411.4	14410.0	14409.9	14402.7
Screening 2nd	14415.6	14414.2	14414.2	14413.3	14412.5	14412.4	14412.0	14411.8	14411.0	14409.9
NLPQL 1st	14414.8	14412.9	14412.2	14411.5	14410.7	14410.6	14409.6	14409.5	14409.5	14409.4
NLPQL 2nd	14414.1	14413.5	14412.3	14412.0	14411.9	14411.9	14411.6	14411.2	14409.7	14409.3
MOGA 1st	14414.1	14412.9	14412.8	14412.8	14411.5	14411.4	14411.2	14411.1	14410.9	14410.5
MOGA 2nd	14415.2	14414.3	14414.2	14413.1	14413.0	14412.5	14411.4	14410.4	14410.4	14407.5
MISQP 1st	14414.1	14413.5	14412.0	14411.3	14411.0	14411.0	14410.7	14409.4	14407.8	14407.8
MISQP 2nd	14412.0	14411.7	14411.6	14411.5	14411.2	14411.0	14410.8	14410.8	14410.5	14409.5

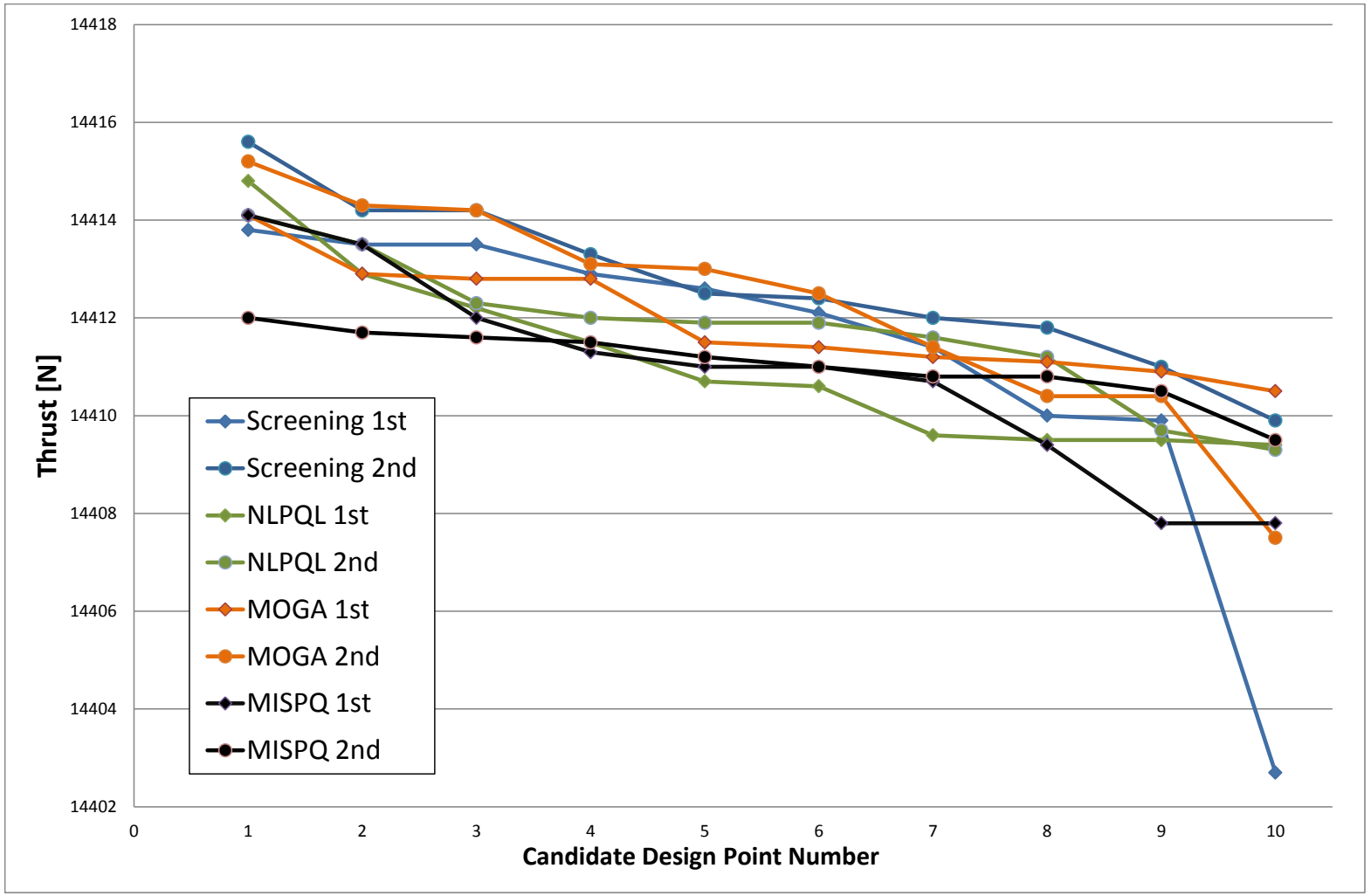

Figure 5.37: Optimisation method comparison - CASE 6

5.7 Summary

A grid independence study showed low sensitivity for the cell sizes considered, namely 3.0 mm to 0.15 mm with results over predicting approx 1.6 to 1.0 % respectively. Results also showed better wall velocity profiles were achieved with wall inflation based meshing when compared with a structured quad mesh with no wall inflation.

A domain sensitivity study showed that at sufficient cell refinement (0.5-0.75 mm cell size) the placement of the upper and lower boundary did not effect thrust results notably.

Experimental and theoretical results were obtained that correspond well with those obtained through CFD. Results showed that the computational method (which included the Menter SST turbulence model) was effective at simulating the tactical SRM nozzle flows focused on in this work with simulations generally over-predicting the experimental results by 1-2 %.

Case 1 and 2 provided a comparison between 2 methods, namely a single 2 DOF control point and 4 single DOF control points respectively. It was shown at low refinement levels for these cases the case 1 method produced more repeatable results with greater amounts of high thrust profiles generated. Case 2 produced a single marginally highest thrust result.

Case 3 showed the ability of the optimisation framework to reduce nozzle length with relatively low thrust losses when compared with length reduction. A 16.35 % reduction in nozzle length produced a 1.28 % reduction in thrust.

Case 4 demonstrated that a parabolic Rao approximation contour is an effective high thrust nozzle geometry for the case 1 constraints and produced marginally higher thrust than the optimised case.

Case 5 compared a full-length Rao approximation to both full length 15° conical and optimised nozzles. The optimised nozzle produced minor thrust improvements when compared with the parabolic nozzle. Both parabolic and optimised nozzles considerably outperformed the 15° conical nozzle.

Case 6 used the case 4 parabolic Rao approximation as a baseline for optimisation and produced the highest truncated (75 %) nozzle thrust result. It also highlighted the importance of which initial geometry is used as well as where the control point is placed to achieve this desired geometry. On further optimisation using all methods available in ANSYS the thrust was increased by only 0.7 N.

6 Experimental Results

A full-scale experimental test firing was conducted as development work at Rheinmetall Denel Munition with a circular arc nozzle (as simulated in case 1 - see section 5.6.1) fitted to the motor. The author at the time was a propulsion technician and part of a multi-skilled team who did the work. The test setup can be seen in Figure 6.1 as well as images of the live test in Figure 6.2 . The motor is ignited remotely from a control room with interlocked blast doors as well as safe working procedures in place. The fire department is present and keeps a safe perimeter.

The experimental setup allows the data capturing of chamber pressure and axial thrust. A 100 kN HBM force transducer and 50 MPa HBM pressure transducer are used to measure thrust and pressure respectively. The signal is fed through a charge amp and the data captured at a 10 kHz sampling rate with a WaveBook data acquisition system. The motor is constrained at the rear by an axially-live steady, allowing the motor to float freely in the axial direction while still safely restraining the motor from side movements. The front of the motor is fitted with a load spreader and threaded adapter allowing it to be safely torqued to the force transducer. The force transducer attachment point and rear live-steady are laser-aligned to give a correct thrust vector. The pressure transducer is fitted at the front of the motor with an adapter through the igniter. Both traducers are part of an external calibration program and are zeroed before firing.

For this experimental firing a nozzle flow simulation using the CFD solution method in section 5.1 was run and compared. The experimental setup was as above. Figure 6.3 shows the experimental performance of the motor. The pressure readings are for total pressure and are measured at the fore end of the motor where velocity is assumed to be zero and therefore considered as stagnation or total pressure. The computational domain in this study (Figure 5.4 - middle) has inlet conditions $50mm$ upstream of the blast tube and required an internal ballistic simulation to get appropriate conditions at the imposed boundary due to losses across the grain, these values being time dependent due to the regressing nature of the propellant grain. The total pressure drop and Mach number at the aft end of the grain/chamber were calculated using proprietary in-house internal

ballistic codes (validated) and data results were supplied in peer communications with Dr. C W Rousseau (Rheinmetall Denel Munition). The adjusted transient inlet conditions (see Appendix D Figure D.2) were applied to the validation case. Start-up and burnout of the validation case were not simulated and only the operating time range of +1 % to 90 % was simulated. High gradients (seen in Figure 6.3) during initial pressurisation of the motor and blow down once the propellant has been consumed in conjunction with flow separation at low pressures prevented the simulation outside of this window. The increased computational time due to the small time step needed to capture the results sufficiently made any attempt prohibitive nor would these phases add any additional information of use. The validation results in Figure 6.4 show how the CFD results accurately predict the thrust across a wide pressure operating range up to 2 seconds in this study. It is known that during the operation of the SRM that the nozzle geometry will change due to the mechanical and chemical erosion of the internal wall at high temperatures. Analysis of these experimental results and post firing measurement of the nozzle throat shows that erosion increased the throat diameter with time, contributing to a 9 % increase in throat area over the full burn time. This accounts for the growing thrust discrepancies with time in comparison to the ones obtained using the CFD model. The one-dimensional theoretical results (see Section 5.5 and included in Figure 6.4) for ideal nozzle confirm this and predict that the nozzle would have to be operating above ideal conditions to produce these thrust values. This could, however, be compensated for by adapting the mesh with time for a fixed erosion rate but falls outside of the scope of this work. For the initial 1 second burn time post the ignition peak the CFD results typically over predict the experimental results by $1-2$ %, there is a cross over at 1.3 seconds where throat erosion has incorrectly brought the experimental and CFD results to within 100 % agreement with each other. Post 1.3 seconds the predicted results begin to under predict with a nearly linear decline continuing down to approx. -8% at peak thrust. It can be concluded for this case that the CFD results will generally overpredict the experimental results with the assumption of zero erosion within the throat. However, throat erosion would need to be accounted for when searching for real-world globally optimised designs.

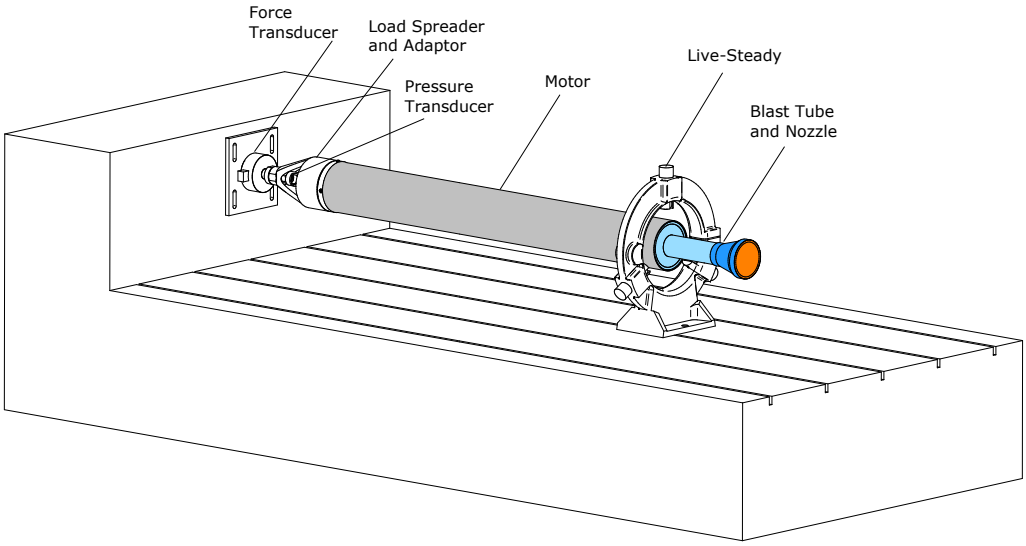

Figure 6.1: Experimental test bench setup

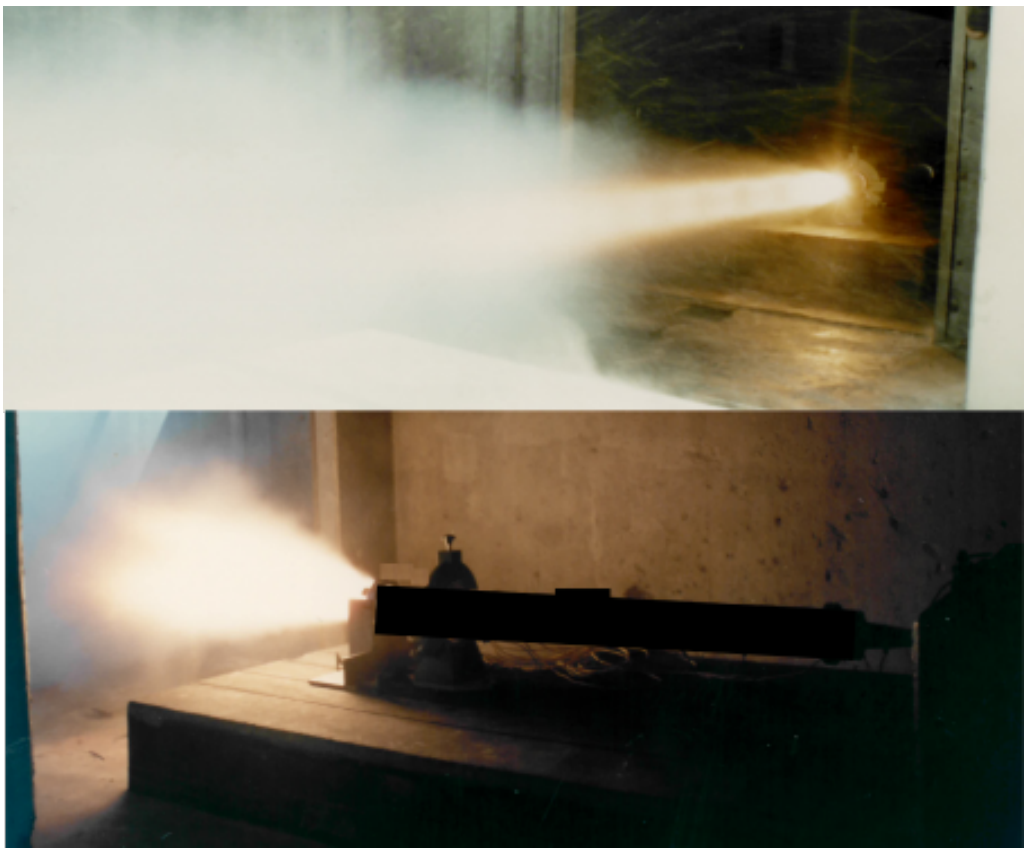

Figure 6.2: Experimental test firing

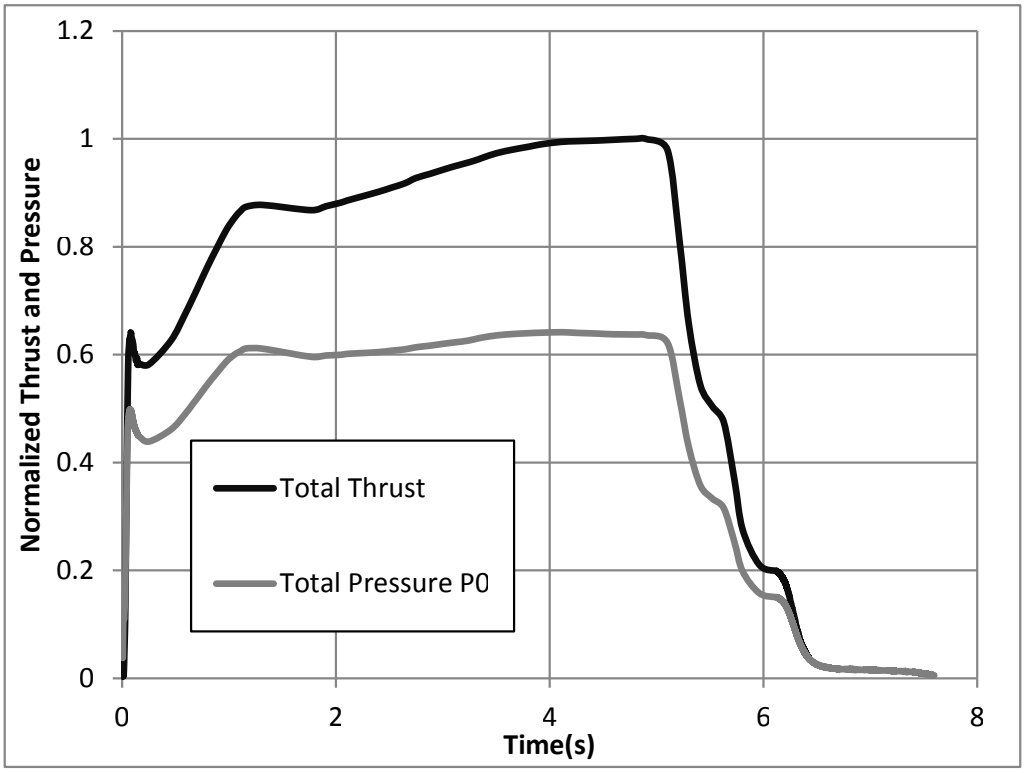

Figure 6.3: Experimental test result for static firing (Thrust normalized) - Smooth X-Y scatter of data sampled at 10 kHz

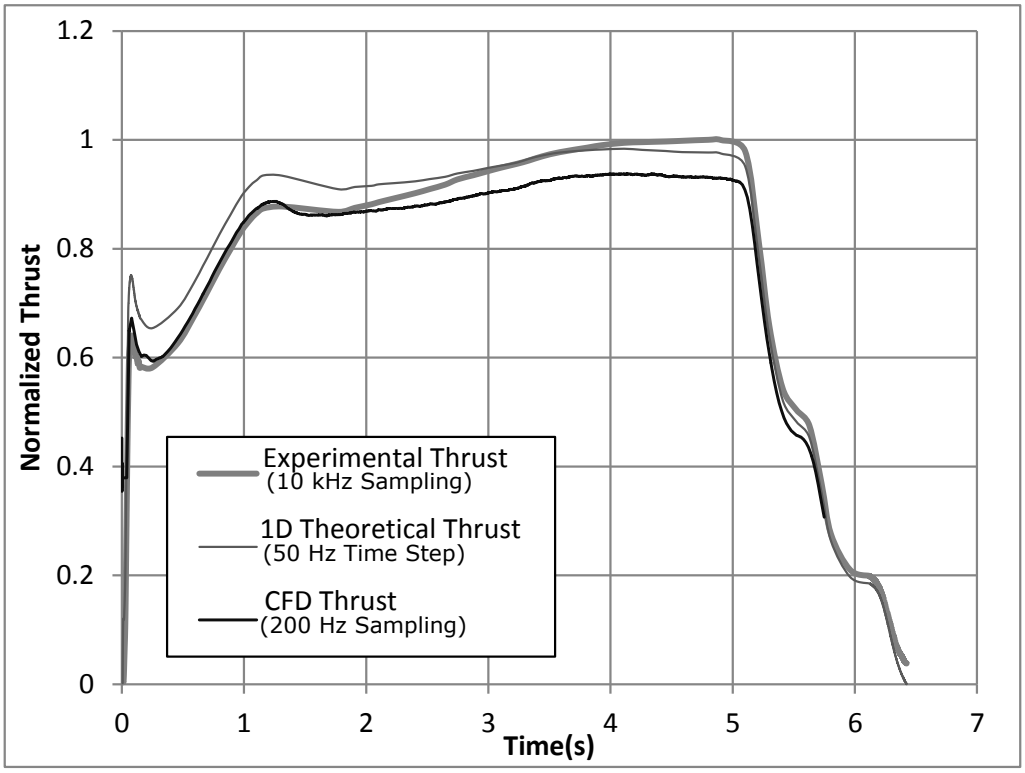

Figure 6.4: Validation of CFD to experimental results (Thrust normalized) - Smooth X-Y scatter of data sampled

7 Conclusion

7.1 Conclusions

A parametric method for optimising SRM nozzle contours using CFD was developed within the Ansys Workbench software environment. While various optimisation objective functions can be implemented through this method the work focused only on optimising thrust. This was achieved through parametric control of the nozzles geometric surfaces. A variable control point spline based exit contour was used successfully.

Full 2^{nd} order polynomial and Kriging response surfaces were successfully used to characterise the response domain and provided a visual interpretation of the effects of variable geometry combinations on thrust. There was no evidence either response surface type provided a better result than the other, however, it was shown that with increased refinement of the response surfaces better thrust results were obtained. The implication being that while the response surfaces drastically reduce the required amount of input data, the interpolation between points with the minimum refinement does not sufficiently predict the optimal results to guarantee convergence between predicted optimum and simulated geometry. The refinement was increased until predicted results converged on simulated (within 1N), with the level of refinement required case dependent. Screening and NLPQL optimisation methods were shown to both provide good thrust results provided the response surfaces were sufficiently refined. At the lower refinement levels, both optimisations successfully provided input points for further refinement, narrowing the search domain. There was no evidence to suggest either optimisation method provided improved results over the other.

A mesh study showed that for meshes with an overall length of 500 mm, reduced element sizes increased the accuracy of the CFD results but with gains becoming marginal with element sizes 0.5 mm and smaller. Overall the results showed a relatively low sensitivity to element size with the results for element sizes between 0.25 mm and 3.0 mm ranging from approximately 1.0 % to 1.5 % (over-predicted in comparison to the experimental

results at a 100:1 expansion ratio from chapter 6) respectively. Results also showed better near wall property resolution when using a wall inflated mesh in comparison to a standard structured quad mesh while still achieving similar thrust results. The results were shown to be relatively insensitive to the domain size with the upstream chamber inlet boundary placement and exhaust plume extended domain achieving similar results when applied in conjunction with the smaller element sizes or grid refinement levels. The chamber inlet boundary position was used based on the available inlet condition results obtained through internal ballistic simulations. Corrected inlet values for total and gauge pressure based on internal ballistic simulations were used to accounted for losses in the grain and improved the simulated results consistently, notably bring results closer to experimental in the initial burn time where the grain still plays a large role in the chamber geometry. All the optimisation results were for full flowing nozzles and therefore any effect of recirculation into the nozzle was not accounted for when considering boundary placement. The solutions of the RANS equations and Menter SST turbulence model proved in this case to be a successful method of simulating super-sonic compressible rocket nozzle flow with the results being in close agreement with an experimental test firing and traditional theoretical calculations with a 0.95 nozzle coefficient. The simulation results tended to over-predict the experimental data by $1 - 2\%$.

The work produced increased thrust results over baseline geometry for all cases. The simulations predicted a near 1 % thrust gain for the geometry arrived at with the parametric optimisation method developed in this work when compared with the baseline geometry for the optimised case 1 nozzle. It also predicted a 0.18 % over the high thrust circular arc contour used in the experimental firing (with all nozzles having equal length and expansion ratios). The work was successful in producing optimised contours for reduced length nozzles with results showing 0.20, 0.48, 0.83 and 1.29 % reductions in thrust for 4.10, 8.18, 12.26 and 16.35 % reductions in length respectively. The work produced similar or better results when compared with conventional thrust optimised parabolic Rao nozzles. The case 1 and 2 optimised contour produced 14409.8 and 14412.1 N respectively in comparison to the case 4 Rao approximation producing 14411.8 N. The case 5 full-length optimised nozzle result produced 14533.9 N compared with a full-length Rao approximation producing 14515.0 N and a 15° conical nozzle producing 14312.0 N. The overall results suggest that the throat turn radius (r_i) is linked to nozzle length (x_t) with all the truncated nozzles producing contours on the smaller boundary of the domain suggesting the optimum lay outside of the current setup. Case 1 results show the high thrust contours results having r_i values of approx 10 mm (the lower limit of the variable for case 1). Case 3 with an increased domain (5 mm as the lower limit) also producing values on the new boundary of 5 mm. The case 5 full-length nozzle results showed a shift towards 12.5 mm and away from the limits, coinciding with the extended length of the nozzle. The

response surfaces indicate for case 5 an increased sensitivity of the results to the initial expansion angle (θ_i). Further work is required to better understand these relationships.

The CFD methodology was validated based on live test firing data. This work produced an alternative method for optimising SRM nozzle geometry. A single nozzle optimisation cycle took on average 48 hrs to run on a i7-5820K desktop computer when running on 5 parallel cores.

7.2 Suggestions for Further Research

Further work is needed with a focused CFD approach on the throat turn radius (r_i) and initial expansion angle (θ_i) effects on nozzle performance and nozzle length. There is room to expand the work done on truncated nozzles to include "super" truncated nozzles and look at minimising nozzle length with the possible reduction in expansion ratios to allow for the shorter expansion path. There is room to explore the boundaries of increased spline control points with high refinement levels to maximise thrust as indicated by case 2, where the highest thrust was obtained but evidently requiring further refinement to ascertain if the limits had been reached. Further work is required into understanding if having the shock wave concentration on the centerline within the nozzle (as in case 5) is an inherent feature of a high thrust full-length nozzle design or if the geometry could be adjusted to produce higher thrusts with the shock wave concentration moved to the nozzle exit and that the optimisation process could not account for this.

The results of the current work were based on a steady operating pressure where an ideal nozzle design pressure could be supplied. Further work is needed to account for the changes in the geometry due to erosion and the operating pressure changes that occur as the fuel combusts. This is, however, beyond the scope of this work and would probably be at the doctoral level.

Further experimental work is required in better validating the CFD results for tactical SRM nozzles, with insufficient experimental data available. To better understand the correlation between experimental and simulation a closer look at the fluid characteristics may be required; a technique of measuring wall pressures and centerline Mach numbers in a full-scale firing without the need for scaling and correlating between gas types and temperatures would add valuable information to the knowledge base.

REFERENCES

Allman, J. G. and Hoffman, J. D. (1981). Design of maximum thrust nozzle contours by direct optimization methods. *AIAA Journal*, 19(6):750–751.

Anderson, J. (1995). *Computational Fluid Dynamics*. Computational Fluid Dynamics: The Basics with Applications. McGraw-Hill Education.

ANSYS (2015a). *ANSYS Design Exploration User's Guide*. 14.0 edition.

ANSYS (2015b). *ANSYS Theory Guide*. 14.0 edition.

Balabel, A., Hegab, A., Nasr, M., and El-Behery, S. M. (2011). Assessment of Turbulence Modeling for Gas Flow in Two-dimensional Convergent–divergent Rocket Nozzles. *Applied Mathematical Modelling*, 35(7):3408 – 3422.

Balabel, A., Hegab, A., Wilson, S., Nasr, M., and El-Behery, S. (2009). Numerical Simulation of Turbulent Gas Flow in a Solid Rocket Motor Nozzle.

Biju Kuttan, P. and Sajesh, M. (2013). Optimization of Divergent Angle of a Rocket Engine Nozzle using Computational Fluid Dynamics. *Optimization*, 2(2):196–207.

Blomgren, P. (2015). Numerical optimization lecture notes 18 - quasi-newton methods — the bfgs method. Department of Mathematics and Statistics San Diego State University.

Cai, G., Fang, J., Xu, X., and Liu, M. (2007). Performance Prediction and Optimization for Liquid Rocket Engine Nozzle. *Aerospace Science and Technology*, 11(2):155–162.

Chen, Y.-S., Chou, T., Gu, B., Wu, J., Wu, B., Lian, Y., and Yang, L. (2011). Multiphysics simulations of rocket engine combustion. *Computers & Fluids*, 45(1):29–36.

Corbera, S., Olazagoitia, J. L., and Lozano, J. A. (2016). Multi-objective global optimization of a butterfly valve using genetic algorithms. *ISA transactions*.

Deshpande, N., Vidwans, S., Mahale, P., Joshi, R., and Jagtap, K. (2014). Theoretical & cfd Analysis of De Laval Nozzle. *International Journal of Mechanical and Production Engineering*, 2(4):33–36.

Dictionary, M.-W. (2006). *The Merriam-Webster Dictionary*. Merriam-Webster, Incorporated.

Diwekar, U. M. and Kalagnanam, J. R. (1997). Efficient sampling technique for optimization under uncertainty. *AIChE Journal*, 43(2):440–447.

Ellis, R. A. and Berdoyes, M. (2012). Srtc short course - nozzle design. *AIAA and Snecma Propulsion Solide*.

Ewing, M. E., Richards, G. H., Iverson, M. P., and Isaac, D. A. (2012). Ablation modeling of a solid rocket nozzle.

Exler, O., Lehmann, T., and Schittkowski, K. (2012). A comparative study of sqp-type algorithms for nonlinear and nonconvex mixed-integer optimization. *Mathematical Programming Computation*, 4(4):383–412.

Hunter, C. (1998). Experimental, Theoretical, and Computational Investigation of Separated Nozzle Flows. *AIAA paper*, 3107:1998.

Javed, A., Sinha, P., and Chakraborty, D. (2013). numerical exploration of solid rocket motor blast tube flow field. *Defence Science Journal*, 63(6):616–621.

Konak, A., Coit, D. W., and Smith, A. E. (2006). Multi-objective optimization using genetic algorithms: A tutorial. *Reliability Engineering & System Safety*, 91(9):992–1007.

Launder, B. E. and Spalding, D. (1974). The numerical computation of turbulent flows. *Computer methods in applied mechanics and engineering*, 3(2):269–289.

Lupoglazoff, N. and Vuillot, F. (1992). Numerical Simulation of Vortex Shedding Phenomenon in 2d Test Case Solid Rocket Motors. *AIAA paper*, 776:1992.

Mason, M., Putnam, L., and Re, R. (1980). The Effect of Throat Contouring on Two-dimensional Converging-diverging Nozzles at Static Conditions. *NASA Technical Paper*, 1704.

Menter, F. (1993). Zonal Two Equation k-turbulence Models for Aerodynamic flows. *AIAA paper*, 2906:1993.

Menter, F., Kuntz, M., and Langtry, R. (2003). Ten Years of Industrial Experience with the sst Turbulence Model. *Turbulence, heat and mass transfer*, 4(1).

Mitchell, M. (1998). *An introduction to genetic algorithms*. MIT press.

Moríñigo, J. A. and Salvá, J. J. (2008). Numerical study of the start-up process in an optimized rocket nozzle. *Aerospace Science and Technology*, 12(6):485–489.

Natta, P., Kumar, V. R., and Rao, Y. H. (2012). Flow analysis of rocket nozzle using computational fluid dynamics (cfd). *Dynamics (Cfd)*, 2(5).

Nave, L. and Coffey, G. (1973). Sea level side loads in high-area-ratio rocket engines. *AIAA paper*, 1284.

Nguyen, A.-T., Reiter, S., and Rigo, P. (2014). A review on simulation-based optimization methods applied to building performance analysis. *Applied Energy*, 113:1043–1058.

Orszag, S. A. (1970). Analytical theories of turbulence. *Journal of Fluid Mechanics*, 41(02):363–386.

Ostlund, J. and Jaran, M. (1999). Assessment of turbulence models in overexpanded rocket nozzle flow simulations. In *AIAA/ASME/SAE/ASEE Joint Propulsion Conference and Exhibit, 35 th, Los Angeles, CA*.

Rao, G. (1958). Exhaust Nozzle Contour for Optimum Thrust. *Journal of Jet Propulsion*, 28(6):377–382.

Rao, G. (1960). Approximation of optimum thrust nozzle contour. *ARS journal*, 30(6):561–561.

Rao, G. (1961). Recent developments in rocket nozzle configurations. *ARS journal*, 31(11):1488–1494.

Sabnis, J., Madabhushi, R., Gibeling, H., and McDonald, H. (1989). On the use of k-epsilon Turbulence Model for Computation of Solid Rocket Internal Flows. In *AIAA, ASME, SAE, and ASEE, 25th Joint Propulsion Conference*, volume 1.

Schittkowski, K. and Zillober, C. (2003a). Nonlinear programming. *Encyclopedia of Life Support Systems (EOLSS), UNESCO, Topic: Optimization and Operations Research*, pages 157–177.

Schittkowski, K. and Zillober, C. (2003b). Nonlinear programming: Algorithms, software, and applications. In *IFIP Conference on System Modeling and Optimization*, pages 73–107. Springer.

Schomberg, K., Doig, G., and Olsen, J. (2014). Design of High Area Nozzle Contours Using Circular Arcs. *AIAA paper*, 3999:2014.

Simmons, F. S. (2000). *Rocket Exhaust Plume Phenomenology*. Aerospace Corporation.

Spalart, P. and Allmaras, S. (1992). A one-equation turbulence model for aerodynamic flows. *AIAA paper*, 0439:1992.

Sutton, G. and Biblarz, O. (2001). *Rocket Propulsion Elements*. John Wiley & Sons.

Tahsini, A. M. and Ebrahimi, M. (2006). Blast tube effects on internal ballistics of srm. In *Proc. of 42nd AIAA/ASME/SAE/ASEE Joint Propulsion Conference & Exhibit*.

Uebel, K., Rößger, P., Prüfert, U., Richter, A., and Meyer, B. (2016). Cfd-based multi-objective optimization of a quench reactor design. *Fuel Processing Technology*, 149:290–304.

Ulas, S. and Diwekar, U. (2006). Role of sampling in process design, optimization and control. *Kirk-Othmer Encyclopedia of Chemical Technology*.

Van Beers, W. C. and Kleijnen, J. P. (2004). Kriging interpolation in simulation: a survey. In *Simulation Conference, 2004. Proceedings of the 2004 Winter*, volume 1. IEEE.

Versteeg, H. and Malalasekera, W. (2007). *An Introduction to Computational Fluid Dynamics: the Finite Volume Method*. Pearson Education.

Wang, C., Ding, H., and Zhao, Y. (2014). Influence of wall roughness on discharge coefficient of sonic nozzles. *Flow Measurement and Instrumentation*, 35:55–62.

Wang, H. (2013). Optimization of nozzle. *International Journal of Applied Research and Studies*, 2(4).

Wilcox, D. C. (2008). Formulation of the kw turbulence model revisited. *AIAA journal*, 46(11):2823–2838.

Yildizlar, B. and Eyi, S. (2014). Analysis and Design Optimization of Three Dimensional Nozzles. *AIAA paper*, 3688:2014.

Yuan, Y.-x. (1995). On the convergence of a new trust region algorithm. *Numerische Mathematik*, 70(4):515–539.

Yumuşak, M. (2013). Analysis and Design Optimization of Solid Rocket Motors in Viscous Flows. *Computers & Fluids*, 75:22–34.

Yumuşak, M. and Eyi, S. (2012). Design Optimization of Rocket Nozzles in Chemically Reacting Flows. *Computers & Fluids*, 65:25–34.

Zikanov, O. (2010). *Essential Computational Fluid Dynamics*. Wiley.

APPENDIX A Parameterized Rocket Nozzle Geometries

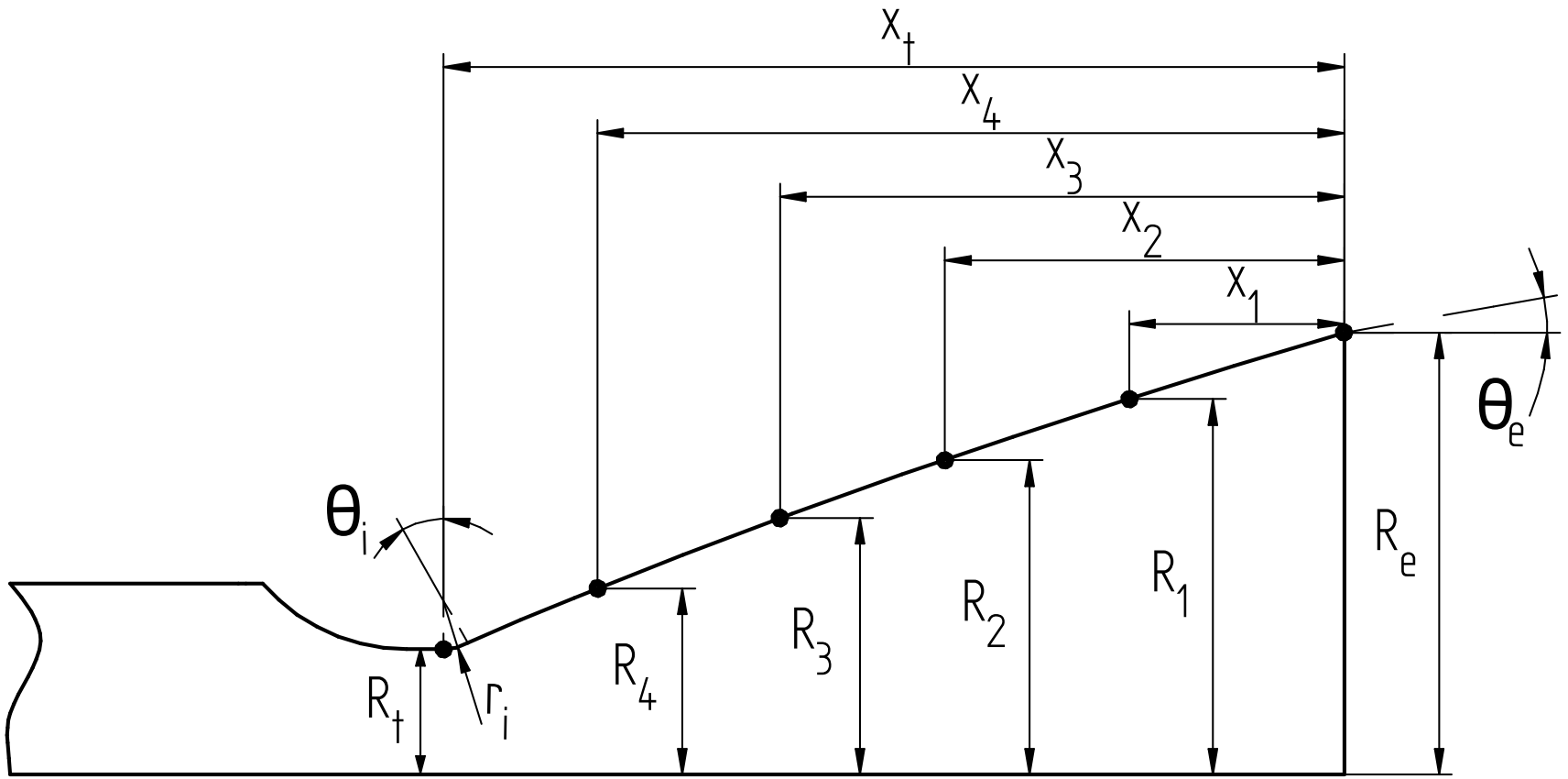

Figure A.1: Parameterized rocket nozzle

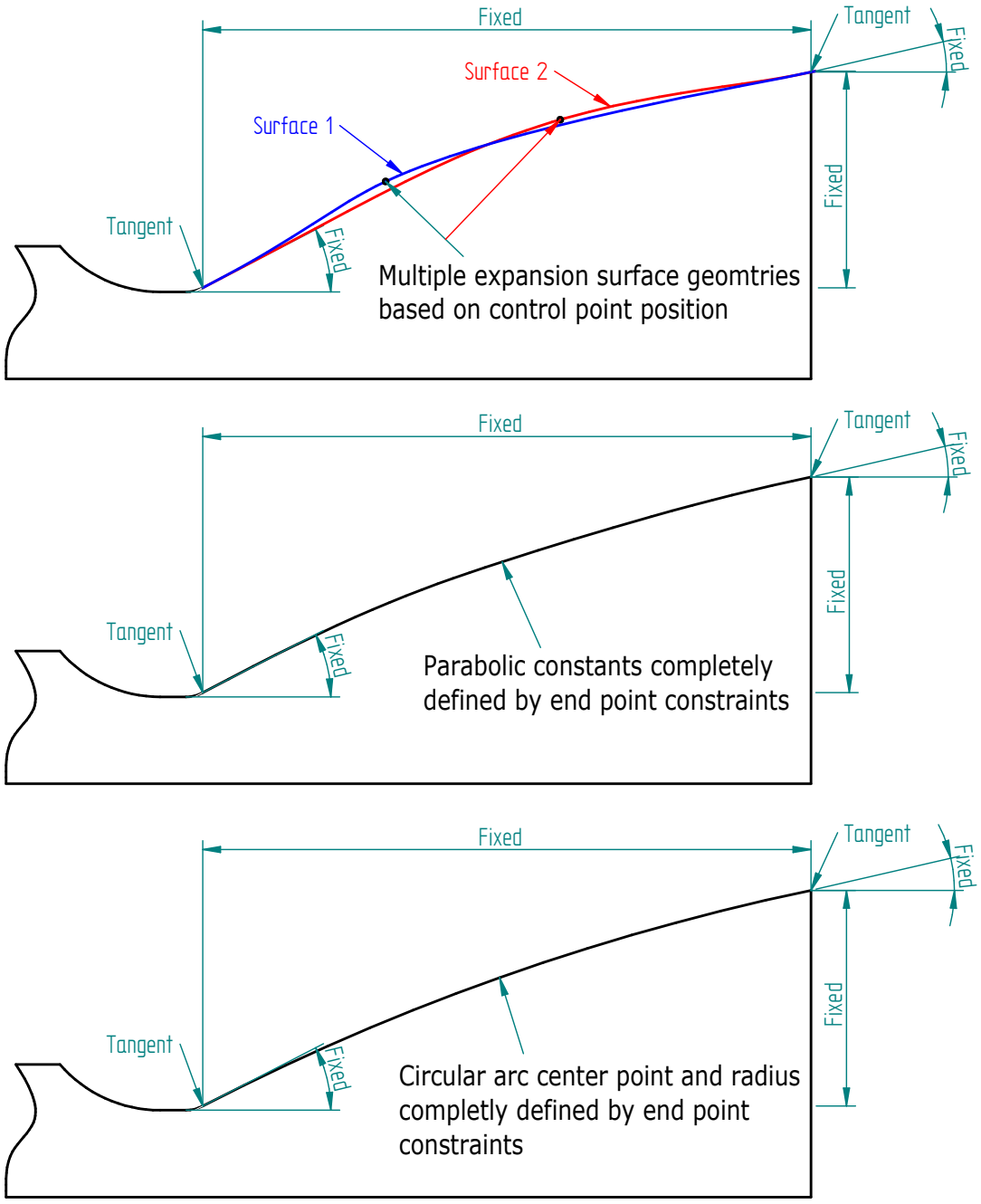

Figure A.2: Spline (top), circular arc (middle) and parabolic Rao (bottom) parametric geometry comparison

APPENDIX B Domains and Meshes

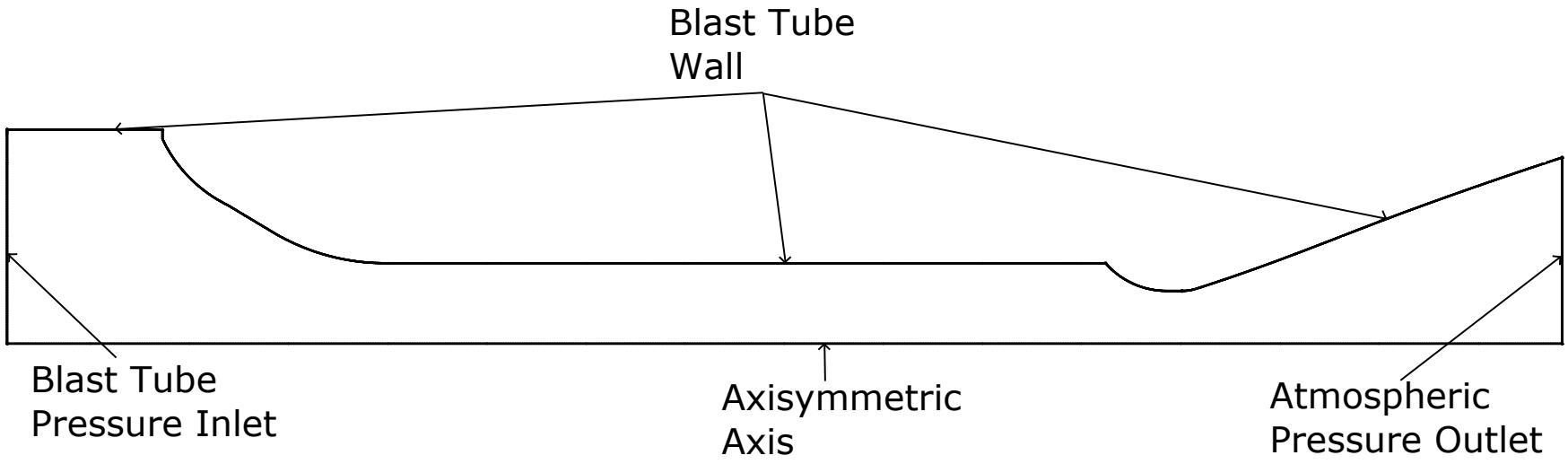

Figure B.1: Truncated exhaust plume domain

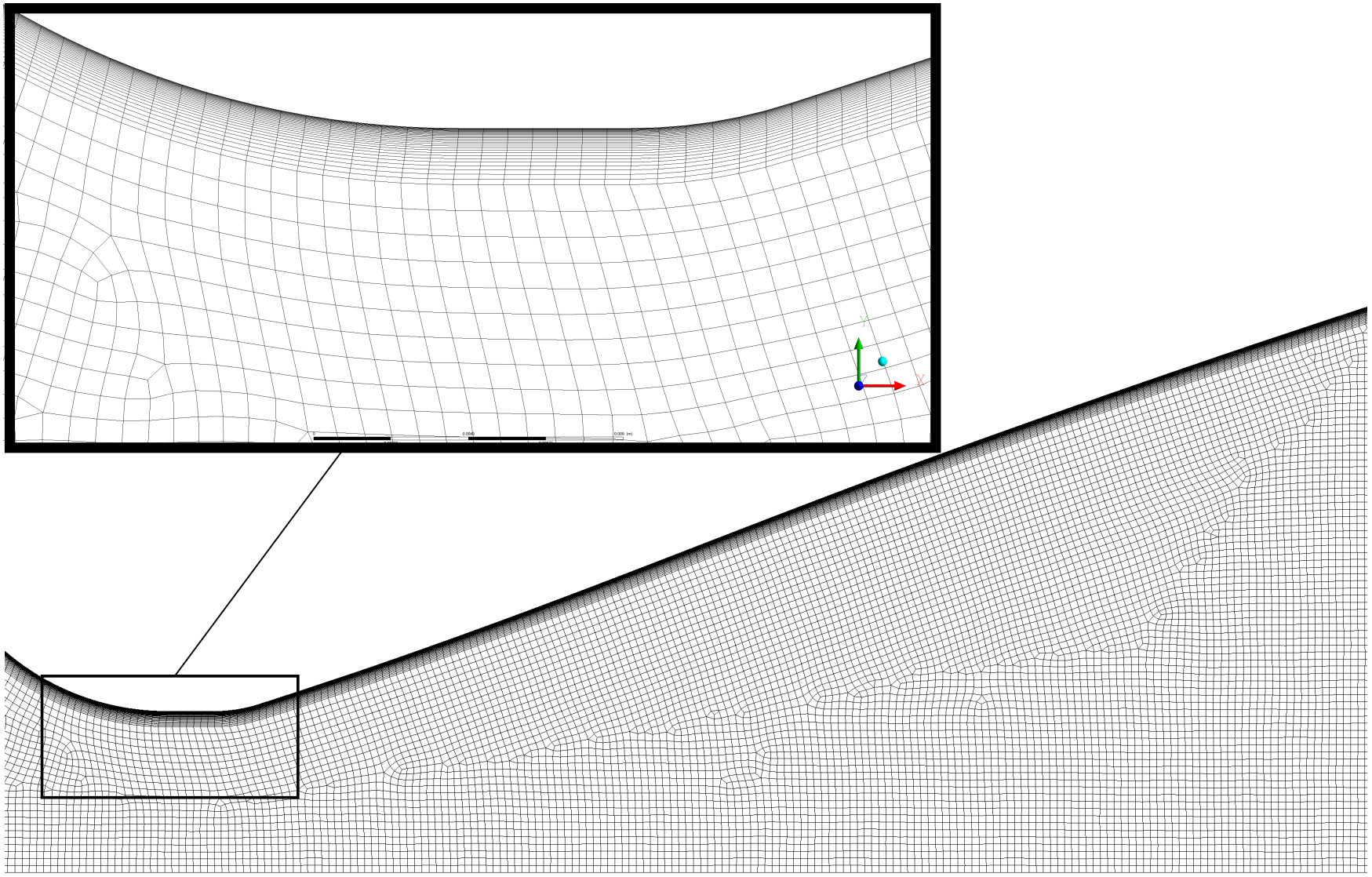

Figure B.2: Truncated exhaust plume mesh (bottom) and inflation detail (top)

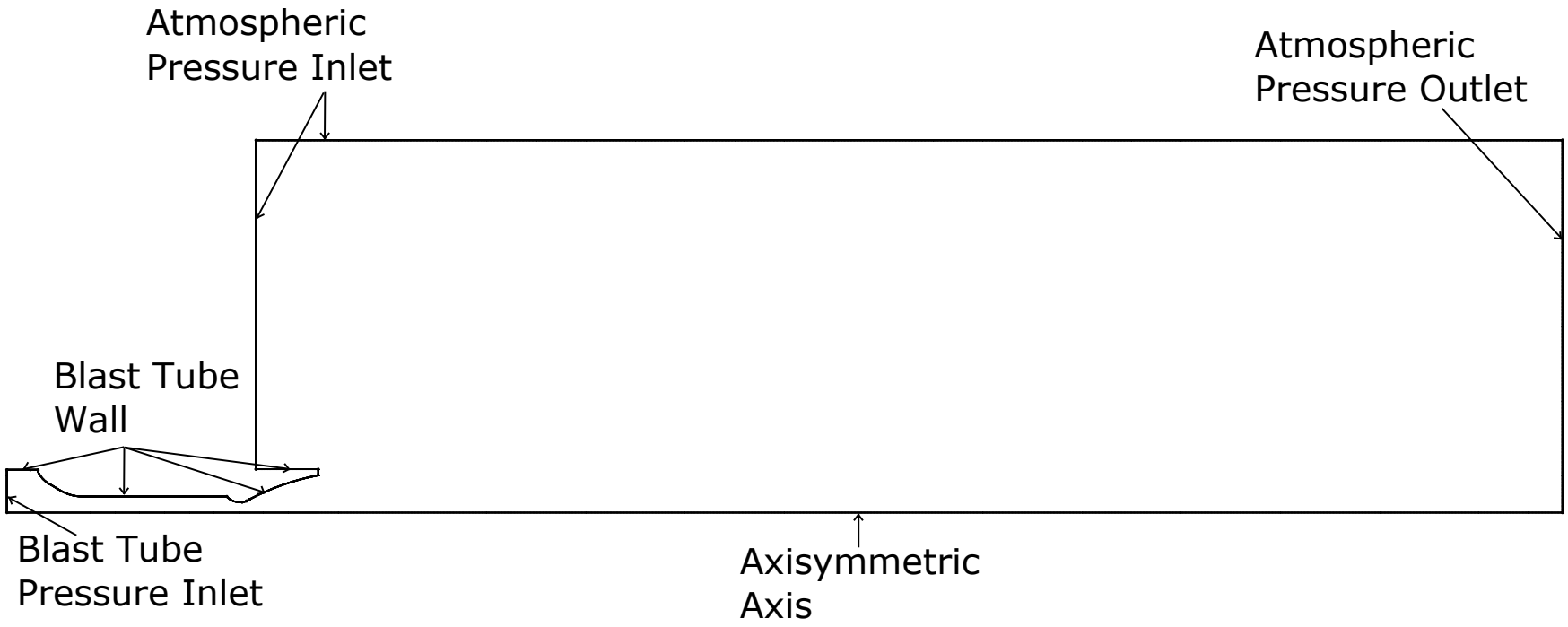

Figure B.3: Extended exhaust plume domain

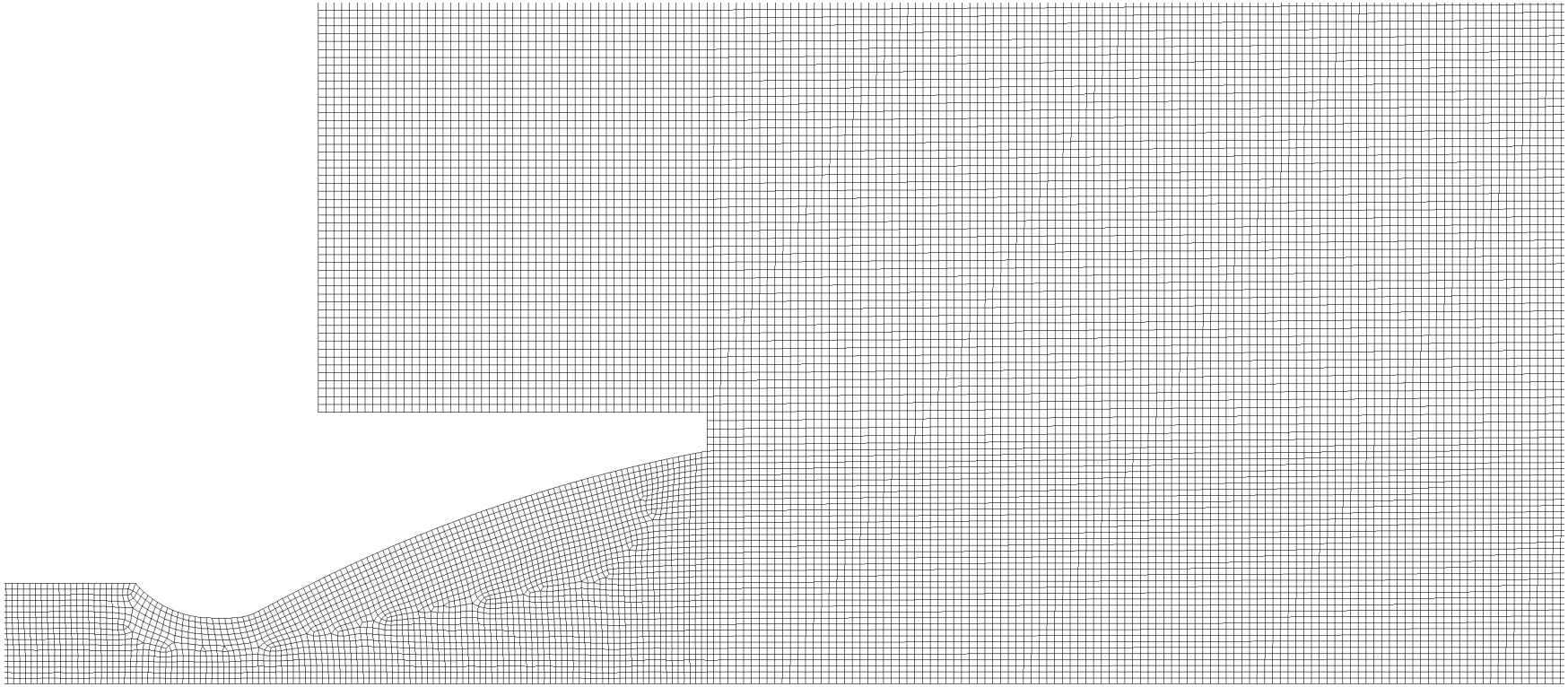

Figure B.4: Extended exhaust plume mesh detail

APPENDIX C Optimisation Method - Process Flow Diagram

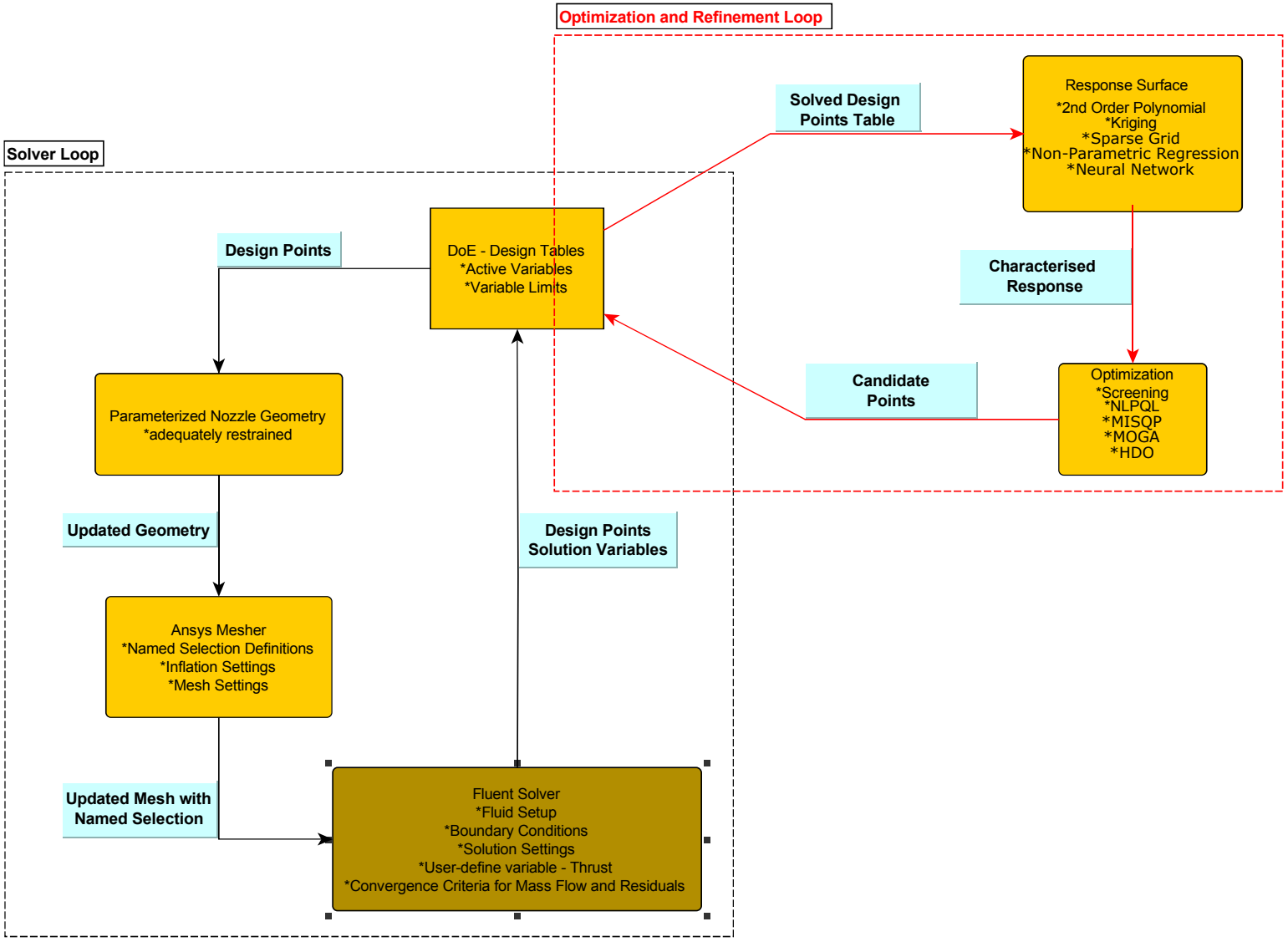

Figure C.1: Optimisation method - Process flow diagram

APPENDIX D Theoretical Spreadsheet Calculations and Transient Inlet Tables

time	p0 corrected	P0	*p* 0	*p**	m dot	Pe	Fideal	Floss
0	5451603.159	5451603	6.716868189	4.15631	3.5299206	56058.13	7.717344	7.254303
0.02	5451603.159	5451603	6.716868189	4.15631	3.5299206	56058.13	7.717344	7.254303
0.04	5451603.159	5451603	6.716868189	4.15631	3.5299206	56058.13	7.717344	7.254303
0.06	8790983.69	8790984	10.83128705	6.702258	5.6921742	90396.56	13.14658	12.35778
0.08	9086220.691	9086221	11.19504574	6.927347	5.8833406	93432.44	13.62658	12.80899
0.1	8798066.913	8798067	10.84001422	6.707658	5.6967606	90469.39	13.15809	12.36861
0.12	8489382.174	8489382	10.4596867	6.472317	5.4968868	87295.23	12.65623	11.89685
0.14	8328211.622	8328212	10.26111	6.34944	5.3925286	85637.93	12.39419	11.65054
0.16	8215715.414	8215715	10.1225045	6.263673	5.3196872	84481.15	12.2113	11.47862
0.18	8247758.821	8247759	10.16198488	6.288103	5.3404353	84810.64	12.26339	11.52759
0.2	8238390.329	8238390	10.15044205	6.28096	5.3343692	84714.31	12.24816	11.51327
0.68	9719591.249	9719591	11.97541555	7.41023	6.2934489	99945.31	14.65633	13.77695
0.7	9822344.371	9822344	12.10201669	7.488569	6.3599817	101001.9	14.82339	13.93398
0.72	9924992.58	9924993	12.22848857	7.566828	6.4264465	102057.4	14.99027	14.09086
0.74	10043873.17	10043873	12.37496021	7.657463	6.5034219	103279.9	15.18355	14.27254
0.76	10154491.21	10154491	12.51125164	7.741798	6.5750472	104417.3	15.3634	14.44159
0.78	10256294.42	10256294	12.63668241	7.819413	6.6409649	105464.2	15.52891	14.59718
0.8	10358555.73	10358556	12.76267759	7.897377	6.7071793	106515.7	15.69517	14.75346
0.82	10460199.19	10460199	12.88791153	7.97487	6.7729936	107560.9	15.86042	14.9088
0.84	10562271.14	10562271	13.0136734	8.05269	6.8390853	108610.5	16.02637	15.06479
0.86	10663758.01	10663758	13.1387144	8.130064	6.9047982	109654.1	16.19137	15.21989
0.88	10748846.56	10748847	13.24355119	8.194936	6.9598931	110529	16.32971	15.34993
0.9	10842509.73	10842510	13.35895269	8.266344	7.0205402	111492.1	16.48199	15.49307
0.92	10943790.57	10943791	13.48373985	8.343561	7.0861197	112533.6	16.64666	15.64786
0.94	11044548.72	11044549	13.607883	8.420379	7.1513607	113569.7	16.81047	15.80184
0.96	11121202.23	11121202	13.70232706	8.47882	7.200994	114357.9	16.9351	15.91899
0.98	11222306.35	11222306	13.82689648	8.555902	7.266459	115397.5	17.09947	16.0735
1	11282507.37	11282507	13.90106958	8.601799	7.3054393	116016.6	17.19735	16.16551
1.02	11350397.69	11350398	13.9847166	8.653559	7.3493983	116714.7	17.30773	16.26926
1.04	11426819.39	11426819	14.07887504	8.711823	7.3988815	117500.5	17.43197	16.38606
1.06	11478461.03	11478461	14.14250221	8.751195	7.4323195	118031.5	17.51593	16.46498
1.08	11530102.68	11530103	14.2061294	8.790566	7.4657576	118562.6	17.59989	16.5439
1.1	11581469.18	11581469	14.26941757	8.829728	7.4990174	119090.8	17.68341	16.6224
1.12	11608300.66	11608301	14.30247638	8.850185	7.5163909	119366.7	17.72703	16.66341
1.14	11659588.75	11659589	14.36566795	8.889287	7.5496	119894.1	17.81042	16.74179
1.16	11686344.59	11686345	14.39863356	8.909685	7.5669244	120169.2	17.85392	16.78268
1.18	11713060.26	11713060	14.43154968	8.930053	7.5842229	120443.9	17.89735	16.82351
1.2	11731570.3	11731570	14.45435573	8.944165	7.5962081	120634.2	17.92745	16.8518
1.22	11741874.92	11741875	14.46705195	8.952022	7.6028804	120740.2	17.9442	16.86755
1.24	11743973.6	11743974	14.46963772	8.953622	7.6042393	120761.8	17.94761	16.87075
1.26	11746284.61	11746285	14.47248509	8.955384	7.6057357	120785.5	17.95137	16.87429
1.28	11724014.64	11724015	14.44504647	8.938405	7.5913158	120556.5	17.91516	16.84025
1.3	11701677.64	11701678	14.41752527	8.921375	7.5768526	120326.8	17.87885	16.80611
1.32	11679503.92	11679504	14.39020524	8.90447	7.5624951	120098.8	17.84279	16.77223
1.34	11633032.51	11633033	14.33294826	8.86904	7.5324048	119621	17.76724	16.70121
1.36	11585855.91	11585856	14.27482242	8.833073	7.5018579	119135.9	17.69054	16.62911
1.38	11555638.03	11555638	14.23759126	8.810034	7.4822917	118825.1	17.64141	16.58293
1.4	11517504.24	11517504	14.19060698	8.780961	7.4576001	118433	17.57941	16.52465

IN	A*	Ae	gamma	Molecu	T0	p0		
	0.000908	0.01131	1.169	25.609	2500	9722877	9722877	
OUT	R	m dot	*p0*	*p**	T*	a*	Me	(Ae/A*)^2
	324.6515	6.295576	11.97946	7.412735	2305.21	935.3436	3.332	155.1777 155.1506
	Te	Pe	*pe*	ae	Ve	F		
	1289.898	99979.09	0.238746	699.6706	2331.302	14661.67		

Fideal/NT	Fcfd/NT	Fexp/NT	P	Norm P	Norm T
		0.94			
0.759395224	0	0.003135	0.060508	19.3	19.3
0.768051088	0	0.003282	0.063333		
0.776698113	0	0.003428	0.066158		
0.786712545	0	0.003574	0.068984		
0.796030945	0	0.003721	0.071809		
0.804606788	0	0.003867	0.074635		
0.813221221	0	0.003965	0.076519		
0.821783607	0	0.004013	0.07746		
0.830382089	0	0.004111	0.079344		
0.838931284	0	0.00416	0.080286		
0.846099094	0	0.004209	0.081228		
0.853989225	0	0.004257	0.08217		
0.862521065	0	0.004306	0.083111		
0.871008873	0	0.004355	0.084053		
0.87746612	0	0.004404	0.084995		
0.885983072	0	0.004453	0.085937		
0.891054371	0	0.004453	0.085937		
0.896773412	0	0.004453	0.085937		
0.903211132	0	0.004404	0.084995		
0.907561394	0	0.004355	0.084053		
0.911911656	0	0.004306	0.083111		
0.91623874	0	0.004306	0.083111		
0.918499009	0	0.004306	0.083111		
0.922819488	0	0.004306	0.083111		
0.925073384	0	0.004306	0.083111		
0.927323897	0	0.004306	0.083111		
0.928883172	0	0.004306	0.083111		
0.929751227	0	0.004257	0.08217		
0.929928018	0	0.004209	0.081228		
0.930122697	0	0.00416	0.080286		
0.928246687	0	0.004111	0.079344		
0.926365031	0	0.004062	0.078402		
0.92449713	0	0.00416	0.080286		
0.920582405	0	0.004257	0.08217		
0.916608276	0	0.004453	0.085937		
0.914062739	0	0.004745	0.091588		
0.910850371	0	0.005136	0.099123		

Figure D.1: Sample Excel one-dimensional calculations

transpzero 2 301 0

time	p0
0	5451603
0.02	5451603
0.04	5451603
0.06	8790984
0.08	9086221
0.1	8798067
0.12	8489382
0.14	8328212
0.16	8215715
0.18	8247759
0.2	8238390
0.22	8179450
0.24	8118838
0.26	8107917
0.28	8144421
0.3	8172286
0.32	8191571
0.34	8225896
0.36	8285383
0.38	8343590
0.4	8409650
0.42	8486142
0.44	8565485
0.46	8647085
0.48	8727606
0.5	8817031
0.52	8913585
0.54	9001795
0.56	9097902
0.58	9194039
0.6	9306123
0.62	9401845
0.64	9504960
0.66	9616118
0.68	9719591
0.7	9822344
0.72	9924993
0.74	10043873
0.76	10154491
0.78	10256294
0.8	10358556
0.82	10460199
0.84	10562271
0.86	10663758
0.88	10748847
0.9	10842510
0.92	10943791
0.94	11044549
0.96	11121202
0.98	11222306
1	11282507
1.02	11350398
1.04	11426819
1.06	11478461
1.08	11530103
1.1	11581469
1.12	11608301
1.14	11659589
1.16	11686345
1.18	11713060
1.2	11731570
1.22	11741875
1.24	11743974
1.26	11746285
1.28	11724015
1.3	11701678
1.32	11679504
1.34	11633033
1.36	11585856
1.38	11555638
1.4	11517504

transp 2 301 0

time	p
0	4412990
0.02	4412990
0.04	4412990
0.06	8122968
0.08	8447645
0.1	8210032
0.12	7945122
0.14	7817671
0.16	7734595
0.18	7784402
0.2	7794552
0.22	7757006
0.24	7715525
0.26	7721943
0.28	7771605
0.3	7812621
0.32	7845020
0.34	7890229
0.36	7960502
0.38	8028117
0.4	8103087
0.42	8191221
0.44	8275405
0.46	8364857
0.48	8452030
0.5	8548954
0.52	8651593
0.54	8746058
0.56	8848006
0.58	8950132
0.6	9067487
0.62	9168972
0.64	9276716
0.66	9392281
0.68	9501169
0.7	9608448
0.72	9715587
0.74	9838588
0.76	9953536
0.78	10058971
0.8	10165600
0.82	10270802
0.84	10377158
0.86	10482147
0.88	10570987
0.9	10668943
0.92	10773632
0.94	10877078
0.96	10957456
0.98	11061887
1	11125951
1.02	11196883
1.04	11276842
1.06	11331954
1.08	11387046
1.1	11441484
1.12	11471631
1.14	11525893
1.16	11555854
1.18	11585716
1.2	11607401
1.22	11620902
1.24	11626214
1.26	11632170
1.28	11613358
1.3	11593999
1.32	11575136
1.34	11531948
1.36	11487281
1.38	11460170
1.4	11425026

Figure D.2: Sample transient inlet boundary conditions for total and gauge Pressure

Time [s]	Web	Burnt	Burning Ar	P_	F_	It	J	K		%Pressure End	Mach Middle	Mach end	**Grain pressure drop pressure loss**	**Time [s]**	Max Press	12.39582
0.04	1	0.261424	5.249904	5.741186	0.008418	0.639782		287.9376023	3.690652474	0.248254874	0.601069	0.690643564	0.04	Min Press	7.692934	
0.041466	1	0.261563	5.815283	6.709755	0.018254	0.638937		288.0833979	4.38924083	0.228489258	0.527525	0.646778628	0.041466	Aveargae a	0.348639	
0.042932	1	0.261707	6.2903	7.494035	0.029242	0.638038		288.235429	4.942950619	0.214630161	0.483339	0.618851372	0.042932	Max Time	7.130805	
0.044398	1	0.261855	6.686533	8.137443	0.04118	0.637101		288.3923934	5.392181529	0.204529432	0.453659	0.599121183	0.044398	Average Pr	10.8583	
0.045865	1	0.262007	7.015153	8.665756	0.053903	0.636133		288.5533159	5.759464615	0.196951785	0.432389	0.584286603	0.045865	Diff Min an	0.379393	
0.047334	1	0.262162	7.286471	9.099811	0.067275	0.635143		288.7174271	6.059444443	0.191140543	0.416734	0.573062371	0.047334	Max Thrus	18.96585	
0.048803	1	0.262319	7.509699	9.455781	0.081183	0.634134		288.8841269	6.304958959	0.186605149	0.404827	0.564180599	0.048803	Min Thrust	9.747722	
0.050274	1	0.262478	7.692934	9.747722	0.095536	0.633112		289.0529427	6.506309112	0.183012561	0.395523	0.556819673	0.050274	Impulse	89.91426	
0.051746	1	0.262639	7.843076	9.987045	0.110257	0.632079		289.2235004	6.67096429	0.18013019	0.388233	0.550845169	0.051746	Time End	5.313436	
0.05322	1	0.262801	7.965917	10.18315	0.125285	0.631037		289.3955011	6.805878401	0.177791251	0.382399	0.545805058	0.05322	Tailoff	1.817368	
0.054696	1	0.262964	8.06634	10.34396	0.140569	0.629989		289.5687058	6.916575358	0.175871494	0.377669	0.54143428	0.054696	J	0.620397	
0.056174	1	0.263128	8.148393	10.4759	0.156068	0.628936		289.7429292	7.007495341	0.17427944	0.373792	0.537601863	0.056174	K	291.1908	
0.057653	1	0.263293	8.21543	10.58426	0.171747	0.62788		289.9180186	7.082285522	0.172945366	0.370579	0.534206767	0.057653	Average Th	15.77736	
0.059135	1	0.263459	8.270214	10.67342	0.18758	0.626821		290.0938483	7.14394885	0.171815265	0.367886	0.531156499	0.059135	Max Mach	0.18013	
0.060618	1	0.263625	8.315013	10.74694	0.203543	0.62576		290.2703171	7.194936586	0.170847218	0.365605	0.528379904	0.060618	Max Mach	0.388233	
0.062103	1	0.263792	8.351684	10.80776	0.219618	0.624697		290.4473433	7.237247356	0.170008437	0.363649	0.525821732	0.062103			
0.063591	1	0.263959	8.381744	10.85823	0.23579	0.623634		290.6248608	7.272509157	0.16927311	0.361952	0.523438752	0.063591			
0.06508	1	0.264127	8.406432	10.90032	0.252047	0.622571		290.8028162	7.302047011	0.168620812	0.360463	0.521196937	0.06508			
0.066572	1	0.264295	8.426758	10.93559	0.268378	0.621507		290.9811664	7.326938631	0.168035312	0.35914	0.519069365	0.066572			
0.068065	1	0.264463	8.443542	10.96532	0.284777	0.620444		291.1598765	7.348060099	0.167503668	0.35795	0.517034654	0.068065			
0.06956	1	0.264632	8.457456	10.99058	0.301237	0.619381		291.3389185	7.366129503	0.167015442	0.356868	0.515069757	0.06956			
0.071058	1	0.264801	8.46904	11.01219	0.317751	0.61832		291.5182697	7.381711341	0.16656253	0.355872	0.51317313	0.071058			
0.072558	1	0.26497	8.478739	11.03077	0.334316	0.617259		291.6979116	7.395233529	0.166138797	0.354948	0.511375701	0.072558			
0.074059	1	0.26514	8.48692	11.04706	0.350929	0.616199		291.8778292	7.407185039	0.165737496	0.354079	0.509572495	0.074059			
0.075563	1	0.265309	8.493864	11.0614	0.367587	0.615139		292.0580109	7.41781557	0.165355095	0.353255	0.507803917	0.075563			
0.077069	1	0.265479	8.49981	11.07418	0.384287	0.614082		292.2384473	7.427375656	0.164988108	0.352469	0.506066096	0.077069			
0.078577	1	0.26565	8.504949	11.08569	0.401027	0.613025		292.4191305	7.436069411	0.164633731	0.351713	0.504353588	0.078577			
0.080087	1	0.26582	8.509438	11.09617	0.417807	0.611969		292.6000545	7.444062358	0.164289698	0.350982	0.502662709	0.080087			
0.0816	1	0.265991	8.513403	11.10583	0.434625	0.610915		292.7812143	7.451488792	0.163954176	0.35027	0.500990485	0.0816			
0.083114	1	0.266162	8.516947	11.11482	0.45148	0.609862		292.9626061	7.458457663	0.163625685	0.349576	0.499334512	0.083114			
0.08463	1	0.266333	8.520155	11.12327	0.468372	0.608811		293.1442269	7.465057358	0.163303026	0.348895	0.497692845	0.08463			
0.086149	1	0.266504	8.523093	11.13129	0.485299	0.60776		293.3260742	7.47135958	0.162985232	0.348225	0.496063907	0.086149			
0.08767	1	0.266676	8.525817	11.13896	0.502262	0.606712		293.5081462	7.477419873	0.162671519	0.347563	0.494452545	0.08767			
0.089192	1	0.266848	8.528367	11.14635	0.519259	0.605664		293.6904414	7.483284851	0.162361323	0.34691	0.492845799	0.089192			
0.090717	1	0.26702	8.530784	11.15367	0.536292	0.604618		293.8729588	7.488997139	0.162054044	0.346264	0.4912486	0.090717			
0.092244	1	0.267192	8.533077	11.16063	0.553359	0.603573		294.0556975	7.494562049	0.161749548	0.345622	0.489667129	0.092244			
0.093774	1	0.267364	8.53529	11.16744	0.570461	0.60253		294.2386569	7.500001949	0.161447232	0.344991	0.488106352	0.093774			
0.095305	1	0.267537	8.537441	11.17415	0.587596	0.601488		294.4218366	7.505126205	0.161146821	0.34441	0.486658977	0.095305			
0.096839	1	0.26771	8.539547	11.18079	0.604766	0.600448		294.6052365	7.510584397	0.160848093	0.343757	0.485039425	0.096839			
0.098374	1	0.267883	8.541626	11.18736	0.62197	0.599408		294.7888566	7.515948802	0.160550795	0.343117	0.483449918	0.098374			
0.099912	1	0.268056	8.54368	11.19388	0.639208	0.598371		294.9726969	7.520981078	0.16025488	0.342535	0.482002329	0.099912			
0.101452	1	0.26823	8.545726	11.20038	0.656481	0.597334		295.1567576	7.526209626	0.159960122	0.341914	0.480460347	0.101452			
0.102994	1	0.268404	8.547769	11.20686	0.673787	0.5963		295.3410389	7.531421754	0.159666455	0.341295	0.478924808	0.102994			
0.104538	1	0.268578	8.549813	11.21334	0.691128	0.595266		295.5255411	7.536763062	0.159373808	0.340651	0.477332901	0.104538			
0.106085	1	0.268752	8.551855	11.21979	0.708503	0.594234		295.7102644	7.541553318	0.159082204	0.340111	0.475992478	0.106085			
0.107633	1	0.268926	8.553908	11.22625	0.725913	0.593203		295.8952093	7.546978382	0.158791488	0.339452	0.474367511	0.107633			
0.109184	1	0.269101	8.555967	11.2327	0.743356	0.592174		296.0803761	7.552307951	0.158501717	0.338811	0.472789602	0.109184			
0.110737	1	0.269276	8.558041	11.23917	0.760835	0.591146		296.2657652	7.557491729	0.158212759	0.3382	0.471284541	0.110737			
0.112292	1	0.269451	8.560131	11.24565	0.778348	0.59012		296.451377	7.562679933	0.157924603	0.33759	0.469785324	0.112292			
0.11385	1	0.269626	8.562237	11.25214	0.795896	0.589095		296.637212	7.567873751	0.157637229	0.336981	0.468291898	0.11385			
0.115409	1	0.269802	8.564362	11.25865	0.813478	0.588071		296.8232706	7.572919731	0.157350624	0.336403	0.466876554	0.115409			
0.116971	1	0.269978	8.5665	11.26517	0.831096	0.587049		297.0095533	7.578121033	0.157064842	0.335797	0.465395201	0.116971			
0.118535	1	0.270154	8.568658	11.2717	0.848748	0.586028		297.1960605	7.583487202	0.156779789	0.335162	0.463849443	0.118535			
0.120101	1	0.27033	8.570836	11.27826	0.866435	0.585009		297.3827927	7.588548064	0.156495453	0.334588	0.462454412	0.120101			
0.121669	1	0.270506	8.57303	11.28482	0.884158	0.583991		297.5697504	7.593916824	0.156211903	0.333958	0.460925102	0.121669			
0.12324	1	0.270683	8.575247	11.29142	0.901916	0.582974		297.756934	7.598720145	0.155929044	0.333439	0.459665187	0.12324			
0.124812	1	0.27086	8.577479	11.29802	0.919709	0.581959		297.944344	7.604217242	0.15564695	0.332789	0.458095833	0.124812			
0.126387	1	0.271037	8.579734	11.30464	0.937537	0.580945		298.1319809	7.609470614	0.15536553	0.33219	0.456648234	0.126387			
0.127964	1	0.271214	8.582012	11.3113	0.955401	0.579932		298.3198453	7.614735546	0.155084792	0.331592	0.455206052	0.127964			
0.129543	1	0.271392	8.584312	11.31796	0.973301	0.578921		298.5079376	7.620011896	0.154804735	0.330994	0.453769261	0.129543			
0.131125	1	0.271569	8.586633	11.32465	0.991236	0.577912		298.6962583	7.625299548	0.154525359	0.330398	0.452337837	0.131125			
0.132709	1	0.271747	8.588976	11.33135	1.009207	0.576903		298.8848079	7.630598412	0.154246662	0.329803	0.450911755	0.132709			
0.134295	1.013264	0.271926	8.59134	11.3381	1.027215	0.575896		299.0734547	7.635920814	0.153959403	0.329207	0.449482035	0.134295			
0.135883	1.030497	0.272104	8.593718	11.34486	1.045258	0.574891		299.2622928	7.641249699	0.153670241	0.328613	0.448055185	0.135883			
0.137473	1.047751	0.272282	8.596109	11.35162	1.063338	0.573886		299.4513626	7.646580479	0.153381942	0.328019	0.446633871	0.137473			
0.139066	1.065029	0.272461	8.598514	11.35841	1.081454	0.572884		299.6405352	7.651923781	0.153093992	0.327426	0.445211679	0.139066			
0.140661	1.082328	0.27264	8.600929	11.36521	1.099607	0.571882		299.8298917	7.656940314	0.152806749	0.326897	0.443945093	0.140661			
0.142258	1.099651	0.272819	8.603349	11.372	1.117797	0.570882		300.0194823	7.662278378	0.152520456	0.326306	0.442532521	0.142258			
0.143858	1.116996	0.272998	8.605782	11.37881	1.136024	0.569883		300.2093081	7.667621206	0.152234932	0.325717	0.441123156	0.143858			
0.14546	1.134363	0.273177	8.608228	11.38563	1.154287	0.568886		300.3992076	7.672973405	0.151949856	0.325128	0.439714706	0.14546			
0.147064	1.151754	0.273357	8.610685	11.39245	1.172588	0.56789		300.5893198	7.678326081	0.151665595	0.324541	0.438311114	0.147064			
0.14867	1.169167	0.273537	8.613153	11.39929	1.190927	0.566895		300.7796694	7.683679925	0.151382181	0.323954	0.43691288	0.14867			
0.150279	1.186604	0.273717	8.615635	11.40613	1.209302	0.565901		300.9701906	7.689374973	0.151099526	0.323303	0.435365663	0.150279			
0.15189	1.204064	0.273897	8.618131	11.41299	1.227715	0.564909		301.1608396	7.694739092	0.150817582	0.322718	0.433976599	0.15189			
0.153503	1.221546	0.274077	8.620641	11.41985	1.246166	0.563919		301.3517277	7.700107044	0.150536446	0.322135	0.432592887	0.153503			
0.155119	1.239053	0.274258	8.623167	11.42673	1.264654	0.562929		301.5428553	7.705137336	0.150256097	0.321619	0.431373581	0.155119			
0.156737	1.256582	0.274439	8.625706	11.43362	1.283181	0.561941		301.7342231	7.710854394	0.14997657	0.320971	0.429844523	0.156737			
0.158357	1.274135	0.27462	8.628263	11.44053	1.301745	0.560954		301.9258313	7.715889011	0.149697782	0.320458	0.42863897	0.158357			
0.15998	1.291711	0.274801	8.630835	11.44745	1.320347	0.559969		302.1176806	7.721278552	0.14941978	0.319879	0.427275942	0.15998			
0.161605	1.309311	0.274982	8.633426	11.45438	1.338987	0.558985		302.3097714	7.727012959	0.149142496	0.319236	0.425765032	0.161605			
0.163232	1.326934	0.275164	8.636039	11.46134	1.357666	0.558002		302.5021043	7.732063324	0.148865918	0.318728	0.42457925	0.163232			
0.164862	1.344581	0.275346	8.638668	11.46831	1.376383	0.55702		302.6946796	7.737477372	0.148590095	0.318153	0.42323285	0.164862			
0.166494	1.362251	0.275529	8.641318	11.47531	1.395138	0.55604		302.8874981	7.743211591	0.14831496	0.317518	0.421750143	0.166494			
0.168128	1.379945	0.275711	8.643985	11.48232	1.413932	0.555061		303.0805601	7.748241123	0.148040563	0.317023	0.420600632	0.168128			
0.169765	1.397663	0.275894	8.646674	11.48936	1.432764	0.554084		303.2738663	7.753781145	0.147766843	0.316432	0.419226371	0.169765			
0.171404	1.415405	0.276077	8.649386	11.49642	1.451635	0.553108		303.467417	7.759550904	0.147493796	0.315799	0.417756924	0.171404			
0.173046	1.43317	0.27626	8.652114	11.5035	1.470545	0.552133		303.661213	7.764608396	0.147221472	0.315308	0.41662458	0.173046			
0.17469	1.45096	0.276443	8.654865	11.5106	1.489494	0.551159		303.8552547	7.77018214	0.146949811	0.31472	0.415264771	0.17469			
0.176336	1.468773	0.276627	8.657638	11.51772	1.508483	0.550187		304.0495426	7.77557487	0.146678813	0.31417	0.414000114	0.176336			
0.177984	1.48661	0.276811	8.660429	11.52486	1.52751	0.549216		304.2440773	7.781471984	0.146408523	0.313523	0.412511302	0.177984			
0.179635	1.504472	0.276995	8.663239	11.53202	1.546577	0.548246		304.4388592	7.786553095	0.146138927	0.31304	0.411407628	0.179635			

Figure D.3: Pressure drop correction data

APPENDIX E Case 1 - Data

	Input Parameters					Output Parameters	
No	⌜i [mm]	Θi [degree]	x2 [mm]	R2 @ x2 [mm]	Θe [degree]	Mass Flow[kg/s]	Total Thrust [N]
1	10.000	27.440	40.000	50.148	13.146	-6.5059	14409.8
2	10.000	27.101	48.550	47.088	14.089	-6.5060	14409.5
3	10.000	27.421	47.779	47.533	13.109	-6.5060	14409.4
4	10.000	27.280	46.676	47.604	14.189	-6.5061	14409.4
5	10.000	27.100	48.700	47.100	14.000	-6.5059	14409.1
6	10.000	27.108	48.654	47.067	14.056	-6.5051	14407.6
7	10.000	26.500	46.500	47.900	12.600	-6.5062	14407.5
8	10.000	26.546	46.556	47.880	12.664	-6.5060	14407.4
9	10.000	27.213	61.716	43.591	14.589	-6.5057	14406.4
10	10.000	25.513	40.000	49.248	18.000	-6.5061	14406.3
11	10.000	27.213	61.716	43.591	14.589	-6.5057	14406.1
12	10.161	26.728	41.300	50.812	14.536	-6.5061	14405.5
13	10.000	27.600	47.900	47.300	13.200	-6.5059	14405.4
14	10.000	27.179	47.384	47.582	11.315	-6.5064	14405.1
15	10.000	26.528	46.473	47.925	12.609	-6.5052	14405.1
16	10.000	27.582	47.851	47.281	13.203	-6.5052	14403.5
17	10.000	27.500	60.000	45.000	13.000	-6.5061	14403
18	11.932	27.804	63.406	42.872	14.387	-6.5065	14402.3
19	11.431	27.976	51.700	45.655	16.518	-6.5062	14401.5
20	11.017	27.635	62.943	42.856	14.573	-6.5052	14401.4
21	11.017	27.635	62.943	42.856	14.573	-6.5052	14401.3
22	11.932	27.804	63.406	42.872	14.387	-6.5058	14400.7
23	12.271	28.168	43.700	49.166	10.687	-6.5063	14399.3
24	12.271	28.168	43.700	49.166	10.687	-6.5059	14398.5
25	11.431	27.976	51.700	45.655	16.518	-6.5056	14397.2
26	11.079	28.840	58.900	45.326	13.170	-6.5061	14396.4
27	12.550	26.974	44.604	48.386	10.907	-6.5060	14396.2
28	10.210	28.532	66.900	41.155	9.205	-6.5061	14396.1
29	11.782	24.520	57.460	44.338	12.120	-6.5062	14396
30	13.540	25.816	53.860	45.490	12.295	-6.5061	14395.6
31	10.610	25.960	59.860	42.472	16.668	-6.5060	14395.6
32	15.669	27.232	45.500	48.919	14.798	-6.5059	14395.2
33	15.093	26.464	63.100	42.555	13.432	-6.5061	14394.2
34	14.946	26.680	55.300	44.502	14.744	-6.5061	14393.6
35	13.583	25.375	65.667	42.167	11.583	-6.5063	14392.9
36	11.577	26.824	61.300	43.460	9.321	-6.5063	14392.7
37	15.000	28.000	37.575	50.948	12.000	-6.5063	14392.6
38	16.587	26.176	51.100	46.395	14.681	-6.5058	14391.4
39	15.000	28.000	42.075	48.838	12.000	-6.5061	14390.4
40	15.000	28.000	81.425	35.459	12.000	-6.5063	14390.2
41	11.382	29.972	68.340	40.168	10.054	-6.5068	14389.3
42	18.638	27.472	47.500	47.767	16.256	-6.5063	14388.5
43	13.583	29.625	65.667	42.167	14.417	-6.5061	14388.4
44	13.911	30.328	41.540	49.331	13.311	-6.5067	14388.4
45	11.724	26.248	42.100	47.850	12.320	-6.5064	14388.1
46	13.013	29.272	47.140	47.026	13.195	-6.5064	14388
47	14.829	29.560	59.140	43.844	11.945	-6.5062	14388
48	15.000	28.000	80.547	35.000	12.000	-6.5062	14387.9
49	15.000	28.000	79.825	35.147	12.000	-6.5061	14387.5
50	15.000	28.000	83.025	35.303	12.000	-6.5064	14387.1
51	15.000	27.500	60.000	45.000	13.000	-6.5066	14385
52	15.000	28.000	43.275	47.901	12.000	-6.5061	14384.9
53	12.857	25.432	45.860	49.660	17.859	-6.5063	14384.3
54	15.000	28.000	35.175	50.010	12.000	-6.5061	14384.1
55	16.417	29.625	65.667	42.167	11.583	-6.5070	14383.7
56	12.251	27.400	56.500	46.313	17.018	-6.5062	14383.1
57	12.505	26.008	40.100	48.343	10.862	-6.5065	14382.5

Figure E.1: Case 1 - Design table - Page 1/3

58	19.536	28.528	41.900	50.072	16.372	-6.5066	14382.1
59	16.417	25.375	65.667	42.167	14.417	-6.5039	14380.9
60	15.415	27.615	53.500	44.749	10.833	-6.5061	14380.9
61	13.583	23.958	67.083	42.167	11.583	-6.5052	14380.2
62	12.720	31.000	56.740	44.832	15.793	-6.5062	14380.2
63	10.493	32.296	52.180	46.642	12.670	-6.5062	14379.4
64	18.814	24.880	55.660	45.243	17.805	-6.5063	14378.6
65	11.858	20.610	79.761	35.656	15.869	-6.5052	14378.4
66	11.372	25.672	47.860	46.533	8.122	-6.5061	14378.3
67	17.896	29.968	43.340	48.426	17.422	-6.5066	14376
68	16.294	29.632	45.340	47.932	9.084	-6.5065	14376
69	15.000	28.000	55.845	46.636	12.000	-6.5063	14375.8
70	16.265	27.904	60.700	44.201	17.280	-6.5064	14375.3
71	15.240	27.500	60.000	45.000	9.259	-6.5062	14375.2
72	11.099	23.848	42.260	48.837	8.238	-6.5062	14374.8
73	15.239	28.768	43.900	46.944	17.830	-6.5062	14374.5
74	15.999	27.500	60.000	45.000	16.501	-6.5063	14374.1
75	15.000	27.500	60.000	45.000	8.000	-6.5067	14372.8
76	13.081	26.660	75.300	37.077	8.130	-6.5060	14372.2
77	15.016	24.012	60.000	45.000	13.000	-6.5064	14372
78	18.130	24.208	40.460	49.084	13.923	-6.5060	14371.5
79	13.364	24.088	44.260	47.685	9.696	-6.5063	14371.5
80	15.990	31.786	60.000	45.000	13.000	-6.5064	14370.8
81	15.000	27.500	60.000	45.000	18.000	-6.5066	14370.5
82	15.000	28.000	40.075	47.979	12.000	-6.5061	14370.3
83	10.200	21.352	46.420	48.179	16.868	-6.5060	14366.4
84	18.345	26.320	57.100	45.572	9.059	-6.5069	14365.2
85	20.000	27.500	60.000	45.000	13.000	-6.5062	14364.5
86	15.000	28.000	35.000	48.986	12.000	-6.5060	14364
87	10.737	22.196	73.620	37.571	8.305	-6.5050	14363.2
88	15.000	28.000	43.475	46.651	12.000	-6.5061	14362.4
89	19.264	27.500	60.000	45.000	15.891	-6.5063	14362.2
90	19.000	25.547	60.000	45.000	13.000	-6.5060	14362.2
91	18.382	27.500	60.000	45.000	9.310	-6.5064	14361.6
92	19.058	25.547	60.000	45.000	13.000	-6.5054	14360.2
93	19.142	31.894	60.000	45.000	13.000	-6.5062	14359.7
94	19.672	21.316	79.450	35.466	10.507	-6.5053	14357.5
95	14.921	21.679	60.000	45.000	13.000	-6.5062	14354.6
96	15.000	27.500	64.886	39.074	13.000	-6.5063	14353.7
97	18.723	22.356	60.000	45.000	13.000	-6.5062	14345.8
98	15.000	27.500	47.665	44.461	13.000	-6.5063	14340.8
99	15.000	28.000	41.875	46.338	12.000	-6.5060	14339.8
100	15.000	27.500	61.859	39.632	13.000	-6.5062	14337
101	19.286	34.283	79.272	35.940	16.867	-6.5055	14327.1
102	15.000	27.500	47.900	43.879	13.000	-6.5053	14322.4
103	15.000	27.500	47.866	43.879	13.000	-6.5053	14320.3
104	15.000	27.500	61.056	47.508	13.000	-6.5061	14293.9
105	15.000	27.500	66.569	36.659	13.000	-6.5061	14279.1
106	15.000	27.500	56.977	39.320	13.000	-6.5064	14248.3
107	15.000	15.000	60.000	45.000	13.000	-6.5041	14223.5
108	13.583	29.625	65.667	47.833	11.583	-6.5062	14192.8
109	15.000	27.500	71.253	45.364	13.000	-6.5069	14185.8
110	15.000	27.500	45.739	41.453	13.000	-6.5062	14170.6
111	13.583	25.375	65.667	47.833	14.417	-6.5067	14148.6
112	16.417	29.625	65.667	47.833	14.417	-6.5062	14146.5
113	16.417	25.375	65.667	47.833	11.583	-6.5068	14143
114	15.000	27.500	55.701	37.846	13.000	-6.5062	14125.9
115	15.000	27.500	53.867	53.001	13.000	-6.5066	14064.3
116	15.000	27.500	42.415	40.637	13.000	-6.5060	14055.5

117	15.000	27.500	60.000	35.000	13.000	-6.4988	13994.2
118	15.000	27.500	51.712	37.126	13.000	-6.5058	13968.7
119	15.000	27.500	51.338	36.457	13.000	-6.5062	13894.2
120	15.000	27.500	80.000	45.000	13.000	-6.5065	13878.4
121	15.000	27.500	59.189	53.282	13.000	-6.5058	13836.5
122	15.000	27.500	68.599	50.698	13.000	-6.5063	13754.4
123	19.623	30.910	40.776	35.551	8.304	-6.5082	13732.6
124	15.000	27.500	76.547	48.365	13.000	-6.5065	13668
125	15.000	27.500	60.000	55.000	13.000	-6.5042	13540.2
126	10.499	20.252	79.944	53.096	10.050	-6.5063	12866.2
127	10.366	34.533	75.958	54.519	16.773	-6.5050	12649.4
128	19.435	34.451	79.322	52.775	17.928	-6.5062	12633.8
129	18.945	34.302	78.700	54.885	8.680	-6.5071	12612.8
130	19.150	20.423	79.761	54.534	16.184	-6.5063	12357.2
131	10.652	20.190	79.862	54.549	17.925	-6.5066	12346.1

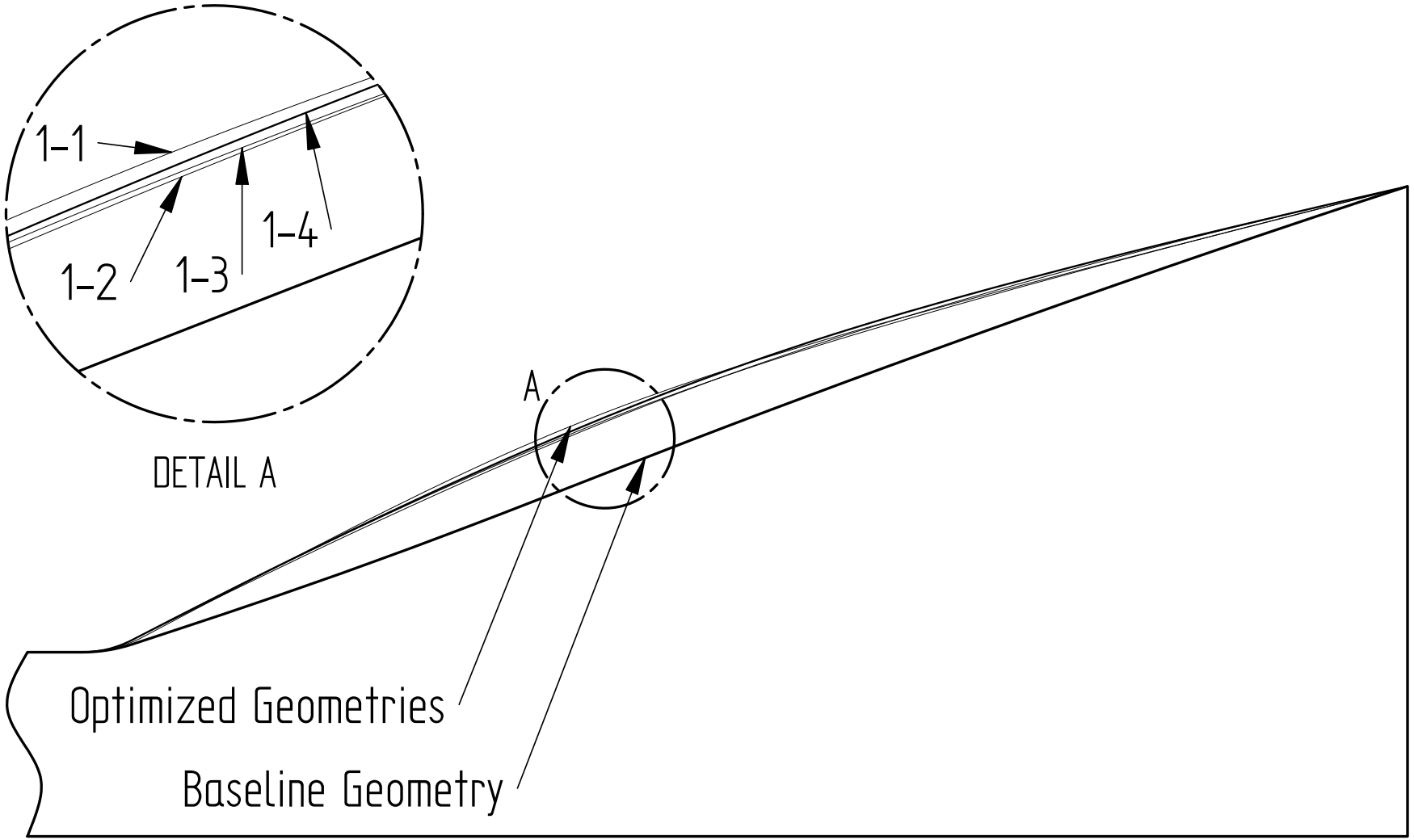

Figure E.2: Case 1 - Geometry comparison

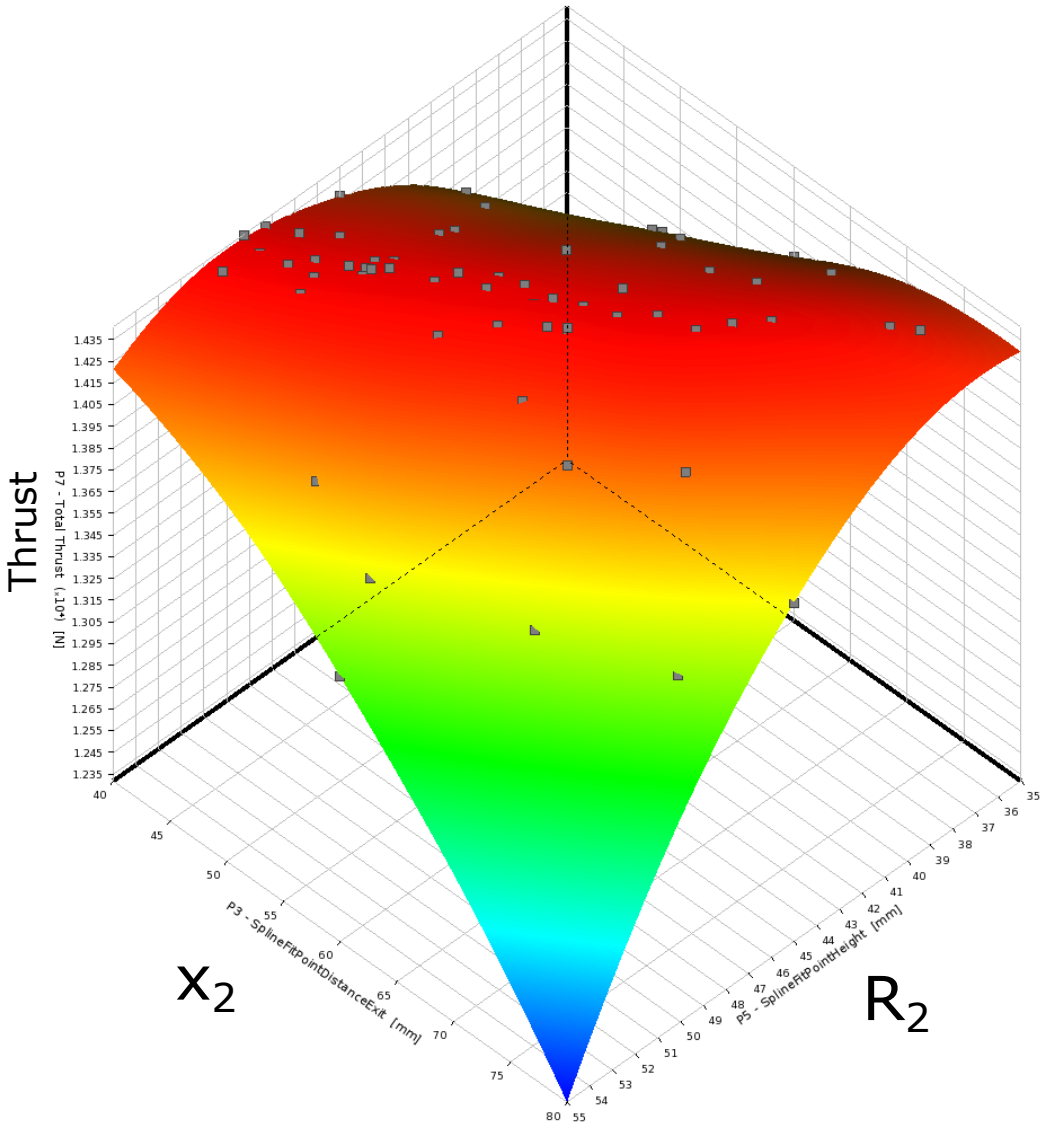

Figure E.3: Case 1 - x_2 vs R_2 Kriging response surface

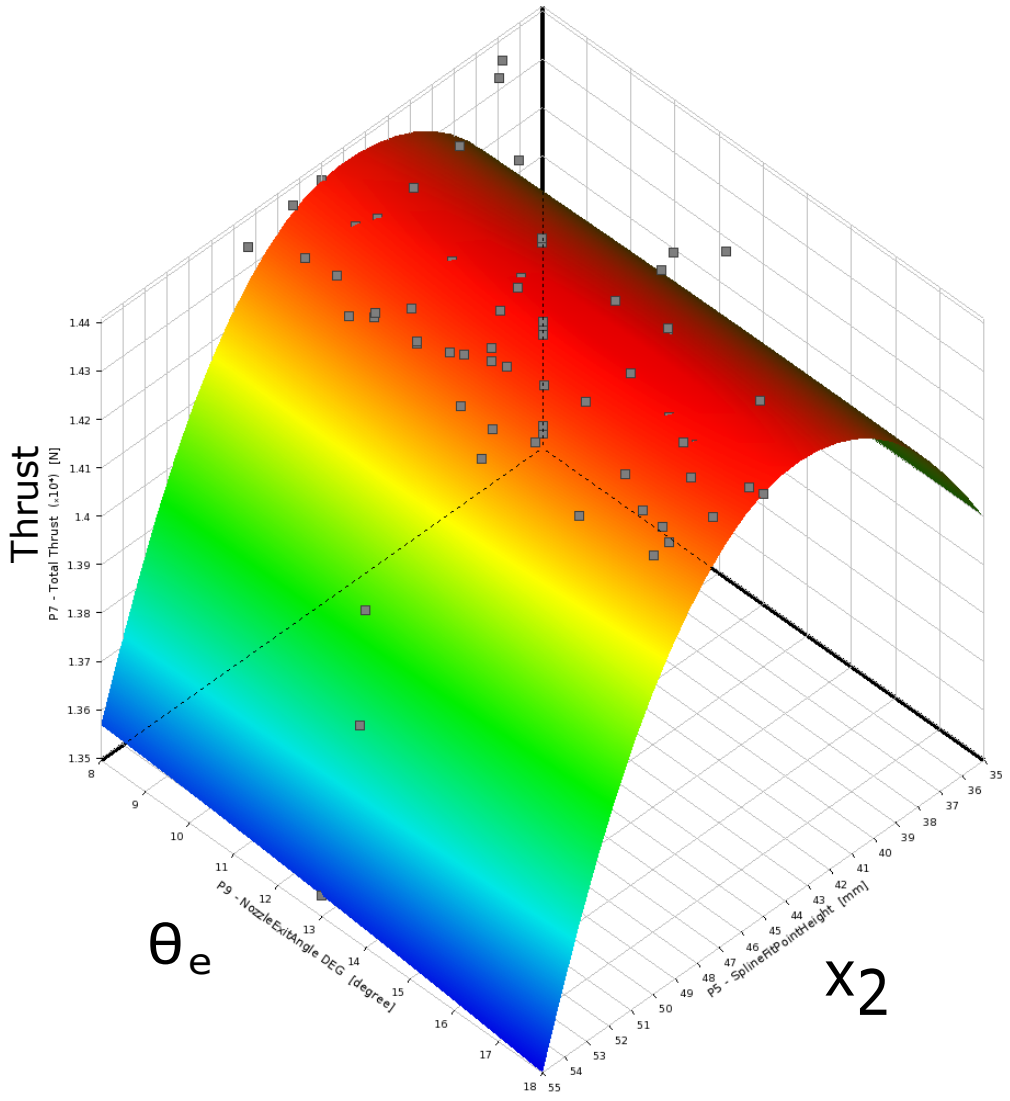

Figure E.4: Case 1 - θ_e vs x_2 Kriging response surface

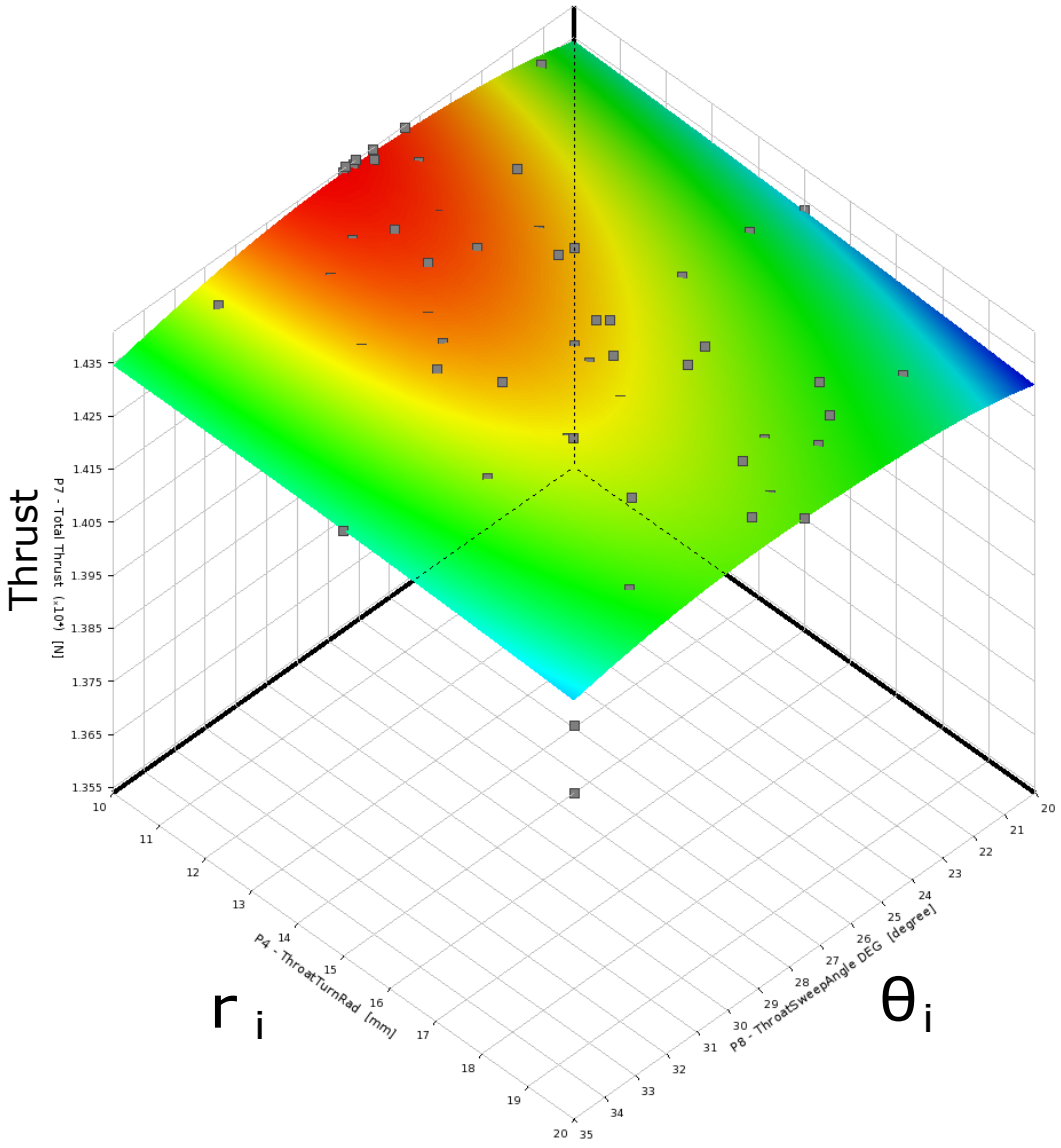

Figure E.5: Case 1 - r_i vs θ_i Kriging response surface

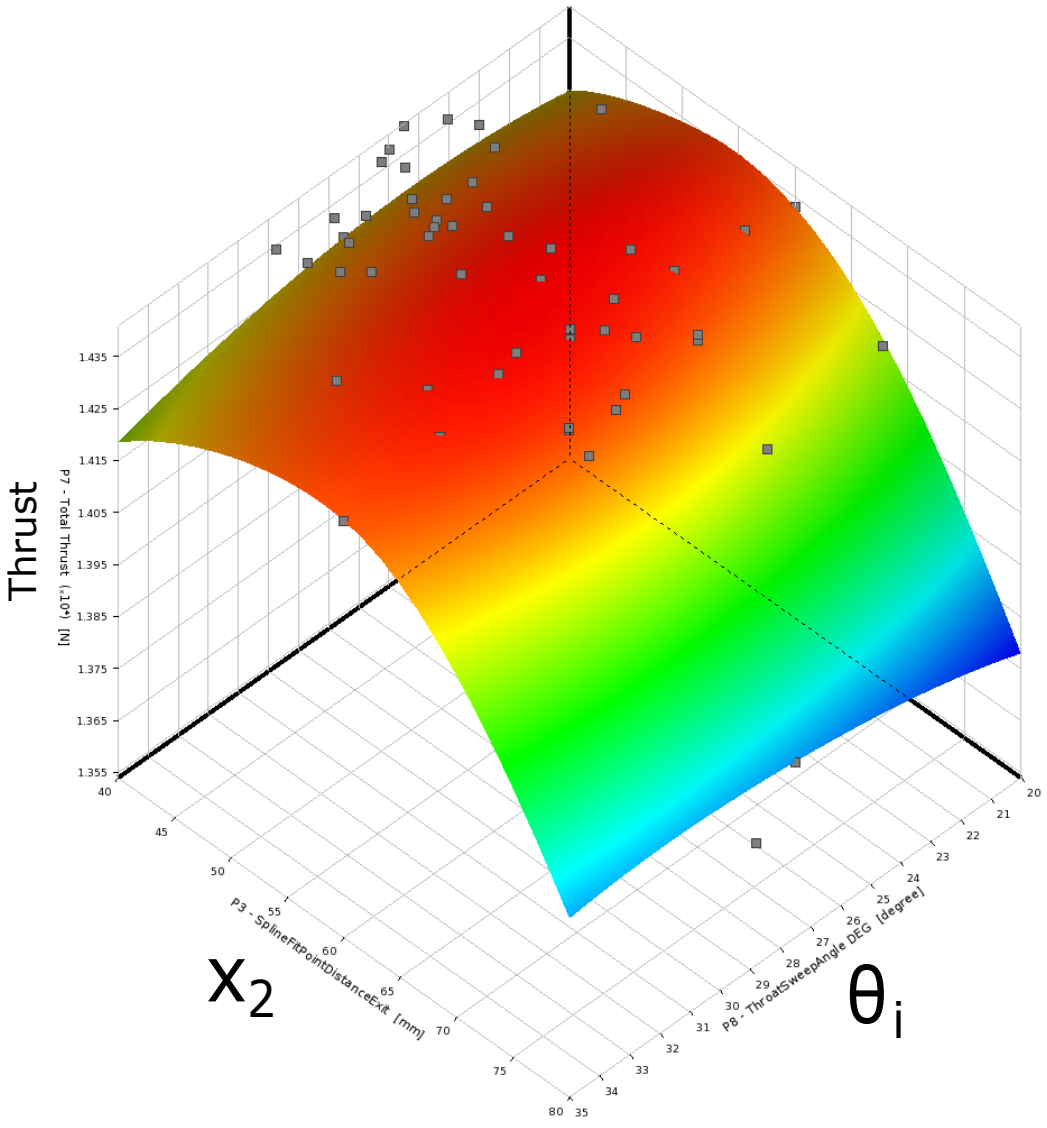

Figure E.6: Case 1 - x_2 vs θ_i Kriging response surface

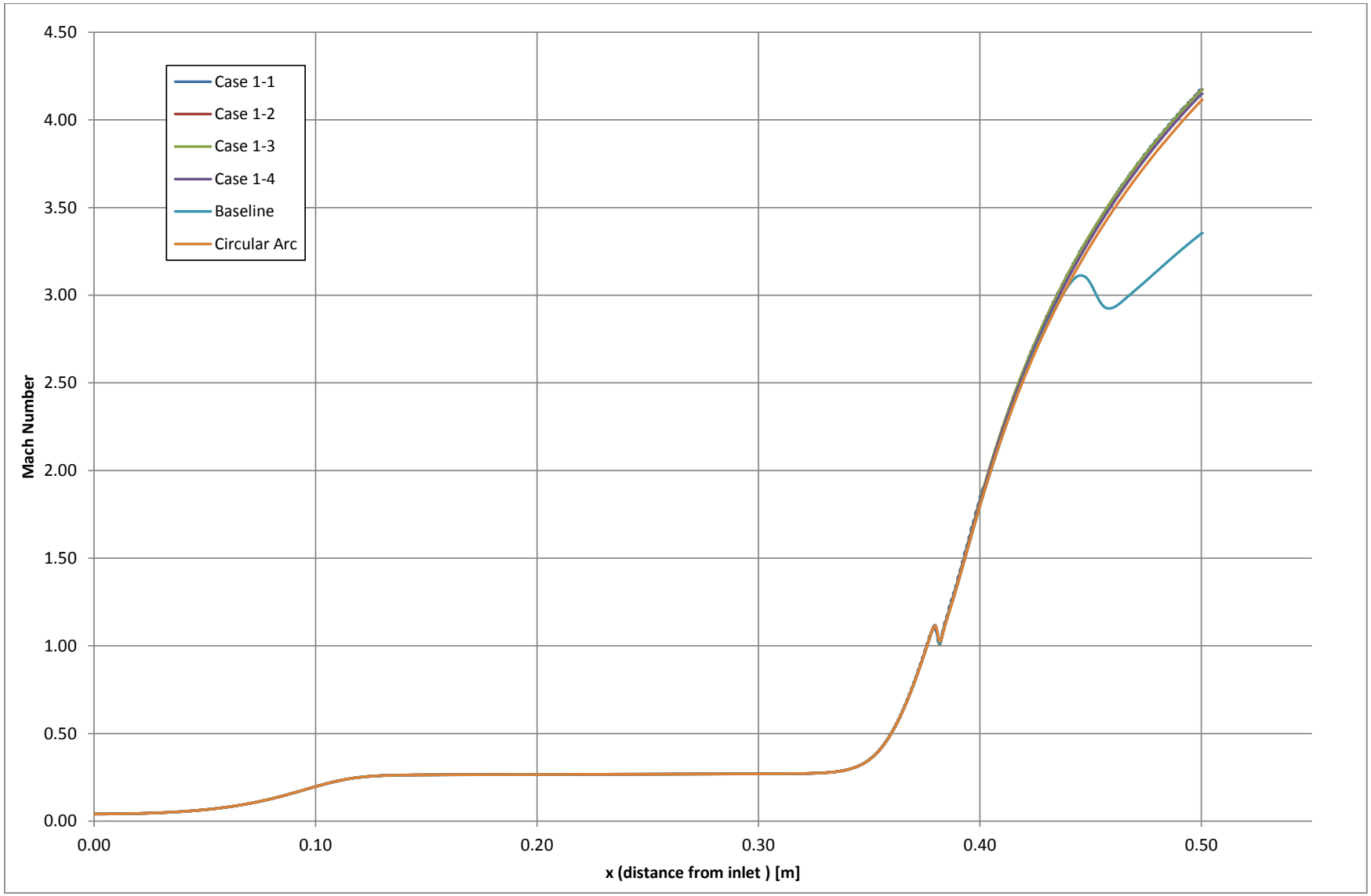

Figure E.7: Case 1 - Centerline Mach numbers

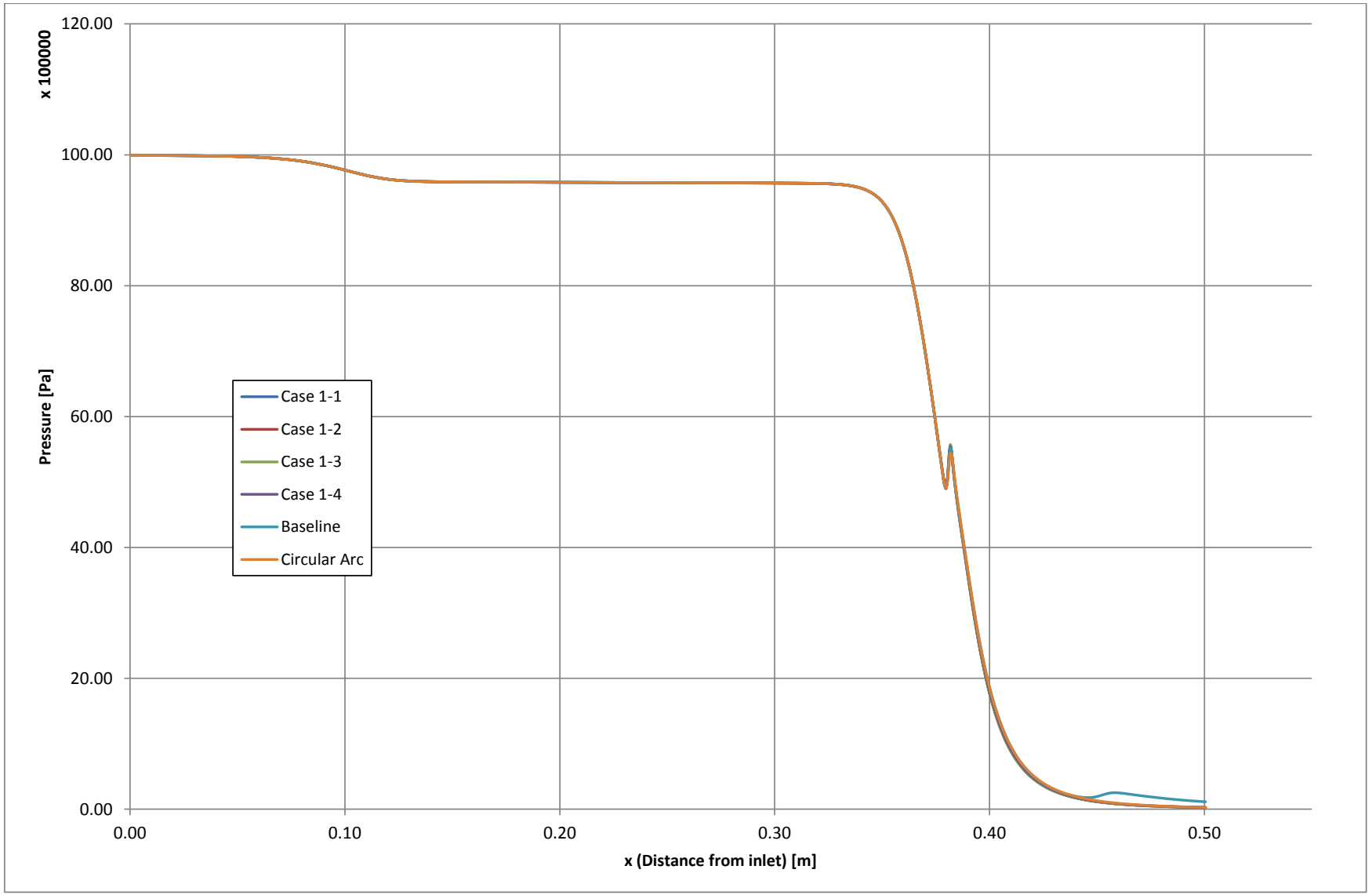

Figure E.8: Case 1 - Centerline pressures

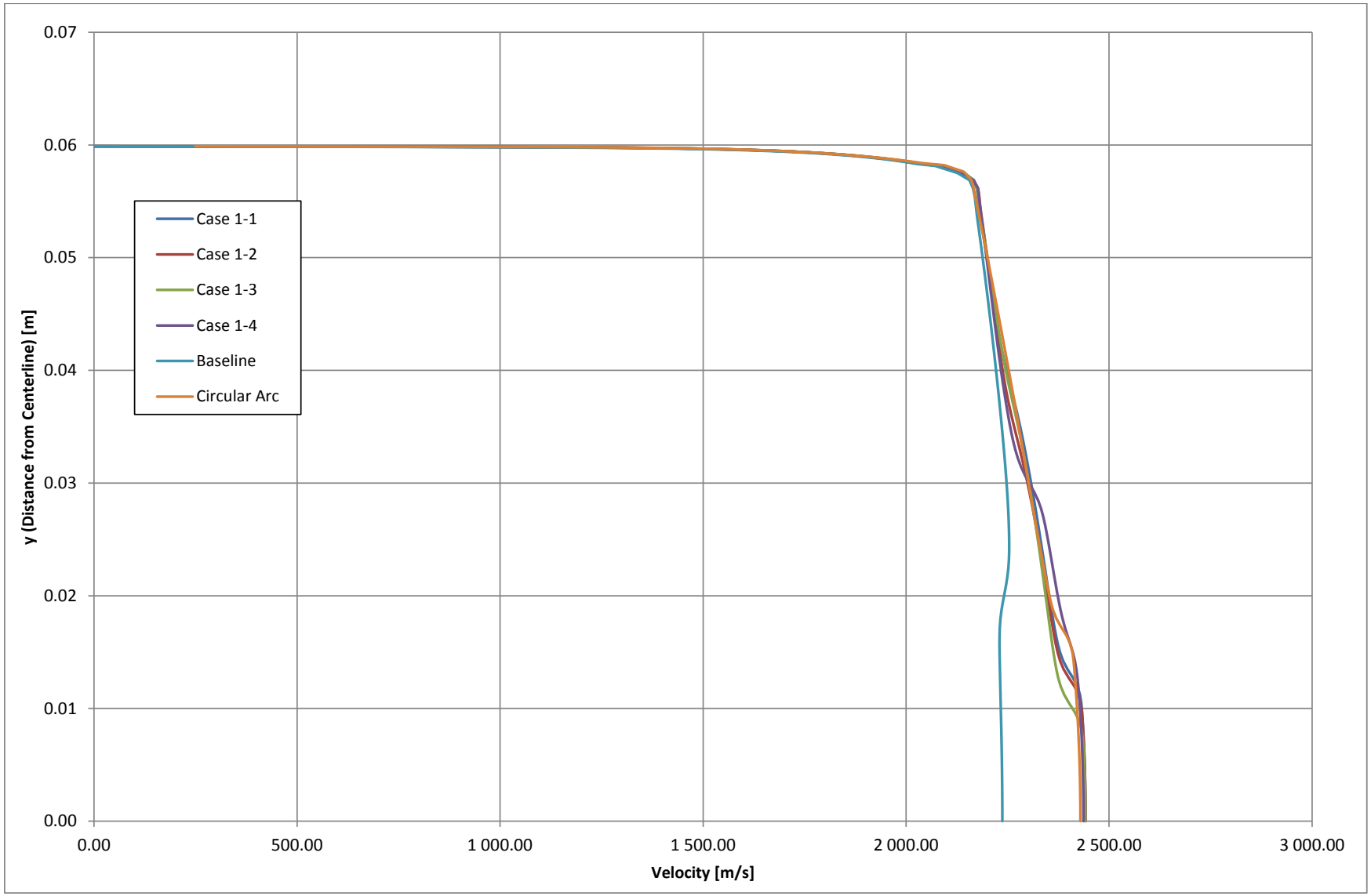

Figure E.9: Case 1 - Exit velocities

Figure E.10: Case 1-1 - Iso Mach numbers

Figure E.11: Case 1-1 - Iso temperatures

Figure E.12: Case 1-1 - Iso pressures

Figure E.13: Case 1-1 - Iso densities

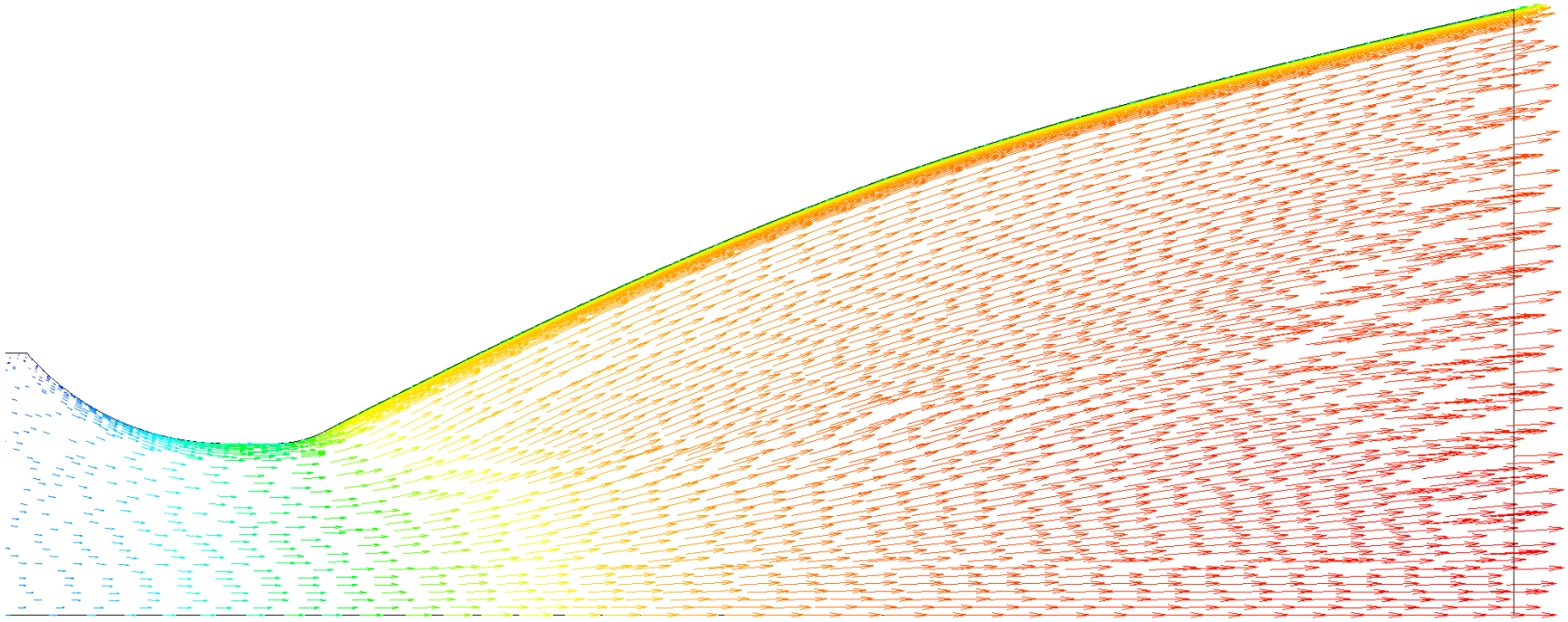

Figure E.14: Case 1-1 - Velocity vectors

Figure E.15: Case 1-2 - Iso Mach numbers

Figure E.16: Case 1-2 - Iso temperatures

Figure E.17: Case 1-2 - Iso pressures

Figure E.18: Case 1-2 - Iso densities

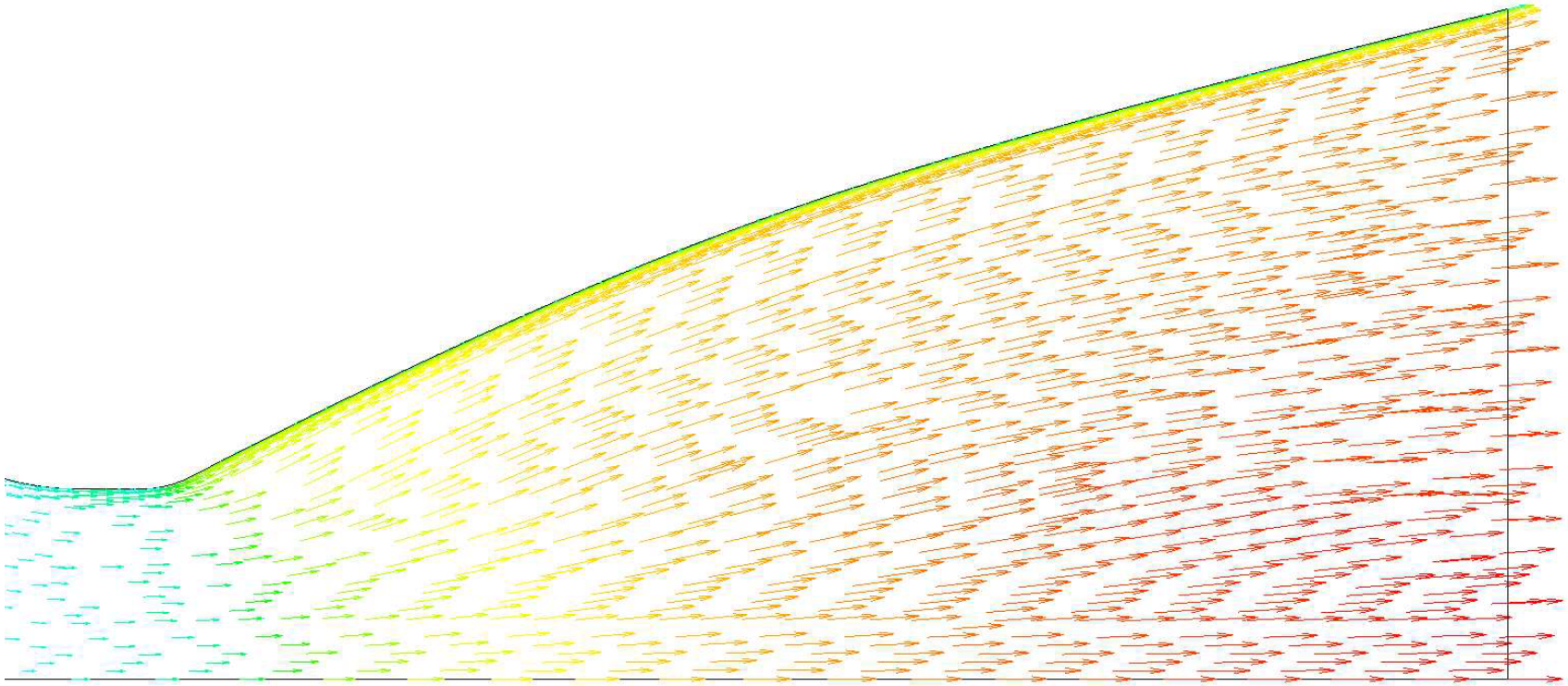

Figure E.19: Case 1-2 - Velocity vectors

Figure E.20: Case 1-3 - Iso Mach numbers

Figure E.21: Case 1-3 - Iso temperatures

Figure E.22: Case 1-3 - Iso pressures

Figure E.23: Case 1-3 - Iso densities

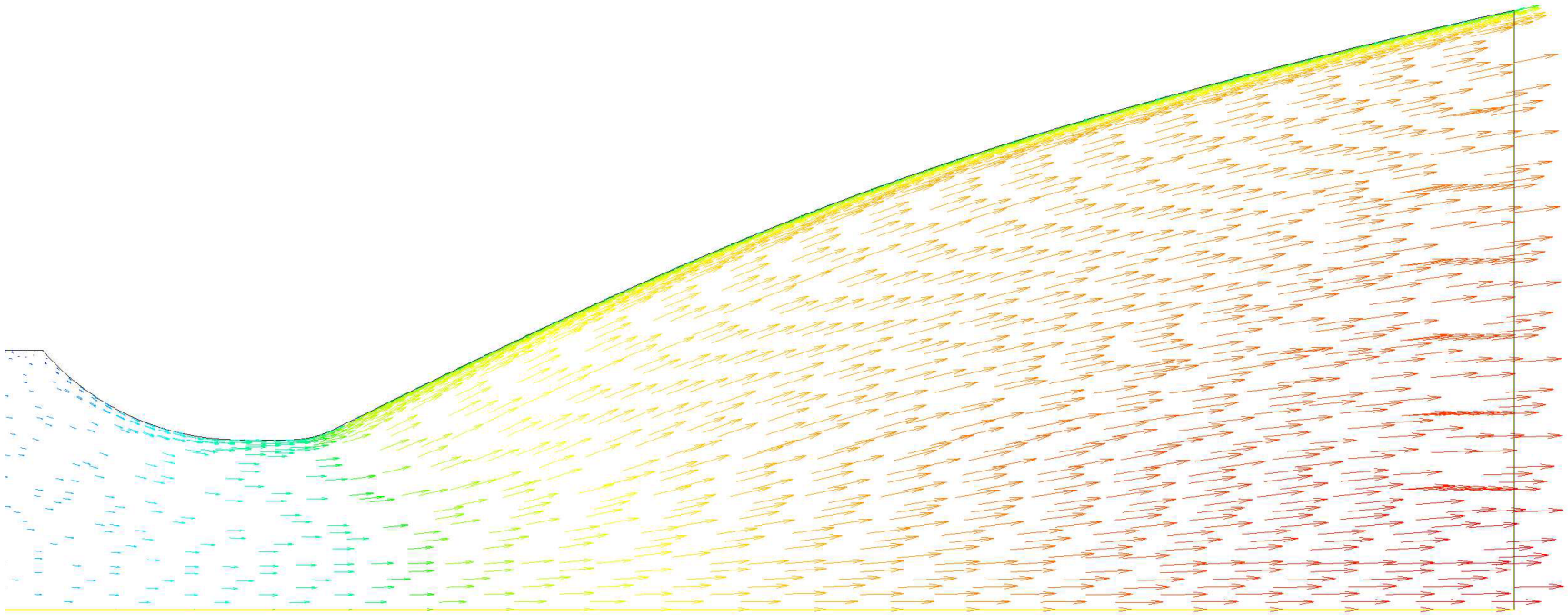

Figure E.24: Case 1-3 - Velocity vectors

Figure E.25: Case 1-4 - Iso Mach numbers

Figure E.26: Case 1-4 - Iso temperatures

Figure E.27: Case 1-4 - Iso pressures

Figure E.28: Case 1-4 - Iso densities

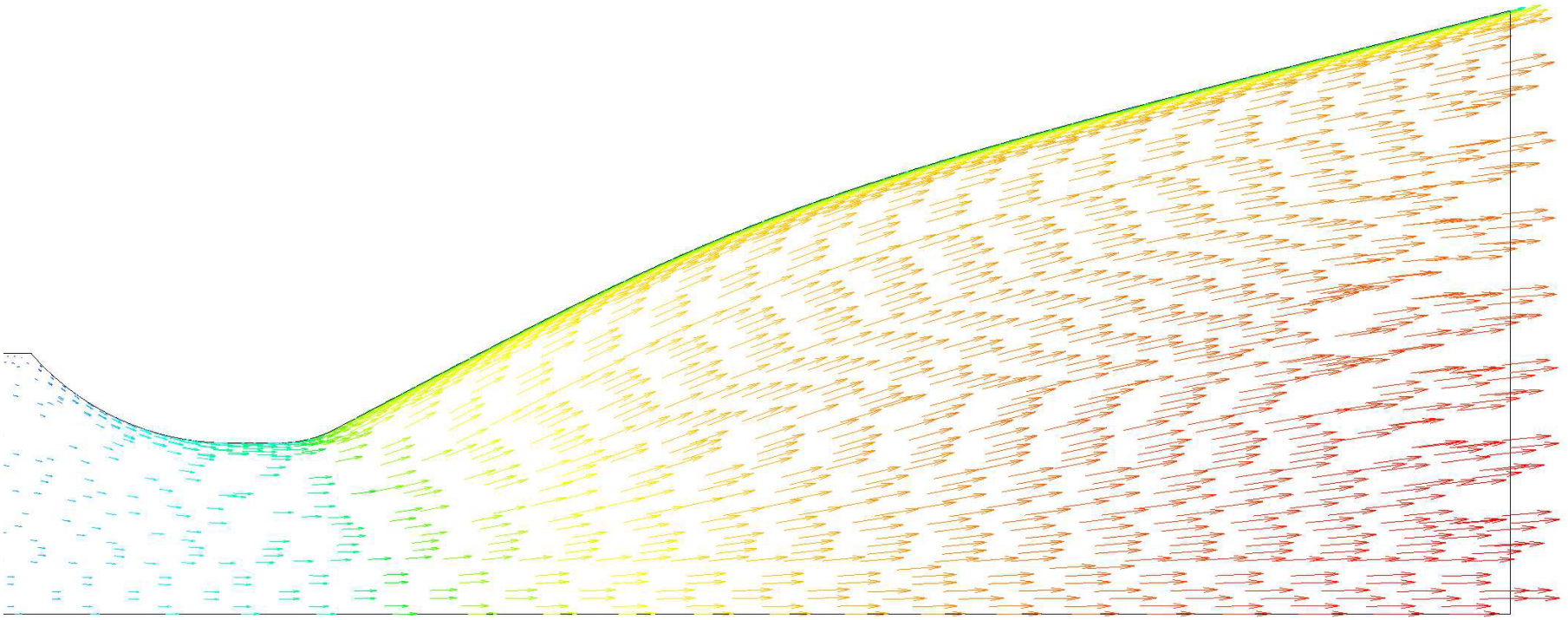

Figure E.29: Case 1-4 - Velocity vectors

APPENDIX F Case 2 - Data

	Input Parameters							Output Parameters	
#	⌜i [mm]	Θi [degree]	R4 @ x4=105[mm]	R3 @ x3=85[mm]	R2 @ x2=55[mm]	R1 @ x1=25[mm]	Θe [degree]	Mass Flow [kg/s]	Total Thrust [N]
1	10.000	25.433	24.367	34.153	45.988	54.656	14.659	-6.50612	14411.9
2	10.000	26.173	24.361	34.319	46.046	54.659	14.680	-6.50528	14409.1
3	10.000	24.485	24.246	33.939	45.893	54.632	14.645	-6.50518	14408.8
4	10.000	25.838	24.244	34.114	45.942	54.563	13.041	-6.5052	14405.9
5	10.000	24.573	24.081	33.695	45.801	54.625	13.044	-6.50586	14405.7
6	10.000	23.924	23.942	33.579	45.744	54.656	13.050	-6.50529	14402.4
7	10.000	28.080	24.766	33.680	45.564	54.594	11.456	-6.50602	14401.8
8	10.384	22.945	23.739	33.586	45.668	54.641	12.990	-6.50626	14400.9
9	10.000	23.163	23.789	33.553	45.700	54.677	13.061	-6.50565	14400.8
10	12.292	23.157	23.865	33.599	45.492	54.288	12.602	-6.50606	14399
11	11.965	23.055	23.785	33.647	45.493	54.355	12.670	-6.50567	14398.9
12	12.434	22.694	23.940	33.681	45.720	54.515	12.568	-6.50615	14398.5
13	11.161	22.993	23.733	33.634	45.607	54.540	12.835	-6.5059	14397.9
14	11.668	23.030	23.753	33.655	45.544	54.438	12.731	-6.50517	14397.2
15	12.389	23.968	23.947	33.673	45.732	54.504	12.589	-6.50523	14397.1
16	12.114	23.080	23.817	33.626	45.471	54.309	12.638	-6.50518	14396.9
17	12.445	23.183	23.961	33.736	45.717	54.495	12.600	-6.50525	14396.9
18	10.000	31.914	25.036	34.434	46.080	54.785	9.902	-6.50625	14396.5
19	12.455	22.505	23.907	33.660	45.746	54.520	12.550	-6.50527	14395.7
20	12.427	22.126	23.895	33.567	45.694	54.500	12.551	-6.50528	14395.7
21	12.383	22.240	23.872	33.641	45.782	54.517	12.570	-6.50522	14395.5
22	12.844	21.478	23.876	33.902	45.987	54.233	13.012	-6.50571	14395.1
23	12.843	22.468	23.900	33.388	45.568	54.459	12.660	-6.50539	14394.6
24	13.465	24.018	23.714	33.245	45.402	54.295	12.371	-6.50581	14394.1
25	13.824	23.665	23.888	33.916	46.002	54.408	12.563	-6.50592	14393.7
26	13.465	24.018	23.714	33.245	45.402	54.295	12.371	-6.50588	14393.7
27	13.118	22.526	23.913	33.151	45.500	54.412	12.832	-6.50579	14393.3
28	13.465	24.018	23.714	33.245	45.402	54.295	12.371	-6.50518	14392.6
29	12.694	21.962	24.011	33.176	45.629	54.433	12.824	-6.50529	14392
30	12.806	22.216	24.077	33.144	45.684	54.466	12.793	-6.50583	14391.6
31	11.164	18.000	23.649	33.615	45.530	54.430	13.764	-6.50596	14390.7
32	14.365	21.030	23.109	32.669	44.976	54.120	14.264	-6.50578	14386.4
33	14.365	21.030	23.109	32.669	44.976	54.120	14.264	-6.50562	14385.8
34	14.365	21.030	23.109	32.669	44.976	54.120	14.264	-6.50519	14384.8
35	14.365	21.030	23.109	32.669	44.976	54.120	14.264	-6.50513	14384.5
36	18.077	18.000	23.149	32.875	45.209	54.340	14.661	-6.50524	14376
37	20.000	18.321	22.960	32.501	44.931	54.304	14.542	-6.50537	14371.2
38	15.425	25.994	24.744	34.946	46.472	54.411	9.811	-6.50514	14370.3
39	20.000	18.639	22.776	32.268	44.769	54.231	13.502	-6.50561	14368.8
40	18.775	30.144	23.828	33.112	43.714	54.182	14.995	-6.5054	14367.9
41	10.346	30.136	24.500	33.000	44.000	55.000	12.000	-6.50534	14365.1
42	12.142	31.005	24.500	33.000	44.000	55.000	12.000	-6.50694	14364.6
43	15.000	26.500	23.340	33.000	44.000	55.000	13.423	-6.5057	14362.9
44	11.104	33.268	24.500	33.000	44.000	55.000	12.000	-6.50655	14360
45	13.165	22.026	23.378	32.340	42.485	52.221	15.346	-6.50531	14358.1
46	16.325	20.017	24.086	35.358	46.046	54.237	11.704	-6.50525	14356
47	15.000	26.500	23.291	32.605	44.000	55.000	12.000	-6.50536	14355.7
48	15.000	26.500	24.500	33.000	46.603	54.745	12.000	-6.50574	14355.2
49	13.389	34.081	24.500	33.000	44.000	55.000	12.000	-6.50578	14354.9
50	17.875	31.340	24.433	32.701	45.057	54.357	13.101	-6.50507	14354.4
51	15.000	26.500	23.858	33.000	44.000	55.000	9.365	-6.50599	14354.1
52	12.254	23.505	24.500	33.000	44.000	55.000	12.000	-6.50542	14353.8
53	15.000	26.500	22.822	33.000	44.000	55.000	16.580	-6.50623	14347.6
54	11.785	23.122	25.327	34.013	46.319	55.195	8.693	-6.5058	14346.2
55	15.255	18.000	23.126	34.073	46.235	55.438	7.708	-6.50656	14345.3
56	12.265	22.723	22.639	32.038	42.911	53.795	13.453	-6.50524	14343
57	15.000	26.500	24.500	35.315	44.725	55.000	12.000	-6.50613	14341.9
58	15.000	26.500	24.500	32.993	47.060	55.000	12.000	-6.50502	14341.5
59	10.826	19.307	24.500	33.000	44.000	55.000	12.000	-6.50608	14341.2
60	15.000	26.500	24.500	36.700	47.621	55.000	12.000	-6.50598	14337.6
61	17.429	34.251	24.500	33.000	44.000	55.000	12.000	-6.50532	14335.1
62	11.365	19.137	22.975	31.626	44.255	55.369	10.478	-6.5058	14331
63	15.000	26.500	24.500	33.000	43.322	51.751	12.000	-6.50505	14330.4
64	15.000	26.500	24.506	33.000	44.000	55.000	7.106	-6.50615	14329.2
65	15.000	26.500	24.512	33.000	44.000	55.000	7.100	-6.50619	14328.9
66	12.405	19.005	22.079	31.297	43.905	54.203	16.825	-6.50597	14327.1
67	13.562	19.047	24.500	33.000	44.000	55.000	12.000	-6.50532	14321.3
68	14.336	23.607	23.462	32.648	45.664	56.149	6.000	-6.5052	14319.3
69	15.000	26.500	23.545	34.585	44.000	55.000	12.000	-6.50549	14318.8
70	12.565	18.042	22.706	32.834	46.745	56.069	9.396	-6.50609	14315.2
71	19.015	25.341	24.500	33.000	44.000	55.000	12.000	-6.50526	14312.7
72	15.000	26.500	22.332	33.000	44.000	55.000	17.674	-6.50545	14311.2
73	15.000	26.500	24.500	33.000	47.793	55.882	12.000	-6.50552	14309.9
74	18.765	21.644	22.428	29.779	42.791	52.754	13.904	-6.50528	14305.5
75	16.781	19.258	24.500	33.000	44.000	55.000	12.000	-6.50528	14300.4
76	15.000	26.500	24.500	33.639	48.716	55.000	12.000	-6.50672	14297.7

Figure F.1: Case 2 - Design table - Page 1/2

77	15.000	26.500	22.002	33.000	44.000	55.000	13.528	-6.50549	14273.2
78	15.000	18.000	21.960	29.240	40.780	51.580	18.000	-6.50514	14267.2
79	15.000	26.500	22.061	33.000	44.000	55.000	7.415	-6.50617	14255.9
80	15.000	26.500	21.759	31.774	44.000	55.000	12.000	-6.5055	14255.8
81	15.000	26.500	22.191	33.937	44.000	55.000	12.000	-6.50521	14247.7
82	15.000	26.500	25.008	36.053	44.000	55.000	12.000	-6.50511	14247.7
83	15.000	26.500	23.625	29.993	44.000	55.000	12.000	-6.50521	14245.5
84	15.000	26.500	24.500	33.000	43.849	57.244	12.000	-6.50627	14209.7
85	15.000	26.500	25.883	33.000	44.000	55.000	6.782	-6.50646	14191.9
86	15.000	26.500	21.687	29.157	44.000	55.000	12.000	-6.50506	14161.9
87	15.000	26.500	24.500	30.051	43.042	55.000	12.000	-6.50559	14151.7
88	15.000	26.500	21.523	29.155	44.000	55.000	12.000	-6.50519	14145.8
89	15.000	26.500	24.500	31.819	40.423	55.000	12.000	-6.50534	14137.1
90	15.000	26.500	26.004	32.120	44.000	55.000	12.000	-6.5052	14130
91	15.000	26.500	24.500	33.000	39.629	52.516	12.000	-6.50589	14127.5
92	15.000	26.500	26.505	33.000	44.000	55.000	16.410	-6.50557	14117.2
93	15.000	26.500	24.500	33.000	42.503	57.697	12.000	-6.51027	14077.7
94	10.403	32.930	22.489	28.256	39.168	51.568	16.677	-6.50571	14058.5
95	15.000	26.500	24.500	33.000	48.684	59.099	12.000	-6.50857	14016
96	15.000	26.500	24.500	33.000	48.528	51.270	12.000	-6.50507	13933.7
97	15.000	26.500	24.500	33.000	49.263	52.031	12.000	-6.50563	13933.6
98	15.000	26.500	24.500	37.260	42.208	55.000	12.000	-6.50554	13835.7
99	15.000	26.500	27.231	30.272	44.000	55.000	12.000	-6.50529	13729.5
100	19.211	33.902	22.296	30.033	47.979	50.074	16.451	-6.50536	13659.5
101	10.373	19.062	21.331	37.394	49.213	59.905	15.659	-6.51124	13642.5
102	10.939	18.837	27.055	29.385	40.159	51.797	17.799	-6.5052	13542.1
103	10.904	19.229	27.923	36.051	39.685	51.039	7.038	-6.50661	13501.9
104	11.632	33.639	28.000	38.000	44.000	60.000	18.000	-6.50506	13407.5
105	13.634	27.062	28.000	38.000	44.000	60.000	18.000	-6.50615	13340.1
106	15.647	33.616	28.000	38.000	44.000	60.000	18.000	-6.51149	13304.7
107	18.523	20.230	27.063	29.266	48.273	50.895	17.661	-6.50553	13278.1
108	11.296	18.897	21.254	37.526	40.673	50.668	17.447	-6.50519	13248.3
109	19.539	31.597	28.000	38.000	44.000	60.000	18.000	-6.51278	13235.6
110	10.631	34.411	22.049	28.249	49.610	51.966	7.454	-6.5054	13187.1
111	10.113	34.608	21.575	35.669	38.631	57.791	17.191	-6.51231	13003.6
112	19.331	18.771	21.093	37.936	38.730	59.934	17.987	-6.51023	12230.3

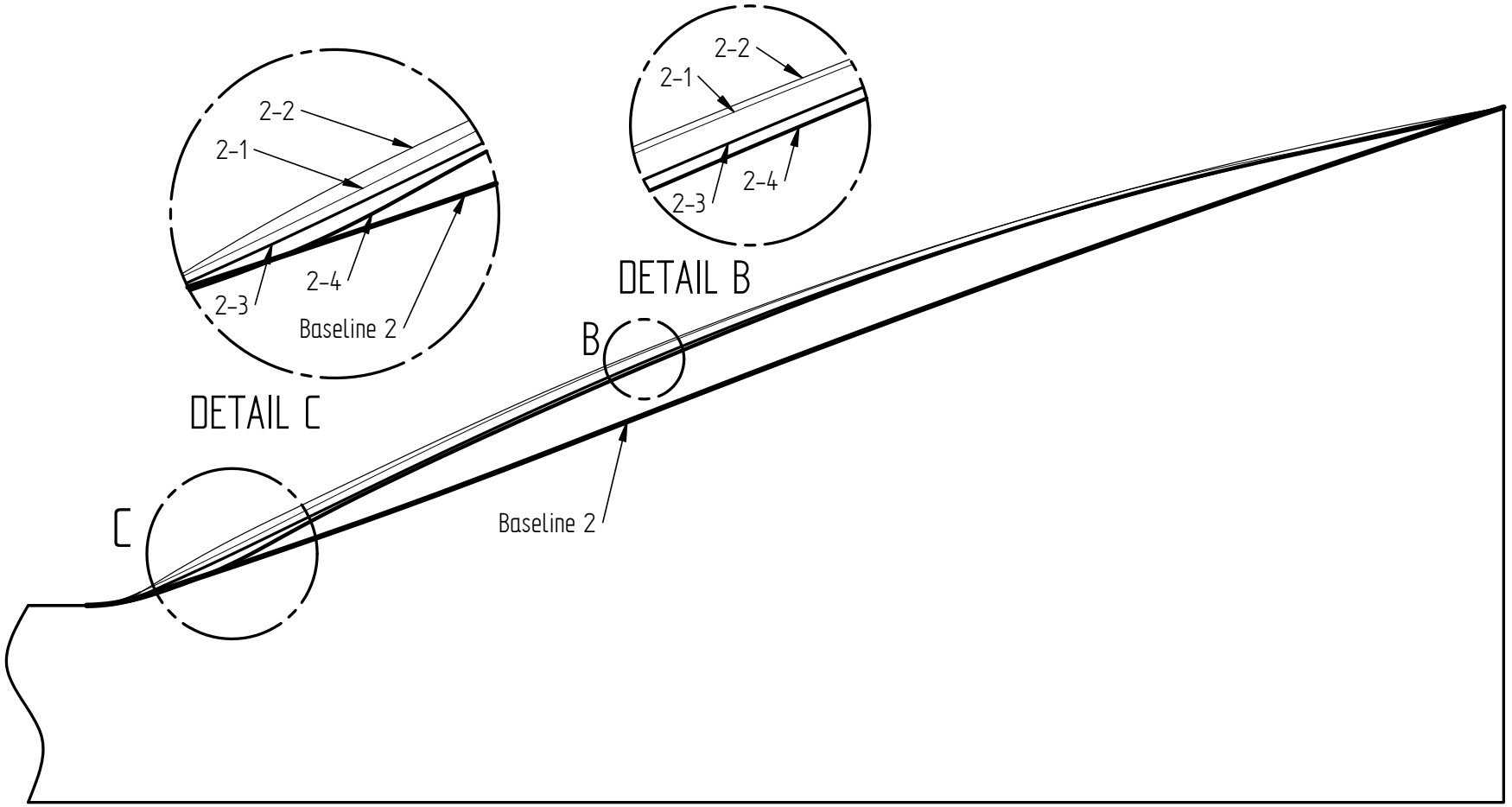

Figure F.2: Case 2 - Geometry comparison

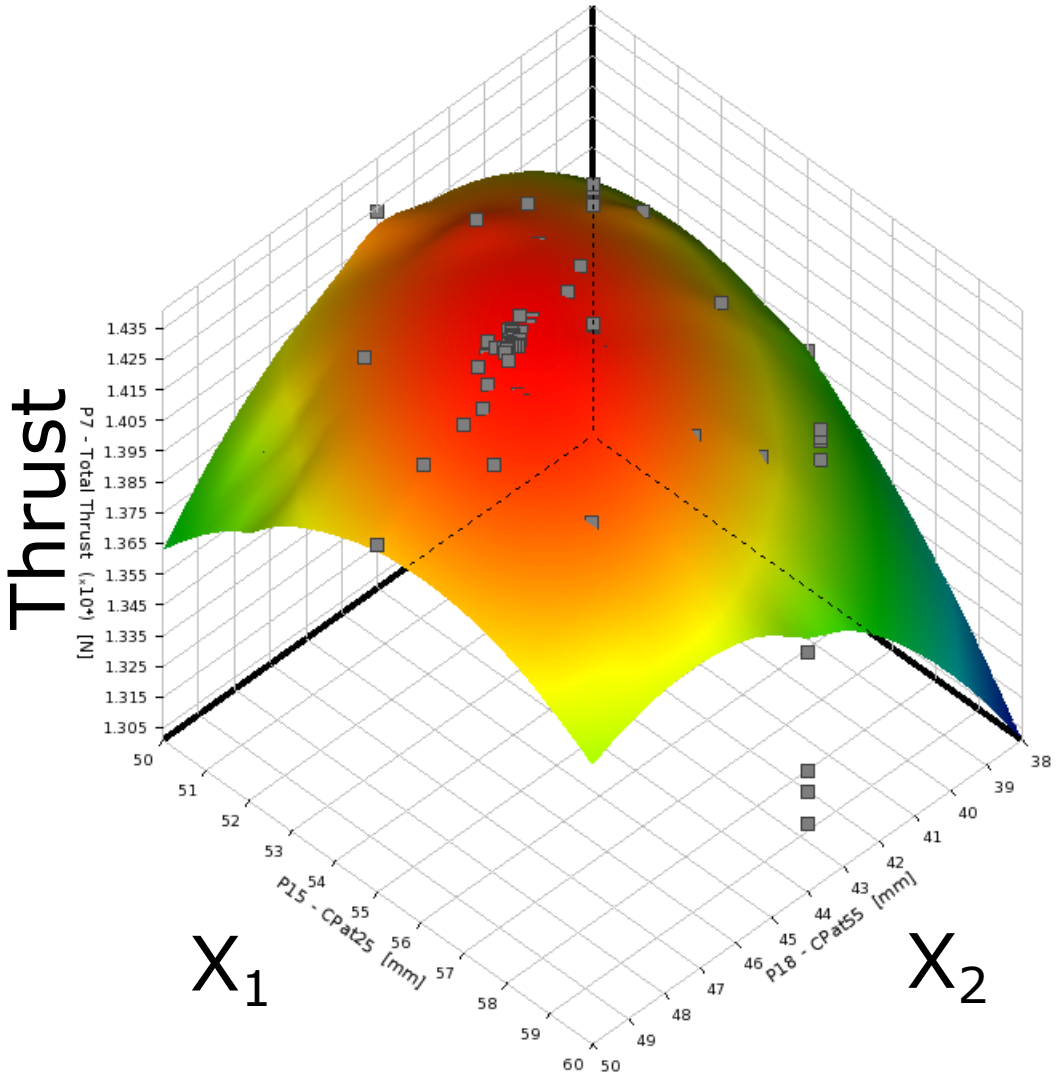

Figure F.3: Case 2 - x_1 vs x_2 Kriging response surface

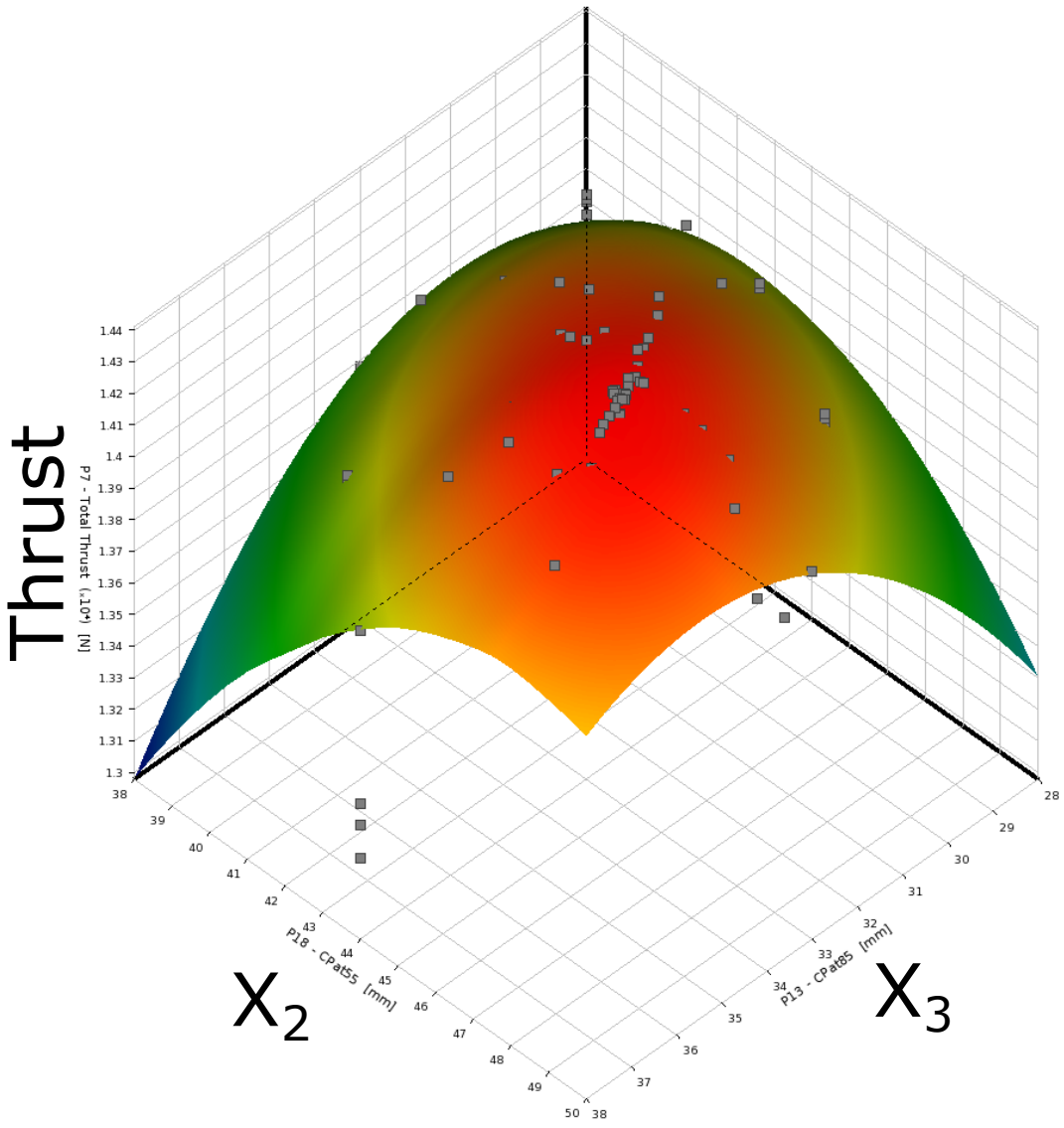

Figure F.4: Case 2 - x_2 vs x_3 Kriging response surface

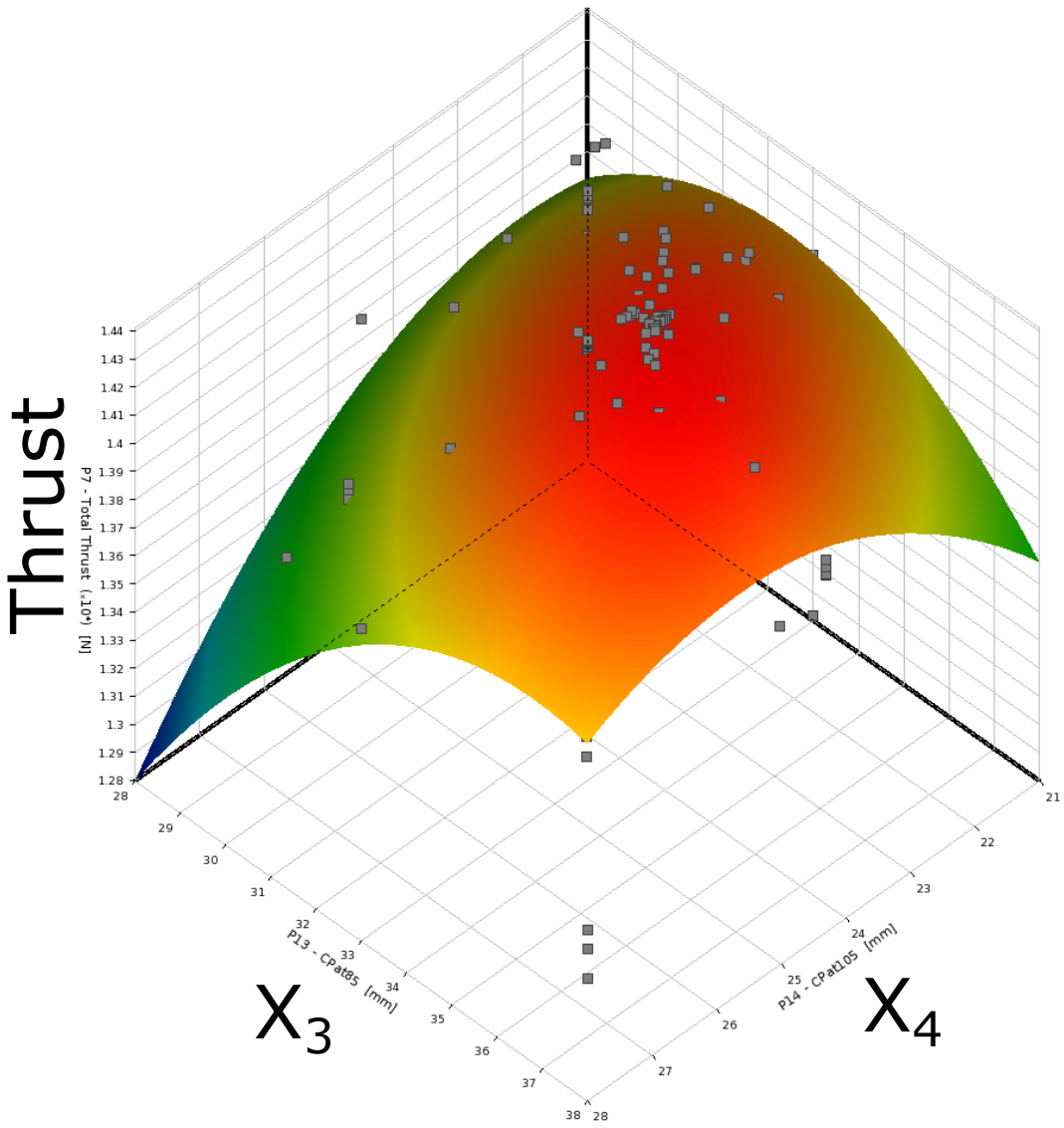

Figure F.5: Case 2 - x_3 vs x_4 Kriging response surface

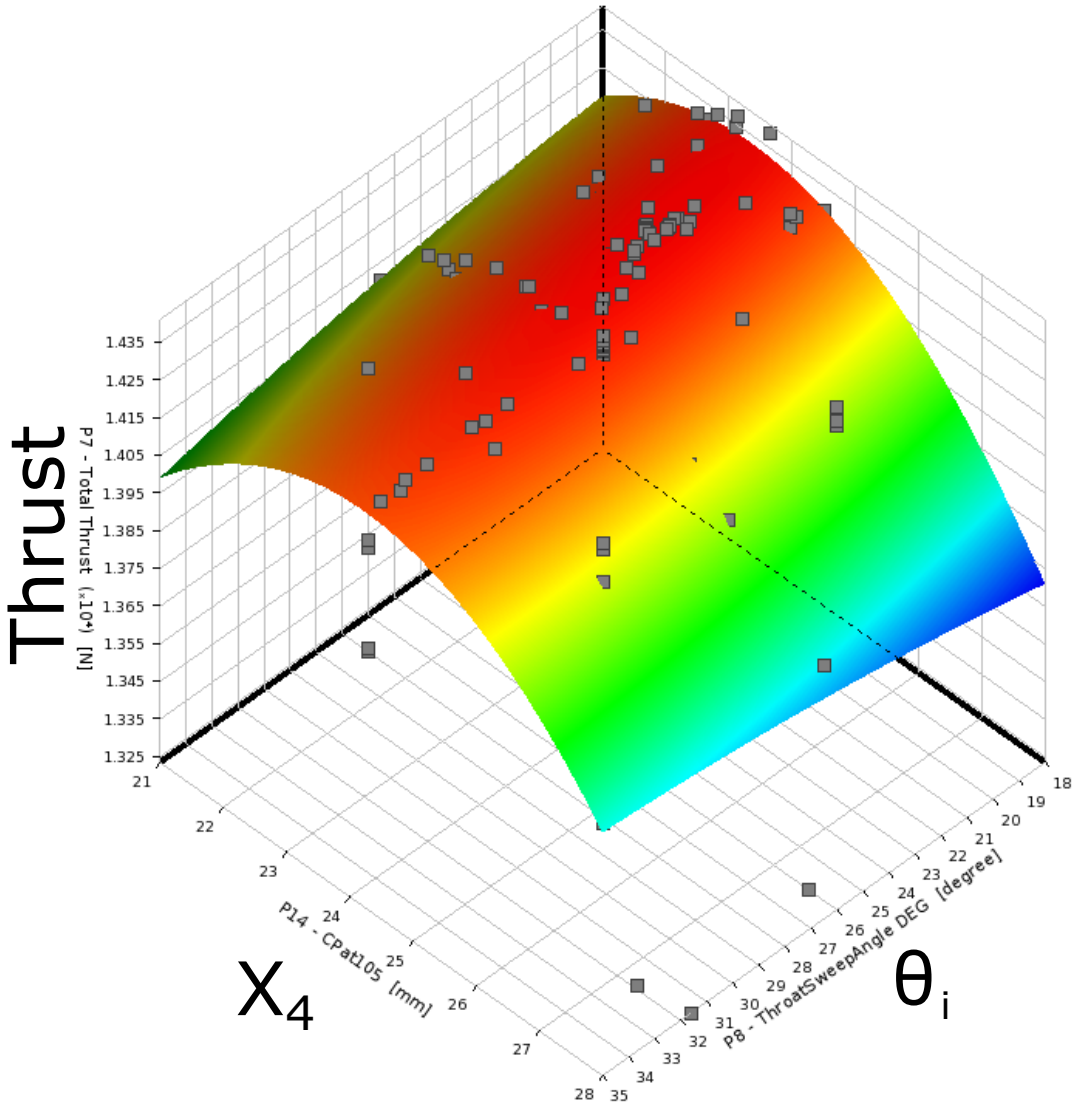

Figure F.6: Case 2 - x_4 vs A_i Kriging response surface

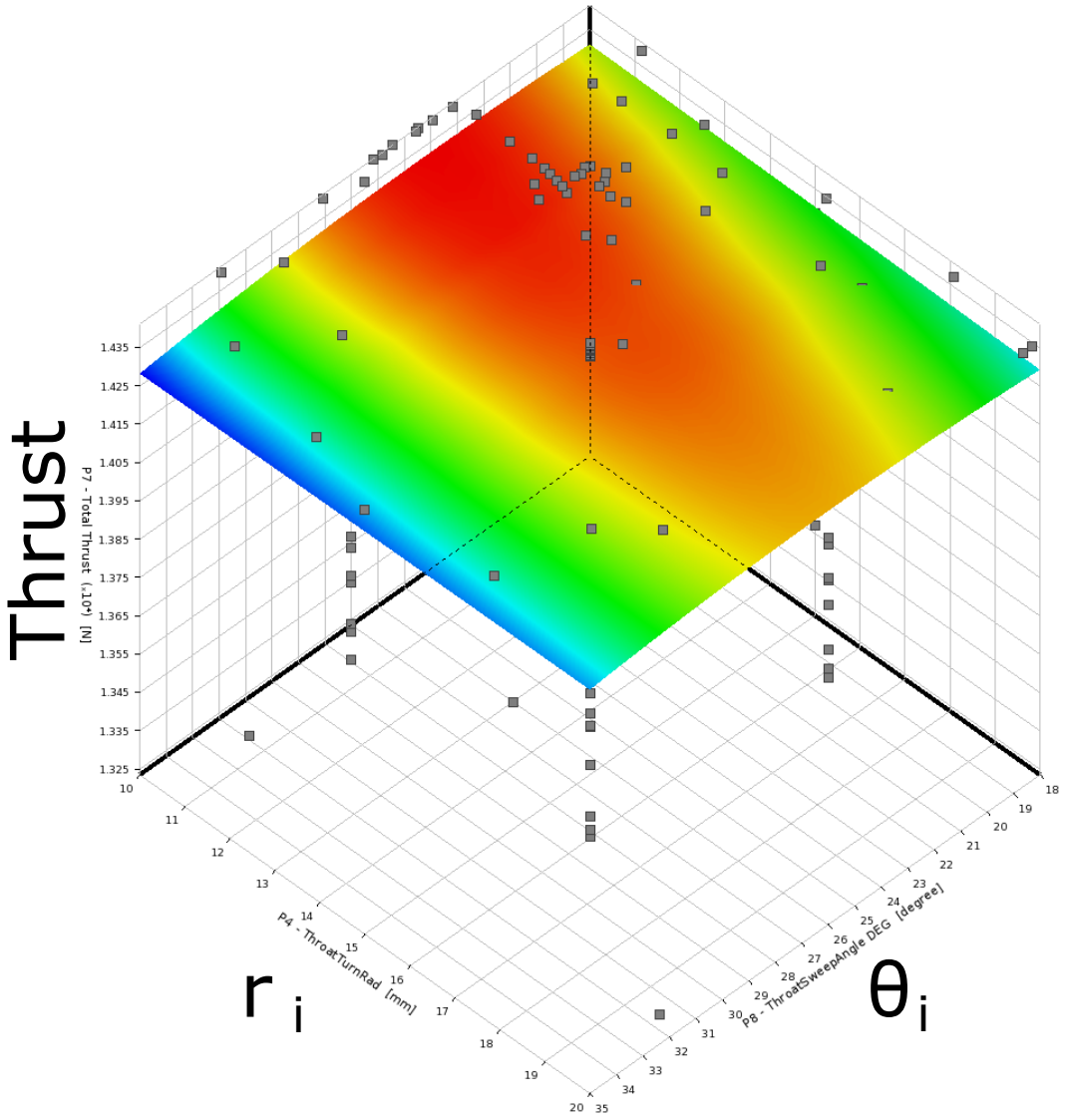

Figure F.7: Case 2 - r_i vs θ_i Kriging response surface

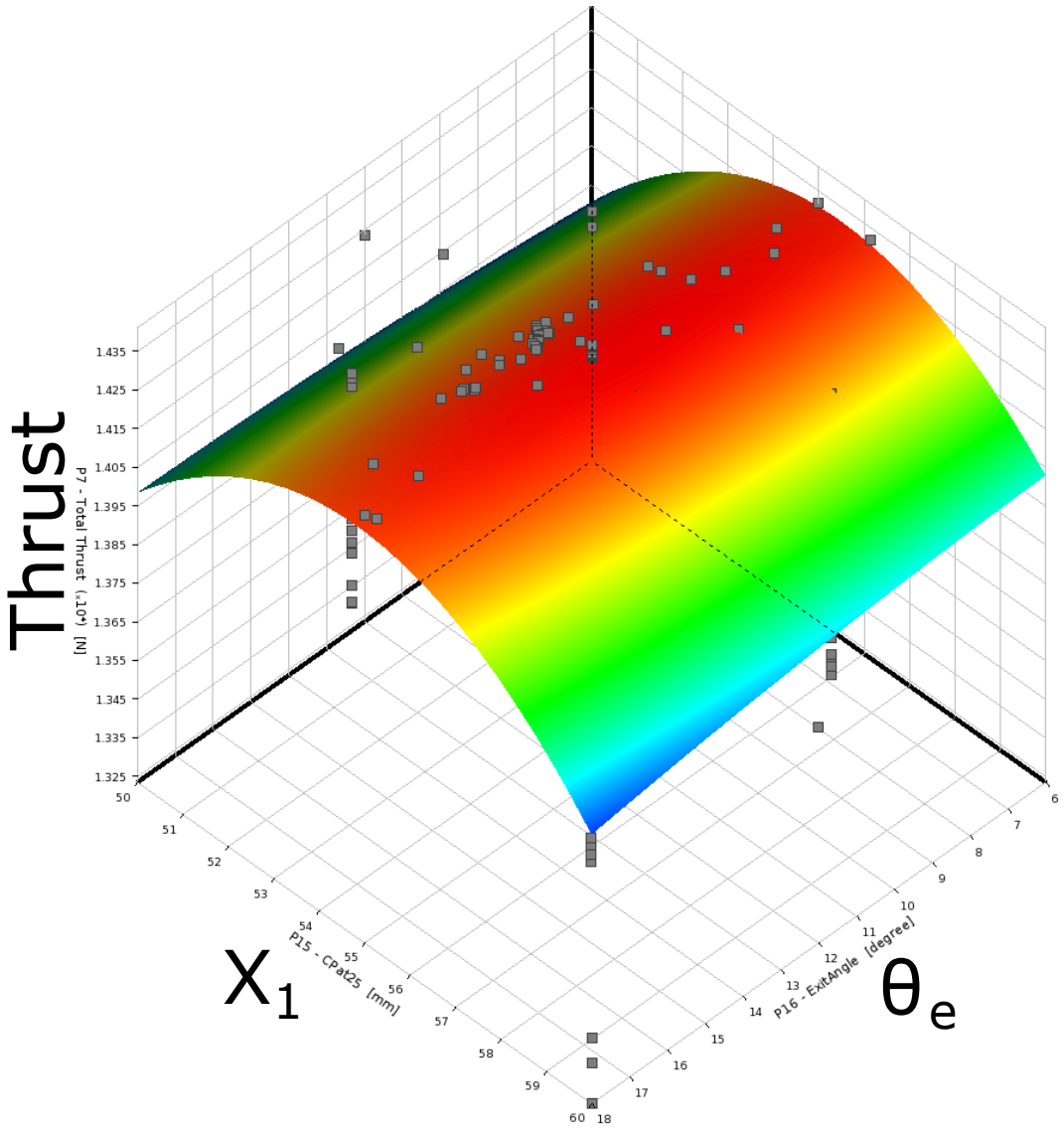

Figure F.8: Case 2 - x_1 vs θ_e Kriging response surface

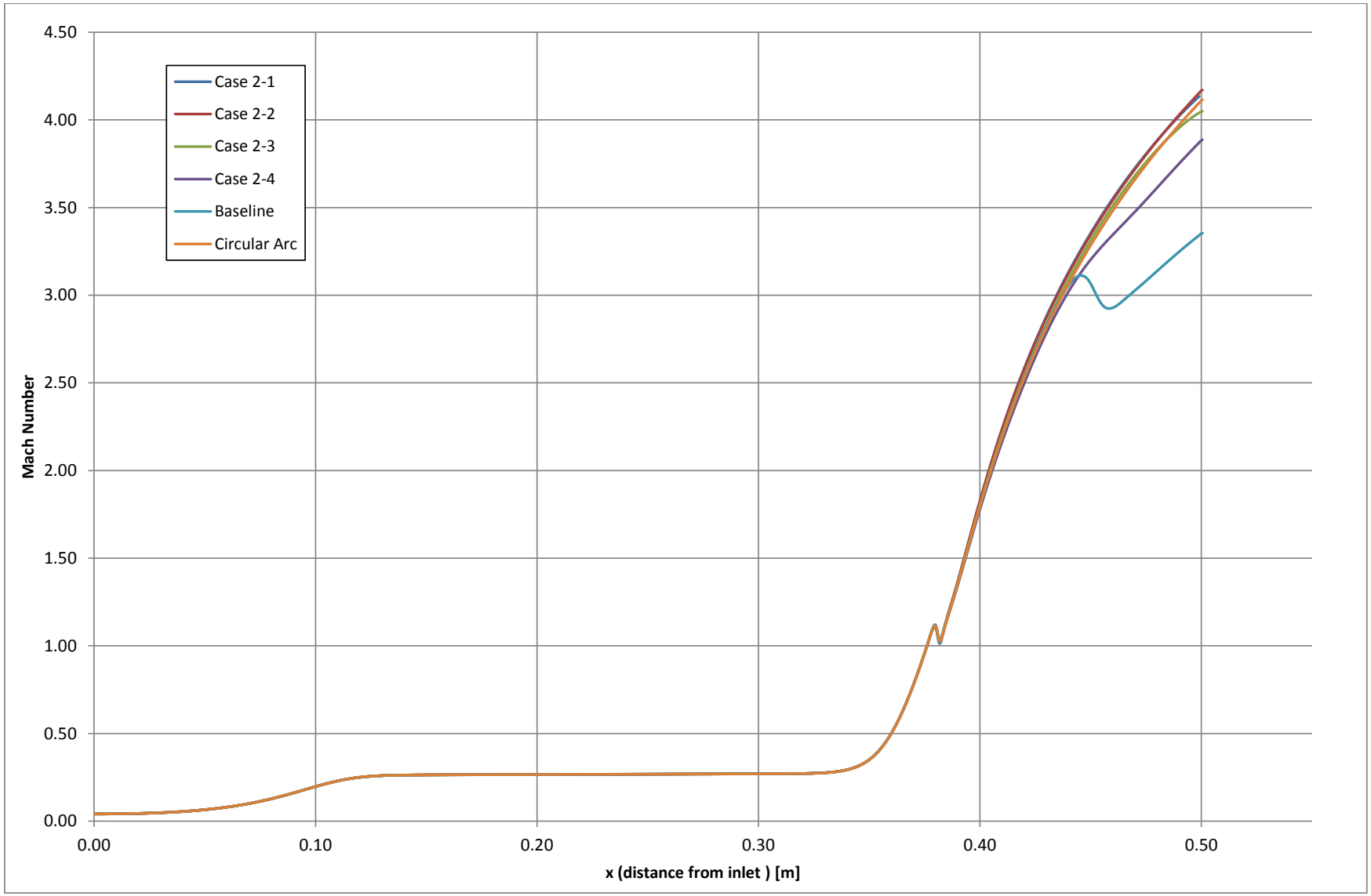

Figure F.9: Case 2 - Centerline Mach numbers

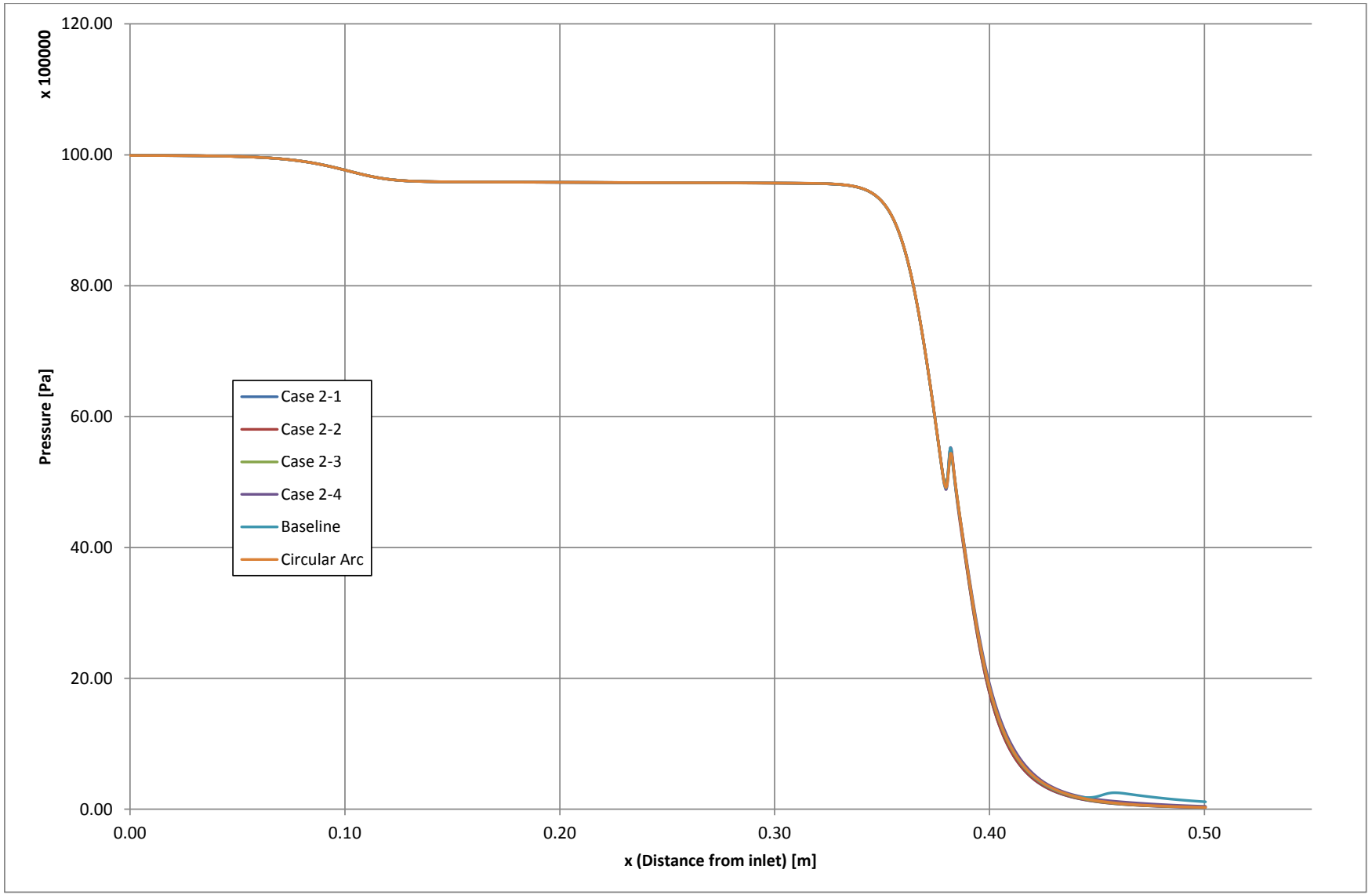

Figure F.10: Case 2 - Centerline pressures

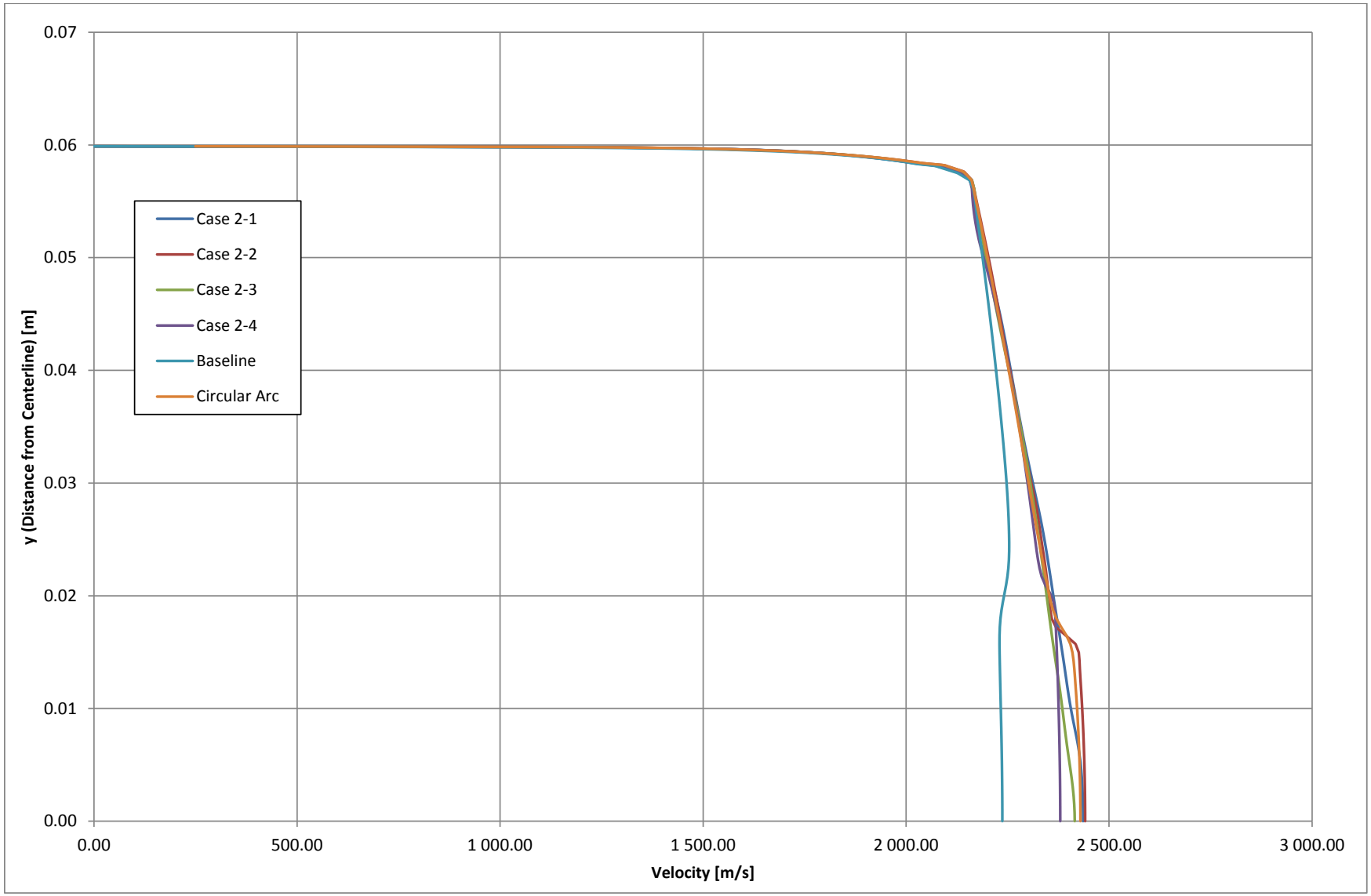

Figure F.11: Case 2 - Exit velocities

Figure F.12: Case 2-1 - Iso Mach numbers

Figure F.13: Case 2-1 - Iso temperatures

Figure F.14: Case 2-1 - Iso pressures

Figure F.15: Case 2-1 - Iso densities

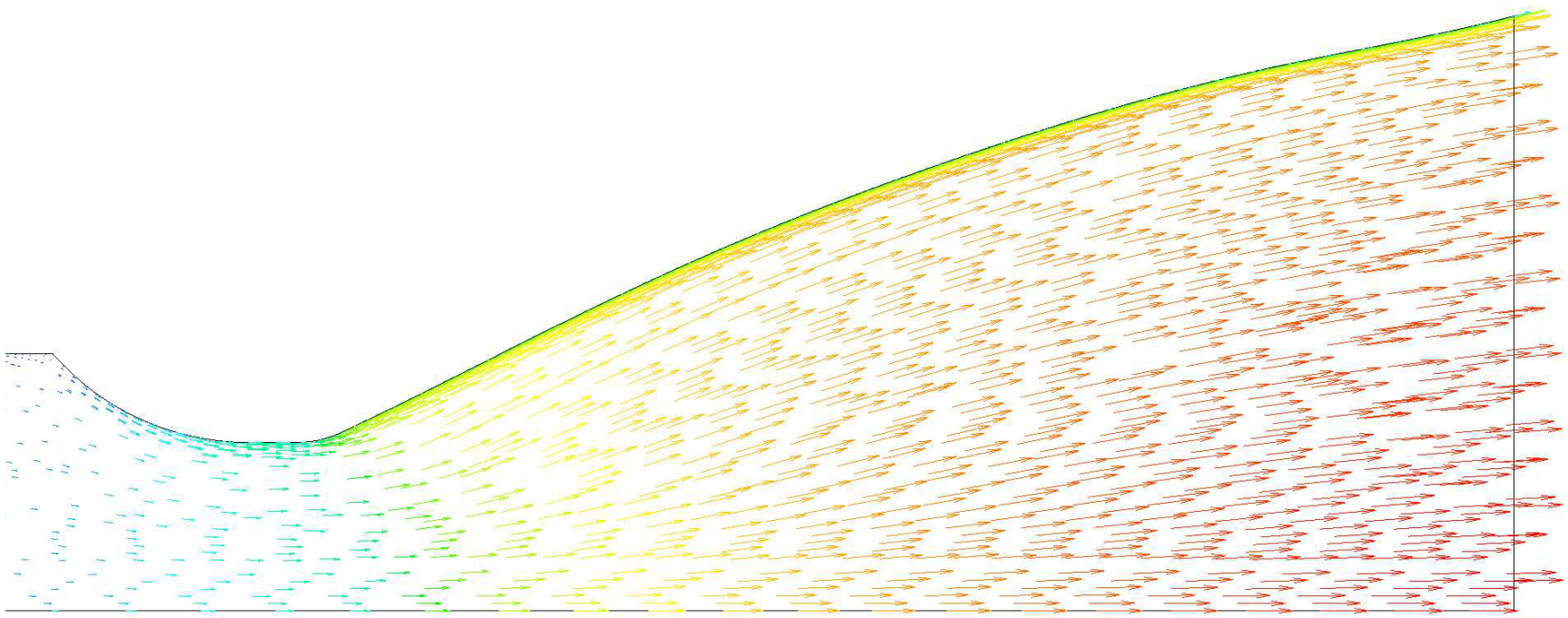

Figure F.16: Case 2-1 - Velocity vectors

Figure F.17: Case 2-2 - Iso Mach numbers

Figure F.18: Case 2-2 - Iso temperatures

Figure F.19: Case 2-2 - Iso pressures

Figure F.20: Case 2-2 - Iso densities

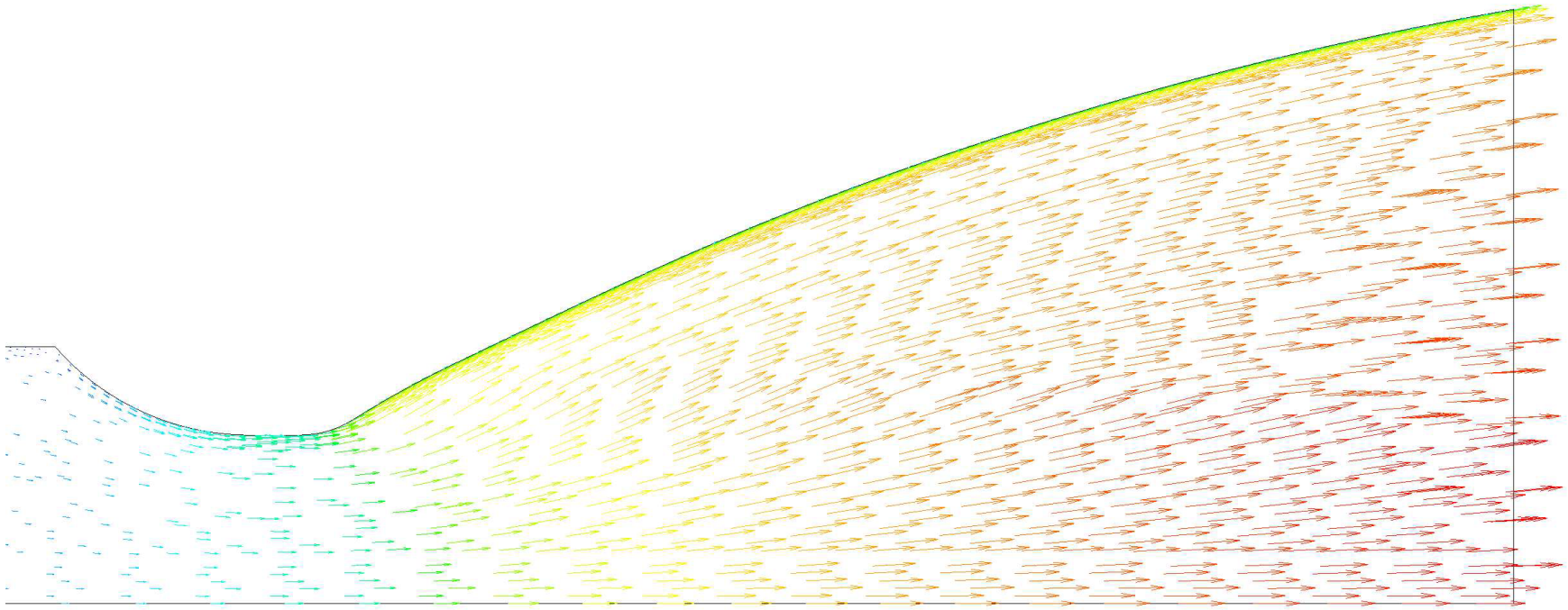

Figure F.21: Case 2-2 - Velocity vectors

Figure F.22: Case 2-3 - Iso Mach numbers

Figure F.23: Case 2-3 - Iso temperatures

Figure F.24: Case 2-3 - Iso pressures

Figure F.25: Case 2-3 - Iso densities

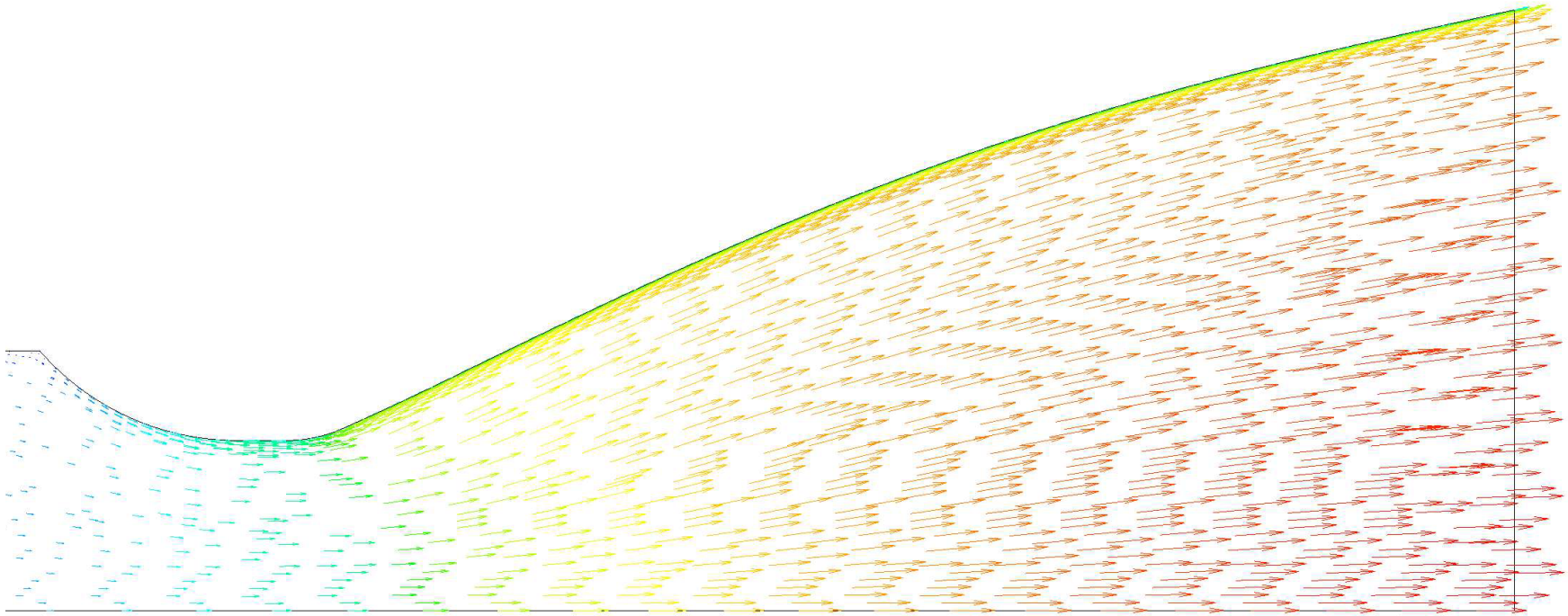

Figure F.26: Case 2-3 - Velocity vectors

Figure F.27: Case 2-4 - Iso Mach numbers

Figure F.28: Case 2-4 - Iso temperatures

Figure F.29: Case 2-4 - Iso pressures

Figure F.30: Case 2-4 - Iso densities

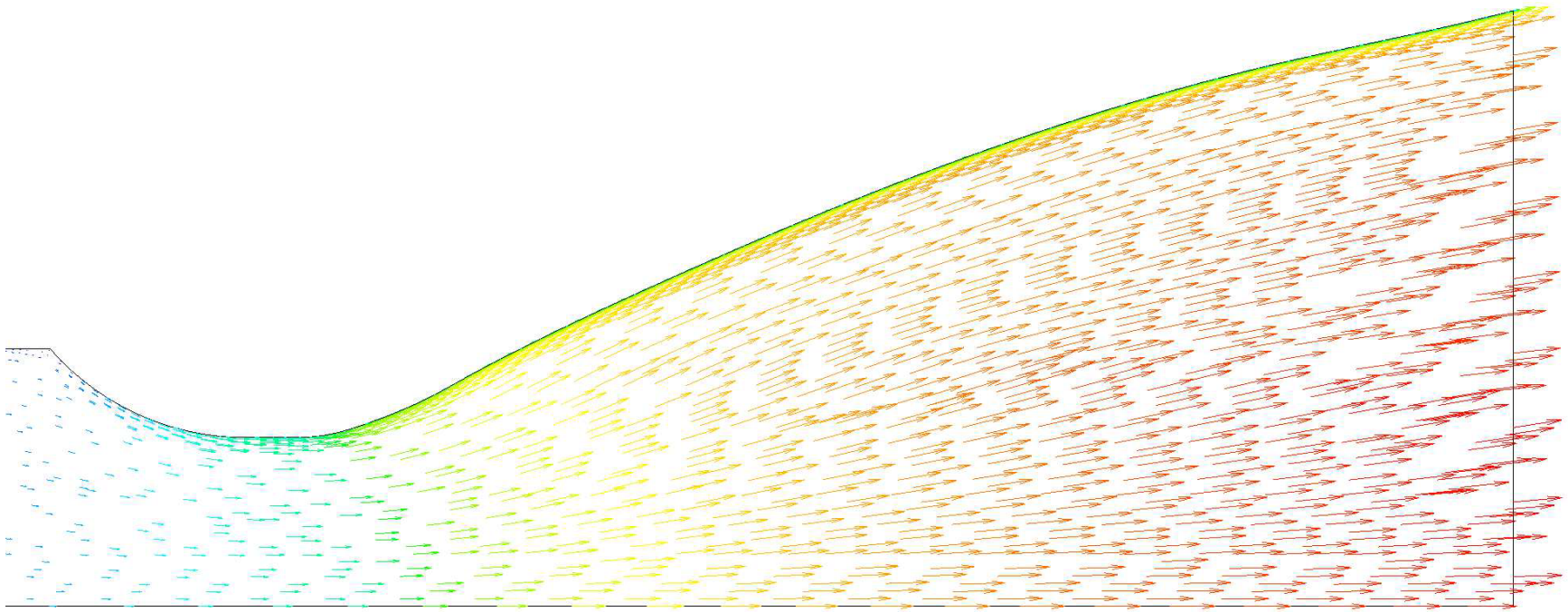

Figure F.31: Case 2-4 - Velocity vectors

APPENDIX G Baseline for Case 1 and 2 - Data

Figure G.1: Baseline - Iso Mach numbers

Figure G.2: Baseline - Iso temperatures

Figure G.3: Baseline - Iso pressures

Figure G.4: Baseline - Iso densities

Figure G.5: Baseline - Velocity vectors

APPENDIX H Circular Arc Contour for Case 1 and 2 - Data

Figure H.1: Circular arc contour - Iso Mach numbers

Figure H.2: Circular arc contour - Iso temperatures

Figure H.3: Circular arc contour - Iso pressures

Figure H.4: Circular arc contour - Iso densities

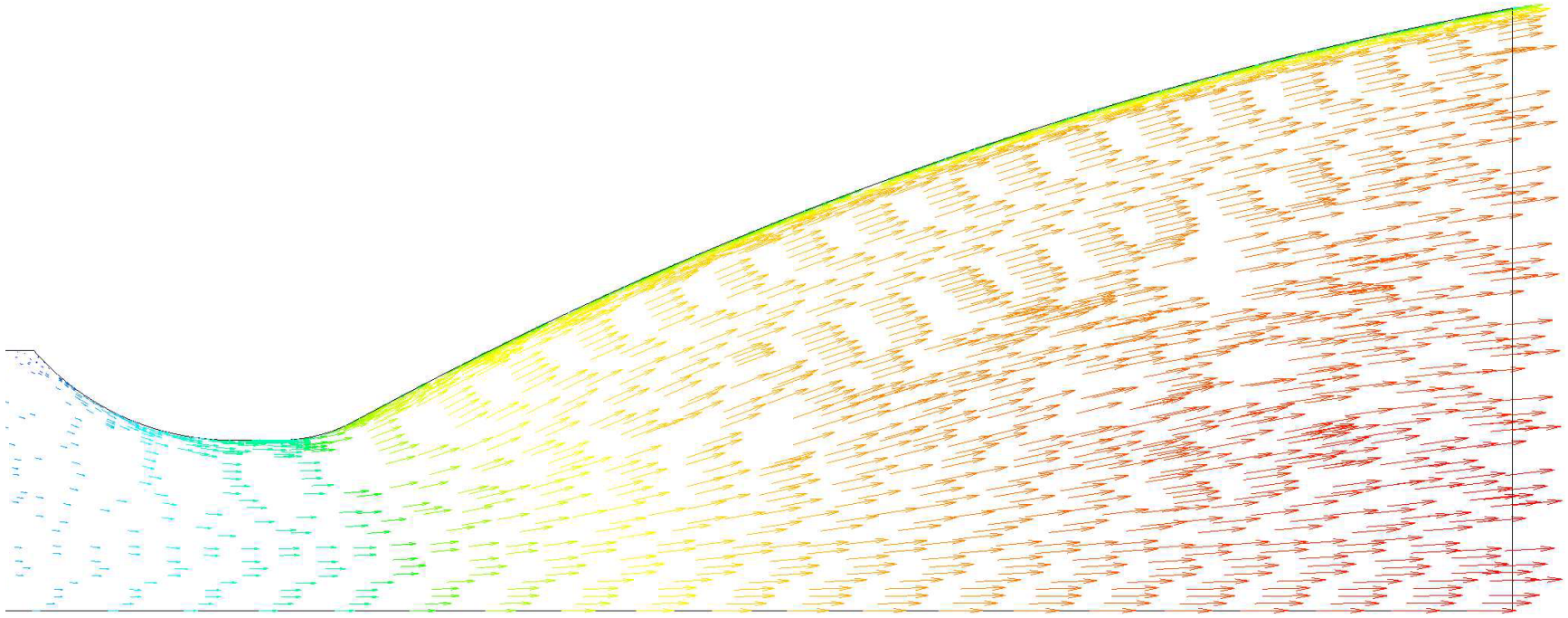

Figure H.5: Circular arc contour - Velocity vectors

APPENDIX I Case 3 - Data

		Input Parameters						Output Parameters	
No	Decription	r_i [mm]	θ_i [degree]	x2 [mm]	R2 @ x2 [mm]	θ_E [degree]	Xt [mm]	Mass Flow [kg/s]	Total Thrust [N]
1	Full Length Case 1	10.000	27.440	40.000	50.148	13.146	122.300	-6.5059	14409.8
2	5mm Length Reduction	5.000	28.447	52.925	45.454	13.000	116.790	-6.5064	14383.0
3	10mm Length Reduction	5.000	27.727	51.969	45.010	14.871	111.790	-6.5061	14341.6
4	15mm Length Reduction	5.000	29.032	51.295	44.159	14.815	106.790	-6.5063	14289.9
5	20mm Length Reduction	5.000	29.821	40.000	46.874	13.000	101.790	-6.5052	14224.7

Figure I.1: Case 3 - Design table

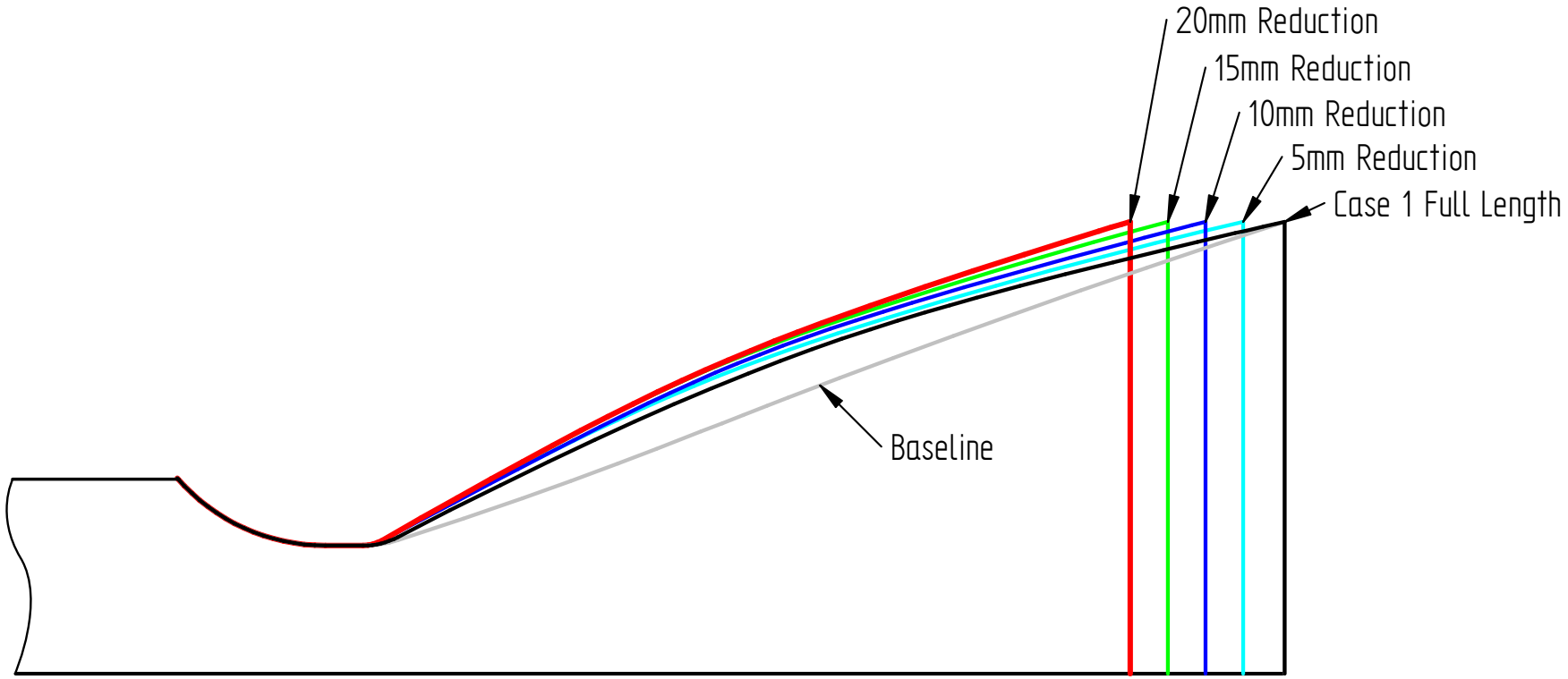

Figure I.2: Case 3 - Geometry comparison

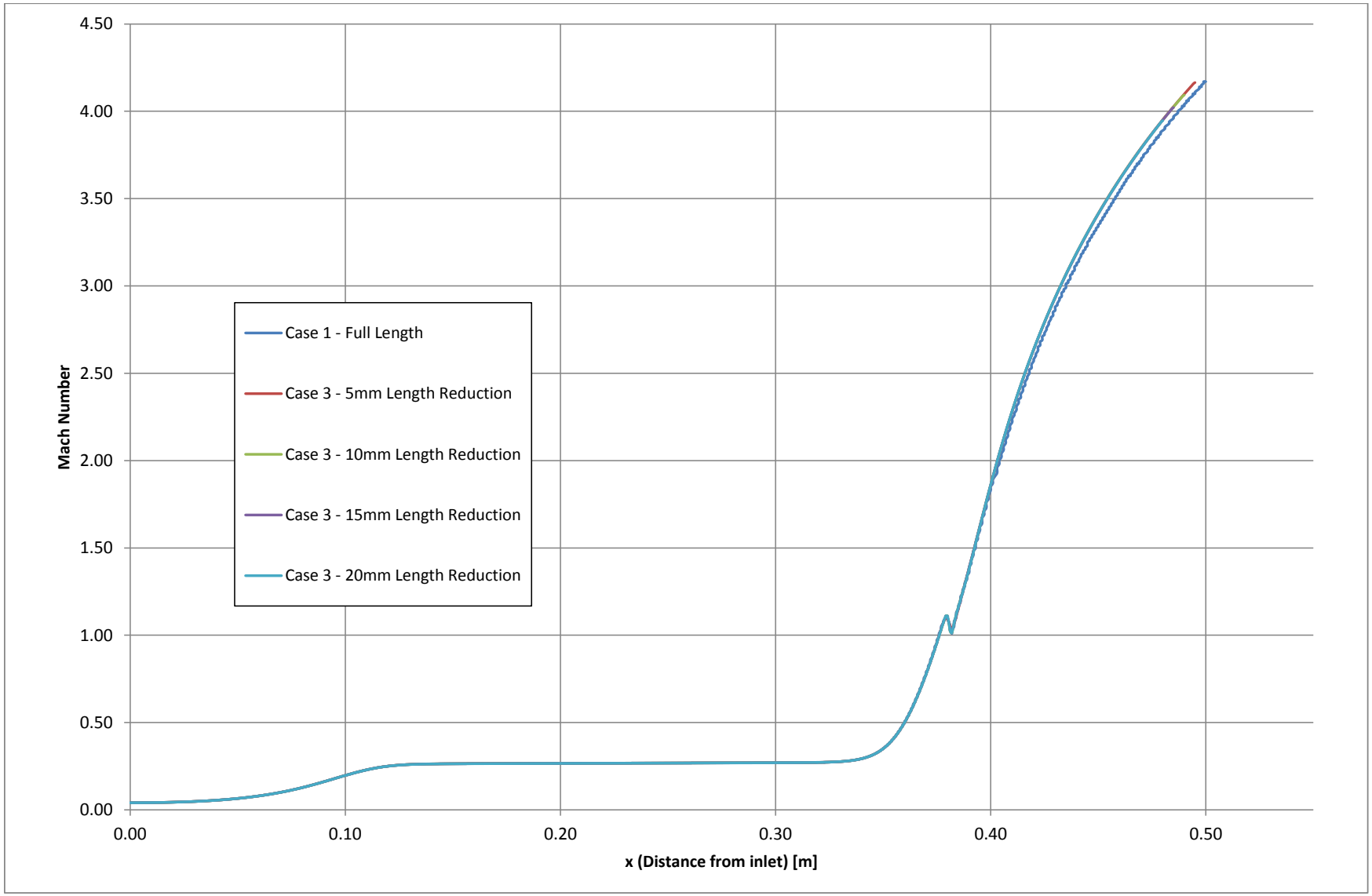

Figure I.3: Case 3 - Centerline Mach numbers

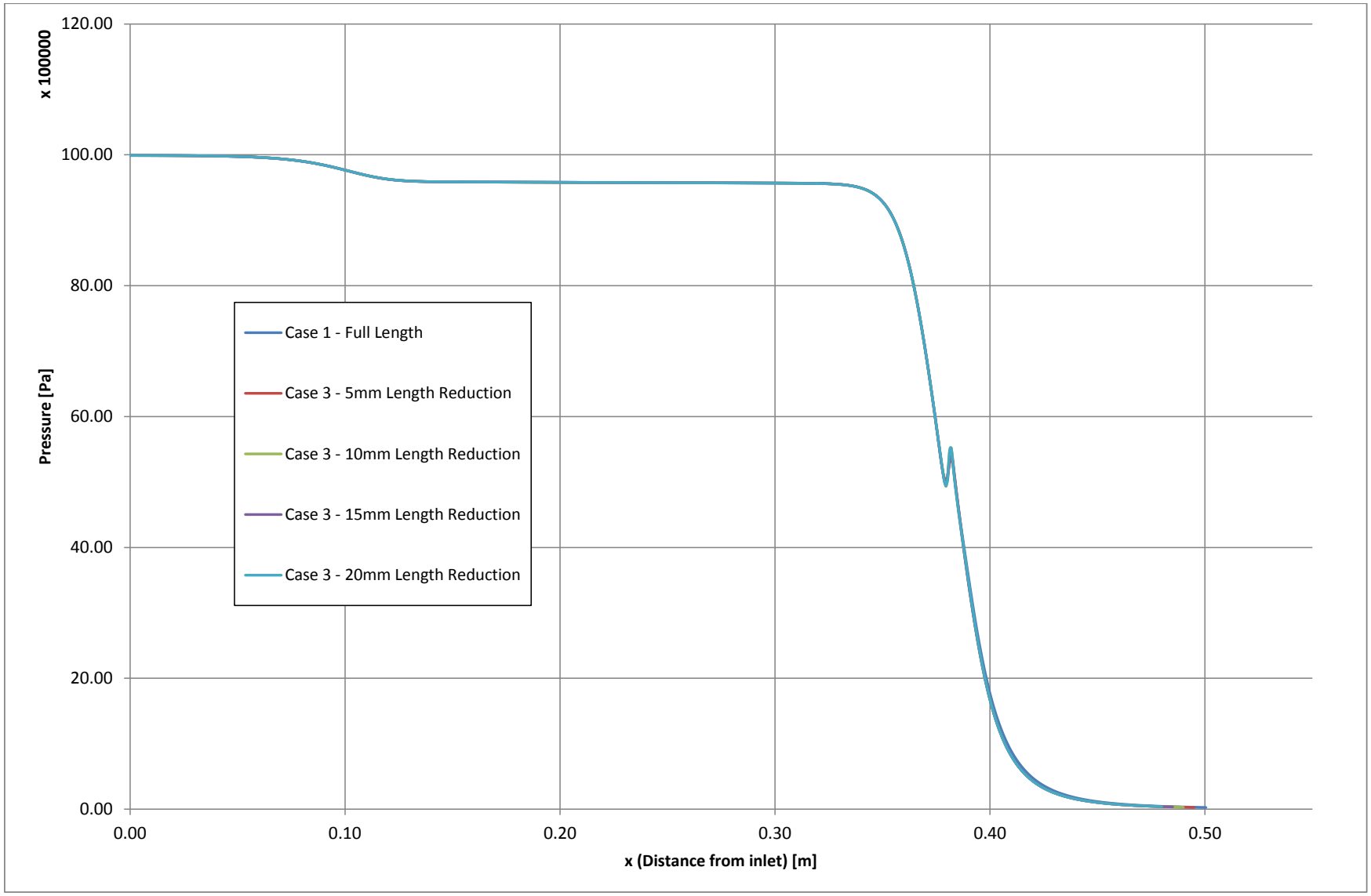

Figure I.4: Case 3 - Centerline pressures

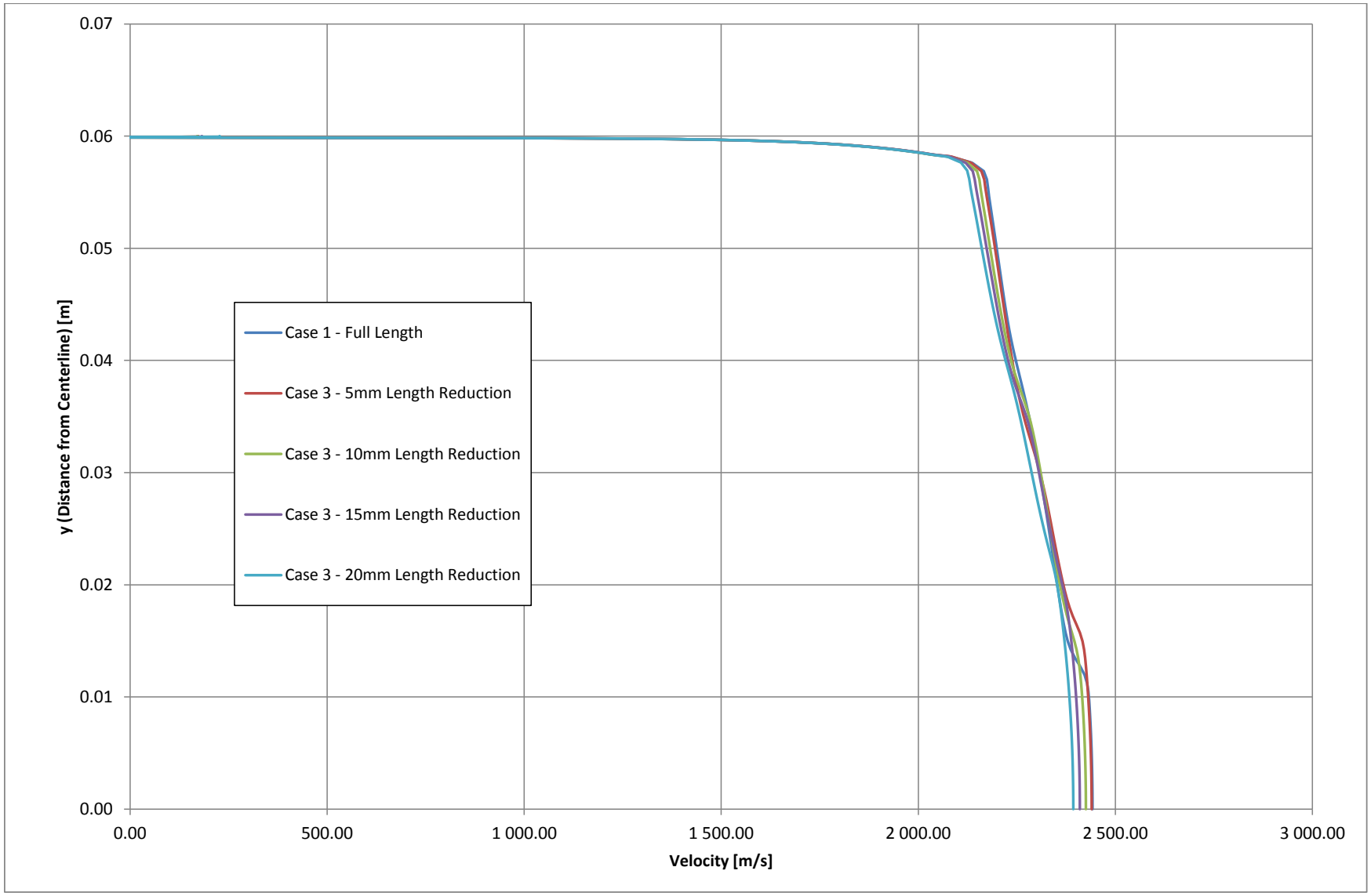

Figure I.5: Case 3 - Exit velocities

Figure I.6: Case 3 - 5 mm reduction - Iso Mach numbers

Figure I.7: Case 3 - 5 mm reduction - Iso temperatures

Figure I.8: Case 3 - 5 mm reduction - Iso pressures

Figure I.9: Case 3 - 5 mm reduction - Iso densities

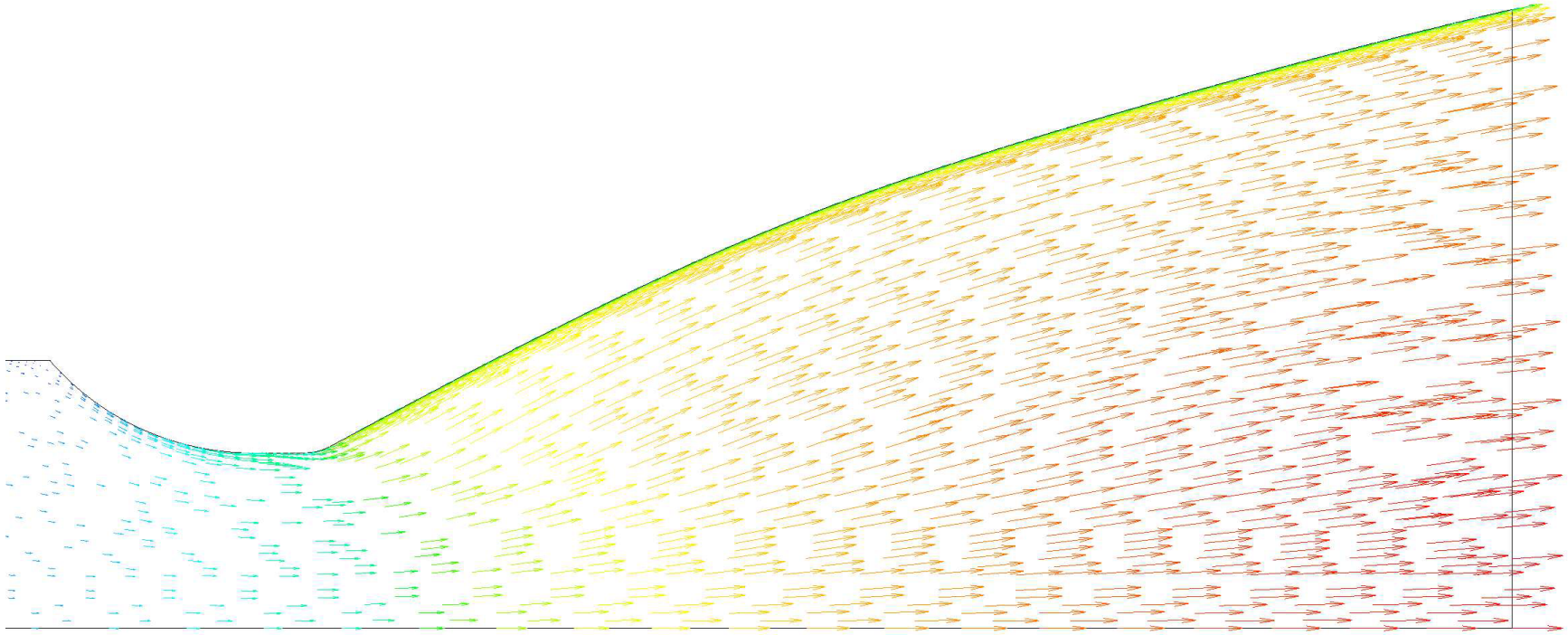

Figure I.10: Case 3 - 5 mm reduction - Velocity vectors

Figure I.11: Case 3 - 10 mm reduction - Iso Mach numbers

Figure I.12: Case 3 - 10 mm reduction - Iso temperatures

Figure I.13: Case 3 - 10 mm reduction - Iso pressures

Figure I.14: Case 3 - 10 mm reduction - Iso densities

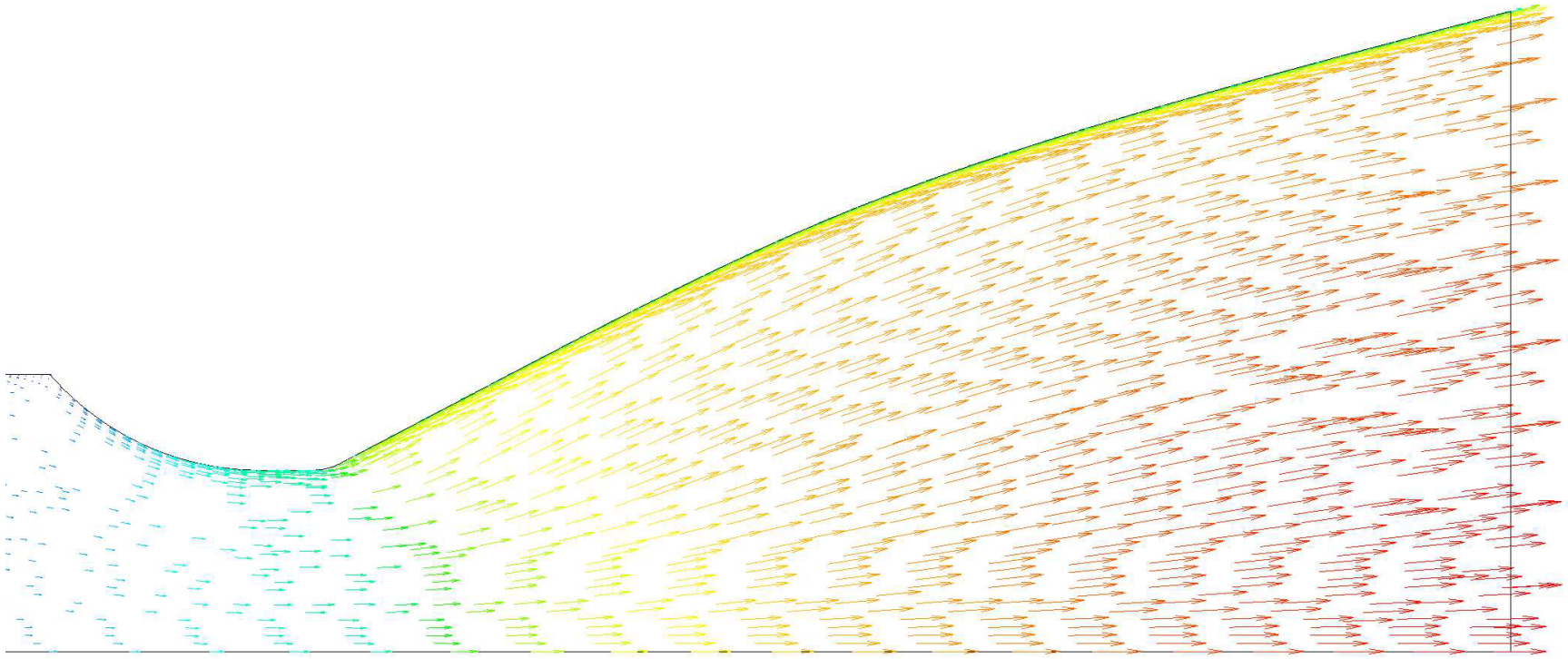

Figure I.15: Case 2 - 10 mm reduction - Velocity vectors

Figure I.16: Case 3 - 15 mm reduction - Iso Mach numbers

Figure I.17: Case 3 - 15 mm reduction - Iso temperatures

Figure I.18: Case 3 - 15 mm reduction - Iso pressures

Figure I.19: Case 3 - 15 mm reduction - Iso densities

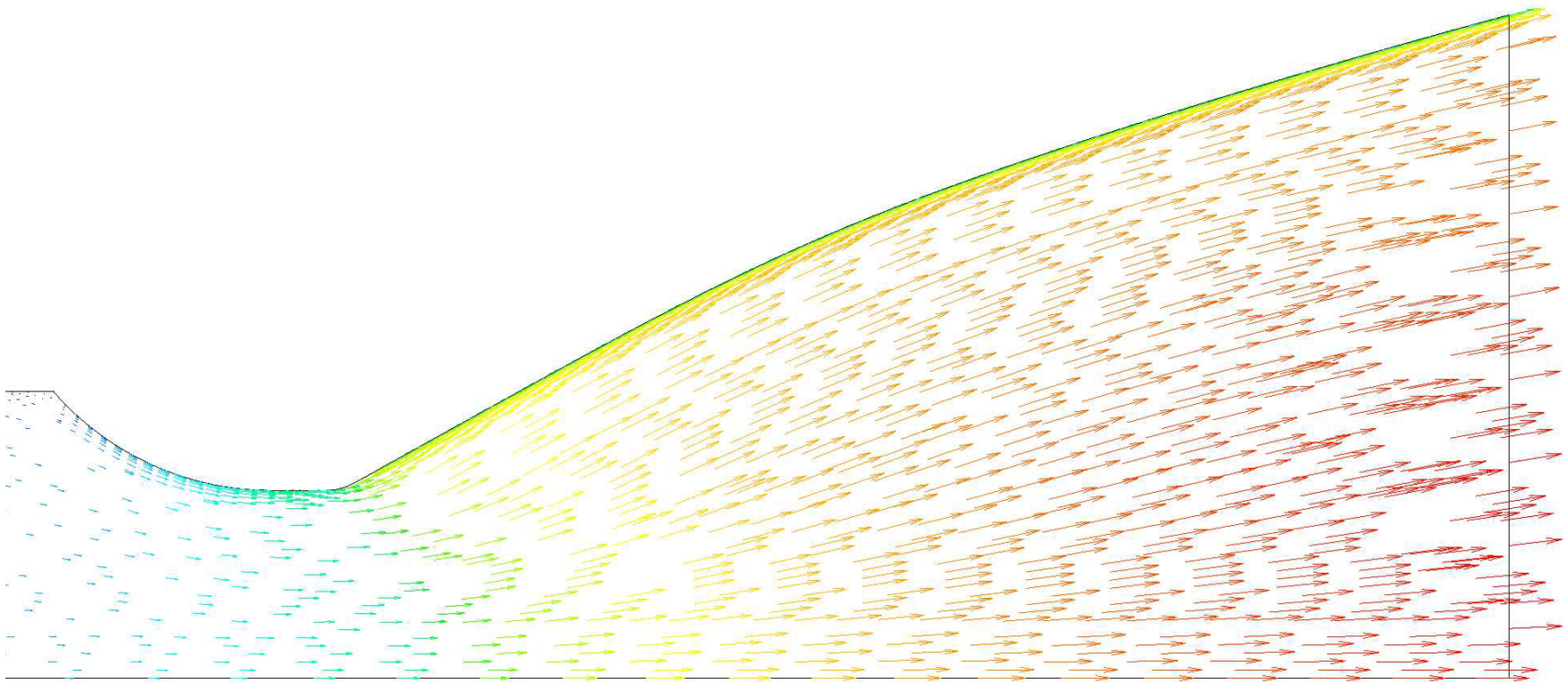

Figure I.20: Case 3 - 15 mm reduction - Velocity vectors

Figure I.21: Case 3 - 20 mm reduction - Iso Mach numbers

Figure I.22: Case 3 - 20 mm reduction - Iso temperatures

Figure I.23: Case 3 - 20 mm Reduction - Iso pressures

Figure I.24: Case 3 - 20 mm reduction - Iso densities

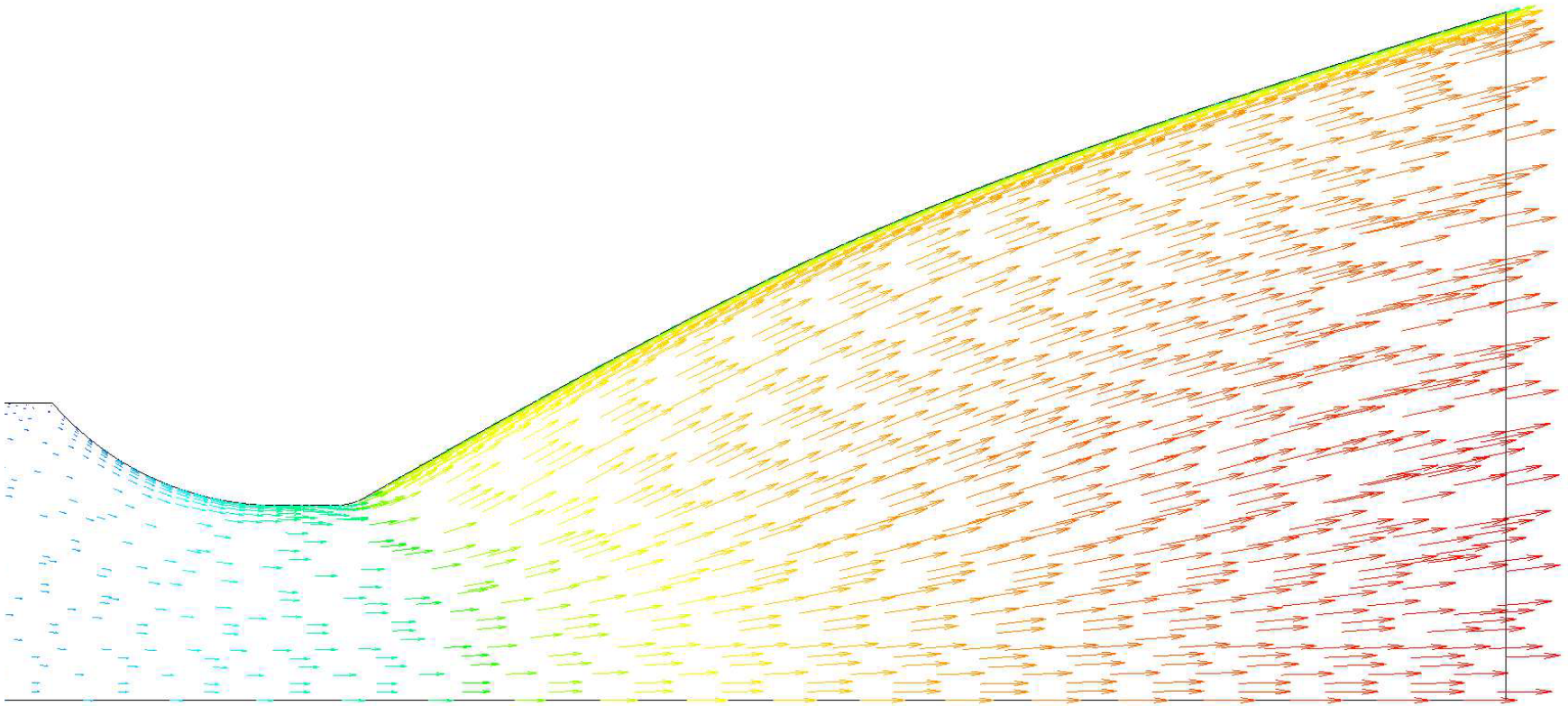

Figure I.25: Case 3 - 20 mm reduction - Velocity vectors

APPENDIX J Case 4 - Data

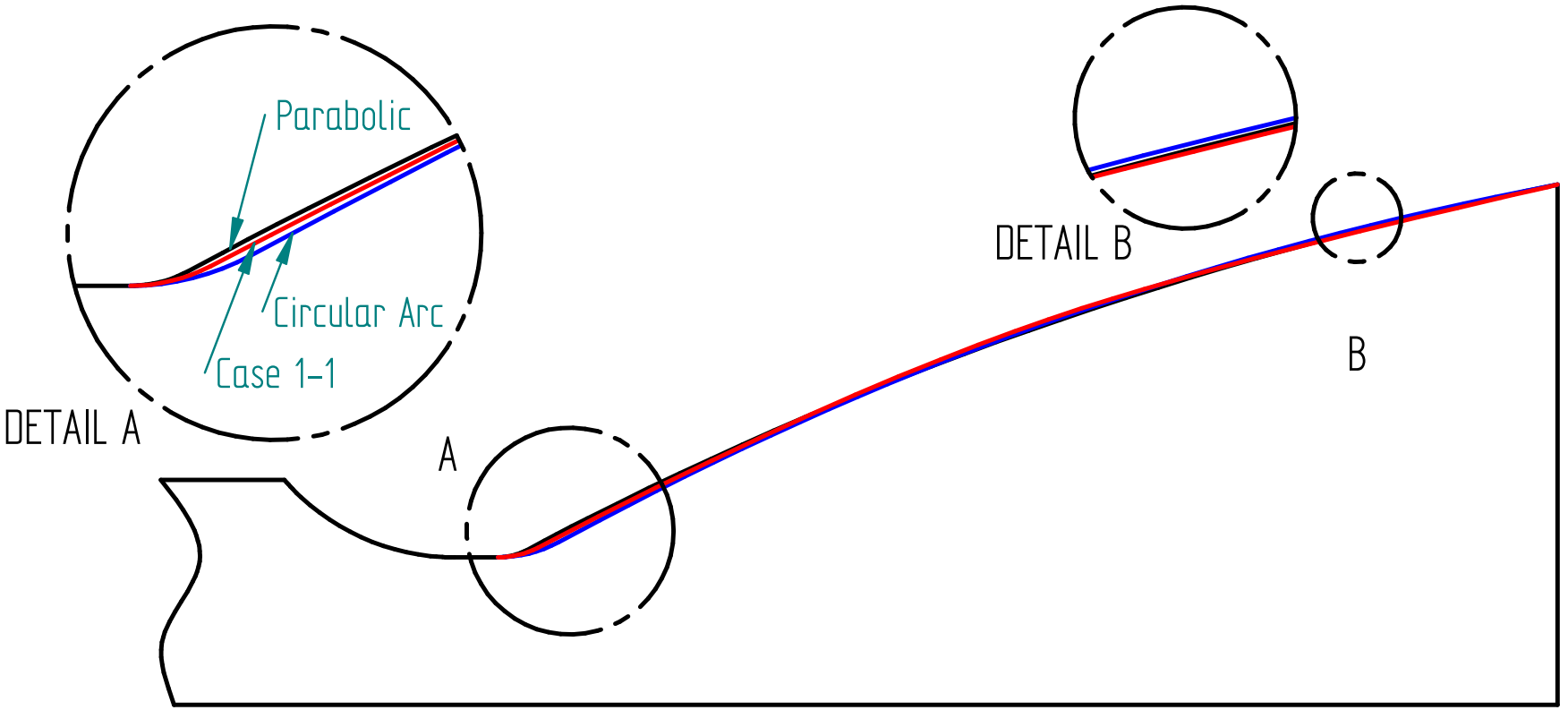

Figure J.1: Case 4 - 75 % Length parabolic geometry comparison

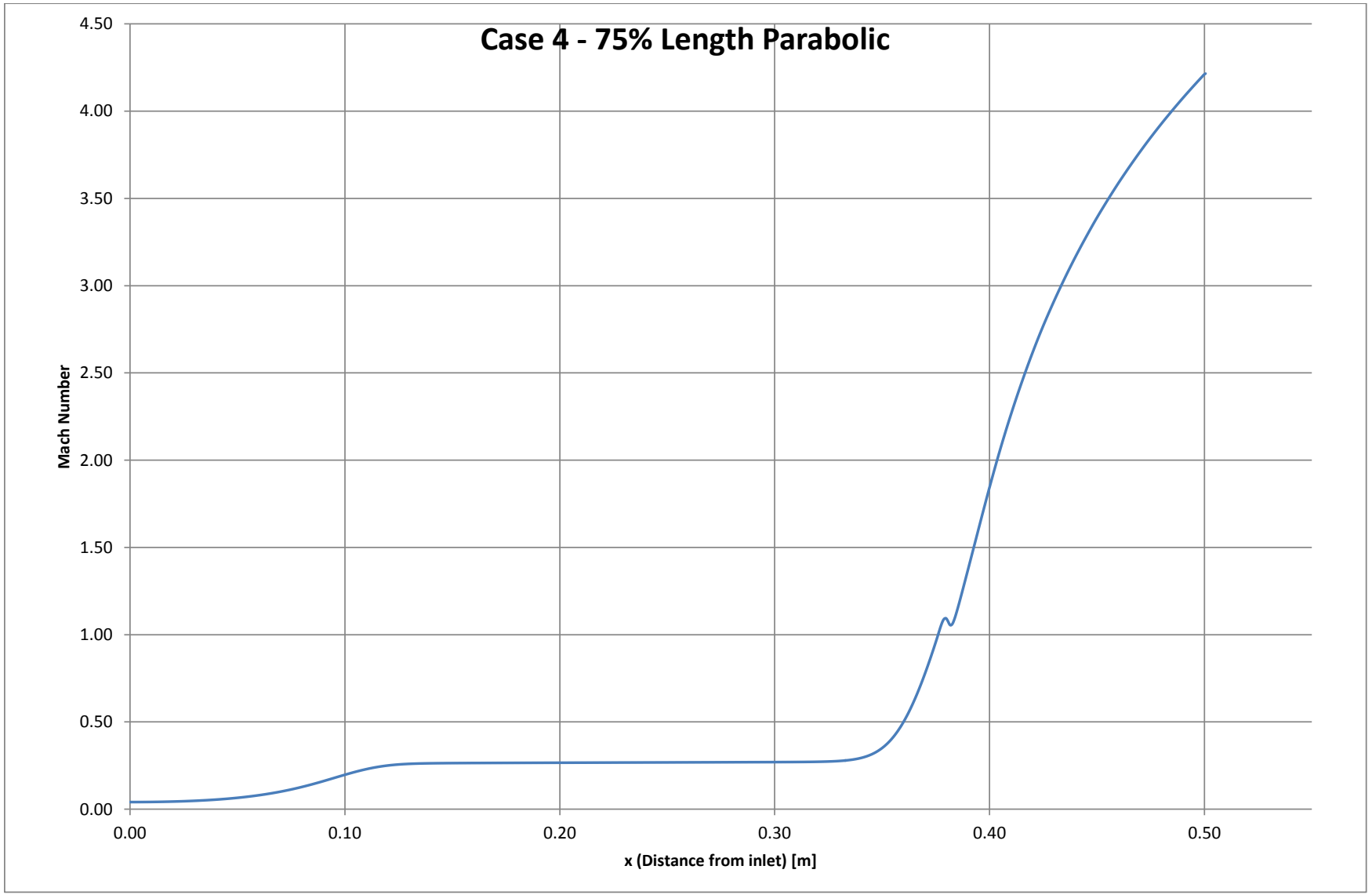

Figure J.2: Case 4 - Centerline Mach numbers

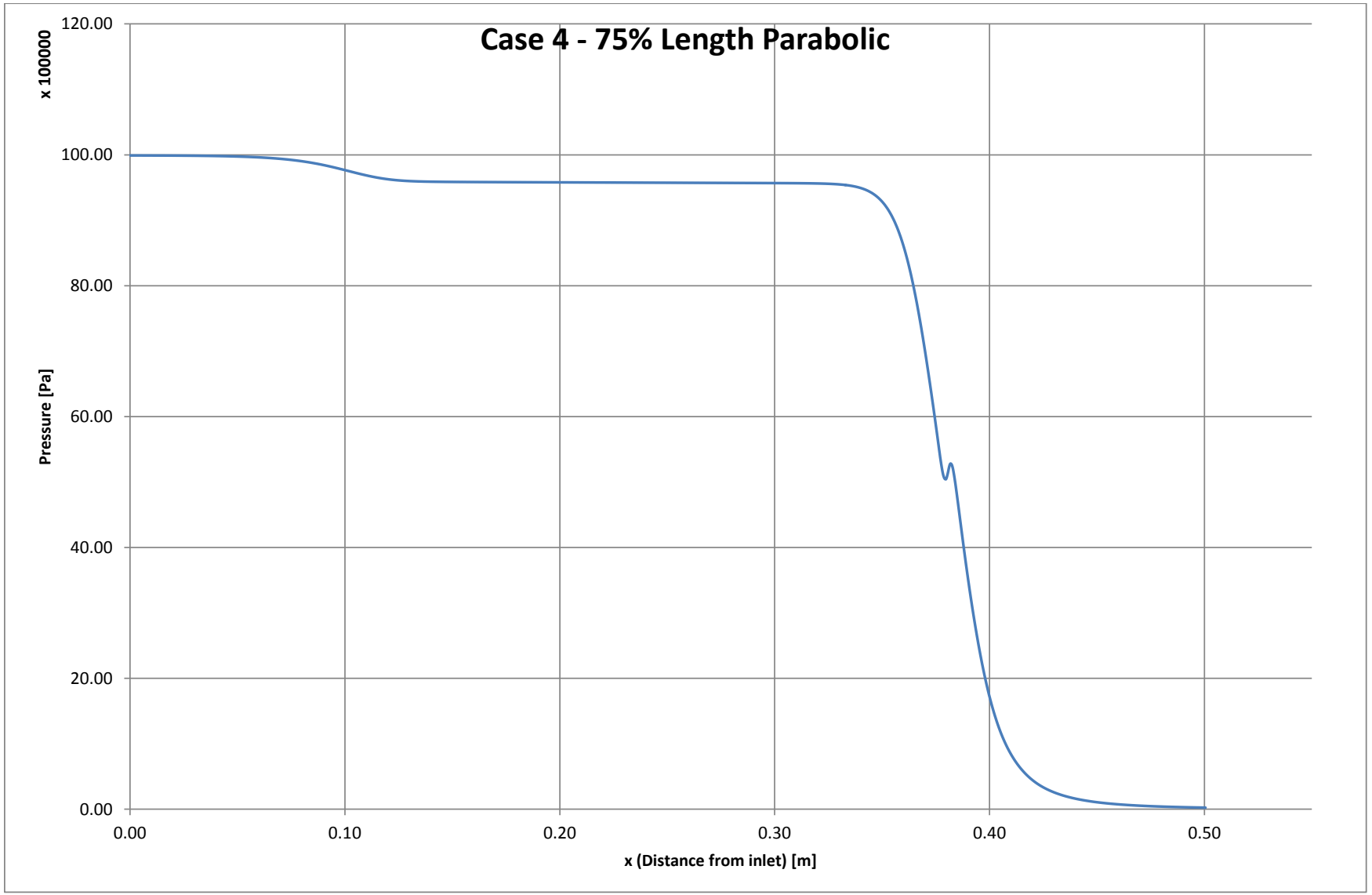

Figure J.3: Case 4 - Centerline pressures

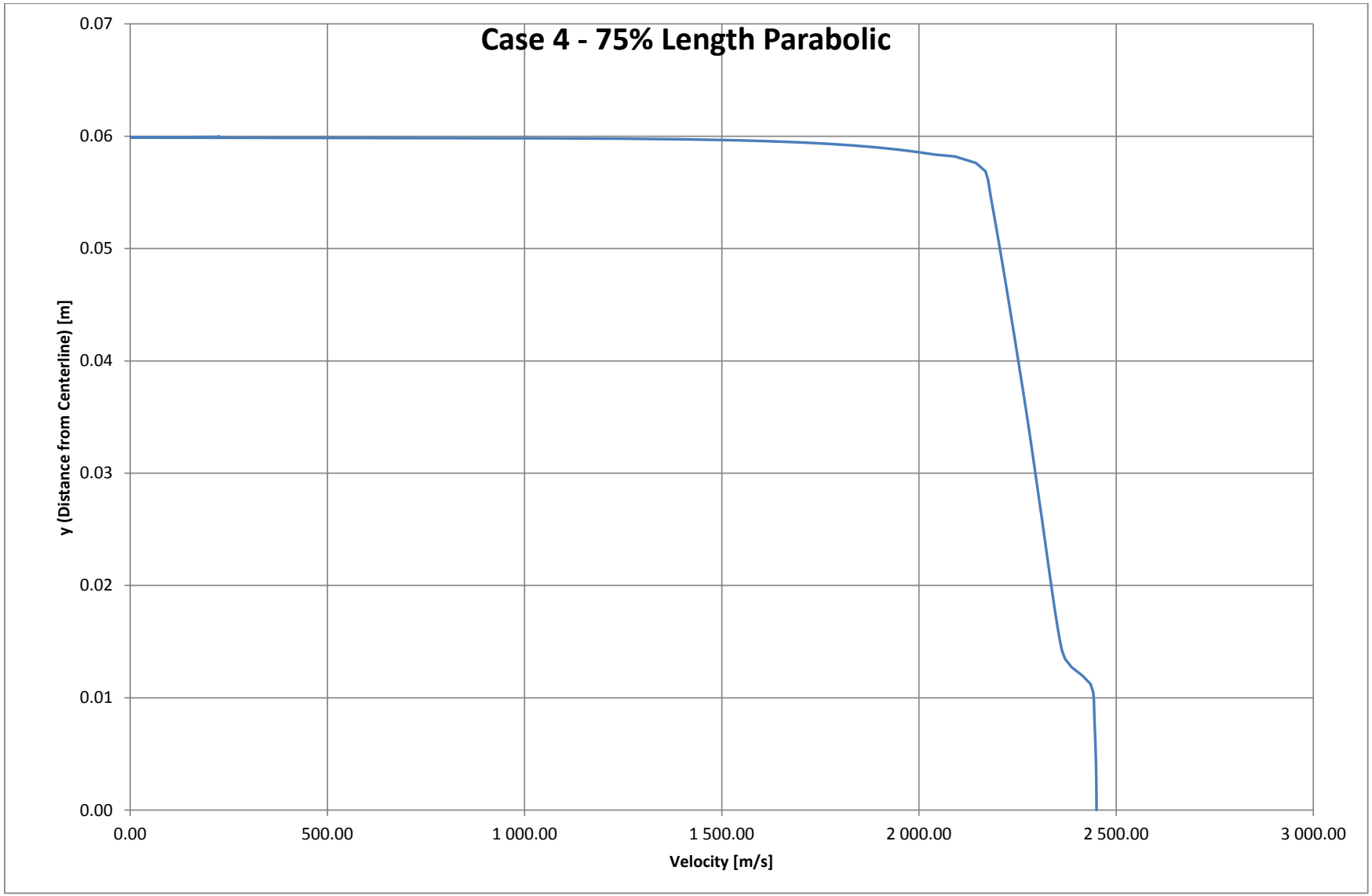

Figure J.4: Case 4 - Exit velocities

Figure J.5: Case 4 - Iso Mach numbers

Figure J.6: Case 4 - Iso temperatures

Figure J.7: Case 4 - Iso pressures

Figure J.8: Case 4 - Iso densities

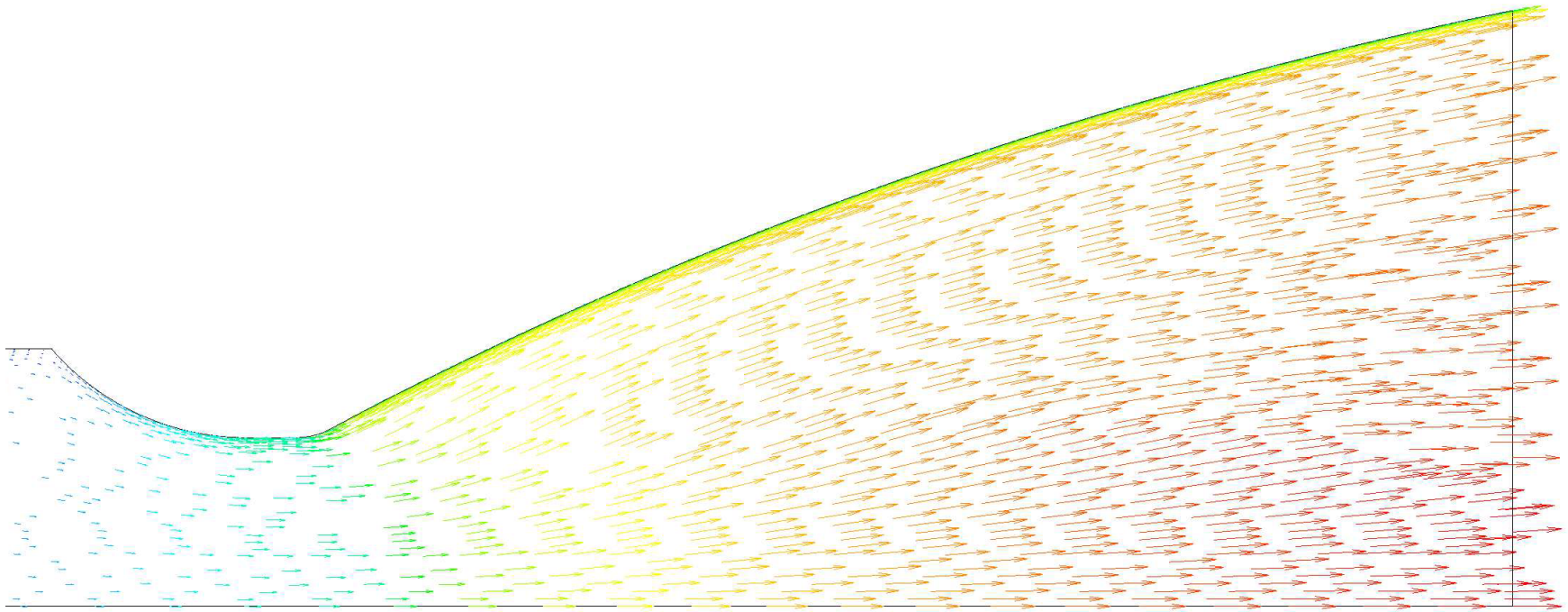

Figure J.9: Case 4 - Velocity vectors

APPENDIX K Case 5 - Data

	Input Parameters					Output Parameters	
No	ri [mm]	θi [degree]	x2 [mm]	R2 @ x2 [mm]	θe [degree]	Mass Flow [kg/s]	Total Thrust [N]
1	12.500	25.000	88.612	43.524	8.000	-6.5065	14533.9
2	12.500	25.000	89.521	43.162	8.000	-6.5062	14533.1
3	12.500	25.000	88.607	43.791	8.000	-6.5063	14532.8
4	12.500	25.000	87.858	43.330	8.000	-6.5065	14532.7
5	12.742	24.207	77.838	46.646	7.683	-6.5063	14532.2
6	12.500	24.999	81.673	45.893	7.975	-6.5065	14532.0
7	12.500	25.000	86.116	44.741	8.000	-6.5065	14531.8
8	12.729	24.216	77.856	46.638	7.687	-6.5062	14531.7
9	12.500	25.000	79.979	46.359	8.000	-6.5064	14531.3
10	15.714	24.441	59.424	50.000	8.857	-6.5067	14530.9
11	12.659	25.274	73.775	46.852	8.019	-6.5063	14530.8
12	12.500	23.619	76.560	47.165	7.994	-6.5064	14530.2
13	16.075	24.526	59.861	50.000	8.944	-6.5064	14530.1
14	16.819	24.291	60.114	50.000	9.114	-6.5067	14529.9
15	12.659	25.274	73.775	46.852	8.019	-6.5063	14529.8
16	15.253	23.791	58.503	50.000	8.729	-6.5063	14529.6
17	12.500	23.646	76.251	47.169	7.994	-6.5065	14529.2
18	14.896	23.082	58.077	50.000	8.626	-6.5064	14528.0
19	12.500	25.000	63.244	48.822	8.000	-6.5063	14528.0
20	12.500	23.952	79.368	46.819	7.986	-6.5061	14527.3
21	20.000	23.029	59.532	50.000	10.497	-6.5067	14523.3
22	12.500	25.000	70.242	49.639	8.000	-6.5066	14522.3
23	12.500	25.000	71.426	49.388	8.000	-6.5066	14521.7
24	8.113	21.903	66.240	49.497	7.729	-6.5064	14520.4
25	12.500	22.999	78.024	47.412	7.994	-6.5065	14519.1
26	6.763	21.080	75.686	46.802	8.420	-6.5064	14518.2
27	13.888	22.140	58.474	49.171	8.332	-6.5064	14517.2
28	10.138	21.601	89.855	44.165	8.382	-6.5065	14516.7
29	6.517	22.974	90.000	45.000	8.000	-6.5067	14516.4
30	20.000	22.212	59.600	49.956	12.000	-6.5064	14512.9
31	16.123	22.982	81.683	46.538	6.823	-6.5067	14512.5
32	12.500	25.000	80.381	47.697	8.000	-6.5064	14511.8
33	12.500	25.000	89.667	41.204	8.000	-6.5066	14511.3
34	11.045	22.948	90.000	45.000	8.000	-6.5069	14509.6
35	12.205	27.351	90.000	45.000	8.000	-6.5069	14508.7
36	13.245	22.078	59.093	48.411	8.148	-6.5064	14507.8
37	13.023	22.293	59.757	48.074	8.087	-6.5064	14505.4
38	16.291	24.389	90.000	45.000	8.000	-6.5068	14505.0
39	15.673	21.464	68.039	48.882	6.439	-6.5064	14504.8
40	14.862	20.970	84.982	45.366	7.591	-6.5062	14503.6
41	18.913	21.171	63.841	49.761	7.360	-6.5065	14503.1
42	14.862	20.970	84.982	45.366	7.591	-6.5062	14503.1
43	19.584	25.293	90.000	45.000	8.000	-6.5065	14499.6
44	12.500	25.000	89.429	45.814	8.000	-6.5065	14498.5
45	16.213	21.501	74.337	48.413	8.743	-6.5064	14498.1
46	16.213	21.501	74.337	48.413	8.743	-6.5065	14498.0
47	12.500	30.000	90.000	44.327	4.353	-6.5070	14496.8
48	12.799	24.097	61.502	47.222	8.037	-6.5065	14496.1
49	12.500	30.000	86.269	45.056	8.000	-6.5065	14494.0
50	14.323	20.641	78.685	47.124	7.191	-6.5065	14493.8
51	12.500	25.000	89.266	40.611	8.000	-6.5064	14493.5
52	12.500	30.000	89.845	43.078	8.000	-6.5064	14493.4
53	19.572	28.318	90.000	45.000	8.000	-6.5065	14492.9
54	7.573	20.915	59.943	48.325	6.961	-6.5065	14492.2
55	5.000	28.447	80.000	45.000	5.000	-6.5052	14487.4
56	18.575	20.000	79.614	46.331	6.888	-6.5065	14486.2
57	19.633	22.269	55.444	49.526	4.288	-6.5064	14484.9

Figure K.1: Case 5 - Design table - Page 1/4

58	12.500	30.000	81.087	47.198	8.000	-6.5065	14484.2
59	12.500	30.000	85.855	46.066	8.000	-6.5068	14483.1
60	19.480	21.697	90.000	45.000	8.000	-6.5065	14482.9
61	12.500	30.000	90.000	45.000	8.000	-6.5065	14481.6
62	10.375	27.167	68.500	46.417	9.133	-6.5065	14481.2
63	9.913	22.342	78.835	48.853	7.422	-6.5064	14480.7
64	12.500	30.000	73.197	49.158	8.000	-6.5066	14479.8
65	12.500	30.000	78.466	48.157	8.000	-6.5064	14479.3
66	14.625	27.167	68.500	46.417	6.867	-6.5064	14479.2
67	12.500	30.000	89.076	42.298	8.000	-6.5065	14478.0
68	12.500	25.000	88.923	40.166	8.000	-6.5064	14476.2
69	14.953	25.415	77.635	49.116	9.511	-6.5067	14469.4
70	7.933	24.866	89.330	47.622	5.425	-6.5065	14462.7
71	12.433	20.806	73.437	49.673	5.578	-6.5065	14461.9
72	5.046	22.199	83.847	40.831	11.380	-6.5065	14461.4
73	12.500	30.000	88.708	41.690	8.000	-6.5065	14460.0
74	12.500	30.000	90.000	46.651	7.352	-6.5062	14455.3
75	12.500	25.000	80.310	49.518	8.000	-6.5064	14454.7
76	12.500	30.000	82.833	43.378	8.000	-6.5065	14453.9
77	7.033	20.586	53.645	48.794	4.657	-6.5064	14452.9
78	12.500	30.000	85.611	42.316	8.000	-6.5064	14451.8
79	19.342	20.564	86.220	41.328	4.561	-6.5065	14451.6
80	12.500	30.000	60.000	50.000	8.000	-6.5065	14448.4
81	12.500	30.000	90.000	47.581	4.654	-6.5063	14445.0
82	18.373	20.184	49.147	48.706	6.592	-6.5065	14438.7
83	10.453	23.330	83.933	48.384	9.726	-6.5065	14432.3
84	12.500	30.000	57.359	49.175	8.000	-6.5065	14430.3
85	12.500	30.000	75.243	44.484	8.000	-6.5064	14429.6
86	6.673	22.561	83.033	49.614	6.500	-6.5064	14427.1
87	12.500	25.000	84.094	49.168	8.000	-6.5066	14426.0
88	8.245	33.417	90.000	45.000	8.000	-6.5067	14425.7
89	13.603	24.592	87.081	47.359	10.263	-6.5065	14425.4
90	12.500	30.000	88.285	40.824	8.000	-6.5065	14425.1
91	17.472	23.805	80.634	49.878	6.131	-6.5065	14422.8
92	5.413	20.257	85.132	48.442	7.268	-6.5065	14422.3
93	12.973	21.793	88.131	47.827	6.039	-6.5065	14418.4
94	12.500	25.000	46.160	48.477	8.000	-6.5067	14418.3
95	17.833	21.830	42.850	49.175	4.595	-6.5064	14415.5
96	18.013	22.817	86.931	47.769	8.435	-6.5065	14415.3
97	15.313	23.439	38.651	49.585	7.975	-6.5064	14414.9
98	14.232	24.098	86.032	48.999	5.271	-6.5064	14413.7
99	12.500	30.000	81.209	49.892	8.000	-6.5065	14413.0
100	12.500	30.000	88.216	40.511	8.000	-6.5065	14412.5
101	12.500	30.000	89.077	47.881	8.000	-6.5064	14412.0
102	11.713	25.634	81.833	49.907	8.650	-6.5065	14410.8
103	10.273	20.367	39.851	49.790	5.886	-6.5064	14408.9
104	16.354	34.778	90.000	45.000	8.000	-6.5065	14406.9
105	19.273	25.122	84.832	49.292	5.824	-6.5063	14402.4
106	14.052	21.135	41.950	48.530	9.111	-6.5065	14401.5
107	12.500	30.000	90.000	45.359	11.575	-6.5064	14400.8
108	12.500	25.000	89.266	48.309	8.000	-6.5063	14396.4
109	12.500	20.000	60.000	45.000	8.000	-6.5064	14395.9
110	18.540	20.902	32.986	49.996	8.856	-6.5065	14391.0
111	18.540	20.902	32.986	49.996	8.856	-6.5064	14390.9
112	12.500	30.000	83.736	49.660	8.000	-6.5063	14390.2
113	10.363	24.811	32.504	46.509	7.806	-6.5067	14390.1
114	18.757	20.845	32.925	49.982	9.537	-6.5065	14389.9
115	18.164	21.250	32.947	49.979	8.208	-6.5066	14389.8
116	18.164	21.250	32.947	49.979	8.125	-6.5066	14389.5

Figure K.2: Case 5 - Design table - Page 2/4

117	18.014	20.876	32.981	49.984	8.789	-6.5065	14389.2
118	17.967	20.876	32.981	49.984	8.789	-6.5064	14389.0
119	18.757	20.697	32.924	49.984	9.534	-6.5065	14387.8
120	5.323	23.714	33.703	46.567	6.884	-6.5064	14387.7
121	6.771	20.769	33.078	49.836	10.717	-6.5063	14384.0
122	5.953	21.245	32.654	49.849	9.572	-6.5065	14381.3
123	12.500	30.000	85.335	49.566	8.000	-6.5070	14380.0
124	14.625	27.167	68.500	43.583	9.133	-6.5064	14378.0
125	12.500	25.000	79.652	40.264	8.000	-6.5063	14374.2
126	6.666	22.046	86.483	49.637	4.486	-6.5063	14371.0
127	10.375	27.167	68.500	43.583	6.867	-6.5065	14370.3
128	14.525	20.833	30.314	49.977	8.758	-6.5066	14368.3
129	14.525	20.833	30.314	49.977	8.758	-6.5067	14368.0
130	12.500	30.000	50.036	49.016	8.000	-6.5070	14363.3
131	14.525	20.000	30.000	50.000	9.608	-6.5065	14359.8
132	20.000	20.000	30.000	50.000	7.812	-6.5070	14359.7
133	14.525	20.000	30.000	50.000	7.996	-6.5065	14357.5
134	12.500	30.000	60.199	46.450	8.000	-6.5067	14356.4
135	19.182	20.678	33.404	45.542	5.440	-6.5066	14355.5
136	18.553	23.147	34.453	48.823	8.896	-6.5068	14353.9
137	12.500	30.000	87.685	49.500	8.000	-6.5065	14344.8
138	16.033	24.464	30.255	49.819	4.903	-6.5065	14342.6
139	12.500	30.000	75.344	42.477	8.000	-6.5065	14341.5
140	12.548	28.926	61.307	45.391	8.004	-6.5065	14338.2
141	9.733	22.013	34.753	48.618	5.118	-6.5066	14335.6
142	10.375	32.833	68.500	46.417	6.867	-6.5058	14323.5
143	10.375	27.167	51.500	46.417	6.867	-6.5065	14322.9
144	14.625	27.167	51.500	46.417	9.133	-6.5065	14320.5
145	7.843	20.422	37.902	47.388	11.185	-6.5065	14313.1
146	20.000	30.000	60.000	45.000	8.000	-6.5070	14297.0
147	12.500	25.000	89.184	49.801	8.000	-6.5064	14295.6
148	14.625	32.833	68.500	46.417	9.133	-6.5062	14295.0
149	9.193	21.025	87.231	49.087	10.494	-6.5066	14291.9
150	12.500	30.000	89.106	49.900	8.000	-6.5065	14291.8
151	12.500	30.000	80.208	40.394	8.000	-6.5064	14289.2
152	12.500	30.000	60.000	45.000	8.000	-6.5065	14274.4
153	12.500	30.000	60.000	45.000	8.000	-6.5065	14268.2
154	12.500	30.000	60.000	45.000	12.000	-6.5063	14266.5
155	12.500	30.000	90.000	47.969	11.815	-6.5065	14263.8
156	12.500	30.000	60.000	45.000	4.000	-6.5065	14260.8
157	5.117	20.827	34.430	41.167	5.302	-6.5066	14256.9
158	12.500	30.000	35.954	49.455	8.000	-6.5064	14236.7
159	12.500	30.000	35.731	49.496	8.000	-6.5064	14235.6
160	19.727	20.940	83.202	49.286	11.618	-6.5068	14232.6
161	16.752	20.513	89.030	49.409	9.203	-6.5065	14222.9
162	12.500	30.000	34.838	45.636	8.000	-6.5064	14222.1
163	19.905	21.914	30.880	47.824	4.338	-6.5064	14218.4
164	12.500	30.000	35.062	49.459	8.000	-6.5064	14211.8
165	12.500	30.000	30.000	45.000	8.000	-6.5064	14211.2
166	12.500	30.000	41.617	47.694	8.000	-6.5064	14201.3
167	10.375	32.833	68.500	43.583	9.133	-6.5065	14181.8
168	14.625	32.833	68.500	43.583	6.867	-6.5091	14174.3
169	14.625	27.167	51.500	43.583	6.867	-6.5064	14146.8
170	12.500	30.000	35.033	42.503	8.000	-6.5065	14113.9
171	10.375	32.833	51.500	46.417	9.133	-6.5066	14094.4
172	14.625	32.833	51.500	46.417	6.867	-6.5070	14081.9
173	19.809	23.710	33.705	40.446	11.517	-6.5065	14009.2
174	12.500	25.000	45.124	41.702	8.000	-6.5063	13984.9
175	12.500	30.000	55.977	41.704	8.000	-6.5062	13977.0

Figure K.3: Case 5 - Design table - Page 3/4

176	5.003	38.187	32.349	49.463	4.492	-6.5064	13917.0
177	10.375	32.833	51.500	43.583	6.867	-6.5055	13905.8
178	12.500	30.000	60.000	40.000	8.000	-6.5064	13891.9
179	6.353	38.603	80.151	48.397	11.841	-6.5054	13878.3
180	14.625	32.833	51.500	43.583	9.133	-6.5048	13867.7
181	5.382	39.384	82.730	41.030	4.855	-6.5066	13660.8
182	12.500	40.000	60.000	45.000	8.000	-6.5055	13629.8
183	5.324	36.506	31.928	41.008	11.540	-6.5057	13493.6
184	19.746	37.775	89.567	49.435	11.707	-6.5061	13259.3
185	17.965	39.696	31.105	49.407	4.066	-6.5096	13061.3
186	18.484	39.519	82.637	40.366	11.751	-6.5071	12903.8
187	5.401	39.844	33.323	40.175	4.018	-6.5076	12313.4
188	19.910	39.534	79.101	49.150	4.226	-6.5153	12163.7
189	19.948	39.549	89.553	40.652	4.101	-6.3722	12106.1
190	19.513	39.885	34.081	48.945	11.628	-6.5034	11746.9
191	19.693	35.364	33.877	40.299	4.032	-6.5064	11407.7

Figure K.4: Case 5 - Design table - Page 4/4

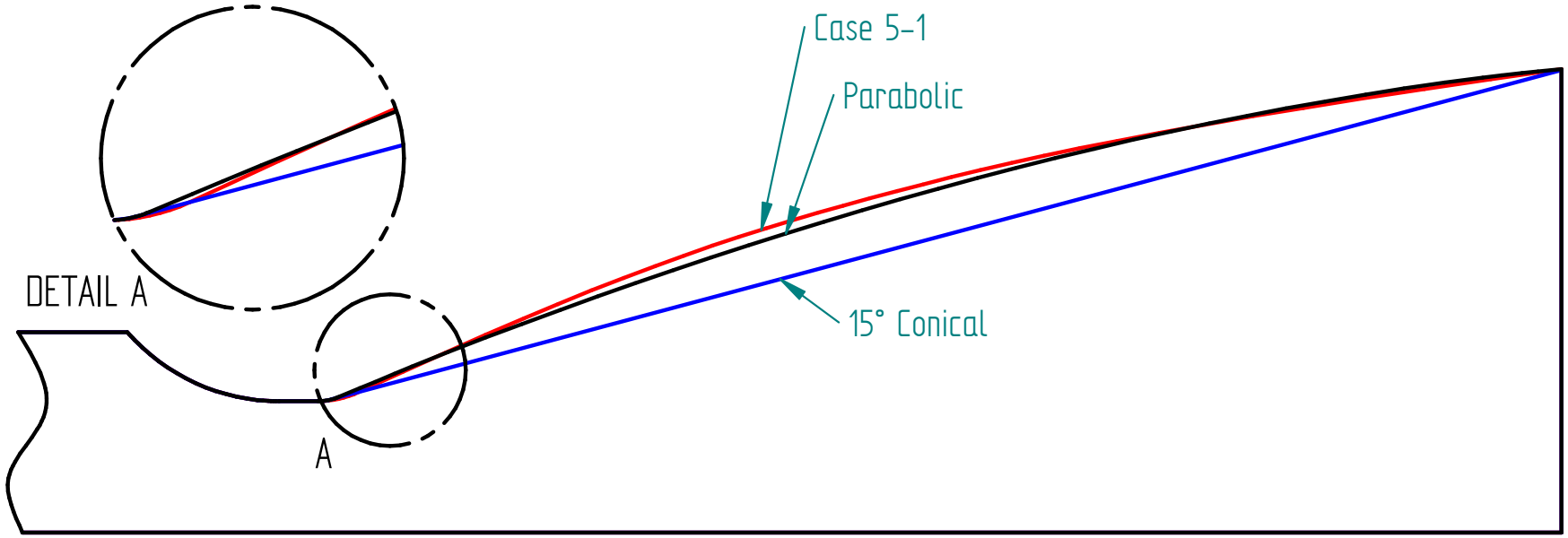

Figure K.5: Case 5 Geometry comparison

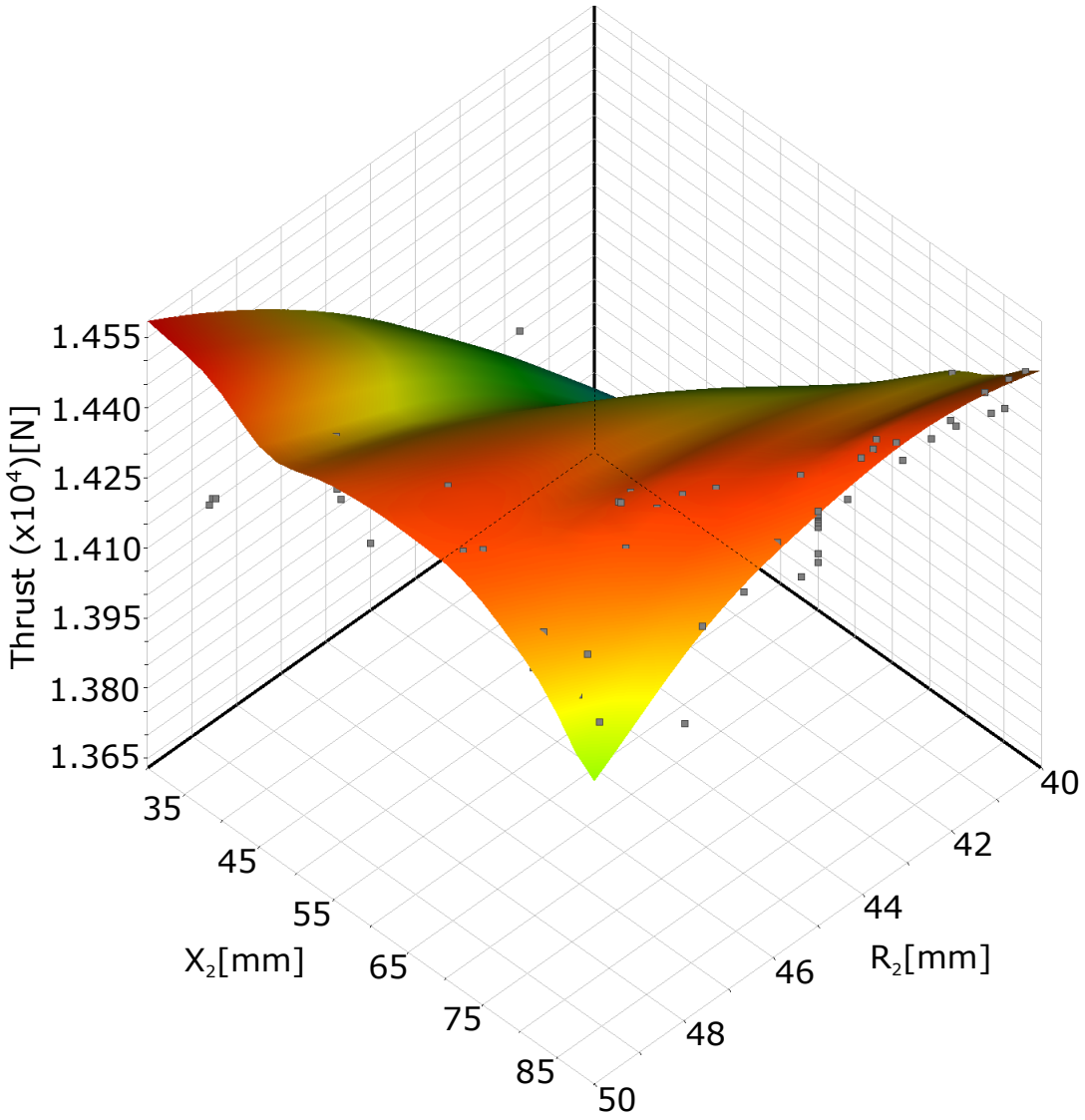

Figure K.6: Case 5 - x_2 vs R_2 Kriging response surface

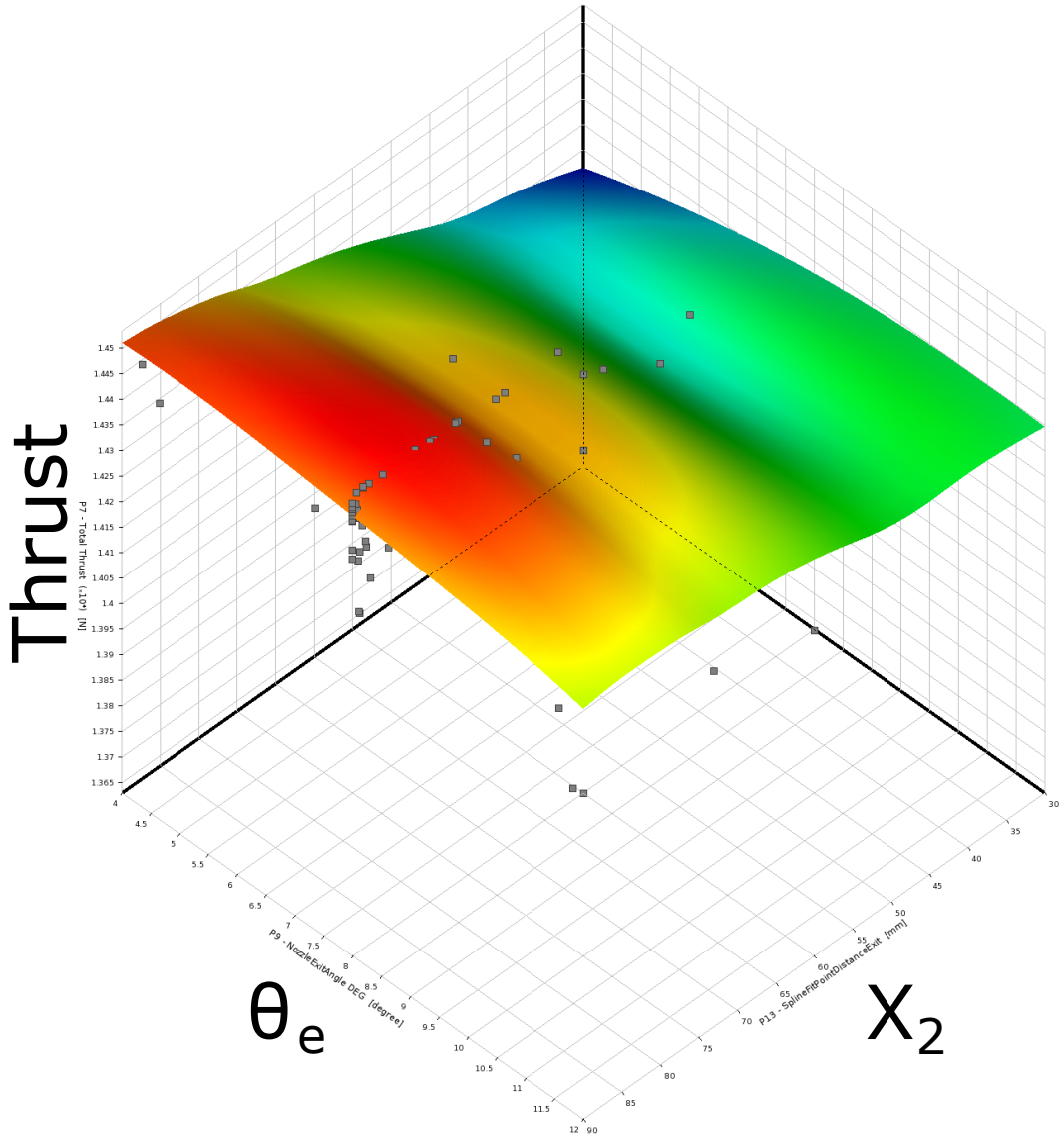

Figure K.7: Case 5 - θ_e vs x_2 Kriging response surface

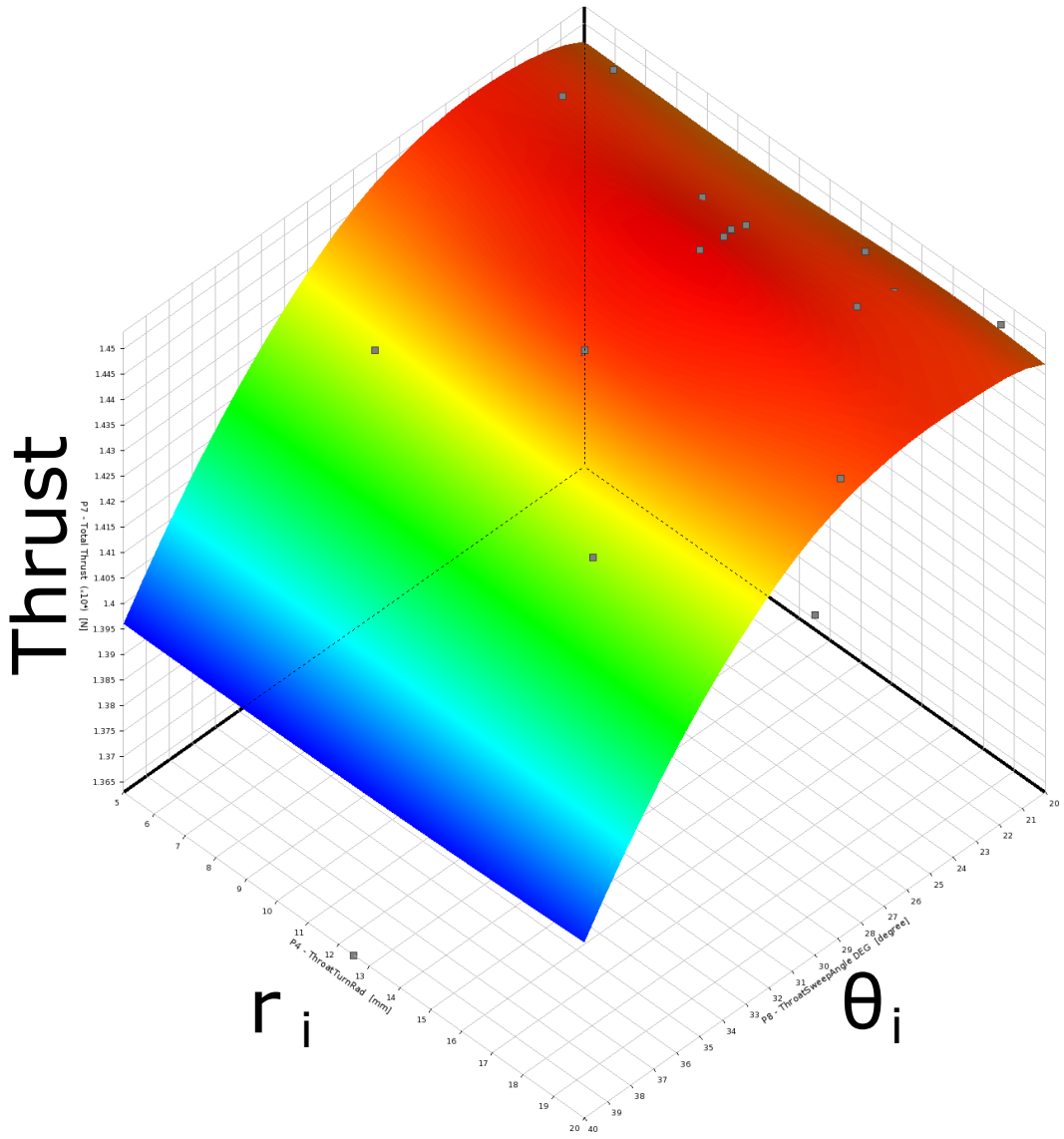

Figure K.8: Case 5 - r_i vs θ_i Kriging response surface

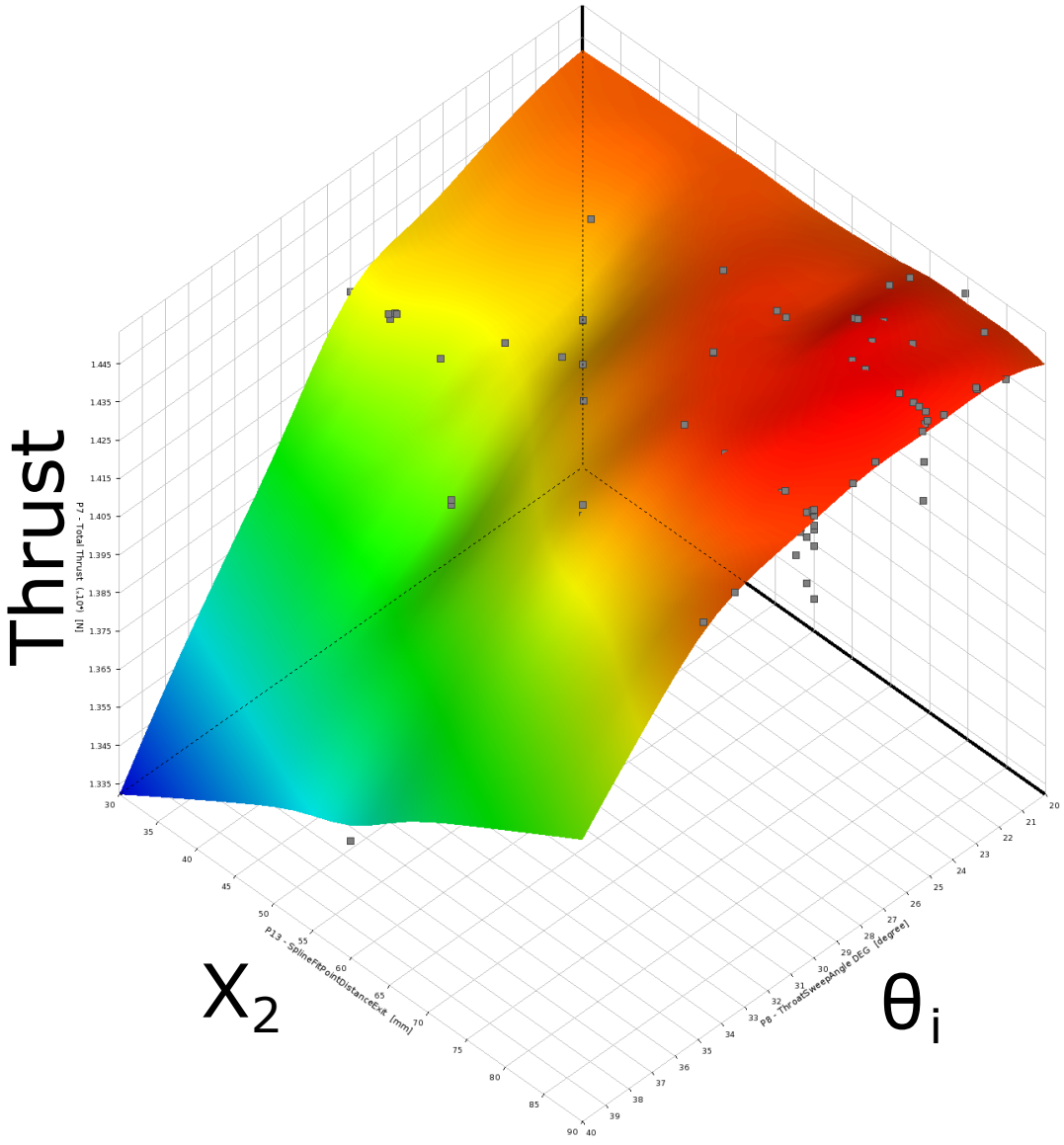

Figure K.9: Case 5 - x_2 vs θ_i Kriging response surface

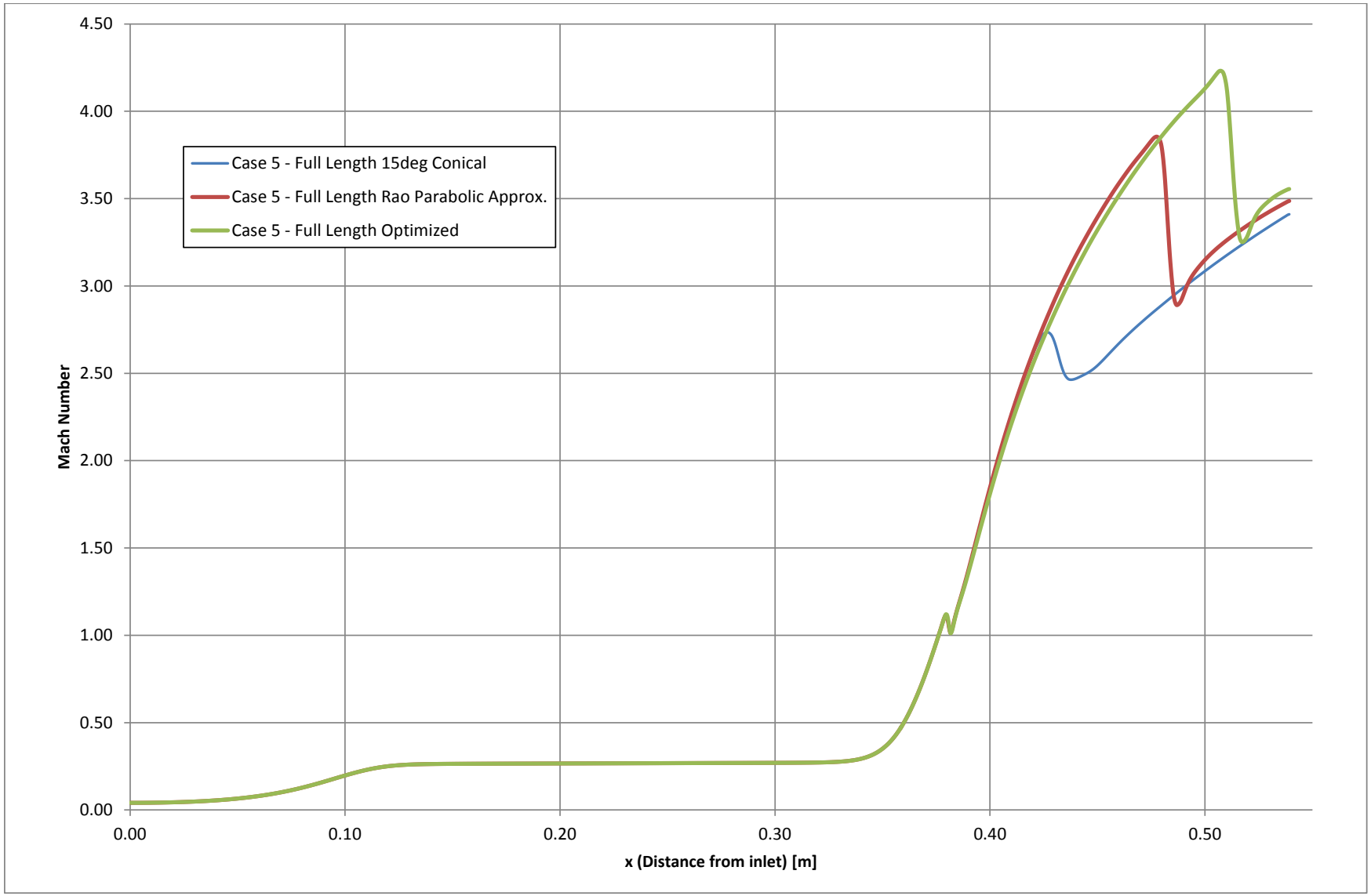

Figure K.10: Case 5 - Centerline Mach numbers

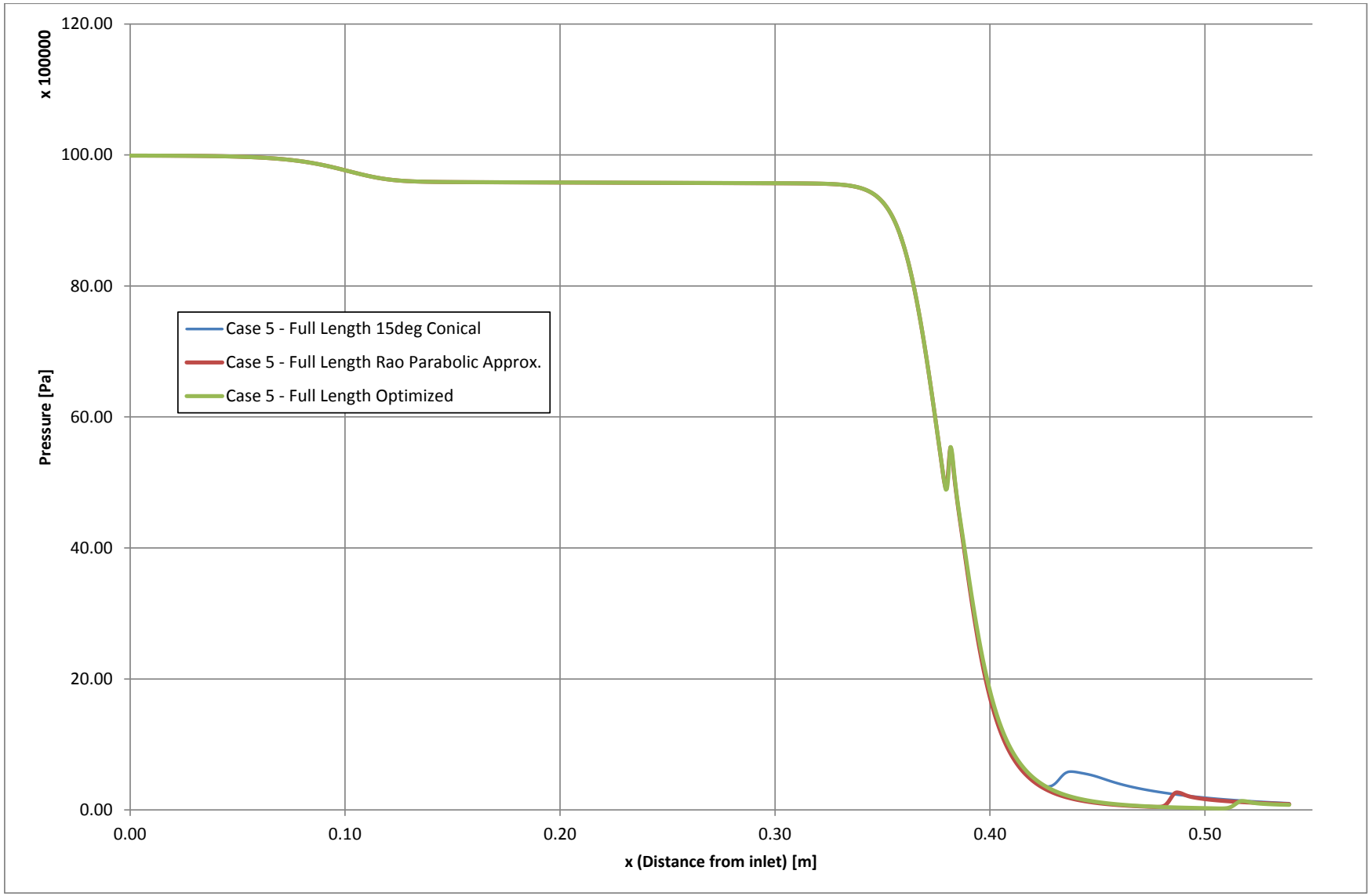

Figure K.11: Case 5 - Centerline pressures

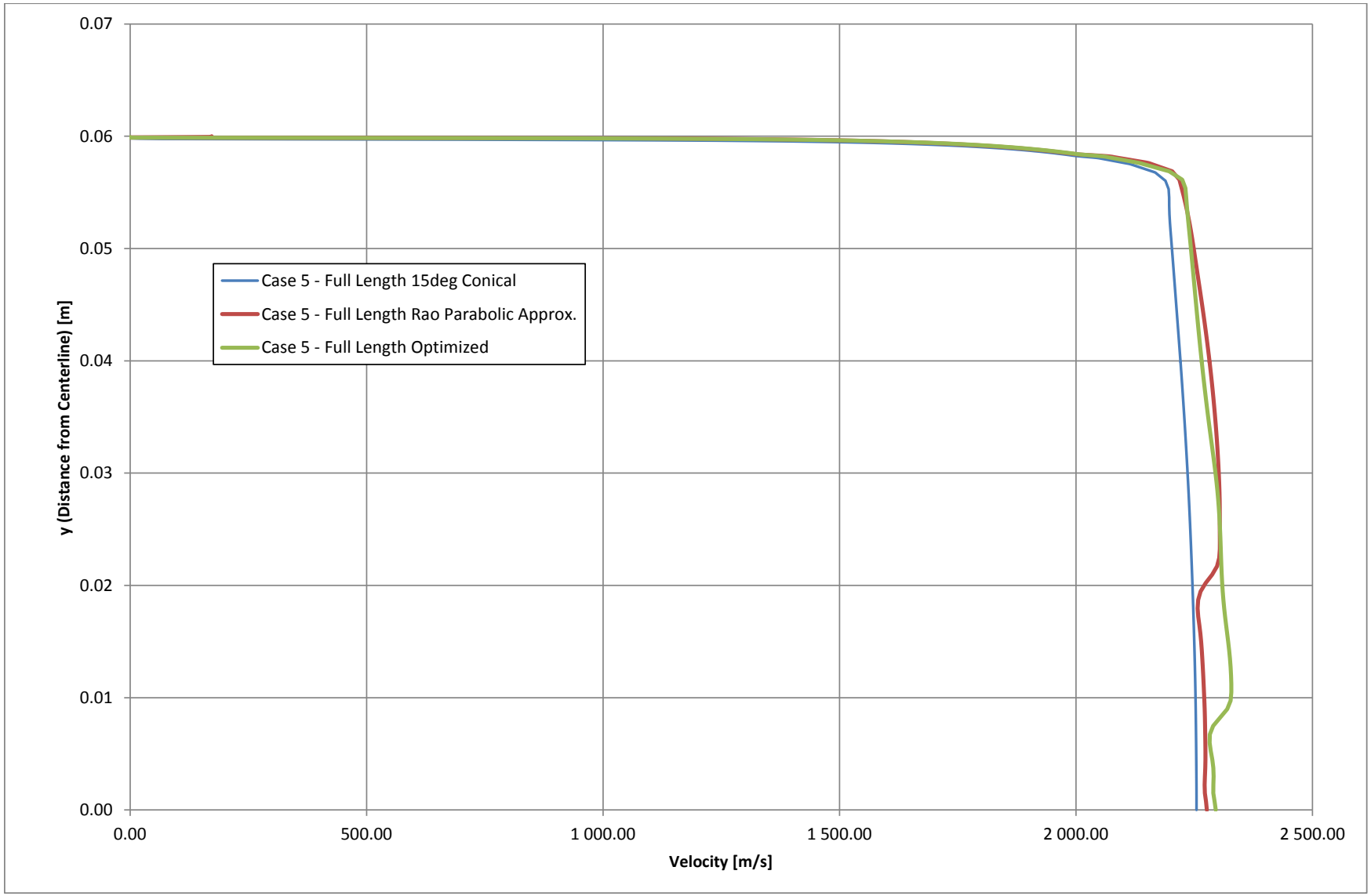

Figure K.12: Case 5 - Exit velocities

Figure K.13: Case 5 - Full length 15°conical - Iso Mach numbers

Figure K.14: Case 5 - Full length 15°conical - Iso temperatures

Figure K.15: Case 5 - Full length 15°conical - Iso pressures

Figure K.16: Case 5 - Full length 15°conical - Iso densities

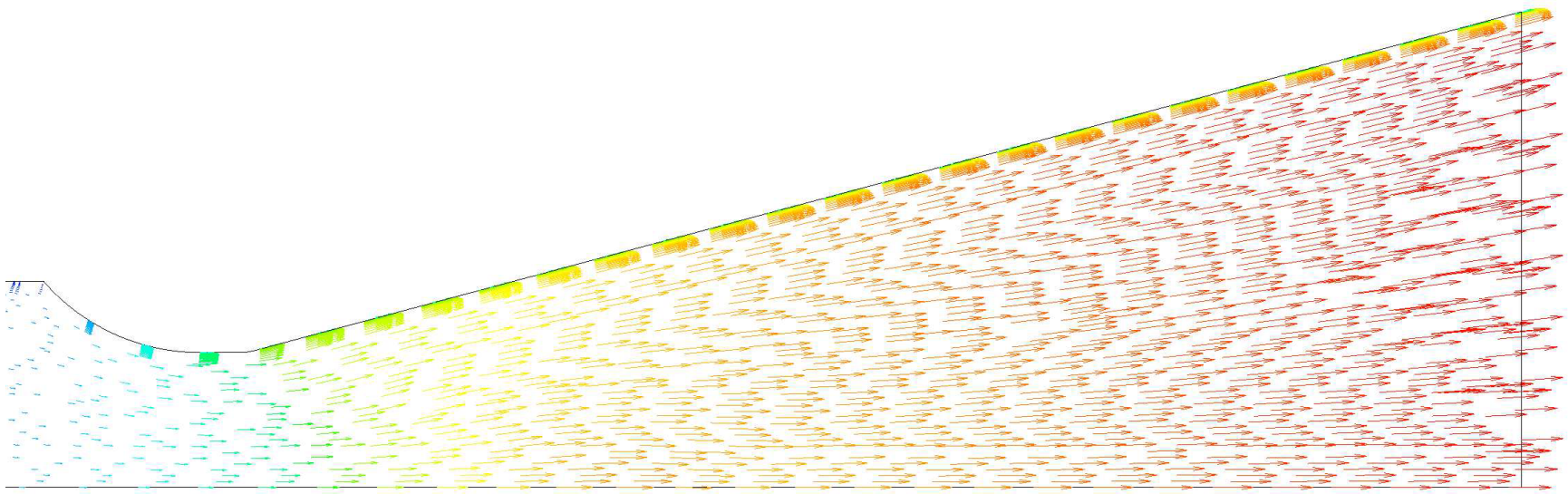

Figure K.17: Case 5 - Full length 15°conical - Velocity vectors

Figure K.18: Case 5 - Full length Rao parabolic approximation - Iso Mach numbers

Figure K.19: Case 5 - Full length Rao parabolic approximation - Iso temperatures

Figure K.20: Case 5 - Full length Rao parabolic approximation - Iso pressures

Figure K.21: Case 5 - Full length Rao parabolic approximation - Iso densities

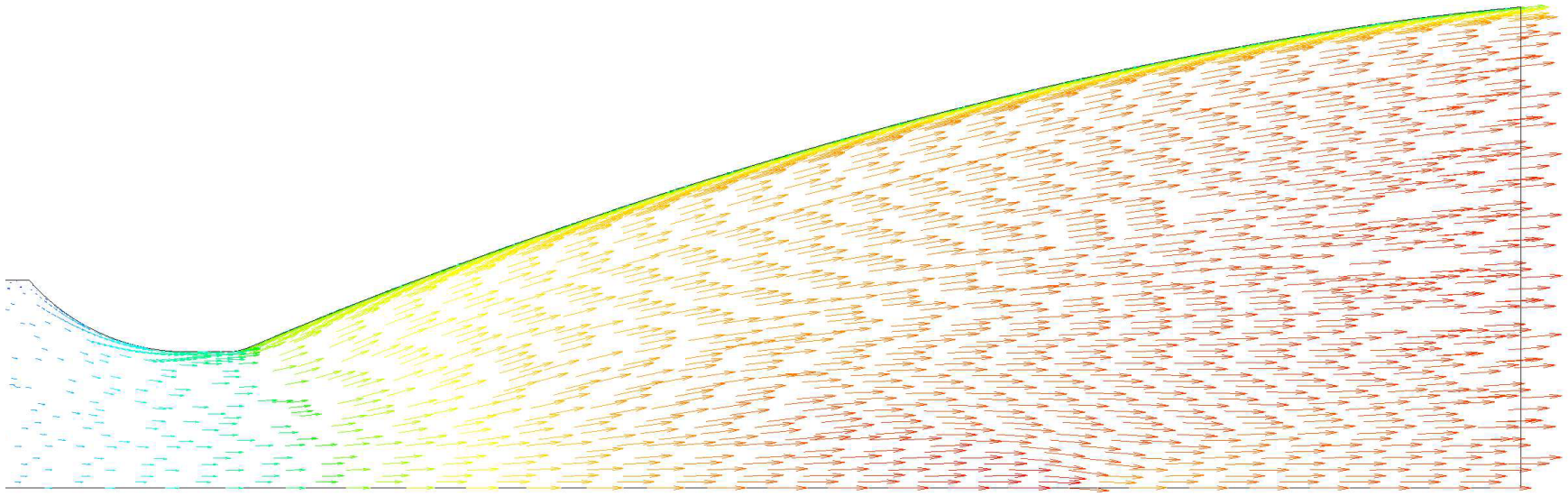

Figure K.22: Case 5 - Full length Rao parabolic approximation - Velocity vectors

Figure K.23: Case 5 - Full length CFD optimised - Iso Mach numbers

Figure K.24: Case 5 - Full length CFD optimised - Iso temperatures

Figure K.25: Case 5 - Full length CFD optimised - Iso pressures

Figure K.26: Case 5 - Full length CFD optimised - Iso densities

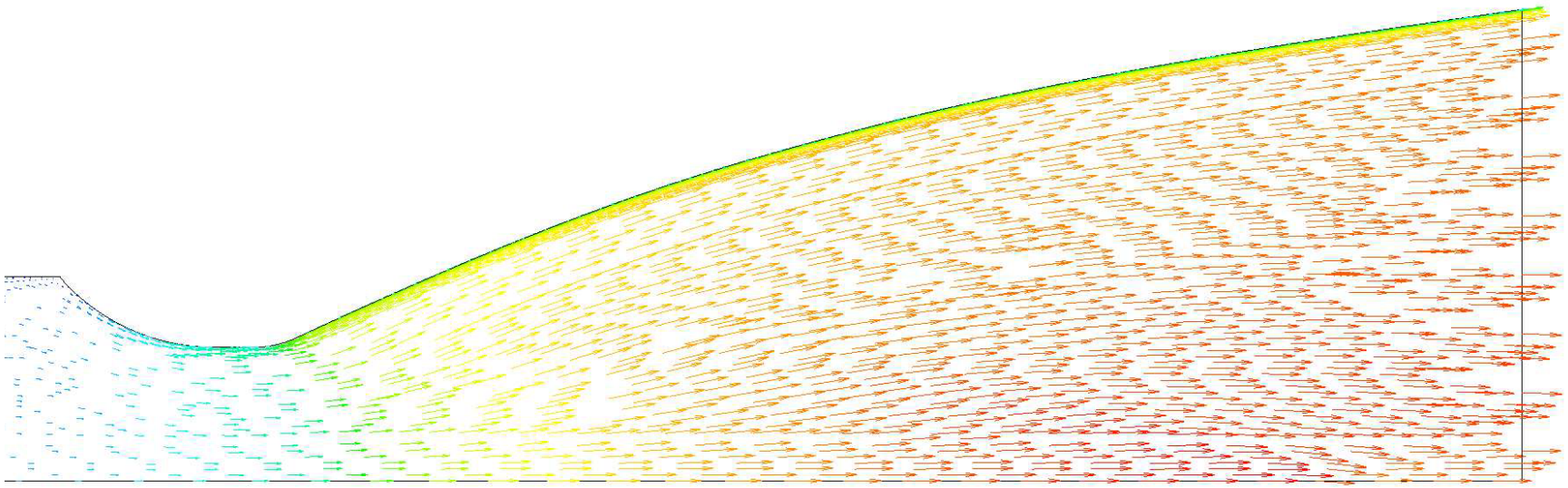

Figure K.27: Case 5 - Full length CFD optimised - Velocity vectors

APPENDIX L Case 6 - Data

	Input Parameters				Output Parameters		
No	Ri [mm]	θi [degree]	x2 [mm]	R2 @ x2 [mm]	θe [degree]	Mass Flow [kg/s]	Total Thrust [N]
1	6.401	25.722	89.384	32.580	11.087	-6.5065	14414.9
2	6.427	26.333	84.322	34.542	11.519	-6.5065	14414.7
3	6.539	25.430	85.238	34.174	11.651	-6.5059	14414.2
4	6.485	25.731	83.929	34.404	12.128	-6.5062	14414.0
5	6.636	25.715	90.293	32.100	11.931	-6.5064	14413.8
6	6.472	25.980	88.075	32.809	11.193	-6.5065	14413.7
7	6.657	25.752	85.565	34.001	10.764	-6.5063	14413.3
8	6.401	25.722	89.384	32.580	11.087	-6.5058	14413.3
9	6.401	25.722	89.384	32.580	11.087	-6.5058	14413.3
10	6.478	26.677	87.376	33.361	11.670	-6.5061	14413.2
11	6.399	25.607	89.965	32.273	10.169	-6.5062	14413.1
12	6.393	25.255	93.456	30.433	11.009	-6.5064	14413.1
13	6.528	26.032	86.984	33.246	12.226	-6.5059	14413.0
14	6.410	25.914	97.529	28.492	10.878	-6.5065	14413.0
15	7.601	26.381	86.640	33.393	11.932	-6.5066	14412.8
16	6.827	25.548	87.147	33.413	11.809	-6.5058	14412.6
17	6.407	26.075	85.893	34.419	10.300	-6.5058	14412.5
18	6.519	26.038	90.620	31.997	11.407	-6.5060	14412.5
19	6.390	25.200	86.279	33.923	11.744	-6.5052	14412.5
20	6.523	26.296	89.311	32.235	11.520	-6.5063	14412.4
21	6.457	27.365	85.631	34.312	11.413	-6.5063	14412.2
22	6.473	26.941	89.704	32.166	11.335	-6.5059	14412.2
23	7.413	25.983	84.665	34.372	11.867	-6.5059	14412.1
24	6.976	25.526	84.420	34.490	10.823	-6.5061	14411.8
25	6.729	25.658	87.747	32.982	12.081	-6.5052	14411.7
26	6.603	25.709	86.656	33.626	10.147	-6.5058	14411.5
27	7.085	25.225	86.820	33.815	12.273	-6.5061	14411.5
28	6.427	26.333	84.322	34.542	11.519	-6.5052	14411.5
29	6.881	25.591	86.056	34.057	12.479	-6.5058	14411.4
30	6.653	25.248	94.365	29.952	12.170	-6.5063	14411.4
31	6.511	25.570	94.693	29.779	11.336	-6.5056	14411.0
32	6.405	25.994	91.711	31.353	10.426	-6.5057	14410.9
33	7.079	27.652	92.278	31.056	11.243	-6.5062	14410.5
34	6.759	25.281	88.456	33.183	11.332	-6.5052	14410.4
35	7.539	27.069	85.985	33.669	11.065	-6.5064	14410.3
36	6.397	25.335	87.638	33.499	10.505	-6.5052	14410.1
37	6.667	25.615	89.056	32.752	11.604	-6.5051	14410.1
38	6.403	26.258	94.038	30.331	10.091	-6.5058	14409.9
39	7.721	25.692	94.214	29.856	11.240	-6.5062	14409.9
40	6.638	25.443	87.965	33.396	12.637	-6.5058	14409.6
41	6.393	25.527	95.784	29.411	10.666	-6.5051	14409.4
42	6.854	25.496	88.238	33.068	10.776	-6.5051	14409.4
43	7.430	25.252	86.411	33.445	12.071	-6.5051	14409.3
44	7.100	27.997	90.961	31.438	11.325	-6.5061	14409.2
45	7.810	27.378	83.647	34.573	11.158	-6.5058	14408.9
46	7.100	28.000	90.910	31.430	11.500	-6.5062	14408.8
47	7.096	27.936	91.578	31.469	11.312	-6.5059	14408.8
48	7.086	27.768	92.224	31.273	11.272	-6.5061	14408.7
49	7.098	27.966	91.411	31.493	11.319	-6.5058	14408.7
50	6.956	25.268	85.729	34.260	10.718	-6.5049	14408.6
51	7.609	25.736	87.338	32.818	11.879	-6.5053	14408.6
52	6.446	25.349	91.275	32.043	12.281	-6.5054	14408.5
53	7.092	27.865	91.887	31.396	11.296	-6.5058	14408.5
54	7.712	25.500	84.829	34.010	11.449	-6.5052	14408.4
55	7.778	26.021	92.355	31.189	10.172	-6.5059	14408.4
56	6.542	25.292	88.729	33.131	12.438	-6.5053	14408.3
57	7.705	26.747	85.876	34.186	12.085	-6.5051	14408.2
58	7.659	25.629	87.011	33.014	12.342	-6.5052	14408.1
59	7.572	25.963	94.578	30.373	10.723	-6.5062	14407.8
60	7.625	28.618	84.371	34.412	11.357	-6.5063	14407.7
61	7.770	25.597	96.881	29.041	10.093	-6.5059	14407.7
62	7.483	28.016	83.978	34.481	11.595	-6.5052	14407.3
63	7.799	27.446	98.238	28.397	10.358	-6.5061	14407.3
64	7.098	27.971	91.378	31.494	11.320	-6.5051	14407.2
65	7.099	27.984	91.189	31.471	11.323	-6.5052	14407.2
66	7.671	26.102	85.265	33.320	12.138	-6.5061	14407.1
67	7.554	26.639	85.331	33.631	12.416	-6.5051	14407.1
68	6.390	30.170	98.906	28.287	10.000	-6.5060	14406.7
69	7.288	25.295	85.320	34.096	10.145	-6.5050	14406.6
70	6.594	25.285	90.729	31.411	10.016	-6.5052	14406.3
71	7.640	28.338	82.996	34.539	11.237	-6.5060	14406.2
72	7.696	26.360	85.004	33.734	10.655	-6.5058	14406.2
73	7.692	28.295	84.305	34.309	11.131	-6.5052	14406.1

Figure L.1: Case 6 - Design table - Page 1/2

74	7.766	25.333	94.295	30.890	10.383	-6.5060	14404.3
75	7.683	25.328	83.956	33.550	12.615	-6.5059	14404.2
76	7.788	26.962	85.658	33.251	11.529	-6.5052	14403.5
77	7.100	30.800	96.708	28.632	10.000	-6.5061	14403.0
78	7.283	25.350	98.638	28.690	11.093	-6.5058	14402.6
79	7.781	29.198	83.389	34.447	10.999	-6.5052	14401.4
80	7.100	30.800	93.997	29.879	10.000	-6.5061	14401.1
81	6.403	30.763	87.121	33.315	12.465	-6.5062	14401.0
82	7.100	30.800	98.068	29.021	10.000	-6.5061	14400.1
83	7.100	30.800	92.059	30.832	10.000	-6.5058	14400.0
84	7.100	29.960	93.252	29.959	10.000	-6.5061	14399.1
85	7.100	28.000	88.532	34.055	11.325	-6.5053	14398.2
86	7.100	30.800	96.073	30.059	10.000	-6.5051	14397.7
87	7.100	29.960	90.732	31.079	10.000	-6.5061	14397.7
88	7.100	28.000	91.027	32.810	11.325	-6.5053	14397.4
89	7.810	29.960	89.078	33.728	10.000	-6.5064	14397.4
90	7.100	30.800	88.297	33.932	10.000	-6.5051	14397.2
91	7.810	29.960	93.131	29.874	10.000	-6.5060	14396.0
92	7.100	30.800	93.298	29.763	10.000	-6.5060	14395.4
93	7.810	29.960	93.887	31.420	10.000	-6.5061	14394.7
94	7.100	30.800	92.783	32.087	10.000	-6.5052	14393.1
95	7.810	29.960	91.056	33.017	10.000	-6.5059	14392.2
96	7.810	29.960	97.389	29.750	10.000	-6.5060	14391.5
97	7.810	29.960	96.806	30.116	10.000	-6.5060	14390.6
98	7.100	30.800	93.095	29.595	10.000	-6.5063	14390.6
99	7.810	29.960	89.066	31.584	10.000	-6.5052	14389.9
100	7.100	30.800	91.555	32.946	10.000	-6.5053	14389.4
101	7.100	30.800	89.403	34.162	10.000	-6.5061	14389.0
102	7.100	30.800	88.897	31.613	10.000	-6.5057	14389.0
103	7.691	25.726	99.063	29.087	10.862	-6.5060	14388.7
104	7.100	30.800	90.683	30.746	10.000	-6.5051	14387.3
105	7.100	30.800	86.139	32.771	10.000	-6.5053	14385.7
106	7.810	29.960	92.677	29.446	10.000	-6.5063	14384.7
107	7.100	29.960	85.923	32.507	10.000	-6.5058	14382.3
108	7.100	29.960	88.228	31.448	10.000	-6.5057	14380.8
109	7.100	30.800	93.863	28.933	10.000	-6.5051	14380.6
110	7.100	30.800	98.422	29.866	10.000	-6.5060	14378.1
111	7.100	30.800	95.094	31.636	10.000	-6.5051	14377.3
112	7.100	29.960	83.749	33.297	10.000	-6.5050	14376.7
113	7.100	30.800	85.119	32.730	10.000	-6.5057	14374.0
114	7.100	30.800	83.288	33.510	10.000	-6.5050	14373.4
115	7.810	29.960	91.338	33.782	10.000	-6.5062	14372.9
116	7.810	29.960	84.271	32.823	10.000	-6.5057	14370.0
117	7.100	30.800	90.150	30.198	10.000	-6.5056	14367.3
118	7.810	29.960	93.158	33.020	10.000	-6.5057	14365.4
119	7.810	29.960	97.521	30.676	10.000	-6.5062	14365.2
120	7.100	30.800	87.228	31.390	10.000	-6.5057	14361.4
121	7.100	30.800	84.935	32.300	10.000	-6.5052	14355.8

Figure L.2: Case 6 - Design table - Page 2/2

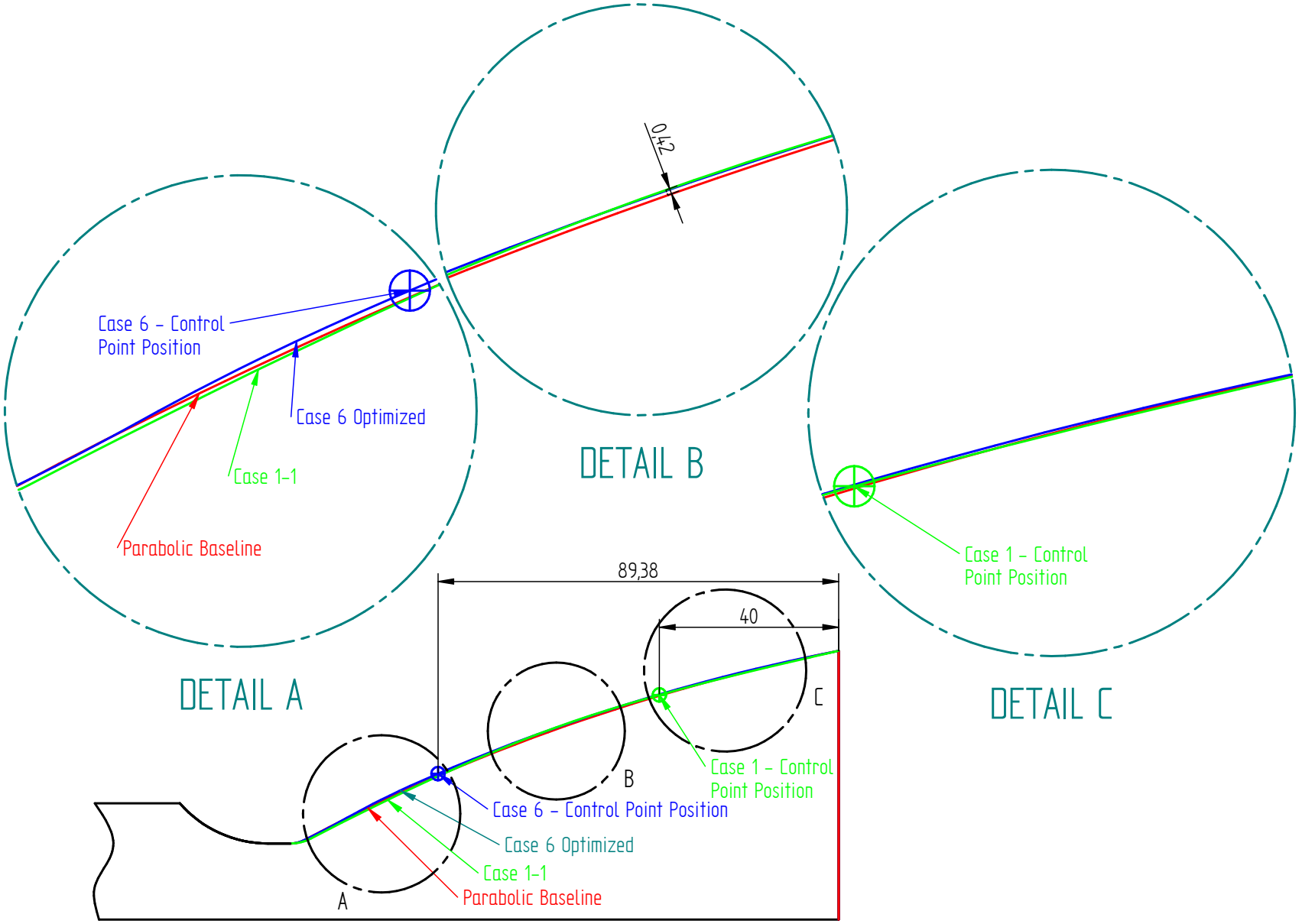

Figure L.3: Case 6 - Geometry comparison

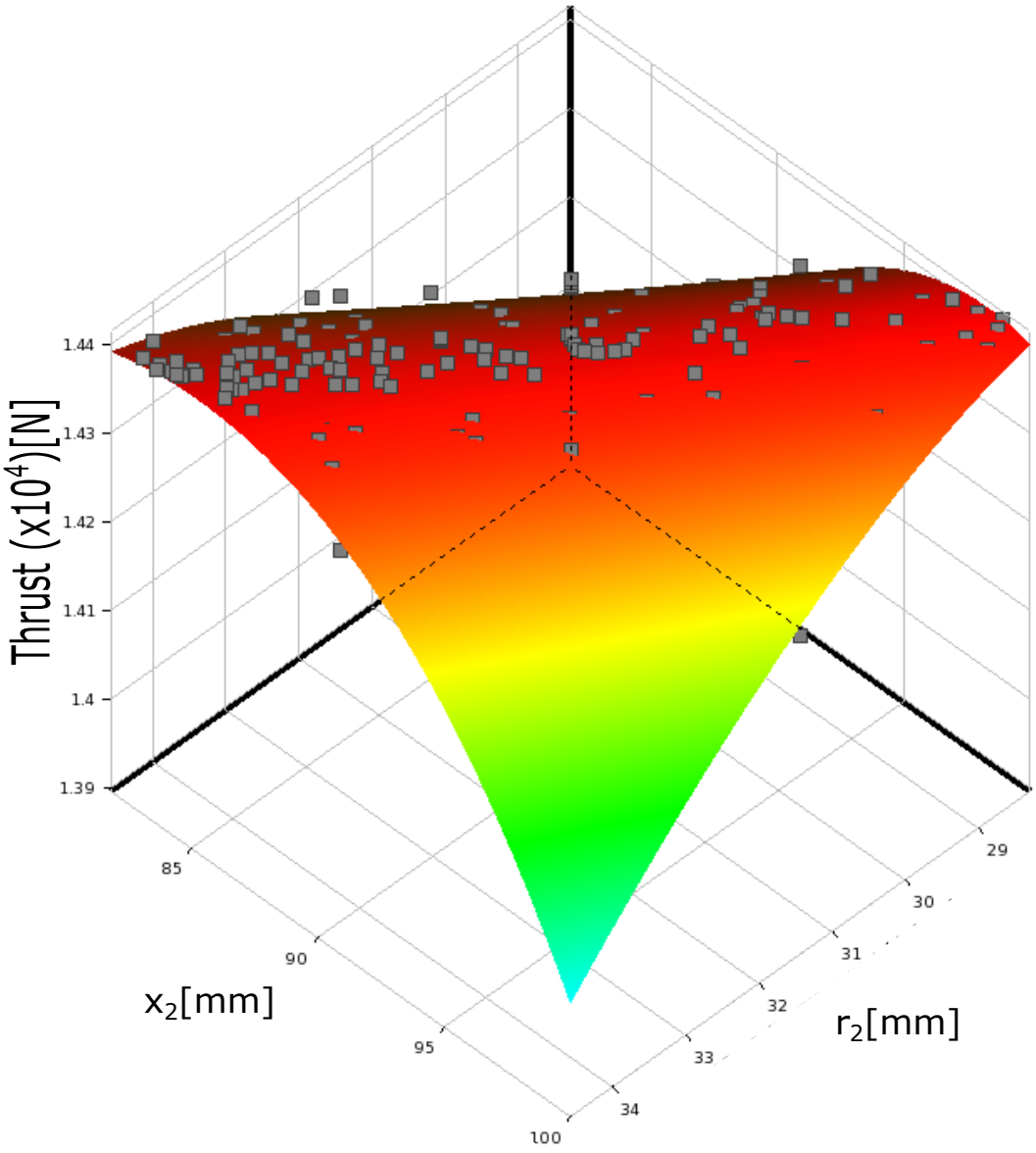

Figure L.4: Case 6 - x_2 vs R_2 Kriging response surface

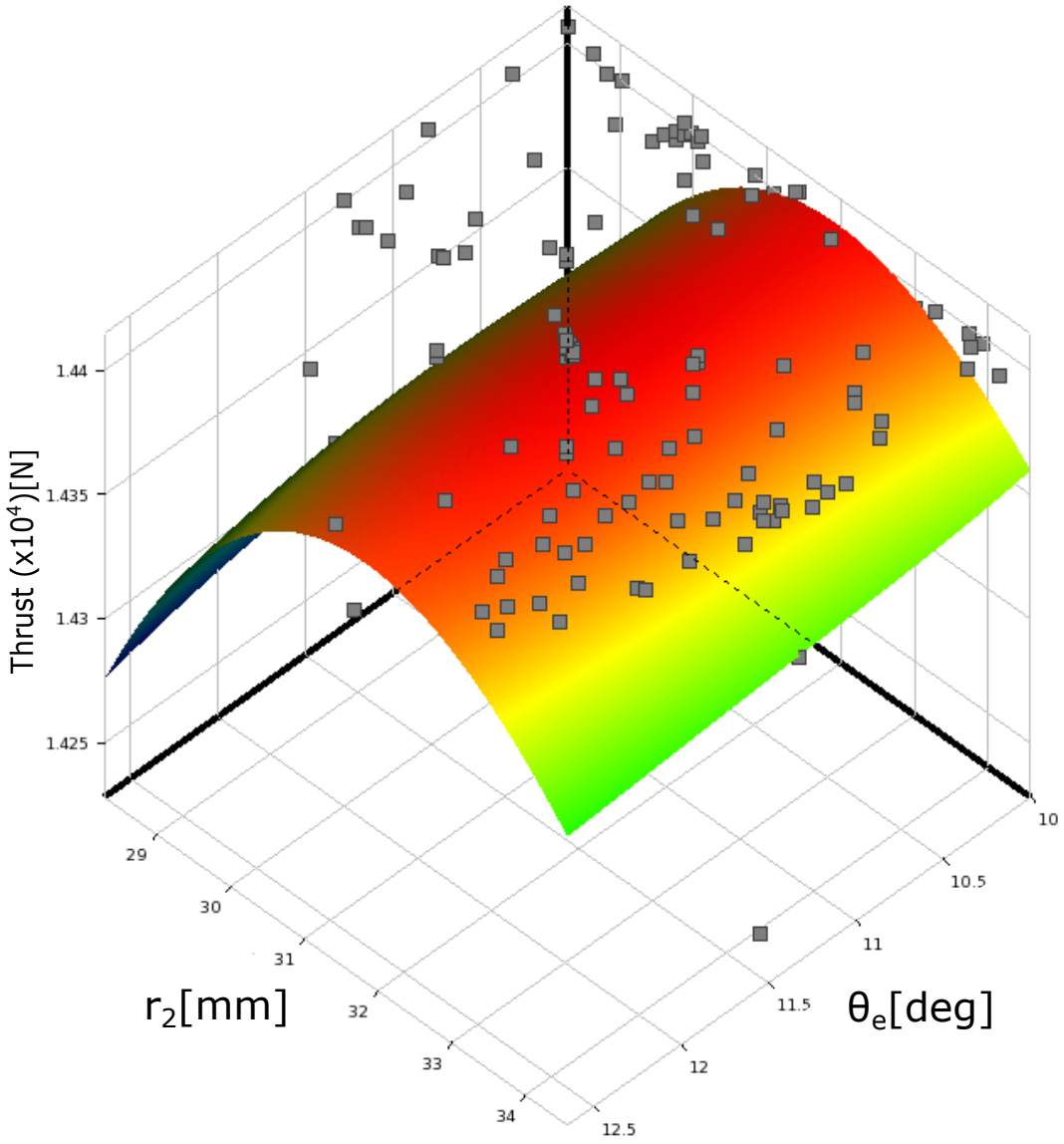

Figure L.5: Case 6 - R_2 vs θ_e Kriging response surface

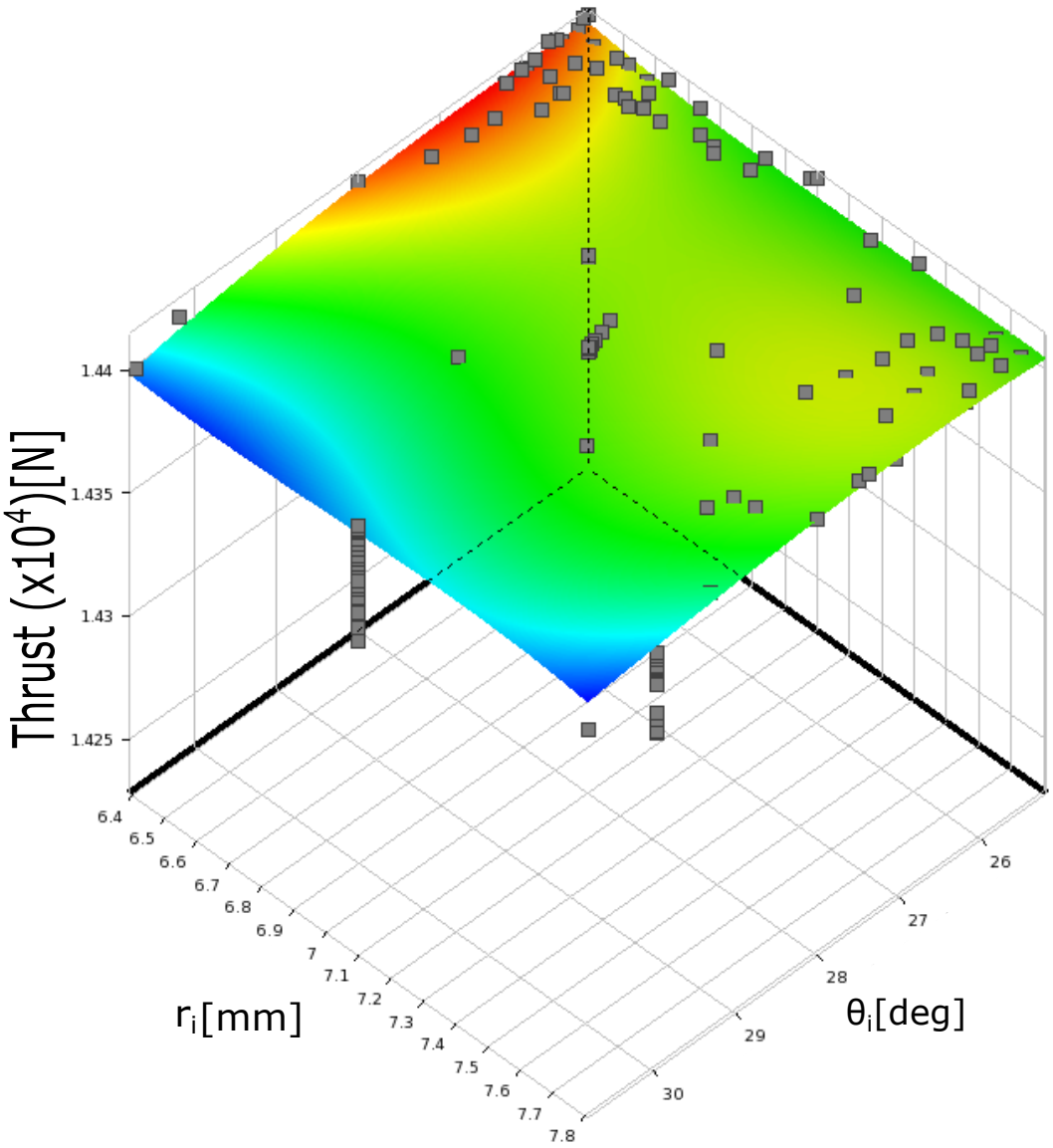

Figure L.6: Case 6 - r_i vs θ_i Kriging response surface

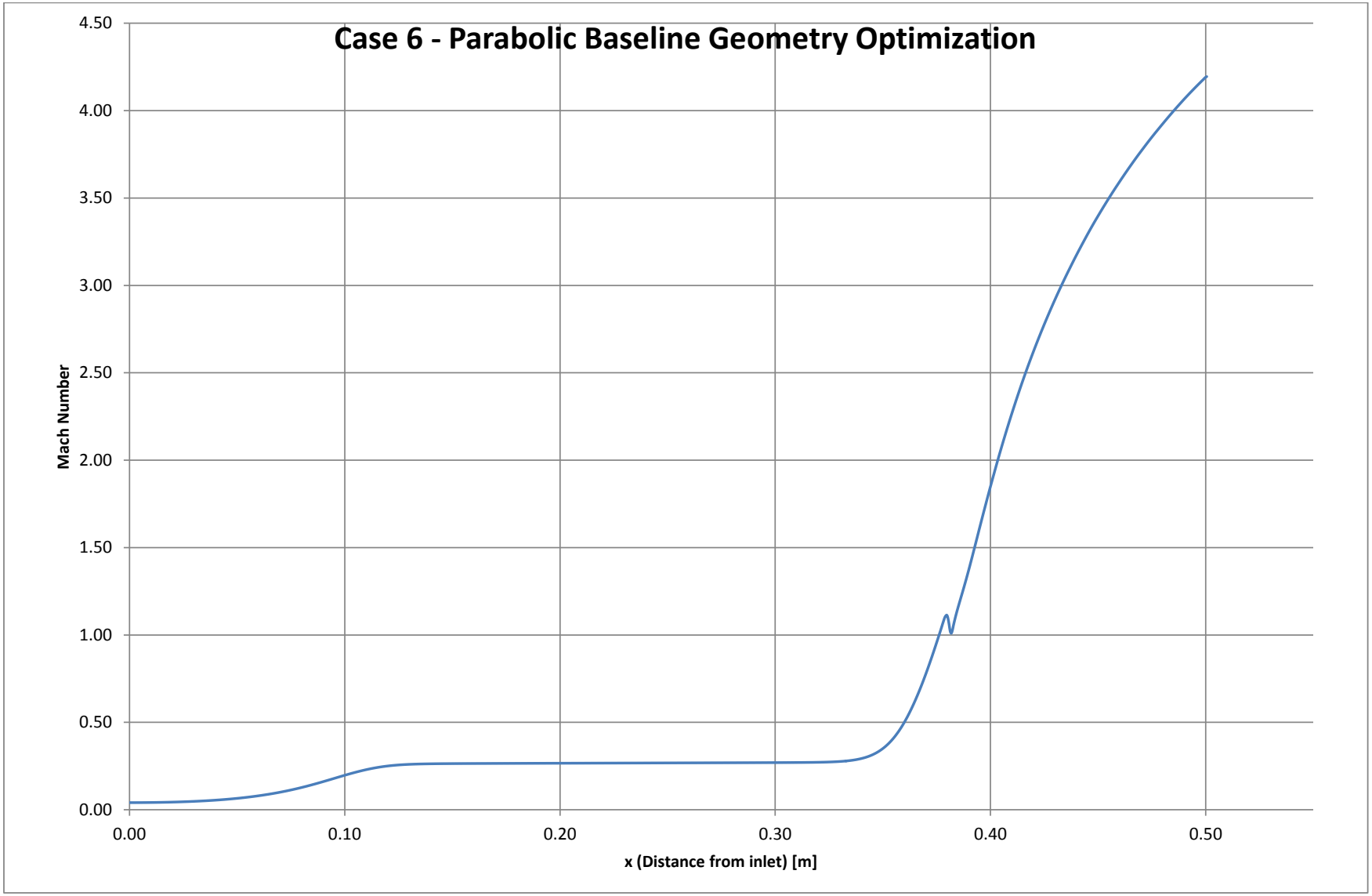

Figure L.7: Case 6 - Centerline Mach numbers

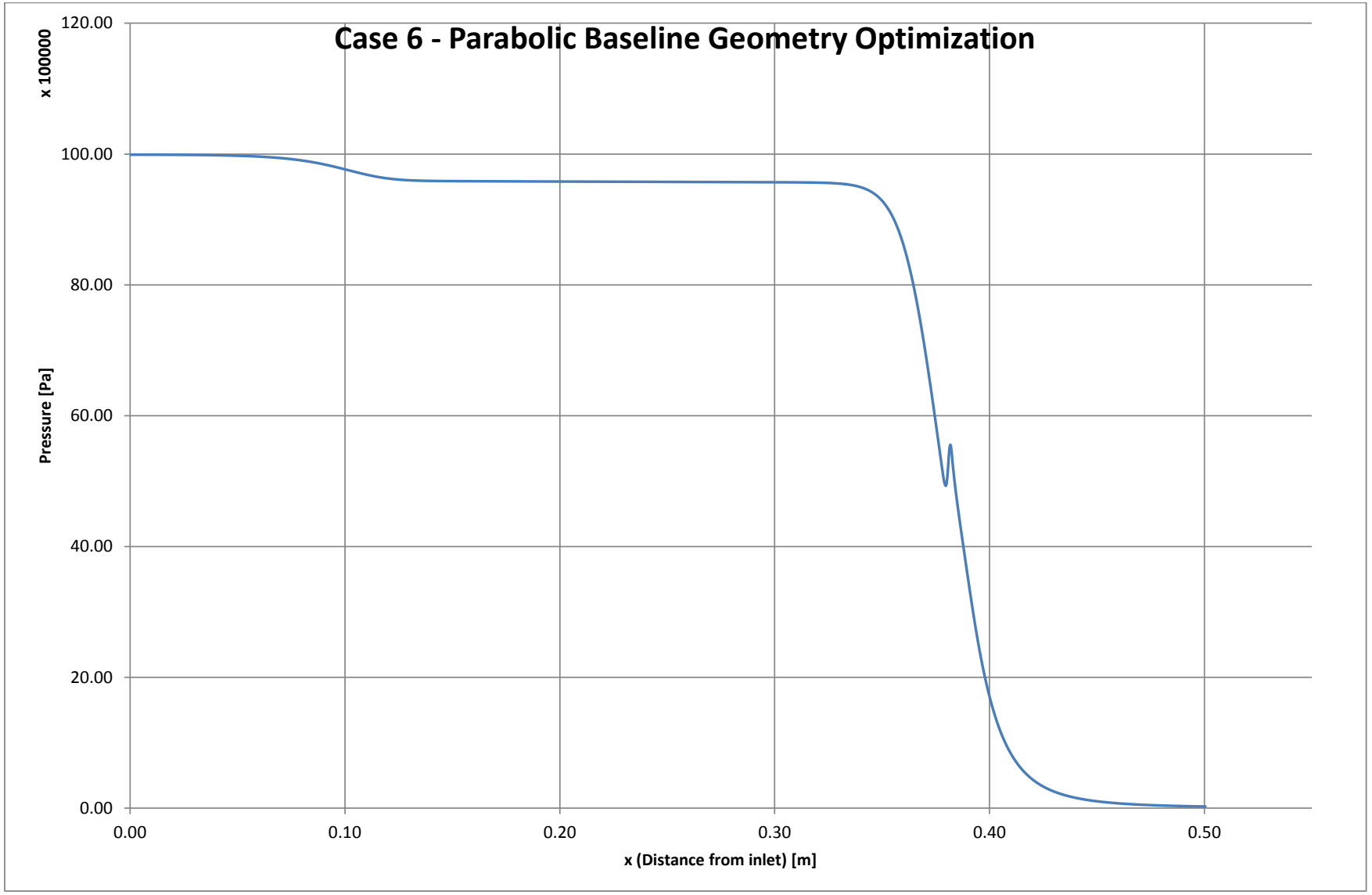

Figure L.8: Case 6 - Centerline pressures

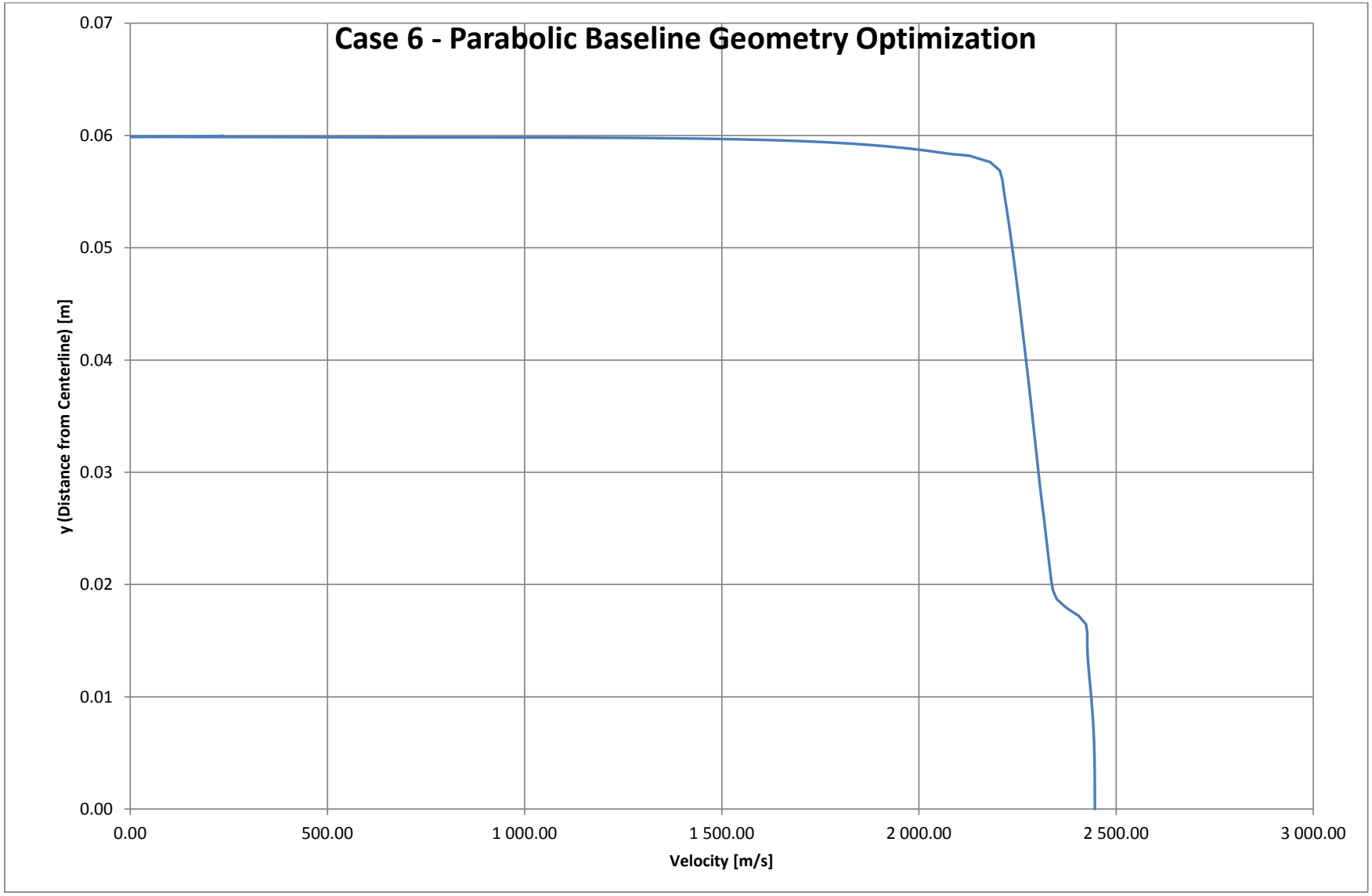

Figure L.9: Case 6 - Exit velocities

Figure L.10: Case 6 - Parabolic geometry baseline optimisation - Iso Mach numbers

Figure L.11: Case 6 - Parabolic geometry baseline optimisation - Iso temperatures

Figure L.12: Case 6 - Parabolic geometry baseline optimisation - Iso pressures

Figure L.13: Case 6 - Parabolic geometry baseline optimisation - Iso densities

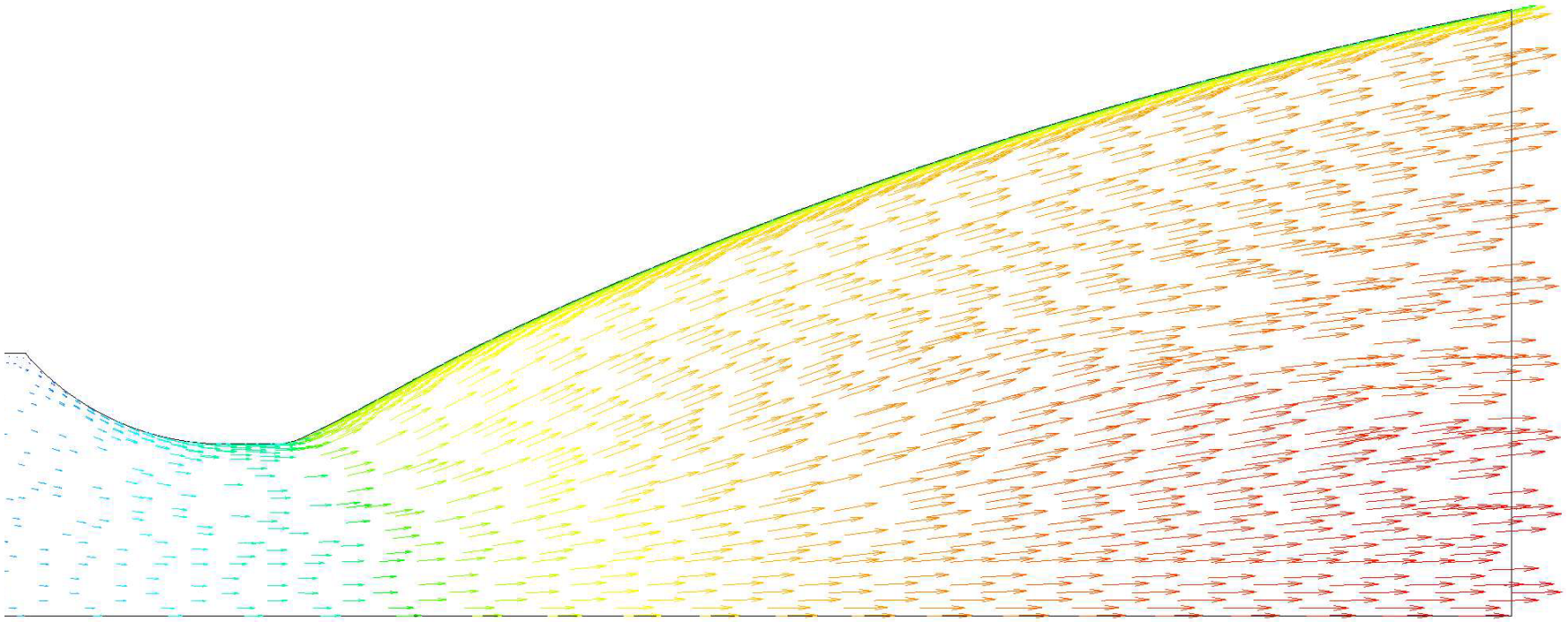

Figure L.14: Case 6 - Parabolic geometry baseline optimisation - Velocity vectors